THE UNIVERSITY *of* EDINBURGH

Micromagnetic Modelling of Imperfect Crystals

Pádraig Ó Conbhuí

THE UNIVERSITY
of EDINBURGH

Thesis submitted for the degree of Doctor of Philosophy

School of GeoSciences

University of Edinburgh

2018

Abstract

In paleomagnetism, practical measurements are rarely made using perfect, isolated, single-phase, ferromagnetic crystals. Experimental observations are typically made using magnetic materials formed by a variety of natural processes. In this thesis, we will look at bridging the gap between current numerical modelling capability and experimental observations.

First, we work towards micromagnetic modelling of multi-phase magnetic materials, including magnetostriction, embedded in a rocky matrix, along with crystal defects. We present a derivation of the Boundary Element Method formulation used by the micromagnetics package, MERRILL, and provide an extension of this from single-phase materials to multi-phase. After discussing issues with previous approaches to modelling magnetostriction, we derive and present a more robust and flexible approach. This model of magnetostriction is suitable for non-uniform magnetizations, for multi-phase materials, and for arbitrary boundary conditions, and can be incorporated into MERRILL. We then outline a method for extending our model to materials embedded in an infinite elastic matrix of arbitrary elasticity. Finally, we present a method for modelling the magnetic response of a material due to crystal defects, along with a concrete example of a magneto-dislocation coupling energy at a magnetite-ilmenite boundary where stress due to lattice misfit is eased by regular edge dislocations.

Second, we work towards being able to verify micromagnetic models against nano-scale experimental data. To do this, we present two techniques for simulating electron holograms from micromagnetic modelling results, a technique capable of imaging magnetic structures at the nano-scale. We also present example electron holograms of commonly occurring magnetic structures in nano-scale rock and mineral magnetism, and highlight some distinguishing features, which may be useful for interpreting experimental electron holography data.

Lay Summary

Paleomagnetism is the study of how rocks record changes in the earth's magnetic field. The recordings made need to remain stable for thousands, millions, or even billions of years since the rock was formed. Verifying that a recording is stable for that length of time is an ongoing problem. One approach to verification is to use a technique called "micromagnetic modelling" to replicate a physical sample in a computer model, which can then be probed in a number of ways, and in more detail, than is available to a physical experiment. These computer experiments can then present some theoretical predictions of the stability of the physical recordings. This approach, however, requires that all the physics of the rock is adequately considered by the numerical model. It also requires that modelling results can be verified against physical samples.

Micromagnetic models in rock and paleomagnetism typically assume a perfect, isolated, stoichiometric crystal. This does not adequately account for the mechanical properties of the crystal, e.g. embedding in a larger rocky matrix, and dislocations due to crystal intergrowths, and their effect on the stability on its magnetic recording. The physical phenomena that can account for these are elasticity, dislocations, and magnetostriction. This thesis derives and presents the math necessary to model magnetostriction in a way that is compatible with current state-of-the-art micromagnetic modelling techniques of non-uniform magnetizations. It then presents some preliminary results for magnetic crystals using these modelling techniques. An extension of this modelling technique for embedding the crystal in a larger rocky matrix is also presented, along with a method for including dislocations (e.g. crystal intergrowths) into micromagnetic models.

For experimental verification, this thesis presents a technique for simulating a widely used experimental technique called "electron holography" for producing "magnetic induction maps." These magnetic induction maps are a measurement of the magnetization of a crystal at the nanometer scale. By simulating these maps for micromagnetic modelling results, it is possible to directly compare these theoretical measurements to experimental measurements as evidence the micromagnetic model produces the currect result.

Acknowledgements

There are a number of people I'd like to thank for their help and support during my PhD. First, and foremost, I'd like to thank Wyn Williams for his continued support and input throughout, and for putting up with my messing. He has been instrumental for putting me on the right track, and for keeping me there. I'd like to thank Les Nagy for help and input on the various problems and codes I've worked on. Karl Fabian has provided great insight and encouragement on most, if not all, topics included in this thesis.

As frequent collaborators, Adrian Muxworthy, Trevor Almeida, Richard Harrisson, and Josh Einsle provided much of the incentive for the work I've done here. Without their demand, their input, and their data, much of the progress made in this thesis might not have happened. Similarly, I've enjoyed and benefited the discussions I've had with Jay Shah and Miguel Valdez, who are in about the same position as I am, but from a more experimental side. I must thank Lawrence Mitchell for introducing me to Wyn, and for his help early in the PhD, pointing me towards some of the tools that would be instrumental to implementing the techniques discussed here. Similarly, Chris Johnson provided some great non-technical feedback and advice.

Most importantly, I need to thank my friends and family, who make life worthwhile. I'd like to thank Anna Curran, for being a beb. She means too much to me to summarize in a sentence. Ann, Pat, and Hazel Conway are each deserving of a medal for putting up with me for this long. Although they didn't really have a choice. I'm sure Ann will have something similar to say in her own thesis. Thanks go to my friends in Edinburgh, who made it worth sticking around, Rory McKavney, Matt Holloway, John Preston, Luca Forresta, and many many others. And Rory, especially, for encouraging my poor habits (and cleaning up after me last year).

Finally, many thanks to Adrian Muxworthy and Ian Main for examining this thesis. Similarly, apologies to Adrian Muxworthy and Ian Main for having to parse my particular style of writing, which likely reads more like code and comments than a flowing narrative. Not to mention my utter inability to write in a formal register.

Declaration

This thesis is my own composition. The work presented here is my own, except where explicitly referenced. This work has not been submitted for any other degree or other professional qualification. There are no other publications included within this thesis.

Pádraig Ó Conbhuí

Contents

Chapter 1

Introduction

Paleomagnetism is the study of changes in the Earth's magnetic field using magnetic recordings from rocks. Rock magnetism is the study of the behaviour of magnetic rocks. Naturally, rock magnetism is often employed in paleomagnetism to extract the recordings from the magnetic rocks. Natural samples tend to be imperfect: they are irregularly shaped, embedded in larger materials under pressure, twinned with other crystals. They are part of, and contain, intergrowths of other materials, and contain dislocations and inclusions. All of these contribute to internal stresses in the material (Appel and Soffel 1984). To account for these, we need techniques for modelling magnetic materials, for modelling inhomogeneous magnetic materials, and for modelling the effects of internal stresses and other mechanical deformations on the magnetization.

Ferromagnetic minerals with a cubic crystal structure are an abundant source of magnetic signal in natural rock samples. Iron oxide and iron titanium oxide minerals are particularly abundant, as in the ulvöspinel-magnetite and ilmenite-hematite series (Tauxe 2010). In this thesis, we will be mainly concerned with modelling magnetite and titanomagnetite with Ti substitution factor of 0.6, or TM60, as these are two are very commonly found in natural samples. We will be looking at magnetite and oxidized shells of magnetite for homogeneous and inhomogeneous materials. We will then look at TM60 when including the mechanical deformation of materials into micromagnetic models, as this material has a particularly strong magneto-mechanical coupling.

Finally, we will look at a magnetite-ilmenite lamellar structure for an inhomogeneous model which includes internal stresses due to incompatible lattice spacings of the two materials.

In this chapter, we will present some history and motivating factors for studying three main topics: micromagnetism, magnetostriction, and electron holography. In brief, micromagnetism is the primary tool we will be using to model magnetic grains, magnetostriction is the phenomenon we will be adding and using to include imperfections, and electron holography is a tool that can be used to verify our predictions.

1.1 Micromagnetism

Micromagnetism is a mathematical technique for describing the magnetic state of a material in terms of a continuous "magnetization" (Kittel 1949). This is distinct from the actual picture of discrete, free electrons each contributing to the overall magnetic state. By using a continuous function and adapting the governing equations of the physics to a continuous function, the problem becomes more tractable. In particular, it allows the equations of motion of the system to be posed in terms of a set of partial differential equations (PDE). In this manner, describing the behaviour of the system, and finding magnetic states which will remain stable over long periods of time can be expressed as well studied PDEs.

As a very brief overview, the most basic elements needed to calculate the energy density, f, of a cubic ferromagnetic crystal due to a magnetization $\vec{M}$ is

$$\begin{aligned} f &= -K_1 \frac{1}{2}(\alpha_1^4 + \alpha_2^4 + \alpha_3^4) + A(\partial_i \hat{M}_j)(\partial_i \hat{M}_j) + (\partial_i \phi) M_i + \vec{H}^{\mathrm{z}} \cdot \vec{M} \\ \partial_i \partial_i \phi &= \partial_i M_i \\ \alpha_1 &= \hat{M} \cdot [100] \,, \quad \alpha_2 = \hat{M} \cdot [010] \,, \quad \alpha_3 = \hat{M} \cdot [001] \\ M_i M_i &= M_s \end{aligned} \tag{1.1}$$

where K_1 is the cubic anisotropy constant, A is the exchange constant, ϕ is the magnetic scalar potential, $\vec{H}^{\mathrm{z}}$ is the Zeeman / external field, α_i is the di-

rectional cosine of the magnetization with the ith cubic axis, and M_s is the saturation magnetization, a constant.

Each of these terms has a rich and detailed background, important for understanding the behaviour and stability of these remanent magnetizations. In this thesis, however, we are more concerned with simply calculating them and studying the results. For an in depth review, Kittel's paper (Kittel 1949) is essential. In particular, we are interested in finding remanent magnetizations. A remanent magnetization is an $\vec{M}$ which locally minimizes f. By locally minimize, we mean $\vec{M}$ is a value such that small perturbations to $\vec{M}$ result in a larger f, i.e. $f(\vec{M} + \vec{\epsilon}) \geq f(\vec{M})$ for any small $\vec{\epsilon}$. A stable remanent magnetization is an $\vec{M}$ such that the value of f continues to increase even at relatively large perturbations of $\vec{M}$. It should be clear from the presented energy, particularly with the presence of the $\hat{M}$ and $M_i M_i = M_s$ terms representing nonlinear components of the energy, that finding remanent magnetizations is not a straightforward task.

Rock magnetism benefits greatly from micromagnetism. Initially, micromagnetism allowed analytic solutions to be found for the behaviour and stability of perfect, regularly shaped grains, with uniform magnetization as found in work by Néel (1949) and Kittel (1949). Uniformly magnetized grains are also called single domain (SD). Of particular interest here are the relaxation equations by Néel (1949) which predict the superparamagnetic (SP) threshold. The SP threshold is a grain size below which the thermal energy of a rock is of the same order of magnitude of the energy barrier between remanent magnetic states. As a result, the grain may spontaneously change magnetic states at a timescale which would render the magnetic recordings unreliable. As SP grains are a subset of SD grains, this means not all SD grains are useful recorders of magnetic signal.

From there, models such as the Amar model (Amar 1958) allowed researchers to reason about multidomain (MD) grains, and the Morrish and Yu model (Morrish and Yu 1955) allowed researchers to reason about single vortex (SV) states, in regular geometries. These single vortex states fall under a category of states called pseudo-single domain (PSD) (Butler and Banerjee 1975), so named because they tend to behave similarly to single domain states. In particular, it

was found that PSD states, in which two domain (TD) states are sometimes also included, make up a significant portion of the stable magnetic signal of natural grains (Moskowitz 1980), and in some cases the SD range can be very narrow (Butler and Banerjee 1975), leaving PSD states as the dominant carriers. This is matched by experimental observations (Day, Fuller, and Schmidt 1977). These analytic approaches, however, suffer from many simplifications to make the equations tractable.

The introduction of 3D numerical micromagnetic models to rock magnetism allowed for reasoning about remanent states of irregular geometries with non-uniform magnetizations (Williams and Dunlop 1989). The introduction of the finite element method (FEM) (Davies 2011) to micromagnetic modelling (Fredkin and Koehler 1987) allowed more accurate consideration of curved surfaces, such as spheres and surface effects. In recent years, an easy to use micromagnetics package, MERRILL, has been released, targeted at the paleomagnetic community.

In this thesis, we will derive the energies and effective fields calculated by MERRILL when looking for remanent magnetizations. This will act as an introduction to the finite element method, and as documentation of the code for MERRILL. It will also present a technique used in MERRILL for handling infinite domains using finite computer space. With the derivations done here, it will be easier to see how later derivations of magnetoelastic and magneto-dislocation energies might be integrated into MERRILL.

Initially, the energies and effective fields will be derived for a single-phase material. That is, a geometry whose material parameters are constant throughout. We will then derive an extension of these to a multi-phase material. A multi-phase material has piece-wise constant material parameters. We will not, however, present the optimization and minimization techniques used by MERRILL to find the remanent magnetizations.

After the derivation, we will present some example results using MERRILL. We will present MERRILL's solution to the Standard Problem No. 3 posed by the μMAG group at NIST (μMAG 2017). This will act as a verification that MERRILL works as expected for single-phase materials. Then we will present a result for a core-shell model of a truncated octahedron of magnetite with a

hematite shell.

1.2 Magnetostriction

Magnetostriction describes a phenomenon where the magnetization can have an effect on the stress and strain of a magnetic material, and vice versa (Kittel 1949). In brief, when a ferromagnet is magnetized along a particular direction, the material tends to stretch along that direction. Typical micromagnetic models tend to simplify magnetostriction by including a term suitable for a uniform magnetization. In the case of a uniformly magnetized, cubic, ferromagnetic crystal, the effect of magnetostriction can be bundled into the anisotropy term, as described by Kittel (1949). However, this approximation is not, as we will show, appropriate for non-uniformly magnetized materials.

Another approximation used for the application of magnetostriction is Kittel's effective uniaxial anisotropy for a uniformly magnetized ferromagnet under a uniaxial tension. Various treatments have used this approach, substituting the cubic anisotropy for this effective uniaxial anisotropy, to determine the behaviours of domain walls for highly magnetostrictive materials

In this thesis, we will derive and present a subset of Brown's magnetostrictive equations of motion (Brown 1966) which should be sufficient for micromagnetic modelling of nano-scale ferromagnets in low magnetic fields, and derive a FEM formulation of these. We will also present some preliminary modelling results, outlining how magnetostriction deforms materials for non-uniform magnetizations, and how including a full description of magnetostriction effects remanent magnetizations.

This formulation of magnetostriction will be the first step needed to model the natural rock samples we've described. The effects of material intergrowths, embedding in rocky matrices, materials under stress, can all be described in terms of mechanical effects, of stresses and strains on the materials. These mechanical effects then affect the magnetic behaviour of the material via magnetostriction. By coupling this with the multi-phase description of magnetic materials discussed in the previous section, we can present a theory capable of

modelling imperfect magnetic crystals.

1.3 Electron Holography

An important step to ensuring the theoretical predictions of the previously discussed models are accurate is by comparing predictions to experiment. Paleomagnetism, again, presents a challenge. Early studies into rock magnetism were primarily of MD states with well defined domain walls using techniques like Bitter patterns (Halgedahl 1991). These magnetic grains could be tens of microns in size. However, the SD and PSD ranges are typically on the submicron scale, typically tens, or hundreds of nanometers. Further, the PSD states represent a rich non-uniform magnetization, not easily understood by measurements of the outside of the material.

Electron holography an experimental technique, capable of measuring magnetic fields on the nano-scale, and and from within the material (Tonomura et al. 1980). In particular, off-axis electron holography is a useful technique for generating electron holograms, and finding the "direction" of the contours in electron holograms, describing the direction of the in-plane magnetic field they represent (Lehmann and Lichte 2002). This represents a viable technique for making meaningful measurements of PSD grains. In particular, with the development of models of electron holography (Keimpema, De Raedt, and De Hosson 2006) to use with models of micromagnetism, we have techniques for quantitatively comparing experimental data with theoretical predictions (Almeida et al. 2016). In this thesis, we will derive two techniques for numerical electron holography simulation for use with the numerical micromagnetic models developed here.

We will present a range of simple remanent SD, flower-state (FS) and PSD states, and their electron holograms from various orientations and angles. This will represent a Rosetta stone for converting from electron holograms back to remanent states for nano-scale materials, as predicted by numerical micromagnetic modelling. This should be a useful reference for reasoning about magnetic states inferred from electron holograms in physical experiments. In

particular, we will discuss features of electron holograms that are indicative of various states and orientations, and features that are red herrings. We will also discuss features that cannot be distinguished in electron holograms, either due to lack of feature resolution or due to symmetries inherent to the process of electron holography.

1.4 Notation

This thesis is rather math-heavy. We present here the notation used, and the typical meaning of various symbols used throughout.

Typically, we will prefer to use a functional notation. For a function $f(x)$, the derivative at x is $\frac{\partial f}{\partial x}(x)$. However, this presents a potential source of confusion. When taking the derivative of $f(x)$, should we take the derivative of only f, or should we apply the chain rule, and take the derivative of x as well? This is particularly confusing when performing partial integration of integrals, or changes of coordinates with derivatives of functions.

Unless otherwise states, one may assume functional notation. We will use the explicit notation $f(x)$ in a number of cases, but it should be reasonably clear from context what is happening. This can, however, get a little confusing when multiplying a function by a brace. For three functions f, g, and h, we can write, in our notation, $f \cdot g + f \cdot h$. The value at x is $(f \cdot g + f \cdot h)(x) = f(x)g(x) + f(x)h(x)$. However, we can also write $f \cdot g + f \cdot h = f \cdot (g + h)$. Without the explicit "$\cdot$" for function multiplication, we would write $f(g + h)$ which could be confused for the evaluation of f at a point $g + h$, or perhaps a function composition of f with $g + h$.

We choose the functional notation, with this in mind, since reasoning about derivatives is harder than confusion with notation. Mistakes or ambiguities in notation can be recovered from context, and from previous lines, while mistakes in derivatives are fundamental errors.

We also use a number of shorthands for vectors, derivatives, and directional derivatives. In particular, we will be using Einstein notation for summation,

and four notations for derivatives, each with its own use. The following are equivalent

$$\begin{aligned}\frac{\partial\phi}{\partial x}+\frac{\partial\phi}{\partial y}+\frac{\partial\phi}{\partial z} &= \vec{\nabla}\phi \\ &= \partial_x\phi+\partial_y\phi+\partial_z\phi \\ &= \phi_{,x}+\phi_{,y}+\phi_{,z}\end{aligned}$$

and using implicit indexing and Einstein notation,

$$\begin{aligned}\frac{\partial^2\phi}{\partial x^2}+\frac{\partial^2\phi}{\partial y^2}+\frac{\partial^2\phi}{\partial z^2}+ &= \nabla^2\phi \\ &= \partial_i\partial_i\phi \\ &= \phi_{,ii}\end{aligned}$$

The $\frac{\partial}{\partial x}$ notation is the familiar derivative notation, and $\vec{\nabla}$ should be familiar from vector calculus. The notation ∂_x is a shorthand for $\frac{\partial}{\partial x}$. This is particularly useful, since it can be easily indexed. For example $\sum_i \partial_i = \partial_x + \partial_y + \partial_z$. It is also useful since it is clearly visible in equations, but still compact. The final notation, the comma notation $\phi_{,x}$ is typical of tensor calculus, where one often needs to manage a large number of indices, and a large number of derivatives applied to a tensor. In brief, everything after the comma is a derivative. The expression $\phi_{,x}$ is equivalent to $\frac{\partial\phi}{\partial x}$. Similar to ∂_i, it is easily indexed. On top of that, it is much clearer which object the derivative applies to. The expression $\partial_i f \partial_i g$, for example, is ambiguous. Do we mean $(\partial_i f)\cdot(\partial_i g)$ or $\partial_i(f\cdot(\partial_i g))$? By writing this as $f_{,i}\cdot g_{,i}$, it is entirely unambiguous. It also allows us to move $f_{,i}$ and $g_{,i}$ about the equation without much thought.

1.4.1 Vectors, Tensors

$$f_i\ g_i = \sum_i f_i\ g_i \quad \text{Using Einstein notation}$$

$$\vec{f} = \text{Vector}$$

$$\vec{f} = (f_1,\ f_2,\ \ldots) \quad \text{Implied vector subscripts}$$

$$\boldsymbol{f} = \text{Matrix or tensor. More than 1 index.}$$

$$\vec{f} \cdot \vec{g} = f_i\ g_i \quad \text{Dot product. Vector multiplication.}$$

$$\boldsymbol{f} : \boldsymbol{g} = f_{ijkl}\ g_{kl} \text{ or } f_{ijkl}\ g_{klmn} \quad \text{Tensor double dot product.}$$

$$\vec{f} \times \vec{g} = \epsilon_{ijk}\ f_j\ g_k \quad \text{Cross product}$$

1.4.2 Functions

$$f(x) = \text{Evaluation of } f \text{ at } x$$

$$f \cdot g = \text{Function multiplication}$$

$$(f \cdot g)(x) = f(x)\ g(x)$$

$$f \circ g = \text{Function composition}$$

$$(f \circ g)(x) = f(g(x))$$

1.4.3 Derivatives

$$\partial_i f = \frac{\partial f}{\partial x_i} \quad \text{Derivative shorthand, } i \text{ an index}$$

$$f_{,i} = \frac{\partial f}{\partial x_i} \quad \text{Derivative shorthand, } i \text{ an index}$$

$$f_{i,j} = \frac{\partial f_i}{\partial x_j} \quad \text{Derivative shorthand, } i, j \text{ are indices}$$

$$\vec{\nabla} = (\partial_x,\ \partial_y,\ \partial_z) \quad \text{Del, or nabla operator}$$

$$\vec{\nabla} f = \left(\frac{\partial f}{\partial x},\ \frac{\partial f}{\partial y},\ \frac{\partial f}{\partial z}\right) \quad \text{Gradient}$$

$$\vec{\nabla} \cdot \vec{f} = \partial_i f_i \quad \text{Divergence}$$

$$\vec{\nabla} \times \vec{f} = \epsilon_{ijk} \partial_j f_k \quad \text{Curl}$$

1.4.4 Integrals

$$\int_\Omega f\ dV = \text{3d volume integral of } f \text{ over } \Omega$$

$$\int_{\partial\Omega} f_i\ n_i\ dS = \text{2d surface integral over } \partial\Omega\text{, the boundary of } \Omega\text{, of } \vec{f} \text{ dotted with the oriented normal of the surface, } \vec{n}$$

$$\int_C f_i\ n_i\ dl = \text{1d line integral over the curve } C \text{ of } \vec{f} \text{ dotted with the oriented tangent of the curve, } \vec{n}$$

1.4.5 Magnetism

$$\vec{M} = \text{Magnetization}$$

$$M_s = \text{Saturation Magnetization } |M|$$

$$\vec{m} = \text{Unit magnetization } \vec{M}/M_s$$

$$\vec{H} = \text{Effective field}$$

$$\phi = \text{Magnetic scalar potential}$$

$$\vec{\nabla}\phi = \vec{H}$$

$$\nabla^2\phi = \vec{\nabla}\cdot\vec{M}$$

$$\vec{B} = \text{Magnetic field}$$

$$\vec{A} = \text{Magnetic vector potential}$$

$$\vec{\nabla}\times\vec{A} = \vec{B}$$

$$\vec{\nabla}\times\vec{\nabla}\times\vec{A} = \vec{\nabla}\times\vec{M}$$

$$\vec{\alpha} = \text{Directional cosines of the magnetization and the crystal axes}$$

$$B_1, B_2 = \text{Magnetostriction coupling constants}$$

$$B^0_{ij} = \text{Magnetostriction coupling tensor}$$

$$B^0_{ij} = \begin{cases} B_1\alpha_i^2 & \text{if } i = j \\ B_2\alpha_i\alpha_j & \text{if } i \neq j \end{cases}$$

1.4.6 Elasticity

$$\sigma_{ij} = \text{Stress}$$

$$\varepsilon_{ij} = \text{Strain}$$

$$\vec{u} = \text{Displacement}$$

$$\varepsilon_{ij} = \frac{1}{2}(u_{i,j} + u_{j,i})$$

$$C_{ijkl} = \text{Stiffness tensor}$$

$$S_{ijkl} = \text{Compliance tensor (inverse of } \boldsymbol{C})$$

$$C_{ijkl}S_{klmn} = \frac{1}{2}(\delta_{im}\delta_{jn} + \delta_{jm}\delta_{in})$$

$$\vec{b} = \text{Burgers Vector}$$

$$b_i = -\oint_C u_i \, dl \quad \text{with } C \text{ counter-clockwise about dislocation line}$$

Part I

Micromagnetic Modelling

Chapter 2

MERRILL and the Finite Element Method

This chapter will start by deriving the equations used by MERRILL to calculate the demagnetizing field (often referred to as the "demag" field) using a joint Finite Element Method (FEM) and Boundary Element Method (BEM) technique. This combines techniques for generating and manipulating FEM weak forms and BEM integrals available in a number of introductory Finite Element texts, and techniques for transforming these forms into linear algebra equations. The primary reference text used while writing this chapter is (Davies 2011), along with a paper by Lindholm (1984) detailing an analytic solution for the BEM integral derived here. A short derivation of the single-phase equations (2.56) can be found in (Fredkin and Koehler 1990), while a thorough derivation will be presented here. After deriving the single-phase weak forms, we will present an extension to multi-phase weak forms.

After deriving the demagnetizing field weak forms, we will outline the transformation of these into linear algebra equations using the FEM, and then the extension of these needed to accommodate multi-phase materials. After that, we will derive the approach taken by MERRILL to calculate energy gradients for the main micromagnetic energies: the demagnetizing, exchange and the anisotropy energies.

The following chapter will present results from two models which incorpo-

rate these derivations: the μMAG problem #3 (μMAG 2017), which should act as a verification that MERRILL works correctly in single-phase; and then a core-shell model as an example of a multi-phase model, along with an efficient approach for finding critical grain sizes where multiple distinct solutions have the same energy.

An original contribution (but unoriginal result) in this chapter is the detailed derivation of the Boundary Element Method formulation by Fredkin and Koehler (1990) using the method outlined by Davies (2011) from the formulation of micromagnetism presented in this chapter and used throughout the thesis. I haven't found a fully worked derivation of the BEM formulation of micromagnetism anywhere. Another, original contribution (and original result) is the extension of this to multi-phase materials. Finally, while the conversion of PDEs, and in particular, micromagnetism, to a Finite Element formulation is well studied, the particular transformation of the magnetic equations to the matrices used in MERRILL has not previously been documented, along with the derivation of the effective fields. While not original, a derivation all in one place should be useful to future students and contributors to MERRILL.

2.1 Demagnetizing Field Calculations

Outline:
We will generate a weak form for an initial scalar magnetic potential, ϕ_M, using finite boundary conditions for a single-phase material. We will then present a weak form for the physical scalar potential, ϕ, in terms of the initial scalar potential, with boundary conditions $\phi = 0$ at infinity.

Next, we will present the transformations necessary to calculate ϕ at a single point in terms of an integral of ϕ_M over a finite domain using the Boundary Element Method. We will then present the final weak form, describing the physical scalar potential ϕ in terms of the initial scalar potential ϕ_M using finite boundary conditions.

Finally, we will present an extension of the single-phase approach to include multi-phase materials.

We want to calculate the demagnetizing field, which has well defined boundary conditions at infinity. To solve this on a computer, however, we need to describe the problem in terms of a finite space.

We will define a space $\Omega = \mathcal{R}^3$ representing all space. This will be split up into a finite magnetic region Ω_M containing a non-zero magnetization, and an infinite non-magnetic region Ω_0 where the magnetization is uniformly zero. The boundary of the magnetic region is entirely separate from the boundary at infinity.

By way of notation, we will denote the boundary of a region ξ as $\partial\xi$. So we can say concisely $\partial\Omega \cap \partial\Omega_M = \emptyset$. It is important to take care of the orientation of boundaries when using this notation and transforming to integrals over one boundary to integrals over another. This notation can become unwieldy quite quickly, so we will try to keep it to a minimum.

In micromagnetism, the demagnetizing field is given

$$\partial_i \partial_i \phi = \partial_i M_i \quad \text{in } \Omega_M \tag{2.1a}$$
$$\partial_i \partial_i \phi = 0 \quad \text{in } \Omega_0 \tag{2.1b}$$
$$\phi = 0 \quad \text{in } \partial\Omega \tag{2.1c}$$

As mentioned, the boundary conditions here are defined at infinity. It is this set of equations that we'll need to transform into an equivalent expression over a finite space.

2.1.1 Weak Form for the Initial Potential ϕ_M

To that end, we will begin by solving a related problem

$$\partial_i \partial_i \phi_M = \partial_i M_i \quad \text{in } \Omega_M \tag{2.2a}$$
$$\partial_i \phi_M = 0_i \quad \text{in } \partial\Omega_M \tag{2.2b}$$

which is defined over the finite volume of the magnetic material, and the boundary conditions are over a finitely sized boundary. The weak form can be found by multiplying by an arbitrary function ϕ' and integrating over the volume

$$\int_{\Omega_M} (\partial_i \partial_i \phi_M) \cdot \phi' \, dV = \int_{\Omega_M} (\partial_i M_i) \cdot \phi' \, dV \tag{2.3}$$

where dV denotes integration over a volume.

For any ξ and χ continuous over Ω, using integration by parts and applying the divergence theorem, we can say

$$\begin{aligned} \int_\Omega \xi \, \partial_i \chi_i \, dV &= \int_\Omega \partial_i (\xi \cdot \chi_i) \, dV - \int_\Omega (\partial_i \xi) \cdot \chi_i \, dV \\ &= \int_{\partial\Omega} n_i \cdot \xi \cdot \chi_i \, dS - \int_\Omega (\partial_i \xi) \cdot \chi_i \, dV \end{aligned} \tag{2.4}$$

where dS integration over a surface. This relation will be used rather frequently in this text.

Using this, we assume ϕ_M, M, and ϕ' are continuous over Ω_M,

$$\int_{\Omega_M} (\partial_i \phi_M) \cdot (\partial_i \phi')\, dV - \int_{\Omega_M} n_i \cdot (\partial_i \phi_M) \cdot \phi'\, dS = \int_{\Omega_M} M_i \cdot (\partial_i \phi')\, dV - \int_{\partial\Omega_M} n_i \cdot M_i \cdot \phi'\, dS \quad (2.5)$$

and setting $\partial_i \phi_M = 0$ in $\partial\Omega_M$

$$\int_{\Omega_M} (\partial_i \phi_M) \cdot (\partial_i \phi')\, dV = \int_{\Omega_M} M_i \cdot (\partial_i \phi')\, dV - \int_{\partial\Omega_M} n_i \cdot M_i \cdot \phi'\, dS \quad (2.6)$$

Moving the derivative off $\vec{M}$ and onto ϕ' is necessary here to properly account for uniformly magnetized materials in a practical computer implementation. For uniform $\vec{M}$, $\partial_i M_i$ would be uniformly 0 in Ω_M, and ϕ_M would therefore be 0.

We now have a finite, well behaved integral over the surface encoding this change instead, which is suitable for a computer implementation. Finite Element formulations of these equations are well studied, and we will derive the equivalent linear algebra expression for this integro-differential equation evaluated over a tetrahedralized domain later in this chapter.

The solution to (2.6) defines ϕ_M up to a gauge freedom, such that $\xi = \phi_M + \chi$ is also an answer for any χ such that $\partial_i \chi = 0$. This freedom does not effect the math laid out here, but in practice it can lead to singular matrices, which lead to numerical instabilities during linear algebra solves. Care should be taken to ensure the ϕ_M solved for in practice is uniquely defined or that the linear algebra solver is not sensitive to singular matrices.

Next, we rewrite (2.1), our original demagnetizing equations, as the homogeneous demagnetizing equations

$$\partial_i \partial_i (\phi - \phi_M) = 0 \quad \text{in } \Omega_M \quad (2.7a)$$

$$\partial_i \phi_M = 0_i \quad \text{in } \partial\Omega_M \quad (2.7b)$$

$$\partial_i \partial_i \phi = 0 \quad \text{in } \Omega_0 \quad (2.7c)$$

$$\phi = 0 \quad \text{in } \partial\Omega \quad (2.7d)$$

This homogeneous form allows us to use a BEM style transform.

2.1.2 The Green's Function

We will start by defining the fundamental solution to the Poisson equation in 3D, a Green's function

$$\psi_{\vec{w}}(\vec{x}) = -\frac{1}{4\pi|\vec{x}-\vec{w}|} \tag{2.8}$$

which is defined such that

$$\partial_i \partial_i \psi_{\vec{w}} = \delta^3(\vec{x}-\vec{w}) \tag{2.9}$$

where $\delta^3(\vec{x}-\vec{w})$ is the Dirac delta function in 3D

$$\delta^3(\vec{q}) = \delta(q_1)\delta(q_2)\delta(q_3) \tag{2.10}$$

For a Poisson equation in 3D

$$\partial_i \partial_i \chi = \xi \quad \text{in } \Omega \tag{2.11a}$$

$$\chi = 0 \quad \text{in } \partial\Omega \tag{2.11b}$$

the solution can be written

$$\chi(\vec{w}) = \int_\Omega \xi \cdot \psi_{\vec{w}} \, dV \tag{2.12}$$

We note there is a singularity in $\psi_{\vec{w}}$ around the point $\vec{w}$. So, in our weak form, we will omit a spherical region about $\vec{w}$ that we will denote Ω_ϵ. We will be defining $\vec{w}$ so it is on the surface $\partial\Omega_M$ (and thereby also on $\partial\Omega_0$. Upon applying the divergence theorem, turning volume integrals into surface integrals, this will make denoting surfaces a bit cumbersome. As a result, we will split the surfaces of integration up as in figure 2.1.

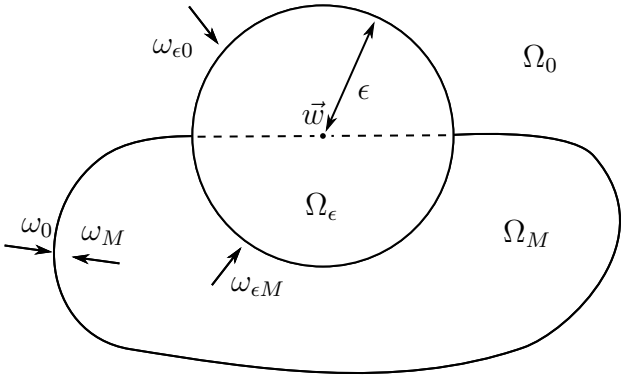

Figure 2.1: Integral domains with ball of size ϵ removed

2.1.3 Weak Form for the Homogeneous Demag Equations

We have the weak form for (2.7), taken with $\psi_{\vec{w}}$, and the integral taken over $\Omega - \Omega_\epsilon$

$$\int_{\Omega_M - \Omega_\epsilon} (\partial_i \partial_i (\phi - \phi_M)) \cdot \psi_{\vec{w}} \, dV + \int_{\Omega_0 - \Omega_\epsilon} (\partial_i \partial_i \phi) \cdot \psi_{\vec{w}} \, dV = 0 \tag{2.13}$$

Applying the divergence theorem twice, we get

$$\begin{aligned} \int_{\Omega_M - \Omega_\epsilon} (\phi - \phi_M) \cdot (\partial_i \partial_i \psi_{\vec{w}}) \, dV + \int_{\Omega_0 - \Omega_\epsilon} \phi \cdot (\partial_i \partial_i \psi_{\vec{w}}) \, dV \\ + \int_{\partial(\Omega_M - \Omega_\epsilon)} n_i (\partial_i (\phi - \phi_M)) \cdot \psi - n_i (\phi - \phi_M) \cdot (\partial_i \psi) \, dS \\ + \int_{\partial(\Omega_0 - \Omega_\epsilon)} n_i (\partial_i \phi) \cdot \psi - n_i \phi \cdot (\partial_i \psi) \, dS = 0 \end{aligned} \tag{2.14}$$

The first two integrals here contain $\partial_i \partial_i \psi_{\vec{w}}$, the Dirac delta function about $\vec{w}$. But the integral domain $\Omega - \Omega_\epsilon$ will never be evaluated at $\vec{w}$, even in the limit as $\epsilon \to 0$. So, these two terms are zero.

$$\begin{aligned} \int_{\partial(\Omega_M - \Omega_\epsilon)} n_i (\partial_i (\phi - \phi_M)) \cdot \psi - n_i (\phi - \phi_M) \cdot (\partial_i \psi) \, dS \\ + \int_{\partial(\Omega_0 - \Omega_\epsilon)} n_i (\partial_i \phi) \cdot \psi - n_i \phi \cdot (\partial_i \psi) \, dS = 0 \end{aligned} \tag{2.15}$$

Already the surface notation is getting a bit unwieldy. Looking at figure 2.1, we will split $\partial(\Omega_M - \Omega_\epsilon)$ up into $\omega_M + \omega_{\epsilon M}$ where ω_M refers to the surface of Ω_M which does not touch the ball Ω_ϵ, and $\omega_{\epsilon M}$ refers to the surface of the ball Ω_ϵ in the region Ω_M, from the Ω_M side. Similarly, the surface $\partial(\Omega_0 - \Omega_\epsilon)$ will be split up into $\omega_0 + \omega_{\epsilon 0} + \partial\Omega$ (remembering the boundary of Ω_0 also contains the infinite boundary)

$$\int_{\omega_M+\omega_{\epsilon M}} n_i(\partial_i(\phi - \phi_M)) \cdot \psi - n_i(\phi - \phi_M) \cdot (\partial_i \psi)\, dS + \int_{\omega_0+\omega_{\epsilon 0}+\partial\Omega} n_i(\partial_i \phi) \cdot \psi - n_i \phi \cdot (\partial_i \psi)\, dS = 0 \quad (2.16)$$

We will now look at cancelling out the terms in ϕ everywhere except the surface of Ω_ϵ. We note that ω_M and ω_0 denote the same surface, but with opposite normal directions. We can write, for $\vec{\xi}$ continuous across the boundary,

$$\int_{\omega_M} n_i \xi_i\, dS = -\int_{\omega_0} n_i \xi_i\, dS \quad (2.17)$$

and so, since ϕ is continuous across the boundary, the integrals of ϕ over ω_0 can be written in terms of integrals over ω_M

$$\int_{\omega_M+\omega_{\epsilon M}} n_i(\partial_i(\phi - \phi_M)) \cdot \psi - n_i(\phi - \phi_M) \cdot (\partial_i \psi)\, dS - \int_{\omega_M} n_i(\partial_i \phi) \cdot \psi - n_i \phi \cdot (\partial_i \psi)\, dS + \int_{\omega_{\epsilon 0}+\partial\Omega} n_i(\partial_i \phi) \cdot \psi - n_i \phi \cdot (\partial_i \psi)\, dS = 0 \quad (2.18)$$

cancelling out the ϕ terms over ω_M

$$-\int_{\omega_M+\omega_{\epsilon M}} n_i(\partial_i(\phi_M)) \cdot \psi - n_i(\phi_M) \cdot (\partial_i \psi)\, dS + \int_{\omega_{\epsilon M}} n_i(\partial_i \phi) \cdot \psi - n_i \phi \cdot (\partial_i \psi)\, dS + \int_{\omega_{\epsilon 0}+\partial\Omega} n_i(\partial_i \phi) \cdot \psi - n_i \phi \cdot (\partial_i \psi)\, dS = 0 \quad (2.19)$$

Next, noting that $\phi = 0$ and $\psi = 0$ on $\partial\Omega$, and their derivatives there are finite, the integral over $\partial\Omega$ is zero, so that domain can be dropped

$$-\int_{\omega_M+\omega_{\epsilon M}} n_i(\partial_i(\phi_M)) \cdot \psi - n_i(\phi_M) \cdot (\partial_i\psi)\, dS$$
$$+\int_{\omega_{\epsilon M}} n_i(\partial_i\phi) \cdot \psi - n_i\phi \cdot (\partial_i\psi)\, dS + \int_{\omega_{\epsilon 0}} n_i(\partial_i\phi) \cdot \psi - n_i\phi \cdot (\partial_i\psi)\, dS = 0 \quad (2.20)$$

and we can combine the integrals over ϕ

$$-\int_{\omega_M+\omega_{\epsilon M}} n_i(\partial_i(\phi_M))\cdot\psi - n_i(\phi_M)\cdot(\partial_i\psi)\, dS + \int_{\omega_{\epsilon M}+\omega_{\epsilon 0}} n_i(\partial_i\phi)\cdot\psi - n_i\phi\cdot(\partial_i\psi)\, dS = 0 \quad (2.21)$$

We now note that the domain $\omega_{\epsilon M} + \omega_{\epsilon 0}$ is the same as $\partial\Omega_\epsilon$ with the opposite normal, so for $\vec{\xi}$ continuous across those borders

$$\int_{\omega_{\epsilon M}+\omega_{\epsilon 0}} n_i\xi_i\, dV = -\int_{\partial\Omega_\epsilon} n_i\xi_i\, dV \quad (2.22)$$

so with ϕ and ψ continuous across that border, we get

$$-\int_{\omega_M+\omega_{\epsilon M}} n_i(\partial_i(\phi_M)) \cdot \psi - n_i(\phi_M) \cdot (\partial_i\psi)\, dS - \int_{\partial\Omega_\epsilon} n_i(\partial_i\phi) \cdot \psi - n_i\phi \cdot (\partial_i\psi)\, dS = 0 \quad (2.23)$$

We can now look at what happens in the limit as $\epsilon \to 0$.

2.1.4 Evaluating Limits

On the surface of the ball Ω_ϵ, which is centered at $\vec{w}$, the normal, facing away from $\vec{w}$, can be given

$$n_i = \frac{x_i - w_i}{|\vec{x} - \vec{w}|} \quad \text{in } \partial\Omega_\epsilon \quad (2.24)$$

For convenience, we work out $\partial_i \psi_{\vec{w}}$,

$$\begin{aligned}
\partial_i \psi_{\vec{w}} &= \frac{\partial}{\partial x_i} \frac{-1}{4\pi|\vec{x}-\vec{w}|} \\
&= -\frac{1}{4\pi} \frac{\partial}{\partial x_i} \frac{1}{\sqrt{(x_j - w_j)(x_j - w_j)}} \\
&= -\frac{1}{4\pi} \frac{w_i - x_i}{\left(\sqrt{(x_j - w_j)(x_j - w_j)}\right)^3} \\
&= \frac{x_i - w_i}{4\pi|\vec{x}-\vec{w}|^3}
\end{aligned} \tag{2.25}$$

and

$$\begin{aligned}
n_i \partial_i \psi_{\vec{w}} &= \frac{x_i - w_i}{|\vec{x}-\vec{w}|} \frac{x_i - w_i}{4\pi|\vec{x}-\vec{w}|^3} \\
&= \frac{1}{4\pi|\vec{x}-\vec{w}|^2} \quad \text{in } \partial\Omega_\epsilon
\end{aligned} \tag{2.26}$$

We will replace ϕ on the surface Ω_ϵ with evaluations of ϕ at $\vec{w}$ and some correction terms

$$\phi(\vec{x}) = \phi(\vec{w}) + \eta_1(\vec{x}) \tag{2.27}$$

$$(n_i \partial_i \phi)(\vec{x}) = (n_i \partial_i \phi)(\vec{w}) + \eta_2(\vec{x}) \tag{2.28}$$

which go to zero as ϵ goes to zero

$$\lim_{\epsilon \to 0} \eta_1 = 0 \tag{2.29}$$

$$\lim_{\epsilon \to 0} \eta_2 = 0 \tag{2.30}$$

We look at the limits of the integrals of ϕ, and their maximum values, starting with the $\partial_i \phi$ term

$$\begin{aligned}
\chi_2 &= \int_{\partial\Omega_\epsilon} n_i (\partial_i \phi) \cdot \psi \, dS \\
&= -\int_{\partial\Omega_\epsilon} ((n_i \partial_i \phi)(\vec{w}) + \eta_2) \cdot \frac{1}{4\pi|\vec{x}-\vec{w}|} \, dS
\end{aligned} \tag{2.31}$$

Since $|\vec{x} - \vec{w}| = \epsilon$ on Ω_ϵ, and the surface area of the sphere is $4\pi\epsilon^2$

$$\begin{aligned} |\chi_2| &= \left| - \int_{\partial\Omega_\epsilon} ((n_i \partial_i \phi)(\vec{w}) + \eta_2) \cdot \psi \, dS \right| \\ &\leq |n_i| |((n_i \partial_i \phi)(\vec{w}) + \eta_2)| \cdot \frac{1}{4\pi\epsilon} 4\pi\epsilon^2 \\ &\leq |((n_i \partial_i \phi)(\vec{w}) + \eta_2)| \epsilon \end{aligned} \tag{2.32}$$

Assuming $\partial_i \phi$ is finite,

$$\begin{aligned} &\lim_{\epsilon \to 0} |\chi_2| \leq \lim_{\epsilon \to 0} |((n_i \partial_i \phi)(\vec{w}) + \eta_2)| \epsilon = 0 \\ \Rightarrow &\lim_{\epsilon \to 0} \int_{\partial\Omega_\epsilon} n_i (\partial_i \phi) \cdot \psi \, dS = 0 \end{aligned} \tag{2.33}$$

And now the ϕ term. Noting our previous definition $\phi(\vec{x}) = \phi(\vec{w}) + \eta_1(\vec{x})$ we will write

$$\int_{\partial\Omega_\epsilon} \phi \cdot (n_i \partial_i \psi) \, dS = \chi_0 + \chi_1 \tag{2.34}$$

$$\chi_0 = \int_{\partial\Omega_\epsilon} \phi(\vec{w}) \cdot (n_i \partial_i \psi) \, dS \tag{2.35}$$

$$\chi_1 = \int_{\partial\Omega_\epsilon} \eta_1 \cdot (n_i \partial_i \psi) \, dS \tag{2.36}$$

Looking at χ_1

$$\begin{aligned} |\chi_1| &= \left| \int_{\partial\Omega_\epsilon} \eta_1 \cdot \frac{1}{4\pi |\vec{x} - \vec{w}|^2} \, dS \right| \\ &\leq |\eta_1| \frac{1}{4\pi |\epsilon|^2} 4\pi\epsilon^2 = |\eta_1| \end{aligned} \tag{2.37}$$

Taking the limit

$$\begin{aligned} &\lim_{\epsilon \to 0} |\chi_1| \leq \lim_{\epsilon \to 0} |\eta_1| = 0 \\ \Rightarrow &\lim_{\epsilon \to 0} \int_{\partial\Omega_\epsilon} \eta_1 \cdot (n_i \partial_i \psi) \, dS = 0 \end{aligned} \tag{2.38}$$

Finally, for χ_0

$$\begin{aligned}\chi_0 &= \int_{\partial\Omega_\epsilon} \phi(\vec{w}) \cdot \frac{1}{4\pi|\vec{x}-\vec{w}|^2}\, dS \\ &= \frac{\phi(\vec{w})}{4\pi} \int_{\partial\Omega_\epsilon} \frac{1}{|\vec{x}-\vec{w}|^2}\, dS\end{aligned} \tag{2.39}$$

On the surface of sphere, $|\vec{x}-\vec{w}|$ is uniformly ϵ, so the integral can be further simplified

$$\chi_0 = \frac{\phi(\vec{w})}{4\pi\epsilon^2} \int_{\partial\Omega_\epsilon} dS \tag{2.40}$$

and then the integral describes the surface area of the ball Ω_ϵ

$$\chi_0 = \frac{\phi(\vec{w})}{4\pi\epsilon^2} 4\pi\epsilon^2 = \phi(\vec{w}) \tag{2.41}$$

and all together

$$\lim_{\epsilon\to 0} \int_{\partial\Omega_\epsilon} \phi \cdot (n_i \partial_i \psi)\, dS = \phi(\vec{w}) \tag{2.42}$$

Putting our results into (2.23)

$$\phi(\vec{w}) = \lim_{\epsilon\to 0} \int_{\omega_M + \omega_{\epsilon M}} (n_i \partial_i(\phi_M)) \cdot \frac{1}{4\pi|\vec{x}-\vec{w}|} - \phi_M \cdot n_i \frac{x_i - w_i}{4\pi|\vec{x}-\vec{w}|^3}\, dS \tag{2.43}$$

We will now tackle the ϕ_M terms. We must be careful about taking the limit of these equations since the convergence of the integral over $\omega_{\epsilon M}$ depends on the shape of $\omega_{\epsilon M}$.

Similar to our treatment of ϕ over Ω_ϵ, we can say

$$\lim_{\epsilon\to 0} \int_{\omega_{\epsilon M}} (n_i \partial_i \phi_M) \cdot \frac{1}{4\pi|\vec{x}-\vec{w}|}\, dS = 0 \tag{2.44}$$

and

$$\lim_{\epsilon\to 0} \int_{\omega_{\epsilon M}} \phi_M \cdot n_i \frac{x_i - w_i}{4\pi|\vec{x}-\vec{w}|^3}\, dS = -\frac{\phi_M(\vec{w})}{4\pi} \lim_{\epsilon\to 0} \int_{\omega_{\epsilon M}} \frac{1}{|\vec{x}-\vec{w}|^2}\, dS \tag{2.45}$$

Noting the minus sign since $n_i = \frac{w_i - x_i}{|\vec{x}-\vec{w}|}$, the opposite of n_i over Ω_ϵ. The integral term here on the RHS is the solid angle integral. Converting to spherical polars

about $\vec{w}$, the surface element becomes

$$dS = |r|^2 \sin(\theta_{\vec{w}}) d\theta d\varphi \tag{2.46}$$

which we will write using the notation $\mathrm{d}\Omega_{\vec{w}}$ for the solid angle element about $\vec{w}$

$$dS = |r|^2 d\Omega_{\vec{w}} \tag{2.47}$$

although this might get confusing, given the notation Ω used throughout this text for general regions. We will be sure to note it is an integral over a solid angle element whenever possible. The limit of the integral then becomes

$$\lim_{\epsilon \to 0} \int_{\omega_{\epsilon M}} \phi_M \cdot n_i \frac{x_i - w_i}{4\pi |\vec{x} - \vec{w}|^3} \, dS = \frac{\phi_M(\vec{w})}{4\pi} \lim_{\epsilon \to 0} \int_{\omega_{\epsilon M}} d\Omega_{\vec{w}} \tag{2.48}$$

If the surface $\partial\Omega_M$ is smooth at the point $\vec{w}$, the region of the surface about $\vec{w}$ will be locally flat, and so the solid angle integral will be over a hemisphere. However, as we will be using a tetrahedral mesh, and $\vec{w}$ will be defined on a vertex on the boundary, we will instead say

$$\lim_{\epsilon \to 0} \int_{\omega_{\epsilon M}} d\Omega_{\vec{w}} = \alpha_{\vec{w}} \tag{2.49}$$

where $\alpha_{\vec{w}}$ is the sum of the internal solid angles of the tetrahedra which share a vertex at $\vec{w}$, at the vertex $\vec{w}$. Finally, we have

$$\lim_{\epsilon \to 0} \int_{\omega_{\epsilon M}} \phi_M \cdot n_i \frac{x_i - w_i}{4\pi |\vec{x} - \vec{w}|^3} \, dS = \frac{\alpha_{\vec{w}}}{4\pi} \phi_M \tag{2.50}$$

The equation for ϕ is now

$$\phi(\vec{w}) = \frac{\alpha_{\vec{w}}}{4\pi} \phi_M(\vec{w}) + \lim_{\epsilon \to 0} \int_{\omega_M} (n_i \partial_i(\phi_M)) \cdot \frac{1}{4\pi |\vec{x} - \vec{w}|} - \phi_M \cdot n_i \frac{x_i - w_i}{4\pi |\vec{x} - \vec{w}|^3} \, dS \tag{2.51}$$

We can apply the boundary conditions $\partial_i \phi_M = 0$ over ω_M

$$\phi(\vec{w}) = \frac{\alpha_{\vec{w}}}{4\pi} \phi_M(\vec{w}) - \lim_{\epsilon \to 0} \int_{\omega_M} \phi_M \cdot n_i \frac{x_i - w_i}{4\pi |\vec{x} - \vec{w}|^3} \, dS \tag{2.52}$$

Converting into spherical polars, assuming ϕ_M is finite, we can get rid of the pole in ψ. Using the polar coordinate transformation, centered about $\vec{w}$

$$\begin{aligned}\phi(\vec{w}) &= \frac{\alpha_{\vec{w}}}{4\pi}\,\phi_M - \lim_{\epsilon\to 0}\int_{\omega_M}(\phi_M)\cdot\frac{n_i\hat{r}_i}{|r|^2}\,|r|^2\,d\Omega_{\vec{w}} \\ &= \frac{\alpha_{\vec{w}}}{4\pi}\,\phi_M - \lim_{\epsilon\to 0}\int_{\omega_M}\phi_M n_i\hat{r}_i\,d\Omega_{\vec{w}}\end{aligned} \tag{2.53}$$

We can now safely take the limit over the surface of integration and say

$$\lim_{\epsilon\to 0}\int_{\omega_M} n_i\xi_i = \int_{\partial\Omega_M-\vec{w}} n_i\xi_i \tag{2.54}$$

since the integrand is not dependant on the shape of $\omega_{\epsilon M}$, so the integral is convergent. And so

$$\phi(\vec{w}) = \frac{\alpha_{\vec{w}}}{4\pi}\,\phi_M - \int_{\partial\Omega_M-\vec{w}}\phi_M n_i\hat{r}_i\,d\Omega_{\vec{w}} \tag{2.55}$$

This now looks like an integral over the unit sphere centered at $\vec{w}$ of the projection of ϕ_M on the surface $\partial\Omega_M$ onto that sphere.

With this, we have each term in ϕ, with its boundary values at infinity well defined for the demagnetizing field, in terms of a surface integral of ϕ_M which encodes the value of $\partial_i M_i$ inside the magnetic region. Some care must be taken when the integral approaches the point $\vec{w}$ since the value $\hat{r}$ is not well defined here.

A matrix expression to evaluate the integral described here over a tetrahedralized mesh, specifically over a triangular surface mesh, is described in (Lindholm 1984). An expression, then, for every ϕ on the surface vertices of the mesh can be expressed in terms of a matrix-vector multiplication. In Lindholm's operator, the issue of $\hat{r}$ at $\vec{w}$ is resolved as the value over triangles containing the point $\vec{w}$ is uniformly zero. It can be shown that $n_i\hat{r}_i$ on a flat surface containing $\vec{w}$ is uniformly zero, which suits our application perfectly.

2.1.5 Final Weak Form

Now defining yet another Poisson equation for a ϕ_0 with Dirichlet boundary conditions in $\partial\Omega_M$ setting $\phi_0 = \phi - \phi_M$ on the boundary, we get

$$\partial_i \partial_i \phi_0 = 0 \qquad \text{in } \Omega_M \tag{2.56a}$$

$$\phi_0 = \phi - \phi_M \tag{2.56b}$$

$$= (\frac{\alpha_{\vec{w}}}{4\pi} - 1)\, \phi_M - \int_{\partial\Omega_M - \vec{w}} \phi_M n_i \hat{r}_i \, d\Omega_{\vec{w}} \quad \text{in } \partial\Omega_M \tag{2.56c}$$

The weak form for this is slightly different again

$$\int_{\Omega_M} (\partial_i \phi_0) \cdot (\partial_i \phi_0') \, dV = 0 \tag{2.57}$$

Here, the test function ϕ_0' is defined such that

$$\phi_0' = 0 \quad \text{in } \partial\Omega_M \tag{2.58}$$

The particulars of the FEM formulation are a little involved to be discussed here, and will not be properly treated in this text. However it is a simple application of pure Dirichlet boundary conditions.

For a given solution ϕ_0, we finally have

$$\phi = \phi_0 + \phi_M \quad \text{in } \Omega_M \tag{2.59}$$

which is our magnetic scalar potential with $\phi = 0$ at infinity.

As a quick check, we can see

$$\begin{aligned} \partial_i \partial_i \phi &= \partial_i \partial_i \phi_0 + \partial_i \partial_i \phi_M \quad \text{in } \Omega_M \\ &= 0 + \partial_i M_i \end{aligned}$$

and

$$\begin{aligned}\partial_i\phi &= \partial_i\phi_0 + \partial_i\phi_M && \text{in } \partial\Omega_M \\ &= \partial_i(\phi - \phi_M) + \partial_i\phi_M \\ &= \partial_i\phi\end{aligned}$$

and

$$\begin{aligned}\phi &= \phi_0 + \phi_M && \text{in } \partial\Omega_M \\ &= \phi - \phi_M + \phi_M \\ &= \phi\end{aligned}$$

Since the values and derivatives of ϕ are consistent at the boundary of Ω_M, we can be happy that the value of ϕ is also correct beyond the boundary, and out to $\partial\Omega$.

2.1.6 Extension to Multi-phase and Non-Magnetic Materials

By multi-phase materials, we mean materials where two or more regions have different material properties, e.g. saturation magnetization, anisotropy axes, exchange constants, which may be distinct regions separated by space, or may share a boundary. In this section, we will look at formulating the demagnetizing field for materials with different saturation magnetizations.

In equation (2.2), the differential equations for ϕ_M, we have $\partial_i\partial_i\phi_M = \partial_i M_i$ on Ω_M and $\partial_i\phi_M = 0_i$ on $\partial\Omega_M$. In this definition, no constraints are made on the function $\vec{M}$. In particular, $\partial_i\vec{M}$ need not be continuous, and $|\vec{M}|$ need not be greater than zero.

We can split up our region Ω_M into, say, 3 non-overlapping regions, illustrated in figure 2.2:

$$\Omega_M = \Omega_{M1} + \Omega_{M2} + \Omega_{M0} \tag{2.60}$$

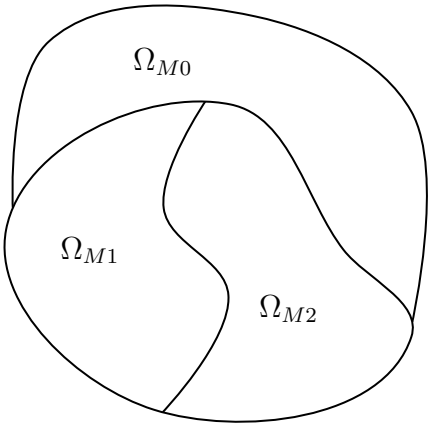

Figure 2.2: Integral subdomains of Ω_M: Ω_{M0}, Ω_{M1}, and Ω_{M2}.

In each region, $\vec{M}$ is defined as follows:

$$\begin{aligned} |\vec{M}| &= M_{s1} \qquad \text{in } \Omega_{M1} \\ |\vec{M}| &= M_{s2} \qquad \text{in } \Omega_{M2} \\ |\vec{M}| &= 0 \qquad\quad \text{in } \Omega_{M0} \end{aligned} \tag{2.61}$$

So Ω_{M1} refers to one magnetic material, Ω_{M2} refers to another magnetic material and Ω_{M0} refers to free space. The important distinction between free space Ω_{M0} here and the free space Ω_0 from earlier is that we are interested in finding the value of the demagnetizing field here, and not simply using it to satisfy boundary conditions.

We define the unit magnetization vector $\vec{m} = \vec{M}/M_s$ which remains continuous across the whole of Ω_M, and write

$$\begin{aligned} \vec{M} &= M_{s1}\,\vec{m} \qquad \text{in } \Omega_{M1} \\ \vec{M} &= M_{s2}\,\vec{m} \qquad \text{in } \Omega_{M2} \\ \vec{M} &= \vec{0} \qquad\quad\;\; \text{in } \Omega_{M0} \end{aligned} \tag{2.62}$$

We redefine (2.2) with this in mind

$$\partial_i \partial_i \phi_M = M_{s1}\, \partial_i m_i \quad \text{in } \Omega_{M1} \tag{2.63a}$$
$$\partial_i \partial_i \phi_M = M_{s2}\, \partial_i m_i \quad \text{in } \Omega_{M2} \tag{2.63b}$$
$$\partial_i \partial_i \phi_M = 0 \quad \text{in } \Omega_{M0} \tag{2.63c}$$
$$\partial_i \phi_M = 0_i \quad \text{in } \partial\Omega_M \tag{2.63d}$$

To accommodate this change, the weak form in (2.6) should be changed to

$$\begin{aligned}\int_{\Omega_M} (\partial_i \phi_M) \cdot (\partial_i \phi')\, dV =& M_{s1} \int_{\Omega_{M1}} m_i \cdot (\partial_i \phi')\, dV + M_{s2} \int_{\Omega_{M2}} m_i \cdot (\partial_i \phi')\, dV \\ &+ M_{s1} \int_{\partial\Omega_{M1}} n_i m_i \phi'\, dS + M_{s2} \int_{\partial\Omega_{M2}} n_i m_i \phi'\, dS\end{aligned} \tag{2.64}$$

Here, only the right hand side has been affected. Since $\vec{M} = \vec{0}$ in Ω_{M0} and in $\partial\Omega_{M0}$, the volume and surface integrals in this region can be ignored. We can see that the LHS is exactly the same as the LHS of (2.6), and the RHS is similar to the RHS of (2.6), except each subdomain has its own volume and surface integral over the entire subdomain volume and surface. From this, it should be clear how to extend this to more than two magnetic subdomains.

It can be shown if $M_{s1} = M_{s2}$ and $\Omega_{M0} = \emptyset$ that equation (2.64) becomes the previously derived single-phase weak form, equation (2.6). In brief, the two volume integrals over Ω_{M1} and Ω_{M2} will have the same factors and integrands, so they can be combined into one integral over Ω_M. Then the two surface integrals will have the same factors and integrands, but will share an integration over a common surface in the interior of Ω_M, but from opposite sides, so with opposite sign normals, so this will cancel, leaving only an integral over the exterior boundary, $\partial\Omega_M$.

This will be particularly useful later, as we integrate over a tessellation of tetrahedra. An integral over a region Ω can be split up into a sum of integrals over the tetrahedra Ω_e, then volume-surface transformations can be written with the volume of the tetrahedron as the volume, and the surface of the tetrahedron as the surface, and again, all summed over. Where neighbouring tetrahedra have the same material parameters, surface integrals over shared facets will cancel out, since the value will be the same, but the normal pointed in opposite

directions, so the sign will be different.

2.2 FEM Matrices From Weak Forms

Outline:
In this section, we use the Finite Element Method to transform our weak forms into a linear algebra equation.

We begin by introducing barycentric coordinates, which are useful for expressing linearly interpolated functions over a tetrahedron, and are easily integrated over the tetrahedron.

From there we express each of our weak forms as a sum of integrals over a tessellation of tetrahedra in terms of the barycentric coordinates and linear interpolation coefficients. We integrate these tetrahedralized forms, and turn them into a set of matrix equations whose solution is the interpolation coefficients. Along with these, we present a code which should assemble the requisite matrices and vectors, similar to the equivalent MERRILL code.

We will introduce a transformation from a volume integral over a tetrahedron to an integral over barycentric coordinates. We will then introduce the analytic results for some integrals over a tetrahedron that will be useful for the Finite Element Method.

We introduce our coordinates $\vec{r}$, and the vertices of our tetrahedron $\vec{v}_1$, $\vec{v}_2$, $\vec{v}_3$, $\vec{v}_4$:

$$\vec{v}_i = (x_i, y_i, z_i) \tag{2.65}$$

Our initial motivation will be to evaluate the integral

$$\int_\Omega \frac{\partial u}{\partial r_i} \frac{\partial u'}{\partial r_i} \, dV \tag{2.66}$$

over a tetrahedron Ω where $u(\vec{v}_i) = c_i$ and $u'(\vec{v}_i) = c'_i$, i.e. the value of u is a scalar value known at each node.

2.2.1 Barycentric Coordinates and Shape Coefficients

We introduce the barycentric coordinates $\vec{\lambda} = (\lambda_1, \lambda_2, \lambda_3, \lambda_4)$ defined

$$\lambda_1\vec{v}_1 + \lambda_2\vec{v}_2 + \lambda_3\vec{v}_3 + \lambda_4\vec{v}_4 = \vec{r} \tag{2.67}$$

$$\lambda_1 + \lambda_2 + \lambda_3 + \lambda_4 = 1 \tag{2.68}$$

which expands to

$$\begin{pmatrix} x_1 & x_2 & x_3 & x_4 \\ y_1 & y_2 & y_3 & y_4 \\ z_1 & z_2 & z_3 & z_4 \\ 1 & 1 & 1 & 1 \end{pmatrix} \begin{pmatrix} \lambda_1 \\ \lambda_2 \\ \lambda_3 \\ \lambda_4 \end{pmatrix} = \begin{pmatrix} r_1 \\ r_2 \\ r_3 \\ 1 \end{pmatrix} \tag{2.69}$$

so that when, say, $\vec{r} = \vec{v}_3$, we have $\vec{\lambda} = (0, 0, 1, 0)$, and a linear interpolation for values of $\vec{r}$ not at $\vec{v}_i$.

We will define the matrix $\boldsymbol{T}$

$$\boldsymbol{T} = \begin{pmatrix} x_1 & x_2 & x_3 & x_4 \\ y_1 & y_2 & y_3 & y_4 \\ z_1 & z_2 & z_3 & z_4 \\ 1 & 1 & 1 & 1 \end{pmatrix} \tag{2.70}$$

so equation (2.69) can be written

$$\boldsymbol{T}\vec{\lambda} = \vec{r}_+ \tag{2.71}$$

with $\vec{r}_+ = (r_1, r_2, r_3, 1)$ equivalent to $\vec{r}$ with a slight extension. It then remains to find the barycentric coordinate function

$$\vec{\lambda}(\vec{r}) = \boldsymbol{T}^{-1}\vec{r}_+ \tag{2.72}$$

With the barycentric coordinates in hand, we can then define the interpolation for u so it is the value c_i at the vertex v_i, and some intermediate value elsewhere. A good example where the value of u is essentially the weighted average of the vertex values $\vec{c}$ with the weighting as the distance from the vertex

$$\begin{aligned} u_\lambda(\vec{\lambda}) &= \lambda_1 c_1 + \lambda_2 c_2 + \lambda_3 c_3 + \lambda_4 c_4 = \lambda_i c_i \\ &= \lambda_i u(\vec{v}_i) \end{aligned} \tag{2.73}$$

So, for example,

$$u(\vec{r}) \approx u_\lambda(\lambda(\vec{r})) \tag{2.74}$$

and

$$\frac{\partial u}{\partial r_i} \approx \frac{\partial u_\lambda \circ \vec{\lambda}}{\partial r_i} = \frac{\partial u_\lambda}{\partial \lambda_j} \circ \vec{\lambda} \cdot \frac{\partial \lambda_j}{\partial r_i} = c_j \cdot \frac{\partial \lambda_j}{\partial r_i} \tag{2.75}$$

Finding the inverse $\boldsymbol{T}^{-1}$ is needed to find the barycentric coordinate function $\lambda(\vec{r})$. Instead of directly tackling the inverse, we will use Cramer's rule, defining the solution of (2.72) in terms of determinants of the matrix $\boldsymbol{T}$ and related matrices. Using the Cramer's rule, we write

$$\lambda_i(\vec{r}) = \frac{\det\left(\boldsymbol{T_i}(\vec{r})\right)}{\det\left(\boldsymbol{T}\right)} \tag{2.76}$$

where $\boldsymbol{T_i}(\vec{r})$ is $\boldsymbol{T}$ with the ith column replaced with $\vec{r}_+ = (r_1, r_2, r_3, 1)$.

It can be shown that the volume V of the tetrahedron described by $\boldsymbol{T}$ is

$$\mathrm{V} = \frac{1}{6}\det\left(\boldsymbol{T}\right) \tag{2.77}$$

so we can write

$$\lambda_i(\vec{r}) = \frac{\det\left(\boldsymbol{T_i}(\vec{r})\right)}{6\mathrm{V}} \tag{2.78}$$

noting V is independent of $\vec{r}$.

Next, with some abuse of notation, defining the determinant applied to a matrix valued function as

$$\det\left(\boldsymbol{T_i}\right)(\vec{r}) = \det\left(\boldsymbol{T_i}(\vec{r})\right) \tag{2.79}$$

we can define derivatives

$$\frac{\partial \lambda_i}{\partial r_j} = \frac{1}{6V} \frac{\partial \det\left(\boldsymbol{T_i}\right)}{\partial r_j} \tag{2.80}$$

Let's look at $\frac{\partial \lambda_2}{\partial r_1}$ as an example. The matrix $\boldsymbol{T_2}(\vec{r})$ is

$$\boldsymbol{T_2}(\vec{r}) = \begin{pmatrix} x_1 & r_1 & x_3 & x_4 \\ y_1 & r_2 & y_3 & y_4 \\ z_1 & r_3 & z_3 & z_4 \\ 1 & 1 & 1 & 1 \end{pmatrix} \tag{2.81}$$

and the term of the determinant with coefficient r_1 is

$$\det\left(T_2(\vec{r})\right) = -r_1 \det \begin{pmatrix} y_1 & y_3 & y_4 \\ z_1 & z_3 & z_4 \\ 1 & 1 & 1 \end{pmatrix} + \text{other terms} \tag{2.82}$$

which is obtained from the typical definition of determinants in terms of its minors. It is worth noting that this determinant will be linear in r_1 from equation (2.72), and the tetrahedron volume V being independent of $\vec{r}$. Then

$$\frac{\partial \lambda_2}{\partial r_1} = -\frac{1}{6V} \det \begin{pmatrix} y_1 & y_3 & y_4 \\ z_1 & z_3 & z_4 \\ 1 & 1 & 1 \end{pmatrix} \tag{2.83}$$

What's notable here is that this is also a constant, independent of $\vec{r}$.

We will therefore define the constant matrix of derivatives $\boldsymbol{D}$

$$D_{ij} = \left(\frac{\partial \det\left(\boldsymbol{T_i}\right)}{\partial r_j} \right) (\vec{0}) \tag{2.84}$$

with the function taken at $\vec{0}$ just to get a value out. And finally, we write the derivatives

$$\frac{\partial \lambda_i}{\partial r_j} = \frac{D_{ij}}{6V} \tag{2.85}$$

As an aside, since λ_i is linear in $\vec{r}$, we can write

$$\lambda_i(\vec{r}) = r_j \frac{\partial \lambda_i}{\partial r_j} + g_i \tag{2.86}$$

where g_i is some constant. We also note

$$\lambda_i(\vec{r}) = T^{-1}_{i1} r_1 + T^{-1}_{i2} r_2 + T^{-1}_{i3} r_3 + T^{-1}_{i4} \tag{2.87}$$

and so

$$\frac{\partial \lambda_i}{\partial r_j} = T^{-1}_{ij} \ , \quad g_i = T^{-1}_{i4} \tag{2.88}$$

We can work out T^{-1}_{i4} by noting that $\lambda_i(\vec{v}_i) = 1$

$$\begin{aligned} 1 &= v_{1j} \frac{\partial \lambda_i}{\partial r_j} + T^{-1}_{i4} \\ \Rightarrow T^{-1}_{i4} &= 1 - v_{(i)j} \frac{\partial \lambda_{(i)}}{\partial r_j} \end{aligned} \tag{2.89}$$

where i is not summed over.

We note from (2.68), the derivatives are not linearly independent and we can write

$$\begin{aligned} \frac{\partial \lambda_4}{\partial r_j} &= \frac{\partial (1 - \lambda_1 - \lambda_2 - \lambda_3)}{\partial r_j} \\ &= -\frac{D_{1j} + D_{2j} + D_{3j}}{6V} \end{aligned} \tag{2.90}$$

We can now write for $\lambda_i(\vec{r})$:

$$\lambda_i(\vec{r}) = \frac{\partial \lambda_i}{\partial r_j}(r_j - v_{(i)j}) + 1 \tag{2.91}$$

2.2.2 Integration Over a Linear Tetrahedron

Returning to the integral (2.66) and replacing $\frac{\partial u}{\partial r_j}$ as in (2.75)

$$\int_\Omega \frac{\partial u}{\partial r_i}\frac{\partial u'}{\partial r_i}\, dV \approx \int_\Omega c_j \cdot \frac{\partial \lambda_j}{\partial r_i} c'_k \cdot \frac{\partial \lambda_k}{\partial r_i} dV = S \tag{2.92}$$

and replacing the $\frac{\partial \lambda_j}{\partial r_i}$ for constant terms as in (2.85)

$$\begin{aligned} S &= \int_\Omega c_j \cdot \frac{D_{ji}}{6V} c'_k \cdot \frac{D_{ki}}{6V}\, dV \\ &= \frac{1}{36V^2}\, c_j\, D_{ji}\, c'_k\, D_{ki} \int_\Omega dV \end{aligned} \tag{2.93}$$

and since the volume of the tetrahedron is given by $V = \int_\Omega\, dV$

$$S = \frac{1}{36V}\, c_j\, D_{ji}\, c'_k\, D_{ki} \tag{2.94}$$

With this formulation in mind, we can state our final goal, which is to turn our differential equations into M equations for M unknowns corresponding to the interpolation coefficients for ϕ.

Suppose we have a differential equation corresponding to the weak form

$$\int_\Omega \partial_i \phi \cdot \partial_i \phi'\, dV = \int_\Omega \phi'\, dV \tag{2.95}$$

which, given the above discussion, can be written

$$\begin{aligned} & \int_\Omega \partial_i \phi \cdot \partial_i \phi'\, dV = \int_\Omega \phi'\, dV \\ \Rightarrow \quad & \int_\Omega c_j \frac{\partial \lambda_j}{\partial r_i} c'_k \frac{\partial \lambda_k}{\partial r_i}\, dV = \int_\Omega c'_k \lambda_k\, dV \\ \Rightarrow \quad & \frac{1}{36V}\, c_j\, D_{ji}\, c'_k\, D_{ki} = \frac{V}{4} \sum_k c'_k \\ & S = F \end{aligned} \tag{2.96}$$

where c_j corresponds to the coefficients of a linearly interpolated function for

ϕ, and c'_k are the coefficients for an arbitrary function ϕ'. We now have the M unknown coefficients c_j we want to know, and the M arbitrary coefficients c'_k whose values are of no importance.

By taking derivatives of the above equation with respect to each of the different c'_k, we can generate M equations for the M unknowns c_j.

$$\begin{aligned} \frac{\partial S}{\partial c'_k} &= \frac{\partial F}{\partial c'_k} \\ \frac{1}{36V}\, c_j\, D_{ji}\, D_{ki} &= \frac{V}{4} \end{aligned} \tag{2.97}$$

By taking derivatives of $\frac{\partial S}{\partial c'_k}$ wrt c_j, we can rewrite this

$$\frac{\partial^2 S}{\partial c'_k \partial c_j}\, c_j = S_{kj}\, c_j = \frac{1}{36V}\, D_{ji}\, D_{ki}\, c_j = \frac{V}{4} \tag{2.98}$$

which can be written as a matrix equation

$$\Rightarrow S_{ij} c_j = F_i \tag{2.99}$$

where $\boldsymbol{S}$ is called the "Stiffness Matrix", the vector $\vec{c}$ is called the "Coefficient Vector", and the vector $\vec{F}$ is called the "Force Vector". The vector $\vec{F}$ is just uniformly $\frac{V}{4}$ here, but in general, it may be more interesting.

2.2.3 Matrix Formulation of an Integral Over Many Tetrahedra

We define an integral over a set of N tetrahedra. We can then say for a set of N tetrahedra, where V^e is the volume of the eth tetrahedron, c^e_j is the interpolation component of u on the jth vertex of tetrahedron e. Likewise for c'^e_j for u',

and $\boldsymbol{D}^e$ is the matrix of derivatives on tetrahedron e

$$\begin{aligned} S' &= \int_{\cup \Omega_e} \frac{\partial u}{\partial r_i} \frac{\partial u'}{\partial r_i} \\ &= \sum_e \frac{1}{36V^e} \, c_j^e \, D_{ji}^e \, c_k'^e \, D_{ki}^e \\ &= \sum_e S'^e \end{aligned} \tag{2.100}$$

Over the global mesh, containing M nodes, the function u will contain M interpolation components c_j, and u' will contain M components c'_j. These components may be shared by a number of tetrahedra, where tetrahedra contain the same point as a vertex. Taking derivatives wrt c'_q to create M equations for our M unknowns c_j we can write

$$S'_q = \sum_e \frac{\partial S'^e}{\partial c'_q} = \sum_e \frac{1}{36V^e} \, c_j^e \, D_{ji}^e \, D_{ki}^e \frac{\partial c_k'^e}{\partial c'_q} \tag{2.101}$$

We define a local-to-global mapping e_j that mapping from the local node index defined on the tetrahedron e to a global node index. If the jth node of tetrahedron e refers to the global node k, we have $e_j = k$, and $c^e_{e_j} = c_k$ Reversing that, we will define e^k as the global-to-local mapping of the node global index to the tetrahedron node index. We can then write

$$\frac{\partial c_k'^e}{\partial c'_q} = \begin{cases} \delta_{ke^q} & \text{if } q \in e \\ 0 & \text{otherwise} \end{cases} \tag{2.102}$$

The cases are necessary here, because the global-to-local mapping is undefined when looking for the local index of a global index not actually contained by the tetrahedron. We can rewrite S'_q, including a qualifier in the summation

$$S'_q = \sum_{\{e \,|\, \vec{q} \in e\}} \frac{1}{36V^e} \, c_j^e \, D_{ji}^e \, D_{e^q i}^e \tag{2.103}$$

Pulling c_j^e outside of the sum, and swapping the local summation over j with

a global summation over p, again including the qualifier in the summation

$$S'_q = \sum_p c_p \sum_{\{e \,|\, \vec{p},\vec{q} \in e\}} \frac{1}{36V^e} \, D^e_{e^p i} \, D^e_{e^q i} \tag{2.104}$$

so we define

$$S'_{pq} = \sum_{\{e \,|\, \vec{p},\vec{q} \in e\}} \frac{1}{36V^e} \, D^e_{e^p i} \, D^e_{e^q i} \tag{2.105}$$

so that

$$S'_q = S'_{pq} \, c_p \tag{2.106}$$

We could have come to a similar result defining

$$S'_{pq} = \frac{\partial^2 S'}{\partial c_p \partial c'_q} \tag{2.107}$$

The implementation details now remaining are the calculation of V^e, $\boldsymbol{D}^e$ and the global to local index map e^i. The matrix defined here is equivalent to the stiffness matrix of a Poisson equation with pure, homogeneous Neumann conditions

$$\frac{\partial u}{\partial r_i} = 0_i \quad \text{on boundary} \tag{2.108}$$

At a glance

Having worked out the details of building the stiffness matrix, we can now look at a simple method of moving from a formulation of the problem to an implementation of a solution. We look at the integral over a single tetrahedron e:

$$S^e = \frac{1}{36V^e} \, c^e_j \, D^e_{jk} \, c'^e_i \, D^e_{ik} \tag{2.109}$$

and simply sum over these for the whole volume

$$S = \sum_e \frac{1}{36V^e} \, c^e_j \, D^e_{jk} \, c'^e_i \, D^e_{ik} \tag{2.110}$$

Replace c^e_j and c'^e_i with the equivalent, globally indexed c_{e_j} and c'_{e_i}, and looking

at a single term in the above sum

$$S = \ldots + \frac{1}{36V^e}\, c_{e_{(j)}}\, D^e_{(j)k}\, c'_{e_{(i)}}\, D^e_{(i)k} + \ldots \tag{2.111}$$

where braces mean we are not summing over those indices. Remembering that e_j is a local to global mapping of index j on tetrahedron e to the equivalent global mesh vertex. We see here that j and i have values 1-4, and need to be mapped from local to global, and k is looping over the x, y and z coordinate index.

Now, we want to build a matrix $\boldsymbol{S}$ so that

$$S_{ij} c_j \tag{2.112}$$

gives us the sum of all the c'_i terms. To do this, we place all terms with c'_i on the ith row, and all the terms with c_j on the jth column, but without including c_j or c'_i in the final matrix.

This can be accomplished with the following code in MERRILL

```
1  S(1:NNODE,1:NNODE) = 0
2
3  ! Loop over all the tetrahedra e
4  DO e=1,NTRI
5
6    ! Loop over all the c'_{e_i} terms
7    DO i=1,4
8
9      ! Loop over all the c_{e_j} terms
10     DO j=1,4
11
12       ! Find the global indices of i and j, ie e_i and e_j
13       iglobal = TIL(e,i)
14       jglobal = TIL(e,j)
15
16       ! Define D^e_{i k} and D^e_{j k}
17       Di = (/ b(e,iglobal), c(e,iglobal), d(e,iglobal) /)
18       Dj = (/ b(e,jglobal), c(e,iglobal), d(e,iglobal) /)
```

```
19
20          ! Loop over x,y,z coordinate
21          DO k=1,3
22            S(iglobal,jglobal) = S(iglobal,jglobal) &
23              + (1/(36*(vol(e))))*Di(k)*Dj(k)
24          END DO
25        END DO
26      END DO
27    END DO
```

and $r = S_{ij}c_j$ evaluated

```
1  r = 0
2  DO j=1,NNODE
3    r = r + S(i,j) * c(j)
4  END DO
```

(although since c is already in used for the shape coefficients in MERRILL, a different variable name would need to be used here in the actual program.)

In MERRILL, the barycentric coordinate derivatives are denoted with `b`, `c`, and `d` with

$$\begin{aligned} D^e_{ix} &= \mathtt{b}(e,i) \\ D^e_{iy} &= \mathtt{c}(e,i) \\ D^e_{iz} &= \mathtt{d}(e,i) \end{aligned} \tag{2.113}$$

with e, here, an enumeration of the tetrahedra ranging from 1 to `NTRI`, and the index i representing the ith index of the tetrahedron. The local to global index array is `TIL` where

$$e_j = \mathtt{TIL}(e,j) \tag{2.114}$$

with e on the left representing the nebulous tetrahedron object and mapping object, but e on the right representing the enumeration of tetrahedron e. The value of `TIL(e,j)` returns the global enumeration of vertex j on tetrahedron e. Finally, the value `NNODE` is the number of global vertices in the mesh.

The assembly steps are written rather simply here. In MERRILL itself, the assembly is a bit more complex, since the matrices are stored in a sparse format,

and can't be indexed directly. Indeed, during the initial assembly, the indices are not known at all. Further, indexing is muddied by the matrices being stored in a column-sparse SLAP Triad format where diagonal entries are stored at the start of the column. While it would be possible to construct the indices before assembly, and have a (reasonably) quick lookup of the matrix indices, the code works as is, and the change wouldn't have a significant effect, other than looking nice, and possibly being a bit slower. It should suffice to outline the "nice" assembly here, and pick apart the "ugly" assembly in the code, if necessary.

From here, including multi-phase to a particular formulation is trivial. Say we have the equation

$$S = \sum_e M_s^e \frac{1}{36V^e} \, c_j^e \, D_{ji}^e \, c_k'^e \, D_{ki}^e \tag{2.115}$$

with M_s^e representing a material parameter, the saturation magnetization in this case, that is constant within a tetrahedron, but may change between different tetrahedra. We will use a "subdomain" enumeration, where tetrahedra with the same material parameters are given the same subdomain. We will build a matrix so the sum of all c_i' terms is given by

$$r = S_{kij} M_{sk} c_j \tag{2.116}$$

In MERRILL

```
1  S(1:NMaterials,1:NNODE,1:NNODE) = 0
2  DO e=1,NTRI
3
4    ! Get the subdomain index
5    sd = TetSubDomains(e)
6
7    DO i=1,4
8      DO j=1,4
9        inode = TIL(e,i)
10       jnode = TIL(e,j)
11
```

```
12          Di = (/ b(e,inode), c(e,inode), d(e,inode) /)
13          Dj = (/ b(e,jnode), c(e,inode), d(e,inode) /)
14
15          DO k=1,3
16            ! Same as before, but extra subdomain index.
17            S(sd,inode,jnode) = S(sd,inode,jnode) &
18              + (1/(36*(vol(e))))*Di(k)*Dj(k)
19          END DO
20        END DO
21      END DO
22    END DO
```

and can be evaluated

```
1   r = 0
2   DO j=1,NNODE
3     DO sd=1,NMaterials
4       r = r + S(sd,i,j)*Ms(sd)*C(j)
5     END DO
6   END DO
```

which is a reasonably small change to the original formulation.

It must be noted that this addition turns the matrices from rank-2 to rank-3. This means they are no longer suitable for the SLAP Triad format, and no longer suitable for passing into solver routines expecting rank-2 matrices. Care must be taken, then, to leave matrix values passed into solvers as rank-2 matrices. Luckily, our formulation of the demagnetizing field produces matrices independent of the material parameters, but the RHS passed in is. However, the RHS is assembled from a force matrix and the magnetization into a rank-1 vector. The inclusion of subdomains turns the force matrix from rank-2 to rank-3, but the assembly still produces a rank-1 vector as before.

2.2.4 The Poisson Equation RHS

We now look at the formulation of the RHS of the demagnetizing equation

$$F = \int_{\cup_e \Omega_e} m_i \cdot \partial_i \phi' \, dV + \int_{\cup_e \partial\Omega_e} n_i \cdot m_i \cdot \phi' \, dS \tag{2.117}$$

The integral over the boundary is a little over-zealous here, defined over the facets of every tetrahedron on the mesh, but where integrands are continuous across shared boundaries, the integrals should cancel out. That is, only facets where the material parameters change between the neighbouring tetrahedra will have a non-zero contribution to F. In practice, we just ignore the surfaces that cancel out.

We will start by looking at the integral of the first term over a tetrahedron Ω_e

$$F_1^e = \int_{\Omega_e} m_i \cdot \partial_i \phi' \, dV \tag{2.118}$$

with ϕ' defined as above and $\vec{m}$ defined similar to $\vec{u}$ We will say at a vertex $\vec{v}_i$ in e that $\vec{m}(\vec{v}_i) = \vec{J_i^e} = (J_{i1}^e, J_{i2}^e, J_{i3}^e)$ so that, over a tetrahedron, we have

$$m_i^e(\vec{r}) = \lambda_j(\vec{r}) \; J_{ji}^e \tag{2.119}$$

along with a global equivalent $\vec{J_i}$, similar to c_i from the previous section. Replacing $\partial_i \phi' = \frac{c_k'^e D_{ki}^e}{6V}$, as previously worked out,

$$F_1^e = \frac{c_k'^e D_{ki}^e}{6V^e} \int_{\Omega'} \lambda_j \; J_{ji}^e \, dV \tag{2.120}$$

It can be shown that for an integration over a tetrahedron Ω_e, the integral of the barycentric coordinates, for any combination and powers of the coordinates, can be written

$$\int_{\Omega_e} \lambda_1^a \lambda_2^b \lambda_3^c \lambda_4^d \, dV = 6 \, |V^e| \, \frac{a!b!c!d!}{(a+b+c+d+3)!} \tag{2.121}$$

so the integral evaluates to

$$\begin{aligned} F_1^e &= \frac{c_k'^e D_{ki}^e}{6V} \sum_j J_{ji}^e 6 \left|V\right| \frac{1}{4!} \\ &= \frac{c_k'^e D_{ki}^e}{24} \sum_j J_{ji}^e \end{aligned} \tag{2.122}$$

Putting that back into F

$$F = \sum_e \frac{c_k'^e D_{ki}^e}{24} \sum_j J_{ji}^e + \int_{\cup_e \partial\Omega_e} n_i \cdot m_i \cdot \phi' \, dS \tag{2.123}$$

Now we tackle the boundary integral. We will look at the integral over a single triangle t of a tetrahedron e. We assume the vertices on the boundary are $\vec{v}_1$, $\vec{v}_2$, and $\vec{v}_3$. In this case, λ_4 will always be 0. Substituting barycentric coordinates for $\vec{m}$ and ϕ', and assuming a constant $\vec{n}$, since integration is over the surface of a flat triangle

$$\begin{aligned} F_2^t &= n_i \int_t \sum_{j=1}^{3} \lambda_j J_{ji}^e \sum_{k=1}^{3} \lambda_k c_k'^e \, dS \\ &= n_i \int_t J_{1i}^e c_1^e \lambda_1^2 + J_{1i}^e c_2^e \lambda_1 \lambda_2 + J_{1i}^e c_3^e \lambda_1 \lambda_3 + J_{2i}^e c_1^e \lambda_2 \lambda_1 + \ldots \, dS \end{aligned} \tag{2.124}$$

Similar to before, there is a closed formula for an integral of barycentric coordinates over a triangle:

$$\int_t \lambda_1^a \lambda_2^b \lambda_3^c \, dS = 2 \left|A^t\right| \frac{a!b!c!}{(a+b+c+2)!} \tag{2.125}$$

where A^t is the area of triangle t.

Since each term in the integrand is either one λ_j^2 term or two $\lambda_j \lambda_k$ terms, the integral evaluates to

$$F_2^t = n_i^t \frac{|A^t|}{12} \sum_{j=1}^{3} J_{ji}^e \sum_{k=1}^{3} c_k'^e (1 + \delta_{jk}) \tag{2.126}$$

Now, instead of specifying $\vec{v}_1$, $\vec{v}_2$, and $\vec{v}_3$ on the surface, we will write $\vec{v} \in t$

$$F_2^t = n_i^t \frac{|A^t|}{12} \sum_{\{j \in t\}} J_{ji}^e \sum_{\{k \in t\}} c_k'^e (1 + \delta_{jk}) \tag{2.127}$$

We can substitute this back into F

$$F = \sum_e \frac{c_k'^e D_{ki}^e}{24} \sum_j J_{ji}^e + \sum_e \sum_{\{t \in e\}} n_i^t \frac{|A^t|}{12} \sum_{\{j \in t\}} J_{ji}^e \sum_{\{k \in t\}} c_k'^e (1 + \delta_{jk}) \tag{2.128}$$

From the previous discussion, this should be sufficient for building the force vector $\vec{F}$ with J_{ji}^e taking the place of c_j^e. Indeed, in the implementation, this is the form used in its assembly. However, for completeness, we can rearrange the terms into a sum over J

$$F = \sum_p J_{pi} \sum_{\{e \,|\, \vec{p} \in e\}} \frac{c_k'^e D_{ki}^e}{24} + \sum_p J_{pi} \sum_{\{e \,|\, \vec{p} \in e\}} \sum_{\{t \,|\, t \in e\}} n_i^t \frac{|A^t|}{12} \sum_{\{k \in t\}} c_k'^e (1 + \delta_{e^p k}) \tag{2.129}$$

We will write this

$$F = \sum_p J_{pi} (F'_{pi} + F''_{pi}) \tag{2.130}$$

The surface integral term here contains more entries than is necessary. It is, however, as general as possible. In practice, instead of including every triangle in an element, only the triangles that contribute to discontinuous border values need to be included. In particular, faces of tetrahedra on the boundary of the space, or where the opposite tetrahedron is in a different subdomain (i.e. with potentially different material properties). While including all triangles will generate the correct results, for numerical purposes, we want to avoid potentially adding and subtracting large numbers which should predictably cancel out.

Oriented Area

We need a formulation of $n_i^t |A^t|$ found in F''. An obvious choice is a cross product. For a triangle with vertices $\vec{v}_1$, $\vec{v}_2$, and $\vec{v}_3$ we can write the oriented

area

$$\vec{A} = \frac{1}{2}(\vec{v}_1 - \vec{v}_3) \times (\vec{v}_2 - \vec{v}_3) \tag{2.131}$$

which can be expressed as the determinants

$$\vec{A} = \frac{1}{2}\left(\begin{vmatrix} v_{12} - v_{32} & v_{13} - v_{33} \\ v_{22} - v_{32} & v_{23} - v_{33} \end{vmatrix}, - \begin{vmatrix} v_{11} - v_{31} & v_{13} - v_{33} \\ v_{21} - v_{31} & v_{23} - v_{33} \end{vmatrix}, \begin{vmatrix} v_{11} - v_{31} & v_{12} - v_{32} \\ v_{21} - v_{31} & v_{22} - v_{32} \end{vmatrix}\right) \tag{2.132}$$

This can be related back to the barycentric coordinates of a tetrahedron with a little reformulation of the original barycentric coordinate equations. Using $\lambda_1 + \lambda_2 + \lambda_3 + \lambda_4 = 1$,

$$\lambda_1(\vec{v}_1 - \vec{v}_3) + \lambda_2(\vec{v}_2 - \vec{v}_3) + \lambda_4(\vec{v}_4 - \vec{v}_3) = r \tag{2.133a}$$

$$\Rightarrow \begin{pmatrix} v_{11} - v_{31} & v_{21} - v_{31} & v_{41} - v_{31} \\ v_{12} - v_{32} & v_{22} - v_{32} & v_{42} - v_{32} \\ v_{13} - v_{33} & v_{23} - v_{33} & v_{43} - v_{33} \end{pmatrix} \begin{pmatrix} \lambda_1 \\ \lambda_2 \\ \lambda_4 \end{pmatrix} = \begin{pmatrix} r_1 \\ r_2 \\ r_3 \end{pmatrix} \tag{2.133b}$$

Denoting the matrix here as T', and denoting $T'_i(\vec{r})$ as before (with column i of T' replaced with $\vec{r}$) we can solve for λ_4 using Cramer's rule (remembering λ_4 is in slot 3!)

$$\lambda_4 = \frac{\det\left(T'_3(\vec{r})\right)}{\det T'} \tag{2.134}$$

Now looking at the r_1 derivative:

$$\frac{\partial \lambda_4}{\partial r_1} = \frac{1}{\det\left(T'\right)} \begin{vmatrix} v_{11} - v_{31} & v_{21} - v_{31} \\ v_{12} - v_{32} & v_{22} - v_{32} \end{vmatrix} \tag{2.135}$$

The determinant here is exactly the x value of $\vec{A}$ in (2.132).

It can be shown that $\det(T') = \det(T)$, and so

$$\frac{\partial \lambda_4}{\partial r_1} = \frac{1}{6V} \begin{vmatrix} v_{11} - v_{31} & v_{21} - v_{31} \\ v_{12} - v_{32} & v_{22} - v_{32} \end{vmatrix} \tag{2.136}$$

and it is then clear that

$$\begin{vmatrix} v_{11} - v_{31} & v_{21} - v_{31} \\ v_{12} - v_{32} & v_{22} - v_{32} \end{vmatrix} = D_{41} \tag{2.137}$$

Doing the same for r_2 and r_3,

$$\vec{A} = \frac{1}{2}(D_{41}, D_{42}, D_{43}) \tag{2.138}$$

so $\vec{A}$ consists of the derivative coefficients of the vertex not in the triangle A. Since $\vec{A} = n_i|A|$, we have

$$n_i|A| = \frac{1}{2}(D_{41}, D_{42}, D_{43}) \tag{2.139}$$

Building The Matrix

We will build (2.128)

$$F = \sum_e \frac{c_k'^e D_{ki}^e}{24} \sum_j J_{ji}^e + \sum_e \sum_{\{t \in e\}} n_i^t \frac{|A^t|}{12} \sum_{\{j \in t\}} J_{ji}^e \sum_{\{k \in t\}} c_k'^e (1 + \delta_{jk})$$

However, to account for multi-phase materials, we must go back and add in the saturation magnetization where we can. This results in the RHS

$$F = \sum_e M_s^e \frac{c_k'^e D_{ki}^e}{24} \sum_j J_{ji}^e + \sum_e M_s^e \sum_{\{t \in e\}} n_i^t \frac{|A^t|}{12} \sum_{\{j \in t\}} J_{ji}^e \sum_{\{k \in t\}} c_k'^e (1 + \delta_{jk})$$

in MERRILL so that

$$F_{pi} = M_{sk} F_{kij} J_{pj} \tag{2.140}$$

```
1  F(1:NMaterials,1:3,1:NNODE,1:NNODE) = 0
2
3  ! Build volume contribution
4  DO e=1,NTRI
5    sd = TetSubDomains(e)
6    DO i=1,4
7      DO j=1,4
8        inode = TIL(e,i)
9        jnode = TIL(e,j)
10
11       D = (/ b(e,jnode), c(e,jnode), d(e,jnode) /)
12
13       DO k=1,3
14         F(sd,k,jnode,inode) = F(k,jnode,inode) + D(k)/24
15       END DO
16     END DO
17   END DO
18 END DO
19
20 ! Build surface contribution
21 DO e=1,NTRI
22   sd = TetSubDomains(e)
23
24   ! Iterate over triangles in e, with a triangle defined by
25   ! the opposite vertex.
26   DO opp=1,4
27
28     ! The oriented area
29     nA = (/ b(e,opp), c(e,opp), d(e,opp) /) / 2
30
31     ! Triangle indices, the indices in e which aren't opp.
32     DO j=1,4
33       IF(j .EQ. opp) CYCLE
34       DO i=1,4
```

```
35          IF(i .EQ. opp) CYCLE
36
37          jnode = TIL(e,j)
38          inode = TIL(e,i)
39
40          ! encode 1 + delta_ij
41          IF(i .EQ. j) THEN
42            factor = 2
43          ELSE
44            factor = 1
45          END IF
46
47          ! The x,y,z index
48          DO k=1,3
49            F(sd,k,jnode,inode) = F(sd,k,jnode,inode) &
50              + nA(k)/12*factor
51          END DO
52        END DO
53      END DO
54    END DO
55  END DO
```

and evaluated

```
1  rhs(1:NNODE) = 0
2  DO i=1,NNODE
3    DO j=1,NNODE
4      DO k=1,3
5        DO sd=1,NMaterials
6          rhs(i) = rhs(i) + F(sd,k,i,j)*Ms(sd)*m(j,k)
7        END DO
8      END DO
9    END DO
10 END DO
```

2.3 Effective Fields and Energy Gradients

Outline:
In this section, we present the relation between the effective fields and the energy gradients used by MERRILL. We also derive the energy gradients for the demagnetizing, exchange, and anisotropy energies, and present the code for assembling these values.

The effective field for a given magnetic system can be defined

$$H_i = -\frac{\partial E}{\partial M_i} \tag{2.141}$$

For $\vec{M} = M_s\vec{m}$ with $|m| = 1$, this can be written

$$H_i = -\frac{1}{M_s}\frac{\partial E}{\partial m_i} \tag{2.142}$$

This definition hides some machinery of functional derivatives, since $\vec{H}$ and $\vec{m}$ here are actually defined pointwise, and E is defined by an integral over the domain of $\vec{m}$.

Now, for $m_i = \lambda_j^e J_{e_j i}$ on a given tetrahedron e, and in the Finite Element Method, we find our minima by varying J_{ji} rather than $\vec{m}$ itself, we would prefer to find a gradient with respect to J_{ji}. The tensor value J_{ij} can be read as the jth component of m on vertex i. We will therefore define the FEM energy gradient

$$G_{ij} = \frac{\partial E}{\partial J_{ij}} \tag{2.143}$$

with G_{ij} the jth component of G on vertex i, and

$$E = \sum_e \int_{\Omega_e} \mathcal{E}(\vec{m})\, dV \tag{2.144}$$

and so

$$G_{ij} = \sum_e \int_{\Omega_e} \frac{\partial \mathcal{E}}{\partial J_{ij}}(\vec{m})\, dV \tag{2.145}$$

Now, since $m_i = \lambda_j J_{ji}$, this can be rewritten

$$\begin{aligned} G_{ij} &= \sum_e \int_{\Omega_e} \frac{\partial \mathcal{E}}{\partial m_k}(\vec{m}) \frac{\partial m_k}{\partial J_{ij}}\, dV \\ &= -\sum_{\{e|j\in e\}} \int_{\Omega_e} M_s H_j(\vec{m}) \lambda_i\, dV \end{aligned} \tag{2.146}$$

with $\{e|j \in e\}$ used to constrain the integration over the barycentric coordinate functions defined at node j for any tetrahedra sharing that node. This is now easily relatable to the usual definition of $\vec{H}$. Once the usual expression including $\vec{m}$ is found, it can then be converted to one using $\lambda_k J_{ki}$, multiplied by λ_i and integrated. In the case where the $\vec{H}$ field becomes independent of $\vec{m}$, the result is dependant only on the geometry.

2.3.1 Demagnetizing Energy Gradient

The demagnetizing energy is

$$E = \int M_i \phi_{,i}\, dV \tag{2.147}$$

The effective field is

$$H_i = -\phi_{,i} \tag{2.148}$$

Placing that into H_{ij}, we have

$$\begin{aligned} G_{ij} &= \sum_{\{e\,|\,i\in e\}} \int_{\Omega_e} \phi_{,j} \lambda_i\, dV \\ &= \sum_{\{e\,|\,i\in e\}} \int_{\Omega_e} c_k \frac{D^e_{kj}}{6V} \lambda_i\, dV \end{aligned} \tag{2.149}$$

with c_k the value of ϕ at vertex k. This is something we have evaluated before in (2.122)

$$G_{ij} = \sum_{\{e \,|\, i \in e\}} c_k \frac{D^e_{kj}}{24} \tag{2.150}$$

This can be written in the form

$$G_{ij} = F_{jik} c_k \tag{2.151}$$

where $\boldsymbol{F}$ can be assembled in MERRILL as

```
1  F(1:3, 1:NNODE, 1:NNODE) = 0
2  DO e=1,NTRI
3    DO j=1,3
4      DO k=1,4
5      DO i=1,4
6        inode = TIL(e, j)
7        knode = TIL(e, k)
8
9        D = (/ b(e, j), c(e, j), d(e, j) /)
10
11       F(j, inode, knode) = F(j, inode, knode) + D(k) / 24
12     END DO
13     END DO
14   END DO
15 END DO
```

and evaluated

```
1  H(1:NNODE, 1:3) = 0
2  DO i=1,NNODE
3    DO j=1,3
4      H(j, i) = 0
5      DO k=1,NNODE
6        H(j, i) = H(j, i) + F(j, i, k) * phi(k)
7      END DO
8    END DO
9  END DO
```

2.3.2 Exchange Energy Gradient

The exchange energy is defined

$$\mathcal{E} = A \cdot m_{k,l} \cdot m_{k,l} \tag{2.152}$$

We will approach this slightly differently. We cast this to the FEM formulation

$$E = \sum_e \int_{\Omega_e} A \lambda_{n,l} J_{nk} \lambda_{o,l} J_{ok} \, dV \tag{2.153}$$

Now, replacing $\lambda_{k,i}$ with $\boldsymbol{D}^e$, and taking derivatives with respect to J_{ij},

$$\begin{aligned} G_{ij} &= \sum_{\{e \,|\, i \in e\}} \int_{\Omega_e} 2A D^e_{nl} J_{nj} D^e_{il} \, dV \\ &= \sum_{\{e \,|\, i \in e\}} 2A^e D^e_{nl} J_{nj} D^e_{il} V^e \end{aligned} \tag{2.154}$$

$$G_{ij} = \sum_{\{e \,|\, i \in e\}} 2A^e D^e_{nl} J_{nj} D^e_{il} V^e \tag{2.155}$$

with A^e representing the exchange coupling in tetrahedron e. Here, the exchange coupling is assumed to be constant over each tetrahedron, but may vary from tet to tet. This looks a lot like the formulation for the Poisson equation we worked out earlier, except with the extra A^e. We can write this

$$G_{ij} = 2A_s F_{sik} J_{kj} \tag{2.156}$$

where A_k represents the value of A for subdomain k. A subdomain here is the set of tetrahedra with the same material parameters. This can be assembled

```
1 F(1:NMaterials, 1:NNODE, 1:NNODE) = 0
2 DO e=1,NTRI
3   sd = TetSubDomains(e)
4   DO i=1,4
5   DO k=1,4
6     inode = TIL(e, i)
```

```
      knode = TIL(e, k)
      F(sd, inode, knode) = F(sd, inode, knode) &
        + ( &
            b(e, inode)*b(e, knode) &
          + c(e, inode)*c(e, knode) &
          + d(e, inode)*d(e, knode) &
        ) * vol(e)
    END DO
    END DO
END DO
```

and evaluated

```
H(1:NNODE, 1:3) = 0
DO i=1,NNODE
  DO j=1,3
    H(i,j) = 0
    DO k=1,NNODE
      DO s=1,NMaterials
        H(i,j) = H(i,j) + 2*A(s)*F(s,i,k)*m(k,j)
      END DO
    END DO
  END DO
END DO
```

2.3.3 Anisotropy Energy Gradient

The anisotropy energy is given

$$\mathcal{E} = K_1 \left(\alpha_1^2 \alpha_2^2 + \alpha_2^2 \alpha_3^2 + \alpha_3^2 \alpha_1^2 \right) \tag{2.157}$$

where K_1 is the anisotropy constant, the 3 cubic axes are $\vec{a}_1$, $\vec{a}_2$, $\vec{a}_3$, and using the notation

$$\vec{a}_i = (a_{i1},\ a_{i2},\ a_{i3}) \tag{2.158}$$

α_i is defined

$$\alpha_i = m_j a_{ij} \tag{2.159}$$

with effective field

$$H_i = K_1\big(2a_{1i}(m_k a_{2k})^2 + 2a_{2i}(m_k a_{1k})^2 + 2a_{2i}(m_k a_{3k})^2 + 2a_{3i}(m_k a_{2k})^2 + 2a_{3i}(m_k a_{1k})^2 + 2a_{1i}(m_k a_{3k})^2\big) \tag{2.160}$$

which has some high order, complex dependencies on $\vec{m}$. The usual approach taken for turning this from a pointwise value to an energy gradient has looked like the following

$$\begin{aligned} G_{ij} &= \sum_e \int_{\Omega_e} H_j \lambda_i \, dV \\ &= H_j(\vec{v}_i) \sum_e \int_{\Omega_e} \lambda_i \, dV \\ &= H_j(\vec{v}_i) \sum_e \frac{|V^e|}{4} \end{aligned} \tag{2.161}$$

This looks like a projection of a pointwise value to an energy gradient value. This is the current approach used in MERRILL for converting pointwise fields to FEM energy gradients.

However, a clear issue arises, which is the value H_i is assumed constant over the tetrahedron. An alternate formulation might be to project the pointwise H_i onto a linear function, and then integrate. This raises the issue that our field isn't linear in the magnetization. However, for an accurate model, variations in the magnetization should be small over a tetrahedron, so any non-linear effects should look locally flat over a tetrahedron, so linear interpolation should not introduce any large errors. We will write the linear interpolation of $\vec{H}$ over a tetrahedron

$$H_i = \lambda_j h_{ji} \quad \text{in } \Omega_e \tag{2.162}$$

with

$$h_{ji} = H_i(\vec{v}_j) \tag{2.163}$$

representing the value of H_i at vertex j, where $\vec{v}_j$ the point at vertex j.

Now we get

$$\begin{aligned} G_{ij} &= \sum_e \int_{\Omega_e} H_j \lambda_i \, dV \\ &= \sum_e \int_{\Omega_e} \lambda_k h_{kj} \lambda_i \, dV \\ &= \sum_e h_{kj} \int_{\Omega_e} \lambda_k \lambda_i \, dV \\ &= \sum_e h_{kj} 6 |V^e| \frac{1+\delta_{ki}}{120} \\ &= \sum_e h_{kj} |V^e| \frac{1+\delta_{ki}}{20} \end{aligned} \tag{2.164}$$

$$G_{ij} = \sum_{\{e \,|\, j \in e\}} \sum_{k \in e} h_{kj} |V^e| \frac{1+\delta_{ki}}{20} \tag{2.165}$$

It would be worth investigating the difference between these approaches, and whether any change is really necessary.

2.4 Projection of Element-wise Multi-phase Expressions to Pointwise Expressions

Outline:
In this section, we present a method of transforming element-wise defined values defined into point-wise defined values.

First, we multiply the element-wise values by the BEM style test function and taking the integral about the point of interest, and perform the usual BEM style integral transforms. Then we take the limit as the radius of integrated region goes to zero, returning a value at that point.

In micromagnetism, a number of pointwise expressions come up, like the anisotropy energy, which have no differential equations and are defined point-

wise

$$\mathcal{E}^{\text{anis}} = K_1 \left(\alpha_1^2\alpha_2^2 + \alpha_2^2\alpha_3^2 + \alpha_3^2\alpha_1^2\right) \tag{2.166}$$

where K_1 is the anisotropy constant, the 3 cubic axes are $\vec{a}_1$, $\vec{a}_2$, $\vec{a}_3$, and using the notation

$$\vec{a}_i = (a_{i1},\ a_{i2},\ a_{i3}) \tag{2.167}$$

α_i is defined

$$\alpha_i = m_j a_{ij} \tag{2.168}$$

We note that $|m| = 1$ and $|a_i| = 1$.

We want a consistent formulation for this energy and the effective field $H_i^{\text{anis}} = \frac{\partial}{\partial m_i}\mathcal{E}^{\text{anis}}$ where K_1 and $\vec{a}_i$ are element-wise constant, but discontinuous across certain boundaries, and $\vec{H}^{\text{anis}}$ is continuous throughout Ω. The approach laid out here is currently used in MERRILL to produce multi-phase FEM energy gradients from pointwise defined fields.

We choose to study the anisotropy energy here as it's a point-wise energy, and since the exchange energy and the demagnetizing energy implicitly require element-wise calculation when evaluating spatial gradients using the FEM. Results here can, for instance, be extended to defining a multi-phase Zeeman energy. The element-wise subdomains can, therefore, be baked into the linear operators used to calculate these values, and the subdomain values added in during evaluation. There are also some concerns when evaluating point-wise multi-phase values including spatial gradients, since it's likely the governing energies and equations were derived assuming the coupling parameters were constant, so spatial gradients of the coupling parameters may have been dropped.

We are reaching a saturation point for subscripts here, so we will use two sets of cubic axes a and b and two anisotropy constants K_{a1} and K_{b1}, and two non-

overlapping magnetic regions Ω_a and Ω_b, and a non-magnetic region Ω_0

$$\begin{aligned}
\mathcal{E}^{\text{anis}} &= K_{a1}\big((m_j a_{1j})^2(m_k a_{2k})^2 \\
&\qquad + (m_j a_{2j})^2(m_k a_{3k})^2 + (m_j a_{3j})^2(m_k a_{1k})^2\big) && \text{in } \Omega_a && \text{(2.169a)} \\
\mathcal{E}^{\text{anis}} &= K_{b1}\big((m_j b_{1j})^2(m_k b_{2k})^2 \\
&\qquad + (m_j b_{2j})^2(m_k b_{3k})^2 + (m_j b_{3j})^2(m_k b_{1k})^2\big) && \text{in } \Omega_b && \text{(2.169b)} \\
\mathcal{E}^{\text{anis}} &= 0 && \text{in } \Omega_0 && \text{(2.169c)}
\end{aligned}$$

The total energy can be given

$$\begin{aligned}
E^{\text{anis}} &= \int_{\Omega_a+\Omega_b} \mathcal{E}^{\text{anis}}\, dV \\
&= \int_{\Omega_a} K_{a1}\big((m_j a_{1j})^2(m_k a_{2k})^2 \\
&\qquad\qquad + (m_j a_{2j})^2(m_k a_{3k})^2 + (m_j a_{3j})^2(m_k a_{1k})^2\big)\, dV \\
&\quad + \int_{\Omega_b} K_{b1}\big((m_j b_{1j})^2(m_k b_{2k})^2 \\
&\qquad\qquad + (m_j b_{2j})^2(m_k b_{3k})^2 + (m_j b_{3j})^2(m_k b_{1k})^2\big)\, dV
\end{aligned} \tag{2.170}$$

From this it's clear that the two regions can be treated separately. Any suitable numerical integration scheme can be used for this.

For the effective field

$$H_i^{\text{anis}} = \frac{\partial}{\partial m_i}\mathcal{E}^{\text{anis}} \tag{2.171}$$

we have the slightly more verbose

$$
\begin{aligned}
H_i^{\text{anis}} &= H_{ai}^{\text{anis}} \\
&= K_{a1}\big(2a_{1i}(m_k a_{2k})^2 + 2a_{2i}(m_k a_{1k})^2 \\
&\qquad + 2a_{2i}(m_k a_{3k})^2 + 2a_{3i}(m_k a_{2k})^2 \\
&\qquad + 2a_{3i}(m_k a_{1k})^2 + 2a_{1i}(m_k a_{3k})^2\big) \quad \text{in } \Omega_a
\end{aligned} \tag{2.172a}
$$

$$
\begin{aligned}
H_i^{\text{anis}} &= H_{bi}^{\text{anis}} \\
&= K_{b1}\big(2b_{1i}(m_k b_{2k})^2 + 2b_{2i}(m_k b_{1k})^2 \\
&\qquad + 2b_{2i}(m_k b_{3k})^2 + 2b_{3i}(m_k b_{2k})^2 \\
&\qquad + 2b_{3i}(m_k b_{1k})^2 + 2b_{1i}(m_k b_{3k})^2\big) \quad \text{in } \Omega_b
\end{aligned} \tag{2.172b}
$$

$$
H_i^{\text{anis}} = 0_i \qquad \text{in } \Omega_0 \tag{2.172c}
$$

This poses a bit more of a challenge, since $\vec{H}^{\text{anis}}$ must be worked out at each point. In addition, we want $\vec{H}^{\text{anis}}$ to be continuous, while $\vec{H}_a^{\text{anis}}$ and $\vec{H}_b^{\text{anis}}$ need not be continuous across shared borders. We seek a reasonable interpolation of H^{anis} which is pointwise defined, but reflects the volume-wise definition of the various anisotropies.

We use the weak form

$$
\begin{aligned}
\int_{\Omega_a+\Omega_b} H_i \cdot \phi_i' \, dV = &\int_{\Omega_a} K_{a1}\big(2a_{1i}(m_k a_{2k})^2 + 2a_{2i}(m_k a_{1k})^2 \\
&\qquad + 2a_{2i}(m_k a_{3k})^2 + 2a_{3i}(m_k a_{2k})^2 \\
&\qquad + 2a_{3i}(m_k a_{1k})^2 + 2a_{1i}(m_k a_{3k})^2\big) \cdot \phi_i' \, dV \\
+ &\int_{\Omega_b} K_{b1}\big(2b_{1i}(m_k b_{2k})^2 + 2b_{2i}(m_k b_{1k})^2 \\
&\qquad + 2b_{2i}(m_k b_{3k})^2 + 2b_{3i}(m_k b_{2k})^2 \\
&\qquad + 2b_{3i}(m_k b_{1k})^2 + 2b_{1i}(m_k b_{3k})^2\big) \cdot \phi_i' \, dV
\end{aligned} \tag{2.173}
$$

where $\vec{\phi'}$ is an arbitrary vector-valued test function. Again, the regions can be treated separately, but the integral isn't linear in $\vec{m}$. We write it in the shorter form

$$
\int_{\Omega_a+\Omega_b} H_i^{\text{anis}} \cdot \phi_i' \, dV = \int_{\Omega_a} H_{ai}^{\text{anis}} \cdot \phi_i' \, dV + \int_{\Omega_b} H_{bi}^{\text{anis}} \cdot \phi_i' \, dV \tag{2.174}
$$

We will again make use of the Green's function defined earlier

$$\psi_{\vec{w}} = -\frac{1}{4\pi|\vec{x}-\vec{w}|}$$

and we will use only ϕ'_γ non-zero, and say

$$\phi'_m = \begin{cases} \partial_i\partial_i\psi_{\vec{w}} = \delta^3(\vec{x}-\vec{w}) & \text{if } m = \gamma \\ 0 & \text{otherwise} \end{cases} \tag{2.175}$$

Using similar tricks to before, we will cut a ball Ω_ϵ out of the region Ω, and split it up into $\Omega_{a'}$, the region of Ω_a without the ball, $\Omega_{\epsilon a}$ the region of Ω_a inside the ball, and $\omega_{\epsilon a}$ for the common surface of the ball between $\Omega_{a'}$ and $\Omega_{\epsilon a}$. We similarly define $\Omega_{b'}$, $\Omega_{\epsilon b}$ and $\omega_{\epsilon b}$. We note that the volume integrals over $\Omega_{a'}$ and $\Omega_{b'}$ will never reach the point $\vec{w}$, and so are uniformly zero.

We will look at the LHS

$$\chi_{\text{LHS}} = \int_{\Omega_{\epsilon a}+\Omega_{\epsilon b}} H_\gamma \cdot \partial_i\partial_i\psi_{\vec{w}}\, dV \tag{2.176}$$

As before, we will split H_γ over Ω_ϵ up into

$$\begin{aligned} H_\gamma(\vec{x}) &= H_\gamma(\vec{w}) + \eta_1(\vec{x}) \\ (\partial_i H_\gamma)(\vec{x}) &= (\partial_i H_\gamma)(\vec{w}) + \eta_{2i}(\vec{x}) \end{aligned} \tag{2.177}$$

with $lim_{\epsilon\to 0}\eta_1 = 0$ and $lim_{\epsilon\to 0}\eta_{2i} = 0$.

Now we can say, using integration by parts and the divergence theorem as before

$$\begin{aligned} \int_{\Omega_{\epsilon a}+\Omega_{\epsilon b}} \partial_i(H_\gamma \cdot \partial_i\psi_{\vec{w}})\, dV &= \int_{\Omega_{\epsilon a}+\Omega_{\epsilon b}} (\partial_i H_\gamma)\cdot(\partial_i\psi_{\vec{w}})\, dV \\ &\quad + \int_{\Omega_{\epsilon a}+\Omega_{\epsilon b}} H_\gamma \cdot (\partial_i\partial_i\psi_{\vec{w}})\, dV \\ &= \int_{\Omega_{\epsilon a}+\Omega_{\epsilon b}} (\partial_i H_\gamma)\cdot(\partial_i\psi_{\vec{w}})\, dV + \chi_{\text{LHS}} \end{aligned} \tag{2.178}$$

Looking at the first term and applying the divergence theorem

$$\begin{aligned}\chi_1 &= \int_{\Omega_{\epsilon a}+\Omega_{\epsilon b}} \partial_i(H_\gamma \cdot \partial_i \psi_{\vec{w}})\, dV \\ &= \int_{\partial\Omega_{\epsilon a}+\partial\Omega_{\epsilon b}} H_\gamma \cdot n_i \partial_i \psi_{\vec{w}}\, dS\end{aligned} \tag{2.179}$$

We can split each region into two regions. For the region $\Omega_{\epsilon a}$, we have the surface of the ball cutting through the volume, $\omega_{\epsilon a}$, and also possibly the boundary of the region Ω_a inside the ball, which includes the point $\vec{w}$, which is defined by a number of tetrahedral faces. We will denote this tetrahedral boundary region $f_{\epsilon a}$.

$$\chi_1 = \int_{\partial\omega_{\epsilon a}+f_{\epsilon a}+\partial\omega_{\epsilon b}+f_{\epsilon b}} H_\gamma \cdot n_i \partial_i \psi_{\vec{w}}\, dS \tag{2.180}$$

As before, we can say

$$\begin{aligned} n_i &= \frac{x_i - w_i}{|\vec{x}-\vec{w}|} && \text{in } \partial\Omega_\epsilon \\ \partial_i \psi_{\vec{w}} &= \frac{x_i - w_i}{4\pi|\vec{x}-\vec{w}|^3} && \\ n_i \partial_i \psi_{\vec{w}} &= \frac{1}{4\pi|\vec{x}-\vec{w}|^2} && \text{in } \partial\Omega_\epsilon \end{aligned} \tag{2.181}$$

and so, looking at the $\omega_{\epsilon a}$ and $\omega_{\epsilon b}$ regions, we find

$$\begin{aligned}\chi_{1\omega} &= \int_{\partial\omega_{\epsilon a}+\partial\omega_{\epsilon b}} H_\gamma \cdot \frac{1}{4\pi|\vec{x}-\vec{w}|^2}\, dS \\ &= H_\gamma(\vec{w}) \int_{\partial\omega_{\epsilon a}+\partial\omega_{\epsilon b}} \frac{1}{4\pi|\vec{x}-\vec{w}|^2}\, dS + \int_{\partial\omega_{\epsilon a}+\partial\omega_{\epsilon b}} \eta_1 \cdot \frac{1}{4\pi|\vec{x}-\vec{w}|^2}\, dS \\ &= \chi_{11} + \chi_{12}\end{aligned} \tag{2.182}$$

Again

$$\begin{aligned} |\chi_{12}| &= \left| \int_{\partial\omega_{\epsilon a}+\partial\omega_{\epsilon b}} \eta_1 \cdot \frac{1}{4\pi|\vec{x}-\vec{w}|^2}\, dS \right| \\ &\leq |\eta_1|\, |\frac{1}{4\pi\epsilon^2}|\, |4\pi\epsilon^2| = |\eta_1| \\ \Rightarrow \lim_{\epsilon\to 0} |\chi_{12}| &\leq \lim_{\epsilon\to 0} |\eta_1| = 0 \\ \Rightarrow \lim_{\epsilon\to 0} \chi_{12} &= 0 \end{aligned} \tag{2.183}$$

and

$$\begin{aligned} \chi_{11} &= \frac{H_\gamma(\vec{w})}{4\pi} \int_{\partial\omega_{\epsilon a}+\partial\omega_{\epsilon b}} \frac{1}{|\vec{x}-\vec{w}|^2}\, dS \\ &= \frac{H_\gamma(\vec{w})}{4\pi} \int_{\partial\omega_{\epsilon a}+\partial\omega_{\epsilon b}} d\Omega_{\vec{w}} \\ &= \frac{H_\gamma(\vec{w})}{4\pi} \left(\alpha_{a\vec{w}} + \alpha_{b\vec{w}}\right) \end{aligned} \tag{2.184}$$

where $\alpha_{a\vec{w}}$ is the solid angle at the vertex $\vec{w}$ in all the tetrahedra with the vertex $\vec{w}$ in the region Ω_a, and similar for $\alpha_{b\vec{w}}$. For H_γ in the interior of a the magnetic region, i.e. not a boundary node, we should have $\chi_{11} = H_\gamma(\vec{w})$.

Now

$$\lim_{\epsilon\to 0} \chi_{1\epsilon} = \frac{H_\gamma(\vec{w})}{4\pi} \left(\alpha_{a\vec{w}} + \alpha_{b\vec{w}}\right) \tag{2.185}$$

Looking at the region over the tetrahedral faces, and converting into polar coordinates centered about $\vec{w}$ and a solid angle integral about $\vec{w}$

$$\begin{aligned} \chi_{1f} &= \int_{f_{\epsilon a}+f_{\epsilon b}} H_\gamma \cdot n_i \partial_i \psi_{\vec{w}}\, dS \\ &= \int_{f_{\epsilon a}+f_{\epsilon b}} H_\gamma \cdot n_i \frac{x_i - w_i}{4\pi|\vec{x}-\vec{w}|^3}\, dS \\ &= \int_{f_{\epsilon a}+f_{\epsilon b}} H_\gamma \cdot n_i \frac{r_i}{4\pi|r|}\, d\Omega_{\vec{w}} \\ &= \frac{1}{4\pi} \int_{f_{\epsilon a}+f_{\epsilon b}} H_\gamma \cdot n_i \hat{r}_i\, d\Omega_{\vec{w}} \end{aligned} \tag{2.186}$$

Now, as $\epsilon \to 0$, a region, say $f_{\epsilon a}$, can be split up into a set of integrals over a set of triangular faces, each of which will contain the vertex $\vec{w}$. On any particular triangle, which contains the vertex $\vec{w}$, we now have the surface normal $\vec{n}$ facing out of the plane of the triangle, and the normal radial vector $\hat{r}$ which is in the

plane of the triangle. It follow, then, that these two vectors are orthogonal, and so the dot produce $n_i \hat{r}_i$ is uniformly zero. So now, while the limit of $\vec{n}$ and $\hat{r}$ will depend on which direction you approach $\vec{w}$ from, the dot product $n_i \hat{r}_i$ does not, and so it is well defined as 0 at $\vec{w}$. And now we can say

$$\lim_{\epsilon \to 0} \chi_{1f} = 0 \tag{2.187}$$

Putting this all together, we have

$$H_\gamma(\vec{w}) \left(\frac{\alpha_{a\vec{w}} + \alpha_{b\vec{w}}}{4\pi} \right) = \int_{\Omega_{\epsilon a} + \Omega_{\epsilon b}} (\partial_i H_\gamma) \cdot (\partial_i \psi_{\vec{w}}) \, dV + \chi_{\text{LHS}} \tag{2.188}$$

Next, we tackle the remaining integral term

$$\begin{aligned} \chi_2 &= \int_{\Omega_{\epsilon a} + \Omega_{\epsilon b}} (\partial_i H_\gamma) \cdot (\partial_i \psi_{\vec{w}}) \, dV \\ &= \int_{\Omega_{\epsilon a} + \Omega_{\epsilon b}} (\partial_i H_\gamma) \cdot \frac{x_i - w_i}{4\pi |\vec{x} - \vec{w}|^3} \, dV \\ &= (\partial_i H_\gamma)(\vec{w}) \int_{\Omega_{\epsilon a} + \Omega_{\epsilon b}} \frac{x_i - w_i}{4\pi |\vec{x} - \vec{w}|^3} \, dV + \int_{\Omega_{\epsilon a} + \Omega_{\epsilon b}} \eta_2 \cdot \frac{x_i - w_i}{4\pi |\vec{x} - \vec{w}|^3} \, dV \end{aligned} \tag{2.189}$$

Taking the maximum value

$$\begin{aligned} |\chi_2| &\leq |(\partial_i H_\gamma)(\vec{w})| \left| \frac{\epsilon}{\epsilon^3} \right| \left| \frac{4}{3} \pi \epsilon^3 \right| + |\eta_2| \left| \frac{\epsilon}{\epsilon^3} \right| \left| \frac{4}{3} \pi \epsilon^3 \right| \\ &= \left(|(\partial_i H_\gamma)(\vec{w})| + |\eta_2| \right) |\epsilon| \\ \Rightarrow \lim_{\epsilon \to 0} |\chi_2| &\leq 0 \\ \Rightarrow \lim_{\epsilon \to 0} \chi_2 &= 0 \end{aligned} \tag{2.190}$$

And now, we have

$$\chi_{\text{LHS}} = \int_\Omega H_\gamma \cdot \partial_i \partial_i \psi_{\vec{w}} \, dV = H_\gamma(\vec{w}) \left(\frac{\alpha_{a\vec{w}} + \alpha_{b\vec{w}}}{4\pi} \right) \tag{2.191}$$

This is quite clearly just the definition of a Green's function. However, given the definition we used here, when our Green's function is used on the bound-

ary of a material, the value at a given vertex will be weighted by the solid angle at the vertex in each material. For the effective field $\vec{H}^{\text{anis}}$, this isn't particularly useful for averaging out multi-phase effects, but it is important for a well defined average when taken at the boundary between a magnetic material and a non-magnetic one.

Returning to the weak form

$$\int_{\Omega_a+\Omega_b} H_i^{\text{anis}} \cdot \phi_i' \, dV = \int_{\Omega_a} H_{ai}^{\text{anis}} \cdot \phi_i' \, dV + \int_{\Omega_b} H_{bi}^{\text{anis}} \cdot \phi_i' \, dV \tag{2.192}$$

From the above discussion, and substituting H_γ for $\xi_{\beta\gamma}$ as appropriate, we find

$$H_i^{\text{anis}}(\vec{w}) \left(\frac{\alpha_{a\vec{w}} + \alpha_{b\vec{w}}}{4\pi} \right) = H_{ai}^{\text{anis}} \left(\frac{\alpha_{a\vec{w}}}{4\pi} \right) + H_{bi}^{\text{anis}} \left(\frac{\alpha_{b\vec{w}}}{4\pi} \right) \tag{2.193}$$

and cancelling the 4π

$$H_i^{\text{anis}}(\vec{w}) \left(\alpha_{a\vec{w}} + \alpha_{b\vec{w}} \right) = H_{ai}^{\text{anis}} \, \alpha_{a\vec{w}} + H_{bi}^{\text{anis}} \, \alpha_{b\vec{w}} \tag{2.194}$$

So now we can find $\vec{H}$ at a point $\vec{w}$ by taking a weighted average of the different, discontinuous values for the field. For many regions, we have

$$\vec{H}^{\text{anis}}(\vec{w}) = \frac{\sum_\beta H_\beta^{\text{anis}}(\vec{w}) \, \alpha_{\beta\vec{w}}}{\sum_\beta \alpha_{\beta\vec{w}}} \tag{2.195}$$

This approach can then be extended to any projection of traits that are element-wise well defined, but must be point-wise well defined.

Finally, the anisotropy energy gradient in MERRILL is defined, as previously discussed, and using the pointwise formulation described here for $\vec{H}^{\texttt{anis}}$

$$G_{ij} = H_j^{\texttt{anis}}(\vec{v}_i) \sum_e \frac{|V^e|}{4} \tag{2.196}$$

Chapter 3

Example MERRILL Modelling Results

We present some example results from single-phase and multi-phase modelling using MERRILL. We begin by running μMAG Standard Problem 3 (μMAG 2017) on MERRILL, as a verification of correctness. Next, we run a simple core-shell model to demonstrate the sort of modelling our extension to multi-phase materials might allow.

The results of each section represent original results. In the case of the μMAG results, while not strictly new, the contribution of MERRILL's results to the existing body of results is a significant contribution.

3.1 μMAG Standard Problem 3

3.1.1 Introduction

The μMAG Standard Problem 3 (μMAG 2017) is a test for the critical edge length of a cube with uniaxial anisotropy for a change in the magnetic phase from a flower state to a single vortex state.

In Standard Problem 3, the material parameters of the cube: the saturation magnetization M_s, the exchange coupling A, and the uniaxial anisotropy constant K_u are related by the following relations

$$K_u = 0.1\frac{1}{2}\mu_0 M_s^2 \tag{3.1}$$

and the exchange length is given

$$l_{ex} = \sqrt{\frac{A}{K_m}} \tag{3.2}$$

This material was realized in MERRILL using

$$\begin{aligned} M_s &= 4.807680 \times 10^5 \text{ A/m} \\ A &= 1.334870 \times 10^{-11} \text{ J/m} \\ K_u &= 1.452282 \times 10^4 \text{ J/m}^3 \end{aligned} \tag{3.3}$$

where M_s and A here are the saturation magnetization and exchange coupling for Magnetite and K_u is derived from the above relation to M_s. This gives us the exchange length

$$l_{ex} = 9.587248 \times 10^{-3} \ \mu\text{m} \tag{3.4}$$

3.1.2 Method

To nucleate a flower state, the mesh is scaled to $7.5\times l_{ex}$ and a Local Energy Minimum (LEM) is found, then rescaled to $8.45\times l_{ex}$ and the LEM found, and then saved to disk. By "scaled to", we mean the mesh is resized until edge

length of the cube is the given value. This two step approach to nucleation is needed, since a flower state isn't guaranteed to nucleate at $8.45 \times l_{ex}$, because this is around the critical edge length. So a flower state is nucleated away from the critical edge length, and then re-minimized around the critical edge length. Re-minimizing at $8.45 \times l_{ex}$ is done primarily to save time during minimization later when finding LEMs for the various edge lengths. An initial flower state is shown in figure 3.1.

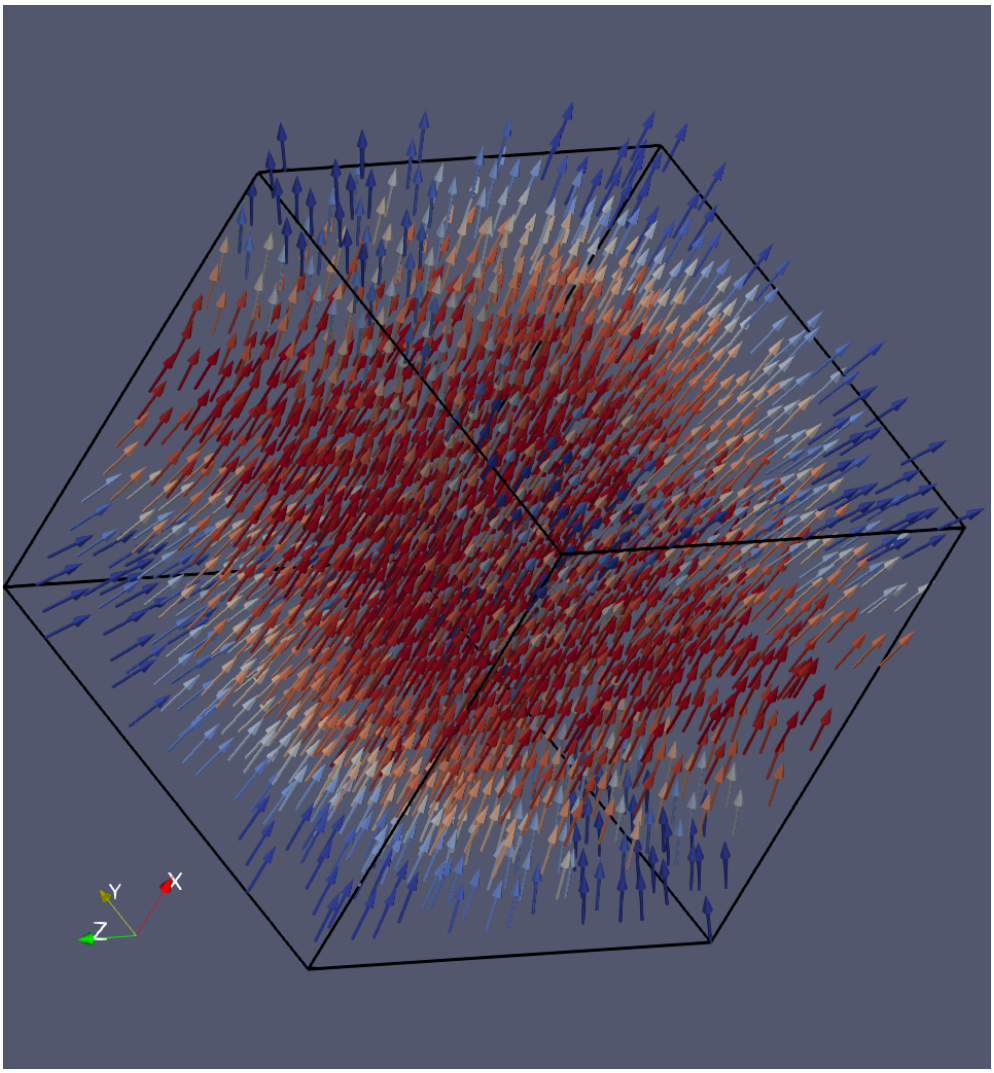

Figure 3.1: An initial flower solution at edge length $8.45 \times l_{ex}$, coloured by helicity ($\vec{M} \cdot (\vec{\nabla} \times \vec{M})$). Blue is lower helicity, red is higher helicity.

To nucleate a vortex state, the mesh is first scaled to $11 \times l_{ex}$ and the LEM found,

then scaled to $8.5 \times l_{ex}$ and the LEM found and saved to disk. Re-minimizing is a particularly useful step here since the vortex at $11 \times l_{ex}$ is much "tighter" than the vortex at $8.5 \times l_{ex}$. By tighter, we mean the vortex core is smaller, with more of the magnetization conforming to the exterior, circular formation. This typically results in a lower overall remanence, despite being a larger grain. This saves a significant amount of time while running the script. An initial state is shown in figure 3.2.

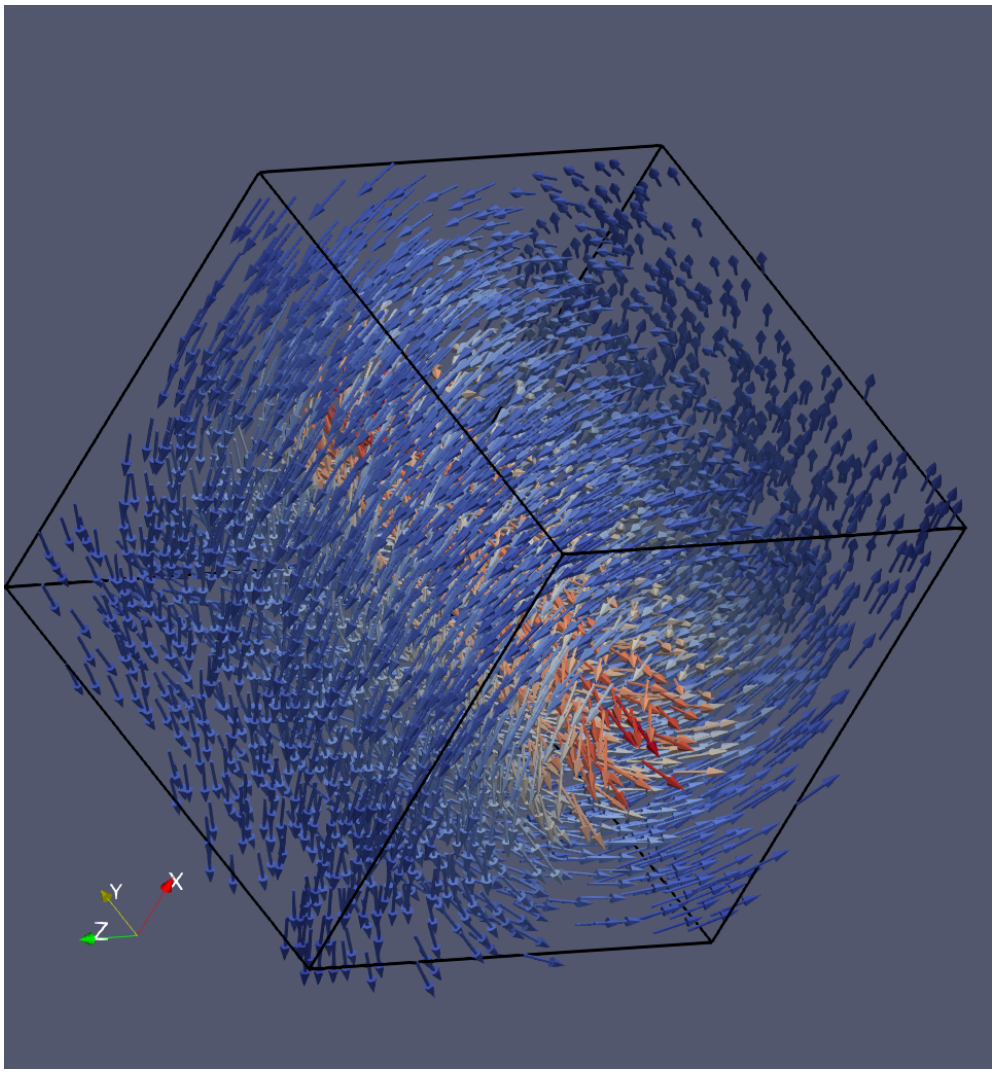

Figure 3.2: An initial vortex state at edge length $8.45 \times lex$ colored by helicity ($\vec{M} \cdot (\vec{\nabla} \times \vec{M})$). Blue is lower helicity, red is higher helicity.

To further save time, these states are first nucleated with a coarse mesh, so

the nucleation and minimization runs much faster, then interpolated onto the target mesh we actually want results for, and re-minimized on the target mesh. The coarse mesh has a node spacing around the exchange length, so the results produced are reasonably accurate. Re-minimizing on the target mesh, then, does not take much time.

To evaluate, say, the flower state energy at a certain cube size, the mesh is scaled to that size, the flower state is loaded from disk, the energy is minimized, and the energy is reported. This is done for the flower and vortex states for a range of cube sizes.

The critical length for the cube is then found by finding the iteration just before the flower state energy passes the single vortex energy and the iteration just after, and using a linear interpolation between the energies of each iteration to find the edge length where they intercept. Denoting the first iteration's flower and vortex energies and length scale as f_-, v_-, l_-, and the second as f_+, v_+, l_+, we can find the intercept length scale by solving for t where

$$v_-(1-t) + v_+t = f_-(1-t) + f_+t \tag{3.5}$$

giving

$$t = \frac{f_- - v_-}{(f_- - v_-) - (f_+ - v_+)} \tag{3.6}$$

and the intercept length l_0 is

$$l_0 = l_-(1-t) + l_+t \tag{3.7}$$

This assumes the energies scale linearly with the edge length, which is incorrect, but for sufficiently small steps of the edge length, it should be accurate enough for this application.

This entire process is then repeated for an increasingly fine mesh. The critical edge length of the cube should scale as the square of the mesh spacing. This is due to higher resolution of derivatives which, for the demagnetizing and exchange calculations are of order 2. By performing a linear fit on the (mesh spacing)^2 versus the intercept length, it should be possible to extrapolate the intercept length for an infinitely fine mesh, i.e. where the mesh spacing is zero.

Two types of mesh were used in this test, a regular one generated by regular subdivision of a cube into tetrahedra, and an irregular one by Delaunay triangulation. The regular mesh was generated using the built in cubic mesh generator in MERRILL. The mesh created by this is very regular, so measuring the average edge length of this mesh is more indicative of a mesh spacing than, say, an irregular mesh, where mesh spacing may vary wildly between different sections of the geometry. The irregular mesh was generated using MEshRRILL, which uses CGAL's Delaunay triangulation algorithm. Example meshes are shown figures 3.3 and 3.4.

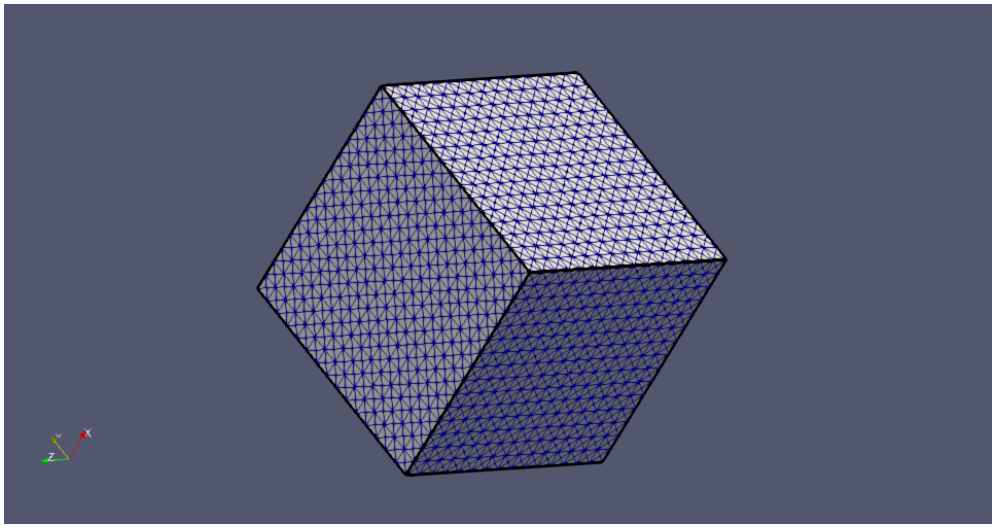

Figure 3.3: Regular cube mesh with a node spacing of $0.5 \times l_{ex}$.

For each mesh, the energies were found for the flower and vortex states for $8.39 \times l_{ex}$ to $4.70 \times l_{ex}$ in steps of $0.01 \times l_{ex}$. The mesh spacings used were $1.0 \times l_{ex}$ to $0.3 \times l_{ex}$ in steps of $0.1 \times l_{ex}$.

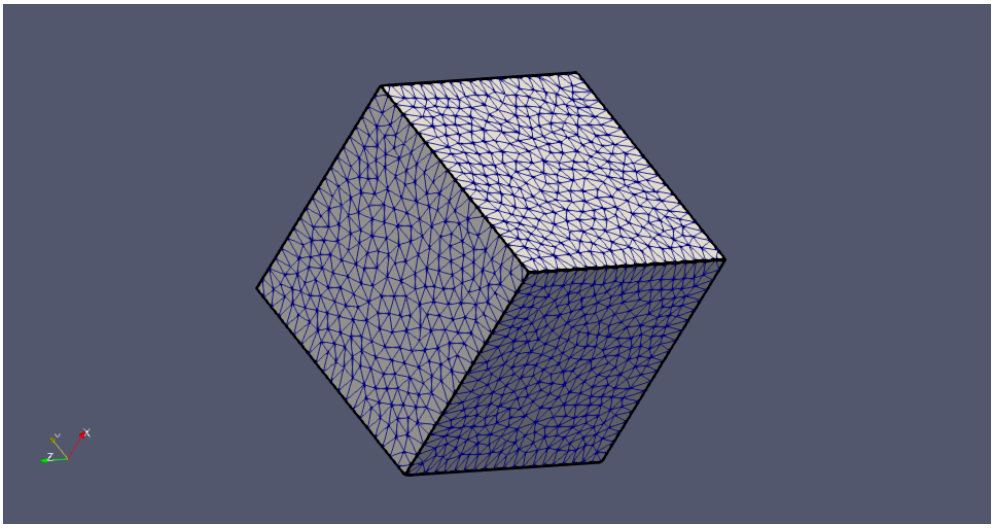

Figure 3.4: Irregular cube mesh with a node spacing of $0.5 \times l_{ex}$.

3.1.3 Results

Regular Mesh

From figure 3.5, the critical edge length for an infinitely fine regular mesh was found to be $(8.4704 \pm 0.0002) \times l_{ex}$, and from figure 3.6, the critical energy was $(0.30261 \pm 0.00001) \times K_d V$.

The extrapolated partial energies are given in units of $K_d V$

	Flower	Vortex
Demag	0.27947 ± 0.00004	0.0785 ± 0.0001
Anisotropy	0.005572 ± 0.000009	0.05218 ± 0.00002
Exchange	0.01757 ± 0.00003	0.1719 ± 0.0001

And the extrapolated magnetizations in units of M_s

	Flower	Vortex
$< m_x >$	0.97118 ± 0.00005	-0.0003 ± 0.0001
$< m_y >$	0.0001 ± 0.0001	0.0 ± 0.22496823
$< m_z >$	-0.0001 ± 0.0001	0.2 ± 0.1

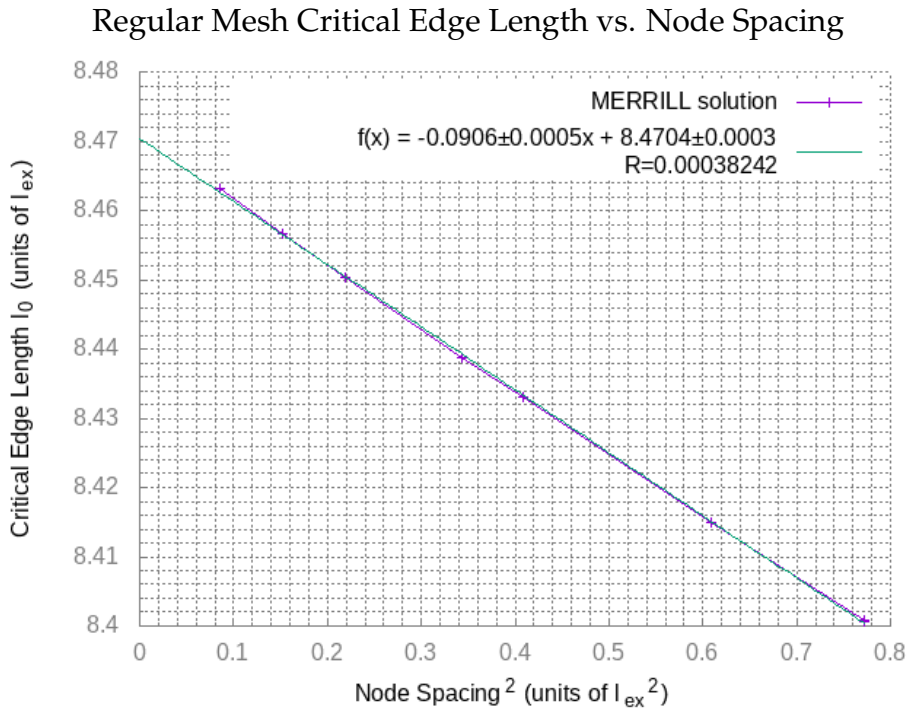

Figure 3.5: The critical length versus the node spacing of the regular mesh, and linear fit extrapolating the node spacing to 0. This shows the critical edge length for an infinitely fine mesh is $(8.4704 \pm 0.0002) \times l_{ex}$.

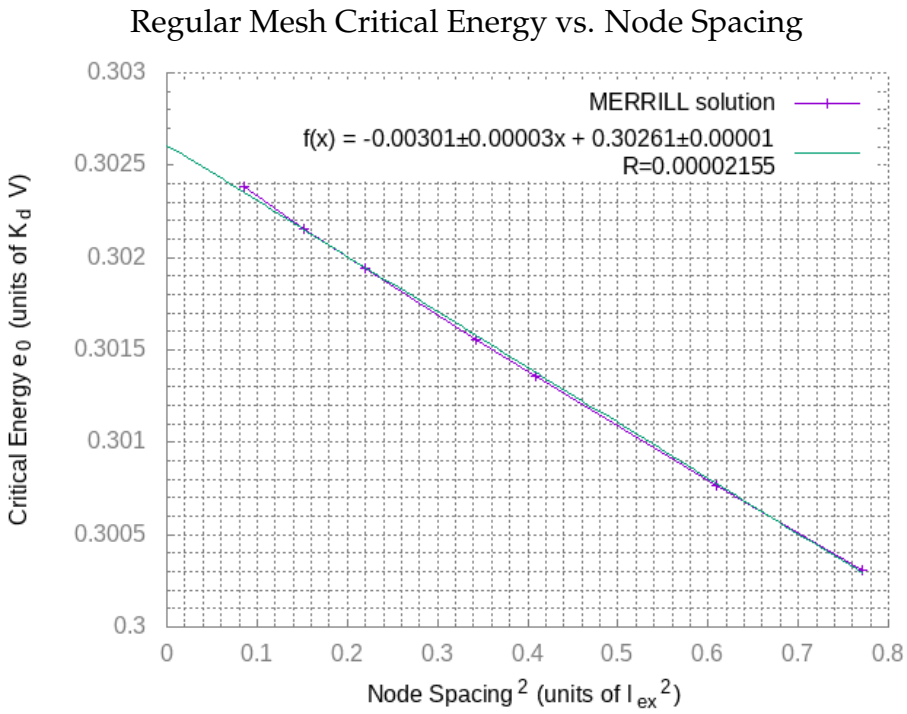

Figure 3.6: The critical energy versus the node spacing of the regular mesh, and linear extrapolating the node spacing to 0. This shows the critical energy for an infinitely fine mesh is $(0.30261 \pm 0.00001) \times K_d V$.

Irregular Mesh

From figure 3.7, the critical edge length for an infinitely fine irregular mesh was found to be $(8.468 \pm 0.002) \times l_{ex}$, and from figure 3.8, the critical energy was $(0.30242 \pm 0.00008) \times K_d V$.

The extrapolated partial energies are given in units of $K_d V$

	Flower	Vortex
Demag	0.2791 ± 0.0001	0.0775 ± 0.0006
Anisotropy	0.00563 ± 0.00002	0.0520 ± 0.0001
Exchange	0.01773 ± 0.00005	0.1729 ± 0.0007

And the extrapolated magnetizations in units of M_s

	Flower	Vortex
$< m_x >$	0.97086 ± 0.00008	-0.0000 ± 0.0008
$< m_y >$	-0.0000 ± 0.0002	0.0 ± 0.3
$< m_z >$	-0.0003 ± 0.0002	0.0000 ± 0.0007

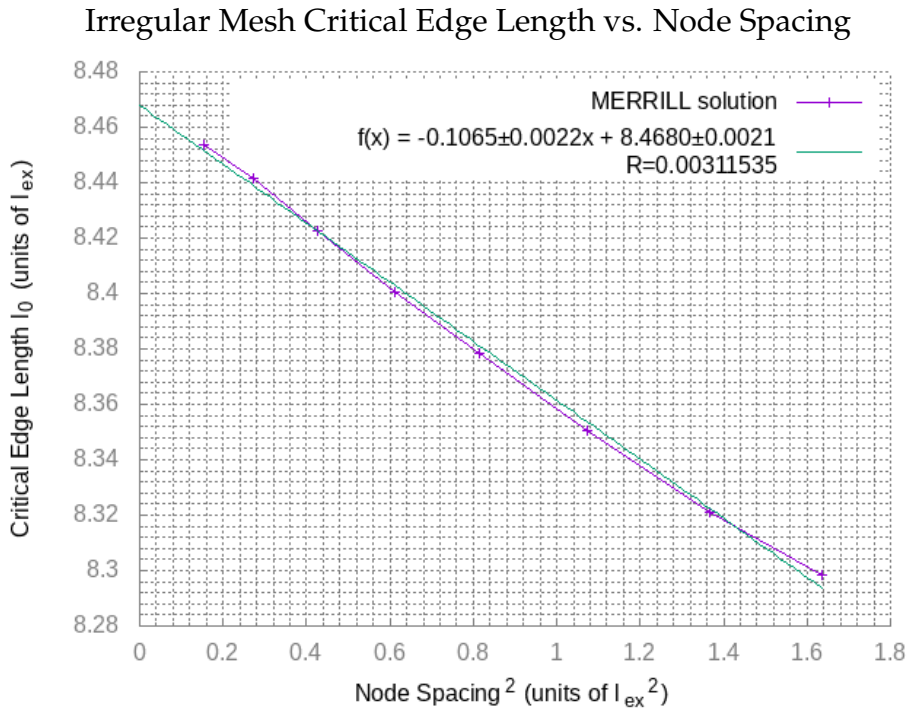

Figure 3.7: The critical length versus the node spacing of the irregular mesh, and linear fit extrapolating the node spacing to 0. This shows the critical edge length for an infinitely fine mesh is $(8.468 \pm 0.002) \times l_{ex}$.

3.1.4 Discussion

The results for the regular and the irregular mesh are in reasonable agreement with each other and with other submissions to the μMAG Standard Problem 3 (μMAG 2017). Potential sources of difference between the regular and irregular meshes are then inherent anisotropy of the regular mesh. In the reg-

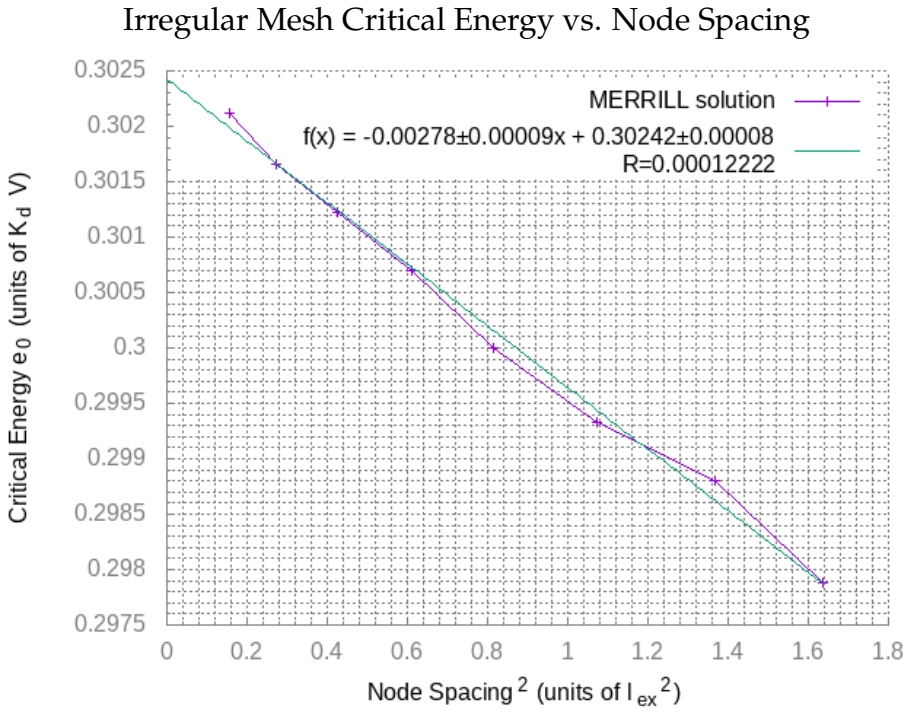

Figure 3.8: The critical energy versus the node spacing of the irregular mesh, and linear extrapolating the node spacing to 0. This shows the critical energy for an infinitely fine mesh is $(0.30242 \pm 0.00008) \times K_d V$.

ular mesh, cubes are split along cube edges and diagonals, admitting a cubic anisotropy, while the irregular mesh has tetrahedra with edges in effectively random directions. I have observed that anisotropic meshes can result in an anisotropic bias of the magnetization. This, in itself, is an interesting result. The irregular mesh, on the other hand, has a broader range of tetrahedron shapes, sizes and orientations. This would tend to average out any anisotropy in the mesh.

The errors presented here are the error in extrapolation of the measured values on the finite meshes to the infinite meshes, not a measurement of the error in the measured values themselves. Indeed, no error measurement was made of these values. In this manner, when comparing between the regular and irregular meshes, and the submissions to the μMAG site, it is more reasonable to roughly compare the measured values, than to compare within the presented errors.

Comparing figures 3.5 and 3.7, and 3.6 and 3.8, it is interesting to note how much more closely the trend lines follow the values of the regular mesh versus the irregular mesh. This is likely due to the node spacing being measured as an average of the edge lengths of the tetrahedra in the mesh. For the regular mesh, this will naturally be quite representative of any given edge in the mesh. However, for the irregular mesh, this represents only the average of the edges. There is no significant constraint on the variance of the edge lengths. As a result, extrapolation using the average tetrahedron edge length for an irregular mesh may not be ideal. However, in this case, the results correspond well enough with those of the regular mesh.

It is, perhaps, worth noting the difference between the values for the critical length and energy in the coarse mesh and the infinite mesh is around 1%. For quantitative measurements, this may be an issue, but for qualitative results, it may be acceptable. In general, however, it is not clear if the results on an infinitely fine mesh would even be within 1% of the real world values, so extrapolating to an infinitely fine mesh, or indeed performing calculations using a very fine mesh, may add precision, but not accuracy to a result. For this reason, and for reasons of time in producing results, we will prefer to use coarse meshes and report trends in this thesis, rather than any hard values, except when comparing models to each other. In this case, coarse means the node spacing will be around the exchange length.

3.2 Core-shell Model

We will explore here the PSD states of a multi-phase material where a magnetic material has a "skin" of a different magnetic material.

3.2.1 Background

We want to model changes in behaviour of magnetite as it becomes oxidized. We will model oxidation of a magnetite grain as it growing a "skin" of constant thickness of maghemite, usually described as a core-shell model. We define the oxidation parameter z by

$$z = \frac{\texttt{Volume Maghemite}}{\texttt{Total Volume}} \tag{3.8}$$

representing the fraction of the grain that has been oxidized to maghemite. No consideration will be given to the exchange coupling between the boundary. The exchange is considered volume-wise constant, so the exchange at the interface will effectively be an average of the two exchange energies. Neither is any consideration given to stresses due to differing lattice sizes between the materials.

Recent work by Nagy et al. (Nagy et al. 2017) has identified easy-axis-aligned Single Domain (SD) and Flower States (FS) as being stable over geological timescales with increasing size, up until the Pseudo-Single Domain (PSD) transition where a Hard-axis-aligned Single Vortex (HSV) are viable LEM states, but highly unstable. Further increases in size to an Easy-axis-aligned Single Vortex (ESV) then rapidly become very stable with increasing size. Therefore, rather than looking at how the coercivities for the grains change with size and oxidation to gauge their magnetic stiffness, which would then be used as a proxy for it's recording fidelity, we will instead identify critical grain sizes where the energies for various local energy minimum states overlap. We will use the results to carve out an "island of instability" where the HSV state energies overlap with the SD/FS and the ESV states and suggest grains smaller and larger than the overlap will be reasonably stable.

We assume that, to move from one state to another, say a [111] SV to a [-111] SV state, the magnetization must move through a state of higher energy. In the worst case scenario, it would move through the highest energy axis, the [100]. However, if the energy of a state along [111] and [100] are the same, or similar, there may be no large energy barrier for the state to pass through. In this case, the state may be in a rather shallow local energy minimum and be quite unstable.

The grains we will look at are truncated octahedra (cuboctahedra). The core-shell model will consist of two concentric cuboctahedra, where the inner octahedron will have the properties of magnetite, and the space between the inner and the outer octahedron will have the properties of maghemite.

We will denote the size of grains using an Equivalent Sphere Volume Diameter (ESVD). That is, for a cuboctahedron of volume, say V, we will denote the ESVD size of that octahedron by the diameter of a sphere with the same volume.

3.2.2 Method

A program was written to generate core-shell octahedron meshes using the CGAL library. Two cuboctahedral polyhedra were built, an inner cuboctahedron and an outer cuboctahedron, and the inner cuboctahedron scaled so

$$\frac{V_{\text{outer}} - V_{\text{inner}}}{V_{\text{outer}}} = z \tag{3.9}$$

to match our definition of the oxidation. A level set was then constructed that returned 1 inside the inner octahedron, 2 between the inner and outer octahedron, and 0 outside the outer octahedron. The sharp edges and corners of the octahedra were added to the triangulation, and then a Delaunay triangulation was performed on the level set, resulting in a tetrahedral mesh representing the core-shell model. The mesh was then subdivided until the average edge length was below the exchange length of magnetite and maghemite. Care must be taken with the edges added to the triangulation that they are the minimum of the exchange length and of the spacing between the two octahedra, or else

the meshing may not terminate.

With the mesh generated for a given oxidation parameter, it was loaded into MERRILL from a custom Fortran program, and the material parameters set for the given subdomains. Three states were then nucleated: a [111] SD/FS state, an anti-clockwise [100] HSV state and an anti-clockwise [111] ESV state. This was done by defining an initial heuristic magnetization that was similar in shape to the desired state, and then each state was minimized near where the overlap edge lengths were expected. Care must be taken here to ensure the expected states actually nucleate. Since there is some overlap between where these states are meta-stable, the desired states are not always guaranteed to nucleate. To this end, a random kick was given to the initial magnetization, the minimization performed, and a conformance check for each state done. If the state failed to conform to the expected parameters (e.g. the average magnetization pointing in the correct direction, and the magnitude of the average magnetization being above or below a given threshold), the nucleation was attempted again.

To find the overlap size between two states, a two step process was employed to reduce the number of minimizations needed. First, the grain was scaled from a minimum size to a maximum size in small increments and the energy of each state evaluated. The minimum and maximum sizes were chosen by trial and error, by manually checking where the energy of the SD/FS state was smaller than that of the HSV and ESV states, and where the energy of the ESV state was larger than that of the SD/FS and HSV states. Once the energy of the second state passed the first, the scaling was stopped and the two states minimized at that size. These two steps were then repeated until the same overlap size was found twice in a row. The minimization step is important because the exact magnetization of a given state, and so the energy, varies slightly with grain size.

This process was done to find the overlap size between the SV/FS and the HSV states, and between the HSV and ESV states. It was done for oxidations of 0, 0.1, 0.2, 0.3 ... 0.9, 1 with 0 representing a whole magnetite grain and 1 a whole maghemite grain.

3.2.3 Results

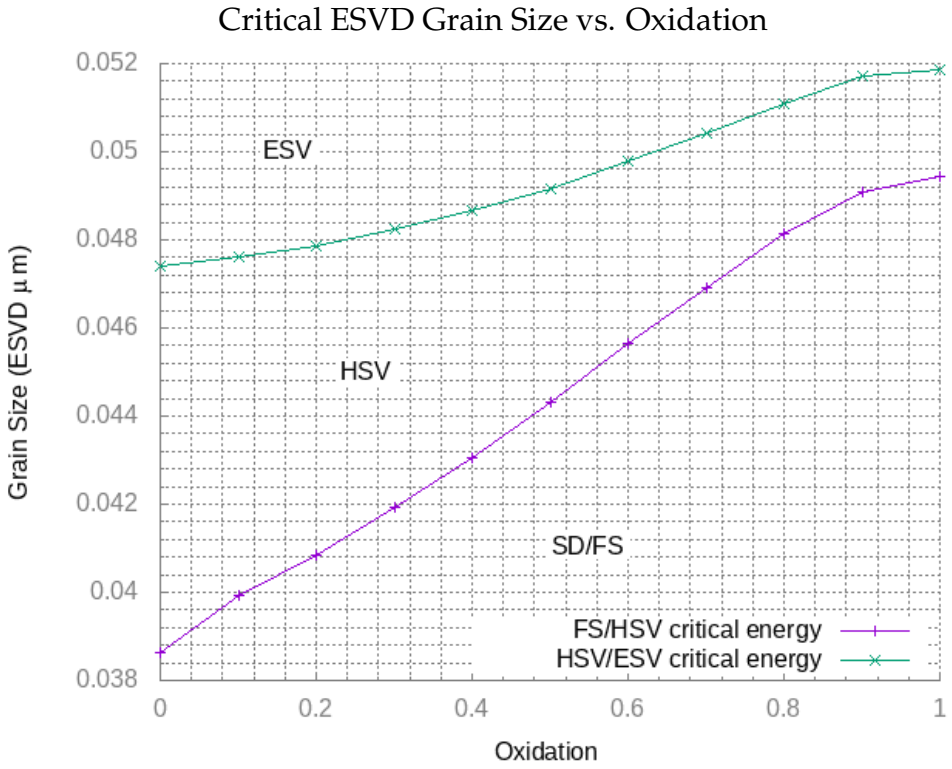

Figure 3.9: The critical ESVD grain size versus oxidation for the SD/FS and HSV states, and the HSV and ESV states.

The critical sizes versus oxidations are shown in figure 3.9. There is a near linear relation between SD/FS and HSV overlap and the oxidation. The relation between HSV and ESV has a shallower slope, and isn't as linear.

The region of instability, where the HSV state is of similar energy to the SD/FS and ESV states is larger for magnetite than for maghemite, and monotonically decreases when moving from $z = 0$ to $z = 1$. The average position of the region, however, increases as the oxidation increases.

3.2.4 Discussion

The results suggest that oxidation raises the minimum stable grain size for PSD grains. For magnetite grains that were on the threshold of stability, oxidation

may push them into an unstable region. In this case, oxidation may effect the recording fidelity of a grain. Similarly, oxidation may move grains which were previously on the lower bound of instability to stability. As a result, SD/FS signals measures from oxidized minerals around the SD/FS and HSV critical size may not be reliable signals.

The inclusion of different boundary exchange values may change the results presented here. This could be included in the model as-is by introducing a third polyhedron in the meshing routine and having an inner, middle, and outer polyhedron, and assigning different subdomains to the inner region, the region between inner and middle, and the region between middle and outer. Setting the thickness the inner-to-middle region to around one exchange length could suffice, and an average of the material parameters could be used. Alternatively, an ab-initio model of the core-shell grain could be done to find the material parameters withing this middle region. Another approach would be to add a surface energy term along the boundary. From previous discussion for constructing the FEM matrices for surface terms, adding this to MERRILL could be straightforward.

Including the magnetostrictive effect between the core and shell could pose quite a challenge. In particular since physical core-shell style grains are typically cracked due to very high stresses. A linear theory of magnetostriction may not be enough to account for this. The inclusion of a linearized theory of dislocations may not even be sufficient to model it. It is likely, however, to have a contribution to the behaviour of the material. A full treatment of magnetostriction is a significant area where multi-phase magnetic modelling tends to be lacking, even for multi-phase magnetic and non-magnetic materials, e.g. from exsolution.

Chapter 4

Conclusions - Micromagnetism

In this part, we presented a thorough derivation of the FEM and BEM formulation for the demagnetizing field in found in Fredkin and Koehler (1990). In particular, we derived it from a boundary condition formulation well suited for a finite geometry, and used in a number of other FEM texts and numerical frameworks, particularly the FEniCS project (Wells, Mardal, and Logg 2012).

From here, we derived an original FEM and BEM formulation of the demagnetizing field for multi-phase materials, along with multi-phase formulations for the exchange, anisotropy and Zeeman fields. We then presented a rough formulation of how these were incorporated into MERRILL.

We also derived formulations for element-wise and point-wise energies. These should be particularly useful for future students and developers adding new physics to MERRILL. Along with formulations for various surface integrals, it should be reasonably straightforward to formulate and implement a number of surface energies, e.g. surface anisotropy and surface exchange energies. These will be of particular concern for accurate modelling of realistic multi-phase materials. In particular, the FEM and BEM volume formulations will be useful for modelling long-range interactions like the demagnetizing field, and the FEM surface formulations will be useful for short-range — e.g. sub-exchange-length sizes — interactions.

In this thesis, however, we will focus on the contributions needed for mod-

elling the elastic interactions between phases, which we will later see for a magnetite-ilmenite lamellar system can be modelled as an effective surface anisotropy.

This represents a significant improvement to MERRILL. In particular, as magnetic materials in geoscience applications are often found as a result of exsolution, or experience partial chemical alteration, real samples are typically multi-phase. Given MERRILL is aimed at the geoscience community, it is of particular interest and importance that it be able to model the sorts of systems encountered in natural samples, and not just representative systems.

To date, modelling of multi-phase ferromagnets for geoscience applications has either been impossible, possible only for cubic meshes using the finite difference method, or has effectively ignored surface effects. In this thesis, we have begun the process of putting all the necessary pieces together for multi-phase modelling of ferromagnetic materials of arbitrary geometry, taking all the necessary physics into account, in a thorough and rigorous manner. With the outline presented here of the multi-phase FEM and BEM formulation, along with surface effects, the ground work has been laid out. In the following chapters, we will begin looking at including magnetostriction, a long ignored effect, and later derive surface effects due to lattice mismatch. Unfortunately, this will just be the initial steps towards the goal of comprehensive simulations of arbitrary materials geometries.

These code modifications will have significant implications. In particular, with accurate modelling, we would expect a significant improvement to our estimations of the magnetic stability of various materials, and more importantly, the interactions between materials. Even more importantly, providing this in an easy-to-use and *fast* program means it can be applied to a wide number of problems. MERRILL has, for example, found recent use in modelling of iron grains in meteor samples (Einsle et al. 2016), greigite with a focus on hydrocarbon exploration (Valdez-Grijalva et al. 2018), and stability analysis of pseudo-single domain grains (Nagy et al. 2017).

It can't be overstated that it is not possible (or at least not easy) to find closed form solutions for LEM magnetizations. It is also currently infeasible to map the whole magnetization of a physical 3D ferromagnet for non-uniform mag-

netizations. As a result, physical experiments are limited to bulk measurements of magnetic materials and detailed surface measurements to determine its behaviour, along with penetrative measurements like electron holography and x-ray holography imagery which suffer from significant loss of data. Micromagnetism presents the most feasible option for researchers to visualize the 3D magnetization held by a material. As a result, it is imperative that work continues to increase the speed, accuracy, and ease-of-use of micromagnetic models.

The results presented here for the μMAG Standard Problem 3 provide good evidence that MERRILL is correct, at least for uniaxial materials. These results, in themselves, represent a contribution to the field of micromagnetism, adding another data point for the critical size problem posed, for which there is no analytic solution. Correctness tests for MERRILL are an important addition, as detailed verification of models against their physical counterparts is not always feasible.

The study by Einsle et al. (2016), is a good example of this. In paleomagnetic systems, there are a very large number of magnetic grains in a typical sample. In this situation, bulk measurements are made against the whole sample to extract the paleomagnetic data (i.e. direction and strength of the Earth's magnetic field at the time and position of cooling), and micromagnetic models are used to get detailed information about representative grains, like the magnetization and its thermal stability. However, the technique used to image the grains in Einsle et al. (2016) was a destructive focused ion beam nano-tomography. In this situation, the grains measured can't be subjected to further study by the physical methods mentioned. The image of the grain geometry, the micromagnetic model, and the bulk measurements of that grain, and the huge number surrounding it are the only data available.

Part II

Magnetostriction

Chapter 5

Including Magnetostriction in Micromagnetic Models

In this chapter, we will discuss two approaches previously taken to include magnetostriction in micromagnetic models. We will present Kittel's formulation (Kittel 1949), which is derived assuming a uniformly magnetized material, in a tensorial style we will be using throughout this thesis. Next, we will discuss some issues surrounding his derivation of the magnetostrictive response of a material as a function of uniaxial pressure. We will then present Fabian and Heider's formulation (Fabian and Heider 1996) in terms of the same tensorial style, and discuss some potential issues surrounding this formulation.

This chapter serves primarily as an introduction to previous approaches, and an introduction to the notation for the magnetostrictive coupling and linear elasticity used in this thesis. The proof of Kittel's mistake in formulating the magnetostrictive response due to uniaxial tension, and demonstrating the decoupling of applied pressure from the magnetic response for SD magnetizations are original works, and a significant result, suggesting Kittel's theory is incomplete. The discussion of Fabian and Heider's formulation is also an original analysis of their results.

5.1 Kittel's Formulation of Magnetostriction

Kittel provided a micromagnetic energy term including magnetostriction in his seminal 1949 paper on ferromagnetism (Kittel 1949). Assuming the magnetostrictive effect was related to the anisotropy, and so expanding the anisotropy in terms of the strain of the material, he found the potential energy f for a cubic material with magnetization $\vec{M}$ due to a linear elastic strain $\boldsymbol{\varepsilon}$

$$\begin{aligned} f =& B_1(\alpha_x^2\varepsilon_{xx} + \alpha_y^2\varepsilon_{yy} + \alpha_z^2\varepsilon_{zz}) \\ &+ B_2(\alpha_x\alpha_y(\varepsilon_{xy} + \varepsilon_{yx}) + \alpha_y\alpha_z(\varepsilon_{yz} + \varepsilon_{zy}) + \alpha_z\alpha_x(\varepsilon_{zx} + \varepsilon_{xz})) \\ &+ \frac{1}{2}C_{11}(\varepsilon_{xx}^2 + \varepsilon_{yy}^2 + \varepsilon_{zz}^2) \\ &+ \frac{1}{2}C_{44}((\varepsilon_{xy} + \varepsilon_{yx})^2 + (\varepsilon_{yz} + \varepsilon_{zy})^2 + (\varepsilon_{zx} + \varepsilon_{xz})^2) \\ &+ C_{12}(\varepsilon_{xx}\varepsilon_{yy} + \varepsilon_{yy}\varepsilon_{zz} + \varepsilon_{zz}\varepsilon_{xx}) \end{aligned} \tag{5.1}$$

where $\varepsilon_{ij} = \varepsilon_{ji}$ is the symmetric strain tensor of the material in a linear elastic theory, α_i is the cosine of the magnetization along axis i (e.g. $\alpha_x = \hat{M} \cdot \hat{x}$ and $\hat{M} = \vec{M}/|M|$), B_1, B_2 are the magnetostrictive coupling constants, and C_{11}, C_{12}, C_{44} are the elastic stiffness constants.

As an aside, it is important to note that the ε_{ij} used in (Kittel 1949) are from the Voigt, or Engineering notation. There is a factor of two difference in the cross terms for ε. Specifically, for $\vec{\varepsilon}^{\text{voigt}}$

$$\vec{\varepsilon}^{\text{voigt}} = \begin{pmatrix} \varepsilon_{xx}^{\text{voigt}} \\ \varepsilon_{yy}^{\text{voigt}} \\ \varepsilon_{zz}^{\text{voigt}} \\ \varepsilon_{yz}^{\text{voigt}} \\ \varepsilon_{zx}^{\text{voigt}} \\ \varepsilon_{xy}^{\text{voigt}} \end{pmatrix} = \begin{pmatrix} \varepsilon_{xx} \\ \varepsilon_{yy} \\ \varepsilon_{zz} \\ \varepsilon_{yz} + \varepsilon_{zy} \\ \varepsilon_{zx} + \varepsilon_{xz} \\ \varepsilon_{xy} + \varepsilon_{yx} \end{pmatrix} \tag{5.2}$$

while for $\vec{\sigma}^{\text{voigt}}$

$$\vec{\sigma}^{\text{voigt}} = \begin{pmatrix} \sigma_{xx}^{\text{voigt}} \\ \sigma_{yy}^{\text{voigt}} \\ \sigma_{zz}^{\text{voigt}} \\ \sigma_{yz}^{\text{voigt}} \\ \sigma_{zx}^{\text{voigt}} \\ \sigma_{xy}^{\text{voigt}} \end{pmatrix} = \begin{pmatrix} \sigma_{xx} \\ \sigma_{yy} \\ \sigma_{zz} \\ (\sigma_{yz} + \sigma_{zy})/2 \\ (\sigma_{zx} + \sigma_{xz})/2 \\ (\sigma_{xy} + \sigma_{yx})/2 \end{pmatrix} \tag{5.3}$$

and for $\boldsymbol{C}^{\text{voigt}}$

$$C_{ij}^{\text{voigt}} = \begin{pmatrix} C_{1111} & C_{1122} & C_{1133} & C_{1123} & C_{1131} & C_{1112} \\ C_{2211} & C_{2222} & C_{2233} & C_{2223} & C_{2231} & C_{2212} \\ C_{3311} & C_{3322} & C_{3333} & C_{3323} & C_{3331} & C_{3312} \\ C_{2311} & C_{2322} & C_{2333} & C_{2323} & C_{2331} & C_{2312} \\ C_{3111} & C_{3122} & C_{3133} & C_{3123} & C_{3131} & C_{3112} \\ C_{1211} & C_{1222} & C_{1233} & C_{1223} & C_{1231} & C_{1212} \end{pmatrix} \tag{5.4}$$

For a rank-2 tensor, say ξ_{ij}, the Voigt vector is roughly built as follows:

$$\vec{\xi}^{\text{voigt}} = \begin{pmatrix} \xi_{11} & \xi_{12} \leftarrow & \xi_{13} \\ & \searrow & \uparrow \\ \xi_{21} & \xi_{22} & \xi_{23} \\ & & \uparrow \\ \xi_{31} & \xi_{32} & \xi_{33} \end{pmatrix} = \begin{pmatrix} \xi_{11} \\ \xi_{22} \\ \xi_{33} \\ (\xi_{23} + \xi_{32})/2 \\ (\xi_{13} + \xi_{31})/2 \\ (\xi_{12} + \xi_{21})/2 \end{pmatrix} \tag{5.5}$$

I say roughly, because the 4th, 5th and 6th elements in $\vec{\sigma}^{\text{voigt}}$ and $\vec{\varepsilon}^{\text{voigt}}$ are built differently. It is because of this inconsistency that we will prefer to present results in the full notation, but we will do a decent amount of calculations in Voigt notation.

The Voigt notation is used because is turns awkward equations of rank-2 and rank-4 tensors, into equations of vectors and matrices, e.g.

$$\sigma_{ij} = C_{ijkl}\varepsilon_{ij} \quad \rightarrow \quad \sigma_i^{\text{voigt}} = C_{ij}^{\text{voigt}}\varepsilon_j^{\text{voigt}}$$

It implicitly assumes symmetries of $\boldsymbol{\varepsilon}$, $\boldsymbol{\sigma}$ and $\boldsymbol{C}$, so it it makes specifying the elasticity tensor much easier, e.g. for a cubic material, it is necessary only to specify C_{11}, C_{12}, and C_{44} and note that

$$C^{\text{voigt, cubic}} = \begin{pmatrix} C_{11} & C_{12} & C_{12} & 0 & 0 & 0 \\ C_{12} & C_{11} & C_{12} & 0 & 0 & 0 \\ C_{12} & C_{12} & C_{11} & 0 & 0 & 0 \\ 0 & 0 & 0 & C_{44} & 0 & 0 \\ 0 & 0 & 0 & 0 & C_{44} & 0 \\ 0 & 0 & 0 & 0 & 0 & C_{44} \end{pmatrix}$$

Here, we will prefer to work in the full notation when working with indices, but use Voigt equations when convenient. We will always, however, use the full ε_{ij} in final formulations, since we later want to say $\varepsilon_{ij} = \frac{1}{2}(\partial_i u_j + \partial_j u_i)$ without fear of spurious factors of 2.

By looking for a ε that minimizes f, Kittel finds

$$\begin{aligned}
\frac{\partial f}{\partial \varepsilon_{xx}} &= B_1\alpha_x^2 + C_{11}\varepsilon_{xx} + C_{12}(\varepsilon_{yy} + \varepsilon_{zz}) = 0 \\
\frac{\partial f}{\partial \varepsilon_{yy}} &= B_1\alpha_y^2 + C_{11}\varepsilon_{yy} + C_{12}(\varepsilon_{zz} + \varepsilon_{xx}) = 0 \\
\frac{\partial f}{\partial \varepsilon_{zz}} &= B_1\alpha_z^2 + C_{11}\varepsilon_{zz} + C_{12}(\varepsilon_{xx} + \varepsilon_{yy}) = 0 \\
\frac{\partial f}{\partial \varepsilon_{xy}} &= B_2\alpha_x\alpha_y + C_{44}(\varepsilon_{xy} + \varepsilon_{yx}) = 0 \\
\frac{\partial f}{\partial \varepsilon_{yz}} &= B_2\alpha_y\alpha_z + C_{44}(\varepsilon_{yz} + \varepsilon_{zy}) = 0 \\
\frac{\partial f}{\partial \varepsilon_{zx}} &= B_2\alpha_z\alpha_x + C_{44}(\varepsilon_{zx} + \varepsilon_{xz}) = 0
\end{aligned} \tag{5.6}$$

with solutions

$$\varepsilon_{ij} = \begin{cases} B_1 \frac{C_{12} - \alpha_i^2(C_{11}+2C_{12})}{(C_{11}-C_{12})(C_{11}+2C_{12})} & \text{if } i = j \\ -B_2\alpha_i\alpha_j/(2C_{44}) & \text{otherwise} \end{cases} \tag{5.7}$$

This particular solution is only for a cubic material with zero stress. We will look for a more general solution to this problem.

5.1.1 A Cleaner Formulation

The Hooke Formulation

The relationship between the problem and solution can be made clearer by using the relationship between stress, strain, and energy and presenting the relationships in Voigt notation. The linear stress $\boldsymbol{\sigma}$ due to an energy f is given

$$\sigma_{ij} = \frac{\partial f}{\partial \varepsilon_{ij}} \tag{5.8}$$

so, already, it is clear we were finding $\boldsymbol{\sigma} = 0$ which looks like a force balance equation. In this case, it is looking for stress-free solutions. If the energy is in

the form of a Hooke energy, namely

$$\begin{aligned} f &= \frac{1}{2}\varepsilon_{ij}C_{ijkl}\varepsilon_{kl} + \sigma^0_{ij}\varepsilon_{ij} \\ &= \frac{1}{2}\varepsilon_i^{\text{voigt}}C_{ij}^{\text{voigt}}\varepsilon_j^{\text{voigt}} + \sigma_j^{0,\text{voigt}}\varepsilon_j^{\text{voigt}} \end{aligned} \tag{5.9}$$

we have the Hooke relation

$$\begin{aligned} \sigma_{ij} &= C_{ijkl}\varepsilon_{kl} + \sigma^0_{ij} \\ \sigma_i^{\text{voigt}} &= C_{ij}^{\text{voigt}}\varepsilon_j^{\text{voigt}} + \sigma_i^{0,\text{voigt}} \end{aligned} \tag{5.10}$$

in particular, we have (which can be confirmed by (5.6))

$$\begin{pmatrix} \sigma_{xx} \\ \sigma_{yy} \\ \sigma_{zz} \\ \frac{1}{2}(\sigma_{xy}+\sigma_{yx}) \\ \frac{1}{2}(\sigma_{yz}+\sigma_{zy}) \\ \frac{1}{2}(\sigma_{zx}+\sigma_{xz}) \end{pmatrix} = \begin{pmatrix} C_{11} & C_{22} & C_{22} & 0 & 0 & 0 \\ C_{22} & C_{11} & C_{22} & 0 & 0 & 0 \\ C_{22} & C_{22} & C_{11} & 0 & 0 & 0 \\ 0 & 0 & 0 & C_{44} & 0 & 0 \\ 0 & 0 & 0 & 0 & C_{44} & 0 \\ 0 & 0 & 0 & 0 & 0 & C_{44} \end{pmatrix} \begin{pmatrix} \varepsilon_{xx} \\ \varepsilon_{yy} \\ \varepsilon_{zz} \\ \varepsilon_{xy}+\varepsilon_{yx} \\ \varepsilon_{yz}+\varepsilon_{zy} \\ \varepsilon_{zx}+\varepsilon_{xz} \end{pmatrix} + \begin{pmatrix} B_1\alpha_x^2 \\ B_1\alpha_y^2 \\ B_1\alpha_z^2 \\ B_2\alpha_x\alpha_y \\ B_2\alpha_y\alpha_z \\ B_2\alpha_z\alpha_x \end{pmatrix} \tag{5.11}$$

which looks exactly like the Voigt version

$$\sigma_i^{\text{voigt}} = C_{ij}^{\text{voigt, cubic}}\varepsilon_j^{\text{voigt}} + \sigma_i^{0,\text{voigt}} \tag{5.12}$$

We will therefore define

$$B^0 = \begin{pmatrix} B_1\alpha_x^2 & B_2\alpha_x\alpha_y & B_2\alpha_x\alpha_z \\ B_2\alpha_x\alpha_y & B_2\alpha_y^2 & B_2\alpha_y\alpha_z \\ B_2\alpha_x\alpha_z & B_2\alpha_y\alpha_z & B_2\alpha_z^2 \end{pmatrix} \qquad B^{0,\text{voigt}} = \begin{pmatrix} B_1\alpha_x^2 \\ B_2\alpha_y^2 \\ B_2\alpha_z^2 \\ B_2\alpha_y\alpha_z \\ B_2\alpha_x\alpha_z \\ B_2\alpha_x\alpha_y \end{pmatrix} \tag{5.13}$$

and we write the magnetostrictive energy in a Hooke form

$$\begin{aligned} f &= \frac{1}{2}\varepsilon_{ij}C_{ijkl}\varepsilon_{kl} + B^0_{ij}\varepsilon_{kl} \\ &= \frac{1}{2}\varepsilon_i^{\text{voigt}}C_{ij}^{\text{voigt}}\varepsilon_j^{\text{voigt}} + B_i^{0,\text{voigt}}\varepsilon_i^{\text{voigt}} \end{aligned} \tag{5.14}$$

which is really nothing more than un-expanding (5.1).

The Magnetostriction Coupling as an Offset

From a purely mechanical point of view, one can view the magnetostrictive coupling as displacing the equilibrium deformation. As in a simple spring model, where the energy is

$$f = \frac{1}{2}m\dot{x}^2 - \frac{1}{2}kx^2 \tag{5.15}$$

or, in a manner closer to our previous Hooke form,

$$f = \frac{1}{2}m\dot{x}^2 - \frac{1}{2}xkx \tag{5.16}$$

the equations of motion are given

$$m\ddot{x} = -kx \tag{5.17}$$

which describes a system with an equilibrium point of 0.

Using a change of variable $x \rightarrow x' - x'_0$, where x'_0 is a constant, we get the energy

$$f = \frac{1}{2}m\dot{x}'^2 - \frac{1}{2}(x' - x'_0)k(x' - x'_0) \tag{5.18}$$

(since $\dot{x}' + \dot{x}'_0 = \dot{x}'$) and the equations of motion

$$m\ddot{x}' = -k(x' - x'_0) \tag{5.19}$$

which now describes a system with equilibrium point x'_0.

The energy term can be expanded

$$f = \frac{1}{2}m\dot{x}'^2 - \frac{1}{2}x'kx' + x'_0kx' - \frac{1}{2}x'_0kx'_0 \tag{5.20}$$

The $x'_0kx'_0$ term can be dropped without effecting the equations of motion, leaving us with

$$f = \frac{1}{2}m\dot{x}'^2 - \frac{1}{2}x'kx' + x'_0kx' \tag{5.21}$$

which now describes a spring system with equilibrium point x'_0.

In an exactly analogous manner, we can say the $B^0_{ij}\varepsilon_{ij}$ term represents an offsetting term, like x'_0kx', to the equilibrium strain of the material. However, this term is missing the necessary elastic stiffness tensor to fit it back into the $\varepsilon_{ij}C_{ijkl}\varepsilon_{kl}$ term.

The Compliance Tensor

We now define the compliance tensor $\boldsymbol{S}$

$$\begin{aligned} S_{ijkl}C_{klmn} &= \frac{1}{2}(\delta_{im}\delta_{jn} + \delta_{in}\delta_{jm}) \\ S^{\text{voigt}}_{ij}C^{\text{voigt}}_{jk} &= \delta_{ik} \end{aligned} \tag{5.22}$$

which is the inverse of $\boldsymbol{C}$.

Using this, we can now rewrite the $B^0_{ij}\varepsilon_{ij}$

$$B^0_{ij}\varepsilon_{ij} = B^0_{ij}S_{ijkl}C_{klmn}\varepsilon_{mn} \tag{5.23}$$

introducing the needed stiffness tensor. We can now see the correspondence of kx' to $C_{klnm}\varepsilon_{mn}$, and x'_0 to $B^0_{ij}S_{ijkl}$. We can, therefore, intuitively identify the new equilibrium position for the strain without need for any extra math or minimization as

$$\varepsilon^0_{ij} = S_{ijkl}B^0_{kl} \tag{5.24}$$

although, one can confirm solving $\frac{\partial f}{\partial \varepsilon_{ij}}(\boldsymbol{\varepsilon}^0) = 0_{ij}$ for $\boldsymbol{\varepsilon}^0$ produces the same result.

Applying the compliance tensor to equations (5.10), we get

$$\begin{aligned} \varepsilon_{ij} &= S_{ijkl}\sigma_{kl} - S_{ijkl}\sigma^0_{ij} \\ \varepsilon_i^{\text{voigt}} &= S_{ij}^{\text{voigt}}\sigma_j^{\text{voigt}} - S_{ij}^{\text{voigt}}\sigma_j^{0,\text{voigt}} \end{aligned} \tag{5.25}$$

For a cubic material, we have

$$S^{\text{voigt}} = \begin{pmatrix} \frac{C_{11}+C_{12}}{(C_{11}-C_{12})(C_{11}+2C_{12})} & \frac{-C_{12}}{(C_{11}-C_{12})(C_{11}+2C_{12})} & \frac{-C_{12}}{(C_{11}-C_{12})(C_{11}+2C_{12})} & 0 & 0 & 0 \\ \frac{-C_{12}}{(C_{11}-C_{12})(C_{11}+2C_{12})} & \frac{C_{11}+C_{12}}{(C_{11}-C_{12})(C_{11}+2C_{12})} & \frac{-C_{12}}{(C_{11}-C_{12})(C_{11}+2C_{12})} & 0 & 0 & 0 \\ \frac{-C_{12}}{(C_{11}-C_{12})(C_{11}+2C_{12})} & \frac{-C_{12}}{(C_{11}-C_{12})(C_{11}+2C_{12})} & \frac{C_{11}+C_{12}}{(C_{11}-C_{12})(C_{11}+2C_{12})} & 0 & 0 & 0 \\ 0 & 0 & 0 & \frac{1}{C_{44}} & 0 & 0 \\ 0 & 0 & 0 & 0 & \frac{1}{C_{44}} & 0 \\ 0 & 0 & 0 & 0 & 0 & \frac{1}{C_{44}} \end{pmatrix} \tag{5.26}$$

which applied to (5.25) with $\vec{\sigma}^{\text{voigt}} = \vec{0}$, and $\vec{\sigma}^{0,\text{voigt}} = \vec{B}^{0\text{voigt}}$, and remembering for directional cosines $\alpha_x^2 + \alpha_y^2 + \alpha_z^2 = 1$, produces the same result as (5.7).

Specifically, we find

$$\begin{aligned} \varepsilon_i^{0,\text{voigt}} &= -S_{ij}^{\text{voigt}} B_j^{0,\text{voigt}} \\ \Rightarrow f &= \frac{1}{2} S_{ij}^{\text{voigt}} B_j^{0,\text{voigt}} C_{jk}^{\text{voigt}} S_{kl}^{\text{voigt}} B_l^{0,\text{voigt}} - B_i^{0,\text{voigt}} S_{ij}^{\text{voigt}} B_j^{0,\text{voigt}} \\ &= \frac{1}{2} B_i^{0,\text{voigt}} S_{ij}^{\text{voigt}} B_j^{0,\text{voigt}} - B_i^{0,\text{voigt}} S_{ij}^{\text{voigt}} B_j^{0,\text{voigt}} \\ &= -\frac{1}{2} B_i^{0,\text{voigt}} S_{ij}^{\text{voigt}} B_j^{0,\text{voigt}} \\ &= -\frac{1}{2} B_{ij}^0 S_{ijkl} B_{kl}^0 \end{aligned} \tag{5.27}$$

which is a significantly more compact, and in fact, more general result than is in Kittel's paper, as this also holds for a non-cubic material.

Relating Back To Kittel's Energy

To demonstrate the equivalence of the result, we'll match this to what Kittel finds, we'll look at a cubic material. We'll first expand the terms including B_1^2

$$\begin{aligned}
B_0^{0,\text{voigt}} S_{0j} B_j^{0,\text{voigt}} &= \frac{B_1^2 \alpha_x^2((C_{11}+C_{12})\alpha_x^2 - C_{12}\alpha_y^2 - C_{12}\alpha_z^2)}{(C_{11}-C_{12})(C_{11}+2C_{12})} \\
B_1^{0,\text{voigt}} S_{1j} B_j^{0,\text{voigt}} &= \frac{B_1^2 \alpha_y^2(-C_{12}\alpha_x^2 + (C_{11}+C_{12})\alpha_y^2 - C_{12}\alpha_z^2)}{(C_{11}-C_{12})(C_{11}+2C_{12})} \\
B_2^{0,\text{voigt}} S_{2j} B_j^{0,\text{voigt}} &= \frac{B_1^2 \alpha_z^2(-C_{12}\alpha_x^2 - C_{12}\alpha_y^2 + (C_{11}+C_{12})\alpha_z^2)}{(C_{11}-C_{12})(C_{11}+2C_{12})}
\end{aligned} \tag{5.28}$$

Using the relation from Kittel,

$$\begin{aligned}
1 &= (\alpha_x^2 + \alpha_y^2 + \alpha_z^2)^2 \\
&= \alpha_x^4 + \alpha_y^4 + \alpha_z^4 + 2(\alpha_x\alpha_y + \alpha_y\alpha_z + \alpha_z\alpha_x) \\
\Rightarrow \alpha_x^4 + \alpha_y^4 + \alpha_z^4 &= 1 - 2(\alpha_x^2\alpha_y^2 + \alpha_y^2\alpha_z^2 + \alpha_z^2\alpha_x^2)
\end{aligned} \tag{5.29}$$

we have

$$\begin{aligned}
&\frac{1}{B_1^2}(C_{11}-C_{12})(C_{11}+2C_{12})(B_0^{0,\text{voigt}} S_{0j} + B_1^{0,\text{voigt}} S_{1j} + B_2^{0,\text{voigt}} S_{2j}) B_j^{0,\text{voigt}} \\
&\qquad = (C_{11}+C_{12}) - 2(C_{11}+C_{12})(\alpha_x^2\alpha_y^2 + \alpha_y^2\alpha_z^2 + \alpha_z^2\alpha_x^2) \\
&\qquad\quad - C_{12}(\alpha_x^2\alpha_y^2 + \alpha_z^2\alpha_x^2 + \alpha_x^2\alpha_y^2 + \alpha_y^2\alpha_z^2 + \alpha_z^2\alpha_x^2 + \alpha_y^2\alpha_z^2) \\
&\qquad = (C_{11}+C_{12}) - 2(C_{11}+C_{12})(\alpha_x^2\alpha_y^2 + \alpha_y^2\alpha_z^2 + \alpha_z^2\alpha_x^2) \\
&\qquad\quad - 2C_{12}(\alpha_x^2\alpha_y^2 + \alpha_z^2\alpha_x^2 + \alpha_y^2\alpha_z^2) \\
&\qquad = (C_{11}+C_{12}) - 2(C_{11}+2C_{12})(\alpha_x^2\alpha_y^2 + \alpha_y^2\alpha_z^2 + \alpha_z^2\alpha_x^2)
\end{aligned} \tag{5.30}$$

which gives

$$\begin{aligned}
&-\frac{1}{2}(B_0^{0,\text{voigt}} S_{0j} + B_1^{0,\text{voigt}} S_{1j} + B_2^{0,\text{voigt}} S_{2j}) B_j^{0,\text{voigt}} \\
&\qquad = \frac{B_1^2}{C_{11}-C_{12}}(\alpha_x^2\alpha_y^2 + \alpha_y^2\alpha_z^2 + \alpha_z^2\alpha_x^2) \\
&\qquad\qquad - \frac{C_{11}+C_{12}}{(C_{11}-C_{12})(C_{11}+2C_{12})}
\end{aligned} \tag{5.31}$$

The B_2^2 terms are much easier

$$-\frac{1}{2}(B_3^{0,\text{voigt}}S_{3j} + B_4^{0,\text{voigt}}S_{4j} + B_5^{0,\text{voigt}}S_{5j})B_j^{0,\text{voigt}} = -\frac{B_2^2}{2C_{44}}(\alpha_x^2\alpha_y^2 + \alpha_y^2\alpha_z^2 + \alpha_z^2\alpha_x^2) \tag{5.32}$$

By setting

$$\Delta K = \frac{B_1^2}{C_{11} - C_{12}} - \frac{B_2^2}{2C_{44}} \tag{5.33}$$

and dropping the terms independent of the magnetization and the strain, we can write the energy

$$f = -\frac{1}{2}B_i^{0,\text{voigt}}S_{ij}^{\text{voigt}}B_j^{0,\text{voigt}} = \Delta K(\alpha_x^2\alpha_y^2 + \alpha_y^2\alpha_z^2 + \alpha_z^2\alpha_x^2) \tag{5.34}$$

Extension to Non-Zero Stress

The compactness of the Hooke formulation with the compliance tensor allows us to quickly evaluate the same equations for a system where $\boldsymbol{\sigma} \neq \mathbf{0}$:

$$\begin{aligned}
\sigma_i^{\text{voigt}} &= \frac{\partial f}{\partial \varepsilon_{ij}}(\boldsymbol{\varepsilon}^0) \\
&= C_{ij}^{\text{voigt}}\varepsilon_j^{0,\text{voigt}} + B_i^{0,\text{voigt}} && \text{(5.35a)} \\
\Rightarrow \varepsilon_i^{0,\text{voigt}} &= S_{ij}^{\text{voigt}}(\sigma_j^{\text{voigt}} - B_j^{0,\text{voigt}}) && \text{(5.35b)} \\
\Rightarrow f(\boldsymbol{\varepsilon}^0) &= \frac{1}{2}\varepsilon_i^{0,\text{voigt}}C_{ij}^{\text{voigt}}\varepsilon_j^{0,\text{voigt}} + B_i^{0,\text{voigt}}\varepsilon_i^{0,\text{voigt}} \\
&= \frac{1}{2}S_{ij}^{\text{voigt}}(\sigma_j^{\text{voigt}} - B_j^{0,\text{voigt}})C_{ik}^{\text{voigt}}S_{kl}^{\text{voigt}}(\sigma_l^{\text{voigt}} - B_l^{0,\text{voigt}}) \\
&\quad + B_i^{0,\text{voigt}}S_{ij}^{\text{voigt}}(\sigma_j^{\text{voigt}} - B_j^{0,\text{voigt}}) \\
&= \frac{1}{2}(\sigma_i^{\text{voigt}} - B_i^{0,\text{voigt}})S_{ij}^{\text{voigt}}(\sigma_j^{\text{voigt}} - B_j^{0,\text{voigt}}) \\
&\quad + B_i^{0,\text{voigt}}S_{ij}^{\text{voigt}}(\sigma_j^{\text{voigt}} - B_j^{0,\text{voigt}}) \\
&= \frac{1}{2}\sigma_i^{\text{voigt}}S_{ij}^{\text{voigt}}\sigma_j^{\text{voigt}} - B_i^{0,\text{voigt}}S_{ij}^{\text{voigt}}\sigma_j^{\text{voigt}} + \frac{1}{2}B_i^{0,\text{voigt}}S_{ij}^{\text{voigt}}B_j^{0,\text{voigt}} \\
&\qquad + B_i^{0,\text{voigt}}S_{ij}^{\text{voigt}}\sigma_j^{\text{voigt}} - B_i^{0,\text{voigt}}S_{ij}^{\text{voigt}}B_j^{0,\text{voigt}} \\
&= \frac{1}{2}\sigma_i^{\text{voigt}}S_{ij}^{\text{voigt}}\sigma_j^{\text{voigt}} - \frac{1}{2}B_i^{0,\text{voigt}}S_{ij}^{\text{voigt}}B_j^{0,\text{voigt}} && \text{(5.35c)}
\end{aligned}$$

And so, for the Hooke style system with a known, constant stress $\boldsymbol{\sigma}$, we have

$$f = \frac{1}{2}\sigma_i^{\text{voigt}} S_{ij}^{\text{voigt}} \sigma_j^{\text{voigt}} - \frac{1}{2} B_i^{0,\text{voigt}} S_{ij}^{\text{voigt}} B_j^{0,\text{voigt}} \tag{5.36}$$

This represents a complete separation of the elastic and magnetic energies. However, it is important to note that $\boldsymbol{\sigma}$ implicitly depends on ε^0. In cases where $\boldsymbol{\sigma}$ is kept constant, independent of variations of $\boldsymbol{B}^0$, say through pure (constant) surface tension conditions, the $\boldsymbol{\sigma}$ term is then independent of the $\boldsymbol{B}^0$ term, with the difference taken up by the deformation of the material itself, i.e. in ε.

It appears the only way to change the behaviour of the magnetization through the deformation, beyond the usual result, is to restrict the deformation of the material, ε, in some way, so it does not correspond directly to a fixed $\boldsymbol{\sigma}$. This could be done, for example, by fixing two sides of the surface by placing the material in a clamp. In this manner, $\boldsymbol{\sigma}$ would need to change as $\boldsymbol{B}^0$ changes, to remain within the clamp. Another situation may be for the material embedded in another elastic material since the outer material will tend to resist change in the inner material, looking like a non-constant surface tension, resulting in a variation of the stress term due to a variation in the $\boldsymbol{B}$ term.

For a $\boldsymbol{\sigma}^0$ Hooke term which does not look like the $\boldsymbol{B}^0$ term presented, however, the second term represents a mixing of the terms linear in ε (as opposed to the pure stress term $\varepsilon_{ij} C_{ijkl} \varepsilon_{kl}$ term which is quadratic in ε). Brown (1966) presents a much fuller magnetostrictive theory involving more terms linear in ε, which may provide more interesting results.

5.1.2 Correction to Uniaxial Stress Result

With this in mind, we can now examine Kittel's results for a magnetostrictive material under a constant uniaxial tension. Kittel (1949) defines a stress with directional cosines γ_x, γ_y, γ_z for the direction of the applied stress with tensile stress T as

$$P_{ij} = T\gamma_i\gamma_j \tag{5.37}$$

In his derivation, however, he used

$$\begin{aligned} \sigma &= P_{ij} \\ \Rightarrow \varepsilon_{ij} &= S_{ijkl} P_{kl} \end{aligned}$$

and substituted this $\boldsymbol{\varepsilon}$ into the energy instead of

$$\begin{aligned} \sigma = \frac{\partial f}{\partial \varepsilon_{ij}}(\boldsymbol{\varepsilon}^0) &= P_{kl} \\ \Rightarrow \quad C_{ijkl}\varepsilon^0_{kl} + B^0_{ij} &= P_{kl} \\ \Rightarrow \qquad \varepsilon^0_{ij} &= S_{ijkl}P_{kl} - S_{ijkl}B^0_{kl} \end{aligned}$$

which uses the proper definition of the stress from (5.8). By setting

$$\vec{P}^{\text{voigt}} = (T\gamma_x^2, T\gamma_y^2, T\gamma_z^2, T\gamma_y\gamma_z, T\gamma_x\gamma_z, T\gamma_x\gamma_y) \tag{5.38}$$

in a manner similar to $\vec{B}^{0,\text{voigt}}$, we get

$$\varepsilon_i^{0,\text{voigt}} = S_{ij}^{\text{voigt}}(P_j^{\text{voigt}} - B_j^{0,\text{voigt}}) \tag{5.39}$$

We see here that $\vec{P}^{\text{voigt}}$ in $\vec{\varepsilon}^0$ here is the same as $\vec{\sigma}^{\text{voigt}}$ in (5.35b), so we can immediately write the energy, similar to (5.35c)

$$f = \frac{1}{2}P_i^{\text{voigt}} S_{ij}^{\text{voigt}} P_j^{\text{voigt}} - \frac{1}{2}B_i^{0,\text{voigt}} S_{ij}^{\text{voigt}} B_j^{0,\text{voigt}} \tag{5.40}$$

It is clear that the second term here is the same as (5.27), and so, the same as, (5.34), the cubic anisotropy form. Also worth note is the first term is purely elastic, and has no dependence on the magnetization. We can therefore conclude that the effective field due to a uniaxial stress, using Kittel's energy, can be no different than for an unstressed material for a uniformly magnetized material. It will always look like the usual cubic anisotropy form.

It is worth emphasizing the importance of this result. The results from Kittel's approach, which leaves out the magnetostrictive term in the stress, leads to a coupling of the stress and the magnetization. This is a result frequently used in research, but doesn't follow from the math. We will show in a later sections

how we might recover Kittel's uniaxial result. One approach will be in simulations by evaluating the magnetostrictive energies when the system is not in thermodynamic equilibrium, specifically when the elastic response is not in equilibrium. Another approach will be by including a theory of continuum defects to incorporate intrinsic, irresolvable stresses.

5.2 Fabian and Heider's Formulation of Magnetostriction

The paper by Fabian and Heider (1996) outlined a set of coupled equations for solving for the stress due to magnetostriction in non-uniformly magnetized materials, and from there, the micromagnetic energy. This technique was based on continuum defects techniques by Kröner (1958; 1981) for resolving stresses and strains due to materials with incompatible equilibrium deformations, as might be found in a non-uniformly magnetized material.

We will show here how the stress, strain, and magnetostrictive coupling derived in the previous section relate to the stress and strain derived in Fabian and Heider's technique. Ultimately, we want to lay out enough of this approach to show how it relates to Kittel's model, the predictions it makes about energies due to uniform vs. non-uniform magnetizations, and ultimately, the issues and difficulties posed by this approach, and why we won't be using it moving forward. While we will not be using it, we want the model we do come up with to *at least* describe the physics and behaviours that Fabian and Heider's approach can describe. In this manner, it is worth outlining in familiar terms.

5.2.1 A Brief Background

Fabian and Heider's formulation uses a number of exotic operators and terms from dislocation theory. A full description of these operators, their origins, behaviours, implications etc. would take up quite a bit of space. Fabian and Heider cite a number of works by Kröner in continuum defects in Fabian and Heider (1996). I have found the piece in the Les Hôches series (Kröner 1981) the easiest to follow, although it omits a treatment of the operations used by Fabian and Heider to transform the stress potential and energy equations into a form suitable for solving on a computer. In this section, however, we will be stopping at the stress potential equations.

Most notably used in Fabian and Heider (1996) is the incompatibility operator

$$-e_{ikm}e_{jln}\partial_k\partial_l \tag{5.41}$$

which can act as a sort of measure of the dislocations of a material. The incompatibility of a material can be found by applying this incompatibility operator to the strain, $\boldsymbol{\varepsilon}$, resulting in the incompatibility tensor $\boldsymbol{\eta}$ with

$$-e_{ikm}e_{jln}\partial_k\partial_l\varepsilon_{mn} = \eta_{ij} \tag{5.42}$$

In particular, a material can be described as "compatible", meaning the deformed material remains in one piece, no cracks, and no dislocations, if $\boldsymbol{\eta} = 0$. This is the Saint-Venant condition, and is a necessary and sufficient condition to describe a rank-2 tensor in terms of a rank-1 potential. In more concrete terms if the strain, $\boldsymbol{\varepsilon}$ satisfies the above condition, it can be described in terms of a potential $\vec{u}$

$$\begin{aligned} &-e_{ikm}e_{jln}\partial_k\partial_l\varepsilon_{mn} = 0 \\ &\Rightarrow \varepsilon_{ij} = \frac{1}{2}(u_{i,j} + u_{j,i}) \end{aligned} \tag{5.43}$$

which is the typical description used for the strain in linear elasticity. From other constructions, and from physical reasoning, it can be shown that this potential $\vec{u}$ corresponds to the displacement of the material. In particular, if one piece of the material occupies a point X before the deformation, and a point x after the deformation, the displacement is defined

$$u = x - X \tag{5.44}$$

Another important relation is that

$$-\partial_j e_{ikm}e_{jln}\partial_k\partial_l\xi_{mn} = 0_i \tag{5.45}$$

for any ξ_{mn}. Using reasoning very similar to the derivation of the magnetic vector potential $\vec{A}$ from the magnetic field $\vec{B}$ due to the divergence / curl relation, i.e.

$$\partial_i B_i = 0 \Rightarrow B_i = e_{ikm}\partial_k A_m \tag{5.46}$$

we can derive a strain potential $\boldsymbol{\chi}$ from the strain $\boldsymbol{\sigma}$ due to the divergence / incompatibility relation, i.e.

$$\partial_j \sigma_{ij} = 0_i \Rightarrow \sigma_{ij} = -e_{ikm} e_{jln} \partial_k \partial_l \chi_{mn} \tag{5.47}$$

This term is used similar to the magnetic vector potential. In particular, it's useful for introducing derivatives into equations and introducing gauge freedoms. This can be a useful mathematical trick for finding solutions to otherwise intractable problems.

5.2.2 The Stress Potential Relation

With this in mind, we can now present the equations and relations used in Fabian and Heider (1996)

$$\sigma_{ij,j} = 0_i \tag{5.48a}$$
$$\sigma_{ij} = -e_{ikm} e_{jln} \chi_{mn,kl} \tag{5.48b}$$
$$-e_{ikm} e_{jln} \varepsilon'_{mn,kl} = \eta_{ij} \tag{5.48c}$$
$$\sigma_{ij} = C_{ijkl} \varepsilon'_{kl} \tag{5.48d}$$
$$\eta_{ij} = e_{ikm} e_{jln} \varepsilon^0_{mn,kl} \tag{5.48e}$$
$$f = \frac{1}{2} \sigma_{ij} \varepsilon'_{ij} \tag{5.48f}$$

where $\boldsymbol{\varepsilon^0}$ is defined as the equilibrium deformation

$$\begin{aligned} \varepsilon^0_{ii} &= \frac{3}{2} \lambda_{100} (m_i^2 - \frac{1}{3}) \\ \varepsilon^0_{ij} &= \frac{3}{2} \lambda_{111} m_i m_j \qquad \text{if } i \neq j \end{aligned} \tag{5.49}$$

which can be derived from the Kittel energy by saying

$$\varepsilon^0_{ij} = \left\{ \varepsilon_{ij} \;\middle|\; \frac{\partial f}{\partial \varepsilon_{ij}} (\varepsilon_{ij}) = 0 \right\} \tag{5.50}$$

the maximum/minimum of f.

We can provide an alternate value for ε^0 by deriving it and rewriting it in terms

we've been using throughout this script. The energy we previously used is

$$f = \frac{1}{2}\varepsilon_{ij}C_{ijkl}\varepsilon_{kl} + B^0_{ij}\varepsilon_{ij} \tag{5.51}$$

so, taking derivatives wrt ε_{ij}, the pointwise max/min strain (by evaluating at $\boldsymbol{\varepsilon}^0$) is

$$\frac{\partial f}{\partial \varepsilon_{ij}}(\boldsymbol{\varepsilon}^0) = C_{ijkl}\varepsilon^0_{kl} + B^0_{ij} = 0 \tag{5.52}$$

and multiplying across by the inverse of $\boldsymbol{C}$, the compliance tensor $\boldsymbol{S}$

$$S_{ghij}C_{ijkl}\varepsilon^0_{kl} + S_{ghij}B^0_{ij} = 0 \tag{5.53}$$

and cancelling SC and moving the $\boldsymbol{B}^0$ term over

$$\frac{1}{2}(\delta_{gk}\delta_{hl} + \delta_{gl}\delta_{hk})\varepsilon^0_{kl} = -S_{ghij}B^0_{ij} \tag{5.54}$$

and expanding the δ terms

$$\frac{1}{2}(\varepsilon^0_{gh} + \varepsilon^0_{hg}) = -S_{ghij}B^0_{ij} \tag{5.55}$$

and since $\varepsilon_{ij} = \varepsilon_{ji}$

$$\varepsilon^0_{gh} = -S_{ghij}B^0_{ij} \tag{5.56}$$

and reindexing

$$\varepsilon^0_{ij} = -S_{ijkl}B^0_{kl} \tag{5.57}$$

Now we can better discuss how the two compare. In (Kröner 1981), a distinction is made between plastic and elastic deformations. Plastic deformations are defined as deformations that result in no elastic stress, while elastic deformations do. The general approach used, then, is when a material undergoes a plastic deformation, described by a (potentially incompatible) strain $\boldsymbol{\varepsilon}^p$, the opposite (potentially incompatible) elastic deformation, $\bar{\boldsymbol{\varepsilon}}^p = -\boldsymbol{\varepsilon}^p$ is applied, returning the material to "normal", but with a resulting stress, and an extra elastic deformation term $\boldsymbol{\varepsilon}$ is added, which is free to vary, and minimize the resulting stress.

The pointwise equilibrium strain due to magnetostriction can be considered a

plastic deformation. That is, if the material is free to assume that strain, there will be zero stress in the material. And so,

$$\boldsymbol{\varepsilon}^p = \boldsymbol{\varepsilon}^0 = -\boldsymbol{S} : \boldsymbol{B}^0 \tag{5.58}$$

with $\boldsymbol{S} : \boldsymbol{B}^0 = S_{ijkl} B^0_{kl}$. Next, we apply an elastic deformation to the material once it's in this state back to the undeformed state, resulting in a stress $\bar{\boldsymbol{\sigma}}$

$$\begin{aligned} \bar{\boldsymbol{\sigma}} &= \boldsymbol{C} : \bar{\boldsymbol{\varepsilon}}^p \\ &= \boldsymbol{C} : (-\boldsymbol{\varepsilon}^p) \\ &= \boldsymbol{C} : \boldsymbol{S} : \boldsymbol{B}^0 \\ &= \boldsymbol{B}^0 \end{aligned} \tag{5.59}$$

and we add an extra, free, compatible strain term that can be used to solve the equations of motion

$$\begin{aligned} \boldsymbol{\sigma} &= \boldsymbol{C} : \boldsymbol{\varepsilon} + \bar{\boldsymbol{\sigma}} \\ &= \boldsymbol{C} : \boldsymbol{\varepsilon} + \boldsymbol{B}^0 \end{aligned} \tag{5.60}$$

with

$$\partial_i \sigma_{ij} = 0_i \tag{5.61}$$

Now, the strain term $\boldsymbol{\varepsilon}'$ used by Fabian and Heider, for which

$$\sigma_{ij} = C_{ijkl} \varepsilon'_{kl} \tag{5.62}$$

is related to our strain term by

$$\varepsilon'_{ij} = \varepsilon_{ij} + S_{ijkl} B^0_{kl} \tag{5.63}$$

for which

$$\begin{aligned} \sigma_{ij} &= C_{ijkl} \varepsilon'_{kl} \\ &= C_{ijkl} (\varepsilon_{kl} + S_{klmn} B^0_{mn}) \\ &= C_{ijkl} \varepsilon_{kl} + B^0_{ij} \\ &= \frac{\partial f}{\partial \varepsilon_{ij}} \end{aligned} \tag{5.64}$$

matching our previous definition of the strain from Kittel's theory.

When taking the incompatibility of ε', we have

$$\begin{aligned} -e_{ikm}e_{jln}\varepsilon'_{mn,kl} &= -e_{ikm}e_{jln}(\varepsilon_{mn,kl} + S_{mnop}B^0_{op,kl}) \\ &= -e_{ikm}e_{jln}\varepsilon_{mn,kl} - e_{ikm}e_{jln}S_{mnop}B^0_{op,kl} \end{aligned} \tag{5.65}$$

As discussed, for a continuous deformation which produces no cracks or discontinuities, the strain can be written

$$\varepsilon_{ij} = \frac{1}{2}(u_{i,j} + u_{j,i}) \tag{5.66}$$

and satisfies the Saint-Venant condition that

$$e_{ikm}e_{jln}\varepsilon_{mn,kl} = 0_{ij} \tag{5.67}$$

Since the strain in a linear elastic theory is based on this $(u_{i,j} + u_{j,i})$ definition, $\boldsymbol{\varepsilon}$ satisfies these properties. So now we have, remembering our equilibrium strain $\boldsymbol{\varepsilon}^0 = -\boldsymbol{S} : \boldsymbol{B}$

$$\begin{aligned} -e_{ikm}e_{jln}\varepsilon'_{mn,kl} &= -e_{ikm}e_{jln}\varepsilon_{mn,kl} - e_{ikm}e_{jln}S_{mnop}B^0_{op,kl} \\ &= -e_{ikm}e_{jln}S_{mnop}B^0_{op,kl} \\ &= e_{ikm}e_{jln}\varepsilon^0_{mn,kl} \\ &= \eta_{ij} \end{aligned} \tag{5.68}$$

with η_{ij} the incompatibility tensor, as used in Fabian and Heider (1996). Here, already, we see a clear connection between the terms in Fabian and Heider (1996), the equilibrium deformation, and the incompatibility tensor, and terms we've been using, i.e. the magnetostriction tensor, and our equilibrium deformation term.

We can now press ahead to write the stress function equation in familiar terms

$$\begin{aligned} \sigma_{ij} &= C_{ijkl}\varepsilon'_{kl} \\ \Rightarrow S_{opij}\sigma_{ij} &= \varepsilon'_{op} \end{aligned} \tag{5.69}$$

and replacing $\sigma_{ij} = -e_{ikm}e_{jln}\chi_{mn,kl}$ and $\varepsilon'_{kl} = \varepsilon_{kl} + S_{klmn}B^0_{mn}$

$$-S_{opij}e_{ikm}e_{jln}\chi_{mn,kl} = \varepsilon_{op} + S_{opmn}B^0_{mn} \tag{5.70}$$

and taking the incompatibility again, remembering the incompatibility of $\boldsymbol{\varepsilon}$ is zero because it's a compatible deformation,

$$e_{sqo}e_{trp}S_{opij}e_{ikm}e_{jln}\chi_{mn,klqr} = e_{sqo}e_{trp}S_{opmn}B^0_{mn,qr} \tag{5.71}$$

which is the core equation being solved in Fabian and Heider (1996). Solving this for $\boldsymbol{\chi}$ will produce the stress $\boldsymbol{\sigma}$ from the definition $\sigma_{ij} = -e_{ikm}e_{jln}\chi_{mn,kl}$, and the strain from $\sigma_{ij} = C_{ijkl}\varepsilon'_{ij}$.

From here, it should be clear that the primary contribution to the stress, and the energy, is from an incompatibility in the $S_{opmn}B^0_{mn}$ term, as might be found for a non-uniform magnetization. This now represents a theory that can account for a physical, compatible strain and a potentially incompatible, non-uniform magnetization.

5.2.3 Discussion of, and issues with this approach

Interpretation of the Stress

An interesting case of Fabian and Heider's formulation is where $S_{opmn}B^0_{mn}$ is compatible. For a uniform magnetization, for example, $S_{opmn}B^0_{mn,qr} = 0$, since $\boldsymbol{B}^0$ is constant. If the RHS is zero, then $\boldsymbol{\chi} = \mathbf{0}$ will solve the equation, and so $\sigma_{ij} = e_{ikm}e_{jln}\chi_{mn,kl} = 0$. If the stress due to incompatibility is be zero, then the stress energy due to incompatibility should be zero. Similarly, if $S_{opmn}B^0_{mn,qr}$ is zero, the η_{op} is zero, and the dislocation energy $\eta_{ij}\chi_{ij}$ is zero.

From here, it can be reasoned that the stress calculated in Fabian and Heider's formulation is the residual, extra stress introduced into the system due to incompatibility in the strain due to incompatibility in the $\boldsymbol{S} : \boldsymbol{B}^0$ term. The strains determined by these stresses should be added to the Kittel strains to produce a physical strain for the magnetostrictive system, which conform to the mechanical equations of motion.

What this usefully suggests is that the extra stresses (and by extension, the difference in energy and magnetic behaviour) that arise from a full treatment of magnetostriction, compared to Kittel's original stress-free formulation, will be entirely from the incompatibility in the $\boldsymbol{S} : \boldsymbol{B}^0$ term.

Isotropic elasticity

To make the final equation more tractable, a number of transformations and constraints are added to turn the $e_{sqo}e_{trp}S_{opij}e_{ikm}e_{jln}\chi_{mn,klqr}$ term into a biharmonic $\chi'_{st,kkrr}$ term. In (Kröner 1981) and (Fabian and Heider 1996), this is done using an isotropic elastic material for $\boldsymbol{S}$, specifying a linear transformation between $\boldsymbol{\chi}$ and $\boldsymbol{\chi}'$, and imposing a gauge fixing on $\boldsymbol{\chi}$. While it may be possible to perform this transformation with a cubic $\boldsymbol{S}$, the equations become large and messy very quickly.

Boundary conditions

As the gauge fixing and boundary conditions are applied on a mathematical construct, $\boldsymbol{\chi}$, the stress potential, it is not clear how the boundary conditions effect the problem. Indeed, it is not clear what valid boundary conditions are, except at infinity. In linear elasticity, for example, the potential used, $\vec{u}$ can be directly related to the displacement of the material. Valid boundary conditions, for example setting $\boldsymbol{u} = 0$ at the boundary, represent clamping the material in place at the boundary. This is clearly a significantly different situation to, say, free boundaries. In imposing boundary conditions on the stress potential, it is no clear how that translates into the conditions placed on the system.

Similarity between magnetic vector potential and stress potential

An interesting observation we used previously is how closely the stress potential for the stress field relates to the magnetic vector potential for the magnetic field. Specifically, the magnetic vector potential $\vec{A}$ is defined for the magnetic field $\boldsymbol{B}$

$$B_i = e_{ijk}A_{k,j} \tag{5.72}$$

which is the curl operator applied to the index of $\vec{A}$ where the stress potential $\boldsymbol{\chi}$ is defined for the stress $\boldsymbol{\sigma}$

$$\sigma_{ij} = -e_{ikm}e_{jln}\chi_{mn,kl} \tag{5.73}$$

which is two curl operators, one applied to each index of χ.

An interesting, and for us unfortunate, takeaway of this is the boundary conditions for χ are only really obvious at infinity. For very similar reasons that $\vec{A} \to 0$ as $\vec{x} \to \infty$ because $\vec{B} \to 0$, we can say $\boldsymbol{\chi} \to 0$ as $\vec{x} \to \infty$ because $\boldsymbol{\sigma} \to 0$. This would necessitate an infinite material. Indeed, much of the mathematical and physical reasoning that applies to magnetic fields would apply to stress fields using this technique, along with the constraints for solutions.

Stable finite element formulation

Another complication arises when constructing a stable Finite Element formulation. A stable formulation for a magnetic vector potential equations use Nédélec elements, a formulation slightly more exotic than the linear elements we've previously used. To formulate a stable Finite Element formulation of the stress potential equations, an even more exotic formulation is needed. While this is not an insurmountable problem, the literature surrounding stable Finite Element formulations and building functions in the various Finite Element spaces can be rather dense. In particular, papers by Arnold (2002), which are working towards a stable Finite Element formulation of a stress potential formulation of elasticity are very abstract with few tangible examples to follow. As a result, efforts to build a Finite Element implementation of Fabian and Heider's formulation of magnetostriction for a cubic material for this thesis could not progress past writing the appropriate weak forms for an infinite material.

Due to all the difficulties mentioned, we won't pursue Fabian and Heider's approach, and instead look to a different formulation. In particular, we want a formulation that will generate the characteristic energies and elongation of materials described by Kittel's theory, but account for non-uniformly magnetized materials, as in Fabian and Heider's theory.

Chapter 6

Magnetostriction of Non-Uniformly Magnetized Materials

The incompatibility of the magnetostriction coupling is an important consideration for the system. In fact, it can be shown that the minimum strain tensors derived using Kittel's formulation are not generally correct. Specifically, since our material is not cracked after deformation, the incompatibility of the equilibrium deformation is zero

$$\texttt{inc}\ \boldsymbol{\varepsilon}^0 = 0 \tag{6.1}$$

(with $\texttt{inc}\ \boldsymbol{\varepsilon}^0$ representing the double curl $e_{ikm}e_{jln}\varepsilon^0_{mn,kl}$) however, we had derived the equilibrium strain

$$\boldsymbol{\varepsilon}^0 = -\boldsymbol{S} : \boldsymbol{B}^0 \tag{6.2}$$

(with $\boldsymbol{S} : \boldsymbol{B}$ representing the contraction $S_{ijkl}B^0_{kl}$) which implies

$$\texttt{inc}\ \boldsymbol{\varepsilon}^0 = -\texttt{inc}\ \boldsymbol{S} : \boldsymbol{B}^0 = 0 \tag{6.3}$$

However, there is no constraint on the magnetization, and so, no guarantee the incompatibility of the $\boldsymbol{S} : \boldsymbol{B}^0$ term vanishes. The derivation of $\boldsymbol{\varepsilon}^0 = \boldsymbol{S} : \boldsymbol{B}^0$ is therefore not, in general, true, since the incompatibility of both sides is not guaranteed to match. It can hold in some simple cases, like for a uniform magnetization, as assumed in section 5.1. This tells us that solving $\frac{\partial f}{\partial \boldsymbol{\varepsilon}}(\boldsymbol{\varepsilon}^0) = 0$ or $\frac{\partial f}{\partial \boldsymbol{\varepsilon}}(\boldsymbol{\varepsilon}^0) = \boldsymbol{\sigma}^0$ will not give us a physically correct equilibrium strain for all

magnetizations, and in fact makes some implicit assumptions about the distribution of the magnetization. Indeed, it gives us pointwise minima, but it fails to account for how one piece of the material deforming to its minimum energy state might impede another piece of the material from doing the same. We will describe approaches using this constant stress approach "Kittel Constant Stress" (KCS). These correspond to the Kittel approach to magnetostriction described in section 5.1.

We can say that the previously derived, pointwise ε^0 represents a lower bound of the magnetostrictive energy, since it is a less constrained solution than we will need. So we would expect the previous anisotropy approximation to underestimate the magnetostrictive energy, and so, the effective anisotropy coupling in non-uniformly magnetized materials. With this in mind, we look at a formulation of a coupled magnetic and linear elastic system, defining the strain ε in terms of the displacement $\vec{u}$, as is typical of a linear elasticity, so that we can find a minimum strain that is physical by solving the mechanical equilibrium equations. We will describe approaches solving Kittel's energy function by a simple substitution of the strain with the equivalent displacement and solving the mechanical equations of motion Kittel Mechanical Equilibrium (KME). This is the approach we will be mainly interested in in this thesis.

The equations of motion derived here have also been derived by Brown (1966) in significantly more detail and rigour, using both thermodynamic and energy equilibrium approaches. Here, we present a formulation which is the intersection between his derivation and Kittel's, derived via an action minimization approach. Indeed, Brown makes passing reference to the KME approach having been used elsewhere. Given how straightforward it is to replace the strain with the displacement and derive the equations of motion, it is a natural next step from Kittel's approach. Indeed, Brown's approach is for a rather different theory, deriving a fully magnetic and elastic material, rather than a simple coupling between the two effects. However, by ignoring certain effects, or setting certain coupling constants to zero, it is possible to recover the KME equations from Brown's.

One example of an effect left out in our derivation is a demag-elastic coupling, the kind of force that causes powerful magnets to pull themselves apart. How-

ever, as we are talking about quite small magnets, with quite small fields, and in quite small fields, this particular consideration is unnecessary. There are others as well, for which there are no good measurements for the materials we are interested in, such as corrections to the exchange coupling parameters as a function of strain.

One major advantage of performing the derivation here, from scratch, is that we can start from Kittel's energy and move forward on familiar ground. In Brown's approach, he takes arbitrary variations of the energy with respect to various parameters, and it is up to the reader to connect the derivative value to the appropriate physical parameter. While his approach is more general, it is significantly less clear for our specific application. Another advantage with performing the derivation here is that we will be generating all the pieces we need to define our weak forms as we go along.

Using an action minimization approach, we are also keenly aware of time in our derivation, and explicitly how we are handling it. In Brown's derivation, he finds equilibrium energy configurations with no mention of the path taken to that equilibrium. Since we are interested in partial simulation of the physics to find energy minima, and minimum action paths for stability calculations (although not in this thesis), we must be able to reason about the non-equilibrium behaviour, and how the partial simulation might deviate from a full simulation.

We will be solving our equations using the Finite Element Method. The Finite Element Method is, at its heart, a minimization problem. One typical application is turning a PDE into a weak form, and then that weak form into a matrix equation. When the best coefficients for the linear interpolation of the function being solved for are plugged into the FEM matrix equation, the residual is minimized. This is the approach we took in building the demag weak forms for MERRILL.

The magnetoelastic equations of motion presented here are not original work, as they have been derived elsewhere, particularly in the more general form by Brown (1966) using an energy variational method. However, a formulation explicitly using Hamilton's principle of least action is something I haven't seen elsewhere. The explicit addition of time, even though we later discard

it, could be an original contribution. The assertion that discarding time implies the equations treat the elastic relaxation time as faster than the magnetic relaxation time is something I haven't seen mentioned elsewhere, so may be an original contribution, and is an important consideration for dynamic simulation. Indeed, the approach laid out here for a Lagrangian formulation including time could be an important part for formulating a correct dynamic micromagnetic model.

The derivation of the magnetoelastic effective fields suitable for finding remanence states is an original contribution. The FEM formulation for a magnetoelastic effective field and energy, while relatively straightforward, is original. The discussion of issues surrounding solving the magnetoelastic FEM equations with free boundaries can be found in various forms, in various places, for solving linear elastic problems with free boundaries. However, I haven't seen them laid out neatly, in one place, as presented here. Finally, the formulation for a magnetoelastic grain embedded in an infinite elastic matrix uses an existing technique, but I haven't found this technique applied to an elastic system elsewhere, so this is likely original.

6.1 Equations of Motion

6.1.1 Weak Forms and the Equations of Motion

One approach for building weak forms is by taking a variational approach to the energy equation. This is why weak forms are sometimes referred to as variational forms. Indeed, these two approaches are linked via the equations of motion.

Take, for example, the energy density

$$\mathcal{E}(x) = \frac{1}{2}m\dot{x}^2 + f(x) \tag{6.4}$$

with the associated Lagrangian

$$\mathcal{L} = \frac{1}{2}m\dot{x}^2 - f(x) \tag{6.5}$$

The Euler-Lagrange equations of motion

$$\frac{\partial L}{\partial q} - \frac{d}{dt}\frac{\partial L}{\partial \dot{q}} = 0 \tag{6.6}$$

where q is a generalized coordinate, suggest the following equations of motion

$$-\frac{\partial f}{\partial x}(x) - m\ddot{x} = 0 \tag{6.7}$$

The typical approach of forming the weak form is to replace x with a test function, u and multiply both sides by a trial function v and integrate over the domain of integration. In this case, we'll use space and time. This gives the weak form

$$\int_T \int_\Omega m\ddot{u}v + \frac{\partial f}{\partial x}(u)v \; dV \; dt = 0 \tag{6.8}$$

The variational form of this energy can be found by assuming the energy is minimized by a value of $x = u$, and then perturbing the system a small distance ϵv from that position.

$$\mathcal{E}(u + \epsilon v) = \frac{1}{2}m(\dot{u} + \epsilon\dot{v})^2 + f(u + \epsilon v) \tag{6.9}$$

Now, since the energy is minimized by u, the energy is minimized when $\epsilon = 0$. Therefore the derivative of this expression for the energy wrt ϵ is zero at $\epsilon = 0$.

$$\mathcal{E}'(\epsilon) = \mathcal{E}(u + \epsilon v) \tag{6.10}$$

$$\frac{\partial \mathcal{E}'}{\partial \epsilon}(\epsilon) = m(\dot{u} + \epsilon\dot{v})\dot{v} + \frac{\partial f}{\partial x}(u + \epsilon v)v \tag{6.11}$$

$$\frac{\partial \mathcal{E}'}{\partial \epsilon}(0) = m\dot{u}\dot{v} + \frac{\partial f}{\partial x}(u)v = 0 \tag{6.12}$$

Now integrating this over space and time, we get

$$\int_T \int_\Omega m\dot{u}\dot{v} + \frac{\partial f}{\partial x}(u)v \; dV \; dt = 0 \tag{6.13}$$

These two weak forms vary in how they treat the derivative terms. In the first, we have $m\ddot{u}v$, and in the second $m\dot{u}\dot{v}$. The difference here is a partial integration of the $m\dot{u}\dot{v}$ term in the time domain. So, in terms of weak forms, they're equivalent. This shouldn't be surprising, since the Euler-Lagrange equations are, themselves, derived in terms of a variational minimization problem.

6.1.2 Elasticity Equations Of Motion

To derive the variational form for a magnetostrictive energy, we will derive the equations of motion of the magnetostrictive system. We will first look at a detailed derivation of the equations of motion for a pure elastic system, and seeing which pieces land where, we will add in the magnetostriction coupling terms.

For a strain ε that leaves the material unbroken, i.e. no cracks, we say it is a compatible deformation. Specifically, we can say the tensor satisfies the Saint-Venant condition

$$e_{ikm}e_{jln}\varepsilon_{mn,kl} = 0_{ij} \tag{6.14}$$

Here, e_{ijk} is the totally antisymmetric Levi-Civita tensor, and we use a comma notation, where indices after the comma represent spatial derivative with respect to that index, e.g.

$$\xi_{ij,kl} = \frac{\partial}{\partial x_k}\frac{\partial}{\partial x_l}\xi_{ij} \tag{6.15}$$

We introduce further notation to avoid having to constantly write the cumbersome $\frac{\partial}{\partial x_i}$ where it is clear what coordinates we are taking derivatives of

$$\partial_i = \frac{\partial}{\partial x_i} \tag{6.16}$$

in case it is not clear, we may write

$$\partial_{\xi_i} = \frac{\partial}{\partial \xi_i} \tag{6.17}$$

For any tensor that satisfies (6.14) in a simply connected domain (i.e. a sane region of space), it can be described by a potential $\vec{\lambda}$ such that

$$\begin{aligned} e_{ikm} e_{jln} \xi_{mn,kl} &= 0_{ij} \\ \Rightarrow \xi_{ij} &= \lambda_{i,j} + \lambda_{j,i} \end{aligned} \tag{6.18}$$

For the strain in (6.14) we define a potential $\vec{u}$, which can be shown to be the displacement of the material at each point under deformation

$$\varepsilon_{ij} = \frac{1}{2}(u_{i,j} + u_{j,i}) \tag{6.19}$$

Using this definition of $\boldsymbol{\varepsilon}$, we can say for the energy f

$$\frac{\partial f}{\partial u_{i,j}} = \frac{\partial f}{\partial \varepsilon_{kl}} \frac{\partial \varepsilon_{kl}}{\partial u_{i,j}} = \frac{1}{2}\left(\frac{\partial f}{\partial \varepsilon_{ij}} + \frac{\partial f}{\partial \varepsilon_{ji}}\right) = \frac{1}{2}(\sigma_{ij} + \sigma_{ji}) = \sigma_{ij} \tag{6.20}$$

since $\sigma_{ij} = \sigma_{ji}$ So we can say f is a function of $\boldsymbol{U}$ with $U_{ij} = u_{i,j}$

$$f = f(\boldsymbol{U}) \tag{6.21}$$

Usually it is also a function of $\vec{m}$, but we will assume here that we have a fixed $\vec{m}$. Remembering that f is a potential energy, we then define the Lagrangian density

$$\mathcal{L} = \frac{1}{2}\rho \dot{u}^2 - f \tag{6.22}$$

where ρ is the density, and we use the notation of a dot meaning derivative with respect to time

$$\dot{\xi} = \partial_t \xi \tag{6.23}$$

We define the Lagrangian as the integral of the Lagrangian density, but also include a surface term

$$L = \int_\Omega \mathcal{L}\, dx - \int_{\partial\Omega} T_i u_i \, dS \tag{6.24}$$

where $\vec{T}$ is a constant force on the surface of the elastic material, so a deformation $\vec{u}$ moves a distance $\vec{u}$ through a force $\vec{T}$, representing thermodynamic "work" done by the surface during deformation. Noting that

$$\frac{\partial L}{\partial q_i} = \int_\Omega \frac{\partial \mathcal{L}}{\partial q_i}\, dx - \int_{\partial\Omega} \frac{\partial T_j u_j}{\partial q_i}\, dS \tag{6.25}$$

for all the coordinates we are interested in, we list derivatives of $\mathcal{L}$ and $T_j u_j$

$$\frac{\partial \mathcal{L}}{\partial u_i} = 0 \tag{6.26}$$

$$\frac{\partial \mathcal{L}}{\partial \dot{u}_i} = \frac{1}{2}\rho \frac{\partial \dot{u}^2}{\partial \dot{u}_i} = \rho \dot{u}_i \tag{6.27}$$

$$\frac{\partial \mathcal{L}}{\partial u_{i,j}} = -\frac{\partial f}{\partial u_{i,j}} = -\sigma_{ij} \tag{6.28}$$

$$\frac{\partial T_j u_j}{\partial u_i} = T_i \tag{6.29}$$

and finally, the action functional

$$S[q] = \int_{t_1}^{t_2} L(q(t))\, dt \tag{6.30}$$

where q represents the generalized coordinates (i.e. all the time varying variables in the Lagrangian) and is a function of time. In our case,

$$q = (\vec{u}, \dot{\vec{u}}, \vec{U}) \tag{6.31}$$

Using Hamilton's principle, we have

$$\begin{gathered} \delta S = 0 \\ \delta q(t_1) = \delta q(t_2) = 0 \end{gathered} \tag{6.32}$$

and so

$$\int_{t_1}^{t_2} \delta L\, dt = \int_{t_1}^{t_2} \frac{\partial L}{\partial q_i} \delta q_i = 0 \tag{6.33}$$

expanding:

$$\begin{aligned}\int_{t_1}^{t_2} \delta L \, dt &= \int_{t_1}^{t_2} \left(\frac{\partial L}{\partial u_i} \delta u_i + \frac{\partial L}{\partial u_{i,j}} \delta u_{i,j} + \frac{\partial L}{\partial \dot{u}_i} \delta \dot{u}_i + \int_{\partial\Omega} T_i \delta u_i \, dS \right) dt \\ &= \int_{t_1}^{t_2} \left(\int_{\Omega} -\sigma_{ij} \delta u_{i,j} + \rho \dot{u}_i \delta \dot{u}_i \, dx - \int_{\partial\Omega} T_i \delta u_i \, dS \right) dt\end{aligned} \tag{6.34}$$

Noting that Ω refers to the undeformed material, and so is independent of time, and also noting that derivatives and variations commute, i.e.

$$\delta \frac{\partial}{\partial q_i} \xi = \frac{\partial}{\partial q_i} \delta \xi \tag{6.35}$$

we can swap the order of integration for the $\delta \dot{u}$ term and perform a partial integration

$$\begin{aligned}\int_{t_1}^{t_2} \int_{\Omega} \rho \dot{u}_i \delta \dot{u}_i \, dx \, dt &= \int_{\Omega} \int_{t_1}^{t_2} \rho \dot{u}_i \delta \dot{u}_i \, dt \, dx \\ &= \int_{\Omega} \int_{t_1}^{t_2} \rho \dot{u}_i \partial_t \delta u_i \, dt \, dx \\ &= \int_{\Omega} (\rho \dot{u}_i \delta u_i)|_{t_1}^{t_2} \, dx - \int_{\Omega} \int_{t_1}^{t_2} \rho \ddot{u}_i \delta u_i \, dt \, dx \\ &= - \int_{\Omega} \int_{t_1}^{t_2} \rho \ddot{u}_i \delta u_i \, dt \, dx \\ &= - \int_{t_1}^{t_2} \int_{\Omega} \rho \ddot{u}_i \delta u_i \, dx \, dt\end{aligned} \tag{6.36}$$

leaving us with a δu term. Looking at the $\delta u_{i,j}$ term, and again performing a partial integration

$$\int_{t_1}^{t_2} \int_{\Omega} \sigma_{ij} \delta u_{i,j} \, dx \, dt = \int_{t_1}^{t_2} \int_{\partial\Omega} n_j \sigma_{ij} \delta u_i \, dS \, dt - \int_{t_1}^{t_2} \int_{\Omega} \sigma_{ij,j} \delta u_i \, dx \, dt \tag{6.37}$$

Where $\partial\Omega$ refers to the boundary of Ω. It's not the best idea, having ∂ hanging about with several roles, but it's widely used notation and we won't reinvent

the wheel (too much) here. Substituting back into δL

$$\int_{t_1}^{t_2} \delta L \, dt = \int_{t_1}^{t_2} \Bigg(\int_{\partial\Omega} n_j \sigma_{ij} \delta u_i \, dS + \int_{\Omega} (-\sigma_{ij,j} \delta u_i + \rho \ddot{u}_i \delta u_i) \, dx - \int_{\partial\Omega} T_i \delta u_i \, dS \Bigg) \, dt = 0 \quad (6.38)$$

Since this holds for any value of variation of δu_i and the variations $\delta\vec{u}$ and $\delta\vec{m}$ are independent, notably for any non-zero value, then the integrands must be uniformly zero (and handily, the integrands of the volume and surface integrals must separately be zero) i.e.

$$\begin{aligned} \sigma_{ij,j} - \rho\ddot{u}_i &= 0_i \quad \text{on } \Omega \\ n_j\sigma_{ij} - T_i &= 0_i \quad \text{on } \partial\Omega \end{aligned} \quad (6.39)$$

which are the equations of motion for our elastic system, with $\vec{T}$ a surface tension.

Noting that $\ddot{u}$ is equivalent to an acceleration, and the density ρ is equivalent to a mass, it is clear that $\rho\ddot{u}$ is equivalent to a force density. The equations of motion, therefore look like a force balance equation.

Looking at the choice of Kittel to choose a $\boldsymbol{\sigma} = \partial_{\boldsymbol{\sigma}} f = \mathbf{0}$ is one specific $\boldsymbol{\sigma}$ which will solve the equations of motion in the absence of body forces since $0_{ij,j} = 0$ and $n_j 0_{ij} = 0$. It is also clear that this solution refers to a zero stress state with free and stress free boundaries. The stress $\sigma_{ij} = T\gamma_i\gamma_j$ also defines a solution with $\partial_j T\gamma_i\gamma_j = 0$ (since γ_i is independent of position) and $n_j T\gamma_i\gamma_j = T\gamma_i$, meaning the surface is free with a surface tension of $(\vec{n} \cdot \hat{T})|T| = \vec{n} \cdot \vec{T}$ at each point of the surface.

From the equations of motion, we can now solve the system in terms of the displacement $\vec{u}$. Most usefully, we can specify boundary conditions that admit non-constant values for $\boldsymbol{\sigma}$. We can, in particular, specify arbitrary boundary conditions for $\vec{u}$, admitting a variety of physical situations, such as a grain in a clamp under a given pressure and see how the grain deforms under these conditions.

To be clear here, the surface tension $\vec{T}$ here was assumed to be independent of the deformation $\vec{u}$ and the strain $u_{i,j}$. This term would be suitable for modelling, for example, a hydrostatic pressure, or a uniaxial static pressure. In a rock magnetic setting, this could be a lithostatic pressure. However, it is not suitable for modelling an embedded material where the response force may not be independent of deformation. It may be possible to use this term to, for example, couple the elastic system to a larger elastic system. If $\vec{T}$ was defined such that it was linearly dependent on $\vec{u}$ with $\vec{T}$ assuming a minimum at $\vec{u} = \vec{0}$, this would look somewhat like coupling to a larger material, or like a deformable clamp. In this case, the variational term would look like

$$\int_{\partial\Omega} -T_i \delta u_i - \frac{\partial T_i}{\partial u_j} \delta u_j u_i \, dS \tag{6.40}$$

and the equations of motion would be

$$\begin{aligned} \sigma_{ij,j} - \rho \ddot{u}_i &= 0_i \quad \text{on } \Omega \\ n_j \sigma_{ij} - T_i - \frac{\partial T_i}{\partial u_j} u_i &= 0_i \quad \text{on } \partial\Omega \end{aligned} \tag{6.41}$$

where the $\vec{T}$ terms now look like a Taylor expansion of $\vec{T}$ with respect to $\vec{u}$.

6.1.3 Magnetostrictive Mechanical Equations Of Motion

The difference between Kittel's magnetostrictive energy and the elasticity energy calculated above is the addition of the magnetostrictive coupling term and the absence of the kinetic term. Our energy density f is

$$f = \frac{1}{2} \varepsilon_{ij} C_{ijkl} \varepsilon_{kl} + B^0_{ij} \varepsilon_{ij} \tag{6.42}$$

with

$$\varepsilon_{ij} = \frac{1}{2}(u_{i,j} + u_{j,i}) \tag{6.43}$$

and the associated Lagrangian density

$$\mathcal{L} = -\frac{1}{2}\varepsilon_{ij}C_{ijkl}\varepsilon_{kl} - B^0_{ij}\varepsilon_{ij} \tag{6.44}$$

with Lagrangian

$$L = \int_\Omega \mathcal{L}\, dx - \int_{\partial\Omega} T_i u_i\, dS \tag{6.45}$$

The associated derivatives are

$$\frac{\partial \mathcal{L}}{\partial u_i} = 0 \tag{6.46}$$

$$\frac{\partial \mathcal{L}}{\partial \dot{u}_i} = 0 \tag{6.47}$$

$$\frac{\partial \mathcal{L}}{\partial u_{i,j}} = -\frac{\partial f}{\partial u_{i,j}} = -\sigma_{ij} - B^0_{ij} \tag{6.48}$$

$$\frac{\partial T_j u_j}{\partial u_i} = T_i \tag{6.49}$$

with

$$\sigma_{ij} = C_{ijkl}\varepsilon_{kl} \tag{6.50}$$

Following the same steps as above for variations and transformations, we get the variational form

$$\begin{aligned}\int_{t_1}^{t_2} \delta L\, dt = \int_{t_1}^{t_2} \Bigg(&\int_{\partial\Omega} n_j(\sigma_{ij} + B_{ij})\delta u_i\, dS \\ &+ \int_\Omega (-(\sigma_{ij,j} + B_{ij,j})\delta u_i)\, dx - \int_{\partial\Omega} T_i \delta u_i\, dS \Bigg)\, dt = 0\end{aligned} \tag{6.51}$$

we get the equations of motion

$$\begin{aligned} \sigma_{ij,j} + B^0_{ij,j} &= 0_i \quad \text{on } \Omega \\ n_j\sigma_{ij} + n_j B^0_{ij} - T_i &= 0_i \quad \text{on } \partial\Omega \end{aligned} \tag{6.52}$$

So here, it can be seen that the magnetostrictive coupling acts similar to a "force" term in the elasticity equation, appearing in place of the body force term in the volume equations and adding to the tension term in the surface

equations. Again, the tension $\vec{T}$ we've used here is independent of the deformation of the material.

It is important to note that this point of view is only a useful way to compare the magnetostrictive and pure elastic results. In fact, the stress is defined $\frac{\partial f}{\partial u_{i,j}}$, so the entirety of $\sigma_{ij} + B^0_{ij}$ is the stress in the magnetostrictive case. That is, if placed under a small deformation, that is the restorative force that will actually be measured. Splitting up the elastic and magnetic contributions to the stress is purely academic when talking about the response of the magnetic systems. This was the fundamental mistake made by Kittel when deriving his uniaxial magnetostrictive energy.

Expanding in terms of $\vec{u}$, we get the KME mechanical equations of motion

$$\begin{aligned} \frac{1}{2}C_{ijkl}(u_{k,lj} + u_{l,kj}) + B^0_{ij,j} &= 0_i \quad \text{on } \Omega \\ \frac{1}{2}n_j C_{ijkl}(u_{k,l} + u_{l,k}) + n_j B^0_{ij} - T_i &= 0_i \quad \text{on } \partial\Omega \end{aligned} \tag{6.53}$$

By substituting solution for $\vec{u}$ into the Kittel magnetostrictive energy, we get the KME energy.

We now, finally, have a formulation for a minimum strain $\boldsymbol{\varepsilon}^0$ in terms of the magnetostrictive coupling $\boldsymbol{B}^0$, in a manner that does not imply that the incompatibility of $\boldsymbol{S} : \boldsymbol{B}$ must be zero. Indeed, no constraints on the incompatibility of $\boldsymbol{S} : \boldsymbol{B}$ are made by the equations of motion derived here, and since the variations of the Lagrangian were made with respect to $\vec{u}$, rather than $\boldsymbol{\varepsilon}$, it follows that the solutions are minimum energy solutions of $\vec{u}$, but not necessarily minimum energy solutions of $\boldsymbol{\varepsilon}$, as we were previously considering. They are, however, the minimum energy, physical solutions of $\boldsymbol{\varepsilon}$, at least as far as linear elasticity applies. As previously mentioned, then, we would expect the KME solutions when $\texttt{inc}\ \boldsymbol{S} : \boldsymbol{B} = 0$ to match the KCS solutions for $\frac{\partial f}{\partial \boldsymbol{\varepsilon}}(\boldsymbol{\varepsilon}^0) = 0$. Indeed, one of the tests made for the implementation of the solver for these equations is that KCS and KME solutions for uniform magnetizations match exactly for a cubic geometry. However, they're not strictly guaranteed to match for finite geometries due to surface and corner effects in the mechanical solver.

6.1.4 Magnetostrictive Energy Gradient

When finding effective fields for our energy, given our displacement depends implicitly on $\vec{m}$, we would normally need to include the complex relation between $\vec{u}$ and $\vec{m}$ when taking derivatives of $\vec{u}$ with respect to $\vec{m}$. We present a novel approach to circumvent this issue.

Solutions to the mechanical equations of motion, as we have formulated them here, represent an extremal solution of the action with respect to $\vec{u}$ for a fixed magnetization $\vec{m}$. For a time-independent formulation, as we have here, the solutions of the equations of motion represent an extremal value of the Lagrangian. For a Lagrangian quadratic in $\vec{u}$, as we have here, the extremal value is a minimum. And for our formulation, this represents an energy minimum.

We write the displacement function which minimizes the energy f' for a given magnetization $\vec{m}$ as $\vec{u}_0(\vec{m})$

$$\min_{\vec{u}} f'(\vec{m}, \vec{u}) = f'(\vec{m}, \vec{u}_0(\vec{m})) \tag{6.54}$$

If we treat our system as though it has instant elastic equilibriation, we can write for our micromagnetic energy $f(\vec{m})$

$$f(\vec{m}) = \min_{\vec{u}} f'(\vec{m}, \vec{u}) = f'(\vec{m}, \vec{u}_0(\vec{m})) \tag{6.55}$$

Now, if we take derivatives of our micromagnetic energy with respect to $\vec{m}$

$$\frac{\partial f}{\partial m_i}(\vec{m}) = \frac{\partial f'}{\partial m_i}(\vec{m}, \vec{u}_0(\vec{m})) + \frac{\partial f'}{\partial u_i}(\vec{m}, \vec{u}_0(\vec{m}))\frac{\partial u_{0i}}{\partial m_i}(\vec{m}) \tag{6.56}$$

Ordinarily, the derivative of $\vec{u}_0$ would be a nebulous and difficult value to pin down. However, we can simply say the equations of motion are reasonably well behaved, so $\vec{u}_0$ is reasonably well behaved, so the derivative $\partial_{m_i}\vec{u}_0$ should be finite. We can then say, since $\vec{u}_0$ represents an extremal value of f', that the

derivative wrt $\vec{u}$ evaluated at $\vec{u}_0$ is zero

$$\begin{aligned} f'(\vec{m}, \vec{u}_0(\vec{m})) &= \min_{\vec{u}} f'(\vec{m}, \vec{u}) \\ \Rightarrow \frac{\partial f'}{\partial u_i}(\vec{m}, \vec{u}_0(\vec{m})) &= 0_i \end{aligned} \tag{6.57}$$

With this term zero, and the other factor finite, we can say

$$\frac{\partial f'}{\partial u_i}(\vec{m}, \vec{u}_0(\vec{m}))\frac{\partial u_{0i}}{\partial m_i}(\vec{m}) = 0 \tag{6.58}$$

and the derivative of the magnetostrictive energy wrt $\vec{m}$ for an instantly equilibrating system is

$$\frac{\partial f}{\partial m_i}(\vec{m}) = \frac{\partial f'}{\partial m_i}(\vec{m}, \vec{u}_0(\vec{m})) \tag{6.59}$$

Now, we can solve the mechanical equations of motion to solve for $\vec{u}_0$ in one step, and substitute the solution into our micromagnetic energy in the next, decoupling the two steps, and eliminating the reverse relationship of how the magnetization effects the mechanical behaviour. To be exact, we should probably be taking derivatives wrt $u_{i,j}$, but the argument remains the same.

The result arrived to by this approach should produce valid solutions at thermal equilibrium. That is, at both magnetic and mechanical equilibrium. This is fine for finding local energy minima of the magnetization, or even the quasi-static equilibrium of a magnetic hysteresis loop, or path energy minimization. However, it is not suitable for dynamical simulation. It is worth noting, though, that the usual approach of including the magnetostrictive response in the anisotropy energy, the KCS approach, also implicitly assumes instant mechanical equilibriation, so it's also unsuitable for dynamical simulation.

6.2 Finite Element Formulation

6.2.1 Magnetostrictive Weak Form

Taking the volume equations of motion and multiplying them by a test function $\vec{v}$, and integrating over the volume we get

$$\int_\Omega \left(\sigma_{ij,j} v_i + B^0_{ij,j} v_i\right)\, dV = 0 \tag{6.60}$$

performing a partial integration, moving the derivative to v_i

$$\int_\Omega \left(n_j \sigma_{ij} + n_j B^0_{ij}\right) v_i \, dS - \int_\Omega \left(\sigma_{ij} v_{i,j} + B^0_{ij} v_{i,j}\right)\, dV = 0 \tag{6.61}$$

From the equations of motion, the term in braces in the surface integral can be replaced with T_i

$$\int_\Omega T_i v_i \, dS - \int_\Omega \left(\sigma_{ij} v_{i,j} + B^0_{ij} v_{i,j}\right)\, dV = 0 \tag{6.62}$$

We move the terms independent of the displacement to the RHS

$$\int_\Omega \sigma_{ij} v_{i,j} \, dV = \int_{\partial\Omega} T_i v_i \, dS - \int_\Omega B^0_{ij} v_{i,j} \, dV \tag{6.63}$$

Replacing $\boldsymbol{\sigma}$ with its equivalent in terms of the displacement

$$\int_\Omega C_{ijkl} \frac{1}{2}(u_{k,l} + u_{l,k}) v_{i,j} \, dV = \int_{\partial\Omega} T_i v_i \, dS - \int_\Omega B^0_{ij} v_{i,j} \, dV \tag{6.64}$$

At this point, there are a number of steps we could take to make this easier to solve, or to reason about. First, taking advantage of the symmetries of $\boldsymbol{C}$ and $\boldsymbol{B}$, specifically $C_{ijkl} = C_{jikl}$ and $B_{ij} = B_{ji}$, we can symmetrize $v_{i,j}$

$$\int_\Omega \frac{1}{4} C_{ijkl}(u_{k,l} + u_{l,k})(v_{i,j} + v_{j,i}) \, dV = \int_{\partial\Omega} T_i v_i \, dS - \int_\Omega \frac{1}{2} B^0_{ij}(v_{i,j} + v_{j,i}) \, dV \tag{6.65}$$

From this, given the symmetry between $\vec{u}$ and $\vec{v}$, we can conclude that the stiffness matrix described by the LHS integral is symmetric.

This form is enough to build a FEM formulation of the problem. The implementation for including surface tension uses this form.

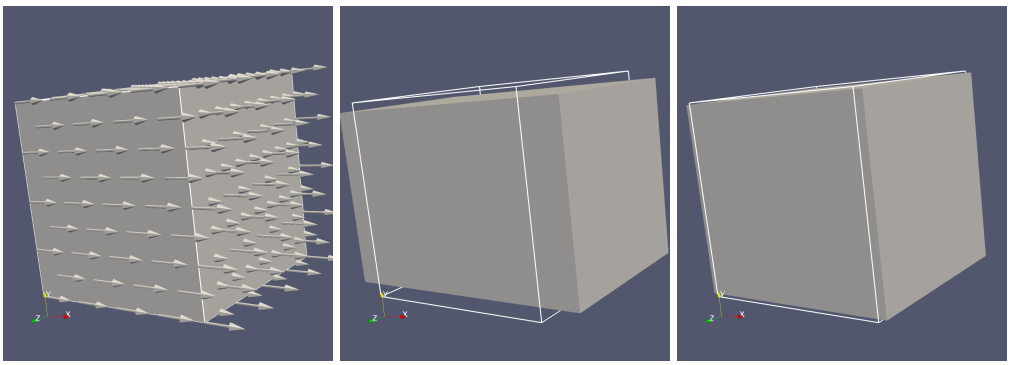

Figure 6.1: The deformation of TM60 due to magnetostriction. On the left is the [100] magnetization, in the center is the magnetostrictive deformation of the material with zero surface forces, on the right is the magnetostrictive deformation with a [100] uniaxial tension applied of around 10^7 Pa.

Figure 6.1 shows the equilibrium deformation of the material in this formulation with and without surface tension. The tension-free result shows the characteristic deformation due to magnetostriction, an elongation of the material parallel to the magnetization. The result with a uniaxial tension applied to counteract the deformation shows that it is a combination of the characteristic magnetostrictive deformation, and the usual elastic deformation under a uniaxial tension.

6.2.2 FEM Matrices

The displacement $\vec{u}$ over a single tetrahedron is given

$$u_i = \lambda_j c_{ji} \tag{6.66}$$

and the test function $\vec{v}$ is

$$v_i = \lambda_j c'_{ji} \tag{6.67}$$

and remembering the integral of barycentric coordinates can be written

$$\int_{\Omega_e} \lambda_1^a \lambda_2^b \lambda_3^c \lambda_4^d \, dV = 6 \, |V^e| \, \frac{a!b!c!d!}{(a+b+c+d+3)!} \tag{6.68}$$

The RHS can be written

$$\begin{aligned}\int_\Omega C_{ijkl}u_{k,l}v_{i,j}\,dV &= \sum_e \int_{\Omega_e} C_{ijkl}u_{k,l}v_{i,j}\,dV \\ &= \sum_e \int_{\Omega_e} C_{ijkl}\lambda_{m,l}c_{mk}\lambda_{n,j}c'_{ni}\,dV \\ &= \sum_e V^e C_{ijkl}\frac{D^e_{ml}}{6V^e}c_{mk}\frac{D^e_{ml}}{6V^e}c'_{mi} \\ &= \sum_e C_{ijkl}\frac{D^e_{ml}D^e_{nj}}{36V^e}c_{mk}c'_{ni}\end{aligned} \tag{6.69}$$

and the stiffness matrix $\boldsymbol{S}$ can be written

```
1  S(1:NNODE,1:3,1:NNODE,1:3) = 0
2
3  DO e=1,NTRI
4    DO m=1,4
5      DO n=1,4
6        col = TIL(e,m)
7        row = TIL(e,n)
8
9        DO i=1,3
10       DO j=1,3
11       DO k=1,3
12       DO l=1,4
13         Dm = (/ b(e,m), c(e,m), d(e,m) /)
14         Dn = (/ b(e,n), c(e,n), d(e,n) /)
15
16         S(row,i, col,k) = S(row, col) + C(i,j,k,l)*Dm(l)*Dn(j)
17
18       END DO
19       END DO
20       END DO
21       END DO
22     END DO
23   END DO
24 END DO
25
```

```
26 u(1:NNODE,1:3) = (/ ... /)
27 v(1:NNODE,1:3) = 0
28 DO i=1,NNODE
29   DO j=1,3
30     DO k=1,NNODE
31       DO l=1,3
32         v(i,j) = S(i,j, k,l)*u(k,l)
33       END DO
34     END DO
35   END DO
36 END DO
```

The LHS can be written

$$\begin{aligned}\int_\Omega B^0_{ij} v_{i,j} &= \sum_e \int_{\Omega_e} B^0_{ij} \frac{D^e_{kj}}{6V^e} c'_{ki}\, dV \\ &= \sum_e \frac{D^e_{kj}}{6V^e} c'_{ki} \int_{\Omega_e} B^0_{ij}\, dV\end{aligned} \tag{6.70}$$

where B^0_{ij} can be written

$$B^0_{ij} = \begin{cases} B_1 \alpha_i^2 & \text{if } i = j \\ B_2 \alpha_i \alpha_j & \text{if } i \neq j \end{cases} \tag{6.71}$$

and for the crystal axes aligned with the coordinate axes

$$B^0_{ij} = \begin{cases} B_1 m_i^2 & \text{if } i = j \\ B_2 m_i m_j & \text{if } i \neq j \end{cases} \tag{6.72}$$

and expanding $m_i = \lambda_j J_{ji}$ in a tetrahedron e

$$B^0_{ij} = \begin{cases} B_1 \lambda_m J_{m(i)} \lambda_l J_{l(i)} & \text{if } i = j \\ B_2 \lambda_m J_{mi} \lambda_l J_{lj} & \text{if } i \neq j \end{cases} \tag{6.73}$$

and the integral is

$$\int_{\Omega_e} B^0_{ij}\, dV = \begin{cases} B_1 \frac{V^e}{20}(1_{ml} + \delta_{ml}) J_{m(i)} J_{l(i)} & \text{if } i = j \\ B_2 \frac{V^e}{20}(1_{ml} + \delta_{ml}) J_{mi} J_{lj} & \text{if } i \neq j \end{cases} \tag{6.74}$$

The force matrix $\boldsymbol{F}$ can be written

```
DO e=1,NTRI
  DO k=1,4
    col = TIL(e,k)
    DO i=1,3
      DO m=1,4
      DO l=1,4
        DO j=1,3
          mm = TIL(e,m)
          ll = TIL(e,l)

          Dk = (/ b(e,k), c(e,k), d(e,k) /)

          IF(i .EQ. j) THEN
            B = B1
          ELSE
            B = B2
          END IF

          IF(m .EQ. l) THEN
            factor = 2
          ELSE
            factor = 1
          END IF

          F(k,i, mm,i,ll,j) = F(k,i, mm,i,ll,j) &
            Dk(j) * B * factor / 120.0
        END DO
      END DO
      END DO
    END DO
```

```
31    END DO
32  END DO
33
34
35  rhs(1:NNODE,1:3) = 0
36  DO i=1,NNODE
37    DO j=1,3
38      DO k=1,NNODE
39        DO l=1,3
40          DO m=1,NNODE
41            DO n=1,3
42              rhs(i,j, k,l,m,n) = rhs(i,j, k,l,m,n) &
43                + F(i,j k,l,m,n)*m(k,l)*m(m,n)
44            END DO
45          END DO
46        END DO
47      END DO
48    END DO
49  END DO
```

6.2.3 Solver Issues

For stress free surface conditions, i.e. pure Neumann conditions, the matrices for the mechanical equations of motion, generated using the FEM, are singular. The current solver in MERRILL, a conjugate gradient solver with partial Cholesky decomposition preconditioner, handles these well enough. However, many solvers, like the unconditioned conjugate gradient method, don't play well with singular matrices, since the solution space is no longer strictly bowl-shaped.

The kernel of the matrix can be found from considering the form of $\vec{u}$ in the mechanical equations of motion

$$\frac{1}{2}C_{ijkl}(u_{k,lj} + u_{l,kj}) + B^0_{ij,j} = 0 \tag{6.75}$$

and, in particular, the $(u_{k,l} + u_{l,k})$ term. It is clear that the kernel of the FEM matrices is the gauge freedom of this term. If $\vec{u}$ is a solution of the equations of motion, then $\vec{\lambda}$ is too if

$$\vec{\lambda} = \vec{u} + l_1(1, 0, 0) + l_2(0, 1, 0) + l_3(0, 0, 1) \tag{6.76}$$

where l_1, l_2, l_3 are arbitrary scalar constants, or if

$$\vec{\lambda} = \vec{u} + l_4(y, -x, 0) + l_5(z, 0, -x) + l_6(0, z, -y) \tag{6.77}$$

again with l_4, l_5, and l_6 arbitrary scalar constants. The first condition represents a rigid body displacement, and the second is a rigid body rotation. Given these six linearly independent conditions, a basis for the kernel of the FEM matrix can be constructed with coordinates $\vec{l}$. However, we will omit the details for constructing this basis for a FEM representation.

Lagrangian Multiplier Approach

Some solvers, e.g. PETSc's Krylov solver, are equipped to solve singular matrices if supplied with the basis of the kernel of the matrix. Others are not so well equipped. Given the gauge conditions above, we can break the singularity by

defining a coupled equation

$$\begin{aligned}
\frac{1}{2}C_{ijkl}(u_{k,lj} + u_{l,kj}) + B^0_{ij,j} = 0_i \quad &\text{on } \Omega \\
\frac{1}{2}n_j C_{ijkl}(u_{k,l} + u_{l,k}) + n_j B^0_{ij} - T_i = 0_i \quad &\text{on } \partial\Omega \\
\int_\Omega u_x \, dV = 0 \\
\int_\Omega u_y \, dV = 0 \\
\int_\Omega u_z \, dV = 0 \\
\int_\Omega (u_x y - u_y x) \, dV = 0 \\
\int_\Omega (u_x z - u_z x) \, dV = 0 \\
\int_\Omega (u_y z - u_z y) \, dV = 0
\end{aligned} \tag{6.78}$$

The coupling is usually achieved using a mixed-element formulation to enforce Lagrange multipliers. The effect is to pad the FEM matrix with a few extra rows and columns, and the result vector with some extra entries. Where the extra constraints are sufficient for gauge fixing, the resulting matrix will be non-singular, and should work well in a conjugate gradient solver. However, it will no longer be symmetric and will not have the same diagonal pattern as the original matrix.

Regularization Approach

Another approach is to add a small regularization term to the energy to break the rigid body symmetry. We add a small u^2 term to the energy

$$f = \frac{1}{4}(u_{i,j} + u_{j,i})C_{ijkl}(u_{k,l} + u_{l,k}) + \frac{1}{2}B^0_{ij}(u_{i,j} + u_{j,i}) + \epsilon \, u_i u_i \tag{6.79}$$

where ϵ is some very "small" value. This translates to a small penalty for having a larger displacement. The resulting equations of motion are

$$\begin{aligned} \frac{1}{2}C_{ijkl}(u_{k,lj} + u_{l,kj}) + B^0_{ij,j} + \epsilon\, u_i = 0_i \quad \text{on } \Omega \\ \frac{1}{2}n_j C_{ijkl}(u_{k,l} + u_{l,k}) + n_j B^0_{ij} - T_i + \epsilon\, u_i = 0_i \quad \text{on } \partial\Omega \end{aligned} \tag{6.80}$$

As can be seen, these consist of our previous equations of motion, plus a $\epsilon\, u_i$ term. As a result, the FEM matrices for the previous formulation can be constructed as usual, and the FEM matrices for $\int_\Omega \epsilon\, u_i v_i\, dV$ constructed separately.

In practice, the original FEM matrix is constructed first. Let's call this $\boldsymbol{S}_1$. Next, the matrix for $\int_\Omega u_i v_i\, dV$ is constructed. Let's call this $\boldsymbol{S}_2$. Then, the smallest non-zero absolute value in S_1 is found, say s, and the largest absolute value in S_2, say t. Finally, the total FEM matrix is constructed

$$\boldsymbol{S} = \boldsymbol{S}_1 + \epsilon' \frac{s}{t} \boldsymbol{S}_2 \tag{6.81}$$

where ϵ' is some number that is small relative to 1, say 10^{-3}. The term $\epsilon' \frac{s}{t}$ should act as an ϵ, such that the largest contribution by the perturbation ϵu^2 should be smaller than the smallest contribution of the actual problem we want to solve. By setting ϵ' to 10^{-3}, we expect the solution $\boldsymbol{u}$ to be off by about 0.1%. This perturbation, then, can break the singularity of the FEM matrices while having a minimal impact on the correctness of the solutions. This was the preferred solution in the implementation made for this thesis, before the MERRILL solver was used.

6.3 Future Work - Embedding in an Infinite Elastic Matrix

We present a technique for modelling magnetostriction in an infinite elastic material. In our section on deriving the demag field for MERRILL, we encountered the issue of dealing with an infinite boundary. There, we dealt with it through application of the BEM. Here, however, we will take a more direct ap-

proach, performing a spatial transformation of the domain of integration from an infinite to a finite domain. This technique is presented for the demagnetizing field in Imhoff, Meunier, and Sabonnadiere (1990) and in Imhoff, Meunier, Brunotte, et al. (1990), with extensions to non-spherical mapped regions in Brunotte, Meunier, and Imhoff (1992). The alterations needed to describe elasticity in an infinite elastic medium using this technique are minimal.

To simulate an infinite elastic material, it is typically necessary to solve over some infinite domain. As we want to solve on a computer, we must transform the calculation over an infinite domain to one over a finite domain. To this end, we use a shell transformation (Imhoff, Meunier, Brunotte, et al. 1990). This is where we embed the grain in two concentric spheres, and define a diffeomorphism (i.e. an invertible and differentiable map), transforming the space between the inner sphere and the outer sphere to a space from the inner sphere to infinity.

A simple map from finite to infinite space, where the boundary of the inner sphere maps to the boundary of the inner sphere, and the boundary of the outer sphere maps to infinity is given

$$f^{\mathtt{simple}}(\vec{x}) = \hat{x}\left(R^{\mathtt{inner}}\frac{R^{\mathtt{inner}} - R^{\mathtt{outer}}}{|x| - R^{\mathtt{outer}}}\right) \tag{6.82}$$

In this map, the space is scaled linearly. In a practical application, where the value of a solution will drop of as some power of the distance from the region of interest (i.e. go to zero at infinity), the scaling of space should be chosen to match this drop off. That is, the value of the solution in the mapped space should drop off linearly as it approaches the outer sphere so the linear elements representing the space can represent the solution well.

6.3.1 A Linear Form Transformation

We will derive the general form for a transformation of coordinate function in the linear forms representing a weak form for a linear elastic problem for an material of infinite extent. We will ignore the linear form on the RHS here which depends on the magnetization, because we assume the embedding

grain is non-magnetic in the transformed region. When actually solving the problem, we will actually be fixing the boundary at infinity, because the difference between using fixed and free boundaries at infinity should be a rigid body motion. This also solves the problem of mappings being poorly defined at the outer sphere boundary, since they will not have to be defined there.

We define two spaces, Ω and Λ representing the real, infinite space and the transformed, spherically bound spaces respectively. These spaces are defined starting from the boundary of the inner sphere on.

$$\Omega = \{\vec{x} \mid |x| \geq R^{\texttt{inner}}\} \tag{6.83a}$$

$$\Lambda = \{\vec{x} \mid R^{\texttt{outer}} \geq |x| \geq R^{\texttt{inner}}\} \tag{6.83b}$$

We define a diffeomorphism $\vec{\psi}$ from Ω to Λ with inverse $\vec{\psi}^{-1}$

$$\begin{aligned} \vec{\psi} &: \Omega \to \Lambda \\ &\vec{x} \to \vec{\psi}(\vec{x}) \\ \vec{\psi}^{-1} &: \Lambda \to \Omega \\ &\vec{y} \to \vec{\psi}^{-1}(\vec{y}) \end{aligned} \tag{6.84}$$

The untransformed integral over Ω is

$$\int_{\Omega} (u_{i,j}(x) + u_{j,i}(x))\, C_{ijkl}\, (v_{k,l}(x) + v_{l,k}(x))\, dx^3 = 0 \tag{6.85}$$

where here, we must be explicit that

$$dx^3 = dx_1 \wedge dx_2 \wedge dx_3 \tag{6.86}$$

with $\wedge$ the wedge product, in order to properly account for changes of variable.

Defining the variable

$$\vec{y} = \vec{\psi}(\vec{x}) \tag{6.87}$$

we get the transformations

$$\begin{aligned} \vec{x} &= \vec{\psi}^{-1}(\vec{y}) \\ dx_i &= \frac{\partial \psi_i^{-1}}{\partial y_j}(\vec{y})\ dy_j = J(\psi^{-1})_{ij}(\vec{y})\ dy_j \\ dx_1 \wedge dx_2 \wedge dx_3 &= |J(\psi^{-1})(\vec{y})| dy_1 \wedge dy_2 \wedge dy_3 \\ \Lambda &= \vec{\psi}(\Omega) \end{aligned} \tag{6.88}$$

The Jacobian $\boldsymbol{J}$ of a vector valued function $\vec{f}$ with vector valued domain at a point $\vec{y}$ is a matrix defined:

$$\begin{aligned} J(f)_{ij}(\vec{y}) &= \frac{\partial f_i}{\partial x_j}(\vec{y}) \\ J(f)_{ij} &= f_{i,j} \end{aligned} \tag{6.89}$$

We use the notation for a matrix M that $|M| = det(M)$.

With all this in mind, we get the transformation of the integral (6.85) over Λ

$$\int_\Lambda \Big(u_{i,j}(\vec{\psi}^{-1}(y)) + u_{j,i}(\vec{\psi}^{-1}(y))\Big) \\ C_{ijkl}\ \Big(v_{k,l}(\vec{\psi}^{-1}(y)) + v_{l,k}(\vec{\psi}^{-1}(y))\Big)\ |\boldsymbol{J}(\vec{\psi}^{-1})(y)|\ dy^3 = 0 \tag{6.90}$$

with $dy^3 = dy_1 \wedge dy_2 \wedge dy_3$, similar to dx^3.

Next, we must change $\vec{u}$ and $\vec{v}$ from functions with domain Ω to functions $\vec{\mu}$ and $\vec{\nu}$ with domain Λ. To that end, we define

$$\vec{\mu} = \vec{u} \circ \vec{\psi}^{-1} \tag{6.91a}$$

$$\Rightarrow \vec{u} = \vec{\mu} \circ \vec{\psi} \tag{6.91b}$$

$$\frac{\partial u_i}{\partial x_j}(\vec{x}) = \frac{\partial \mu_i}{\partial y_k}(\vec{\psi}(\vec{x}))\ \frac{\partial \psi_k}{\partial x_j}(\vec{x}) \tag{6.91c}$$

$$u_{i,j} = (\mu_{i,k} \circ \vec{\psi}) \cdot \psi_{k,j} \tag{6.91d}$$

and similarly for ν

$$\vec{v} = \vec{\nu} \circ \vec{\psi} \tag{6.91e}$$

$$v_{i,j} = (\nu_{i,k} \circ \vec{\psi}) \cdot \psi_{k,j} \tag{6.91f}$$

From here we find

$$\begin{aligned} u_{i,j} \circ \vec{\psi}^{-1} &= ((\mu_{i,k} \circ \vec{\psi}) \cdot \psi_{k,j}) \circ \vec{\psi}^{-1} \\ &= (\mu_{i,k} \circ \vec{\psi} \circ \vec{\psi}^{-1}) \cdot (\psi_{k,j} \circ \vec{\psi}^{-1}) \\ &= \mu_{i,k} \cdot (\psi_{k,j} \circ \vec{\psi}^{-1}) \\ &= \mu_{i,k} \cdot (J(\vec{\psi})_{kj} \circ \vec{\psi}^{-1}) \end{aligned} \tag{6.92}$$

From the Inverse Function Theorem, we have for the diffeomorphism $\vec{\psi}$,

$$\boldsymbol{J}(\vec{\psi}) \circ \vec{\psi}^{-1} = \left[\boldsymbol{J}(\vec{\psi}^{-1})\right]^{-1} \tag{6.93}$$

with $[\cdot]^{-1}$ the matrix inverse function, $[\boldsymbol{M}]^{-1}_{ik} M_{kj} = \delta_{ij}$. And so

$$\begin{aligned} u_{i,j} \circ \vec{\psi}^{-1} &= \mu_{i,k} \cdot \left[\boldsymbol{J}(\vec{\psi}^{-1})\right]^{-1}_{kj} \\ v_{i,j} \circ \vec{\psi}^{-1} &= \nu_{i,k} \cdot \left[\boldsymbol{J}(\vec{\psi}^{-1})\right]^{-1}_{kj} \end{aligned} \tag{6.94}$$

Looking at

$$(u_{i,j}(\vec{\psi}^{-1}(y)) + u_{j,i}(\vec{\psi}^{-1}(y))) \, C_{ijkl} \tag{6.95}$$

and using the substitutions in (6.94), we get

$$\left(\mu_{i,m}(\vec{y}) \left[\boldsymbol{J}(\vec{\psi}^{-1})\right]^{-1}_{mj}(\vec{y}) + \mu_{j,m}(\vec{y}) \left[\boldsymbol{J}(\vec{\psi}^{-1})\right]^{-1}_{mi}(\vec{y})\right) \, C_{ijkl} \tag{6.96}$$

and finally, (6.85) can be written, dropping the explicit coordinate,

$$\int_{\Lambda} \left(\mu_{i,m} \cdot \left[\boldsymbol{J}(\vec{\psi}^{-1}) \right]^{-1}_{mj} + \mu_{j,m} \cdot \left[\boldsymbol{J}(\vec{\psi}^{-1}) \right]^{-1}_{mi} \right) \cdot C_{ijkl} \cdot \left(\nu_{k,m} \cdot \left[\boldsymbol{J}(\vec{\psi}^{-1}) \right]^{-1}_{ml} + \nu_{l,m} \cdot \left[\boldsymbol{J}(\vec{\psi}^{-1}) \right]^{-1}_{mk} \right) \cdot |\boldsymbol{J}(\vec{\psi}^{-1})| \cdot dy^3 = 0 \quad (6.97)$$

which is over the finite domain Λ with every function in that domain. This means the time needed to evaluate the integral is now finite and the storage needed to store the functions is finite.

6.3.2 A Good Linear Form Transformation

Now a suitable ψ must be found so the functions $\vec{\mu}$ and $\vec{\nu}$ can be well represented by linear finite elements.

Tetrahedron Integral Independence

One approach is to ensure the FEM integrals are independent of the coordinate. This would ensure the problem is dependent only on the geometry of the mesh, and the resulting FEM matrices are numerically stable. To do this, we will find the order of one of these integrals in terms of the interpolation coefficients, $\vec{c}$, the transformation function, $\vec{\psi}^{-1}$, and the coordinate $|y|$.

Taking the order of y of one of the factors as

$$\mathcal{O}(\left(\mu_{i,m} \cdot \left[\boldsymbol{J}(\vec{\psi}^{-1}) \right]^{-1}_{mj} + \mu_{j,m} \cdot \left[\boldsymbol{J}(\vec{\psi}^{-1}) \right]^{-1}_{mi} \right)) = \mathcal{O}(\frac{\partial \mu}{\partial y}) \, \mathcal{O}(\left[\boldsymbol{J}(\vec{\psi}^{-1}) \right]^{-1}_{mi}) \quad (6.98)$$

we can say the order of the integrand is

$$\mathcal{O}(\text{integrand}) = \mathcal{O}(\frac{\partial \mu}{\partial y}) \, \mathcal{O}(\left[\boldsymbol{J}(\vec{\psi}^{-1}) \right]^{-1}) \, \mathcal{O}(\frac{\partial \nu}{\partial y}) \, \mathcal{O}(\left[\boldsymbol{J}(\vec{\psi}^{-1}) \right]^{-1}) \, \mathcal{O}(|\boldsymbol{J}(\vec{\psi}^{-1})(y)|) \quad (6.99)$$

We remember that, for a linearly interpolated function,

$$\mu_i(\vec{y}) = \lambda(\vec{y})_k c_{ik}$$

with $\vec{\lambda}$ defined and evaluated element-wise, and $0 \leq \lambda(\vec{y})_i \leq 1$ on each element, and derivatives

$$\begin{aligned}\mu_{i,j}(\vec{y}) &= \frac{\partial \lambda_k}{\partial y_j}(\vec{y}) c_{ik} \\ &= D_{kj} c_{ik}\end{aligned}$$

with D_{kj} dependent only on the tetrahedron geometry, and independent of $\vec{y}$. Therefore, we can say for the trial function term $\mu_{i,j}$

$$\begin{aligned}\mathcal{O}(\frac{\partial \mu}{\partial y}) &= \mathcal{O}(D)\mathcal{O}(c) \\ &= \mathcal{O}(c)\end{aligned} \tag{6.100}$$

and the test function term $\nu_{i,j}$, where $\boldsymbol{c} = 1$ or $\boldsymbol{c} = 0$, to build the appropriate matrix equations

$$\mathcal{O}(\frac{\partial \nu}{\partial y}) = \mathcal{O}(D) = 1 \tag{6.101}$$

Using some very rough approximations, and assuming $\dim(\Lambda) = 3$:

$$\mathcal{O}(\vec{\psi}^{-1}(\vec{y})) = |y|^n \tag{6.102}$$

$$\mathcal{O}(\mu(\vec{y})) = \mathcal{O}(c) \tag{6.103}$$

$$\mathcal{O}(\nu(\vec{y})) = 1 \tag{6.104}$$

$$\mathcal{O}(\boldsymbol{J}(\vec{\psi}^{-1})(\vec{y})) = \mathcal{O}(\frac{\partial \vec{\psi}^{-1}}{\partial y})(\vec{y}) = \frac{\mathcal{O}(\vec{\psi}^{-1})(\vec{y})}{|y|} \tag{6.105}$$

$$\mathcal{O}(|\boldsymbol{J}(\vec{\psi}^{-1})(y)|) = \mathcal{O}(\boldsymbol{J}(\vec{\psi}^{-1})(\vec{y}))^3 = \frac{\mathcal{O}(\vec{\psi}^{-1}(\vec{y}))^3}{|y|^3} \tag{6.106}$$

$$\mathcal{O}(\left[\boldsymbol{J}(\vec{\psi}^{-1})\right]^{-1}(\vec{y})) = \frac{1}{\mathcal{O}(\boldsymbol{J}(\vec{\psi}^{-1})(\vec{y}))} = \frac{|y|}{\mathcal{O}(\vec{\psi}^{-1}(\vec{y}))} \tag{6.107}$$

which gives us

$$\begin{aligned}\mathcal{O}(\text{integrand}) &= \mathcal{O}(c)\frac{|y|}{\mathcal{O}(\vec{\psi}^{-1}(\vec{y}))}\frac{|y|}{\mathcal{O}(\vec{\psi}^{-1}(\vec{y}))}\frac{\mathcal{O}(\vec{\psi}^{-1}(\vec{y}))^3}{|y|^3} \\ &= \mathcal{O}(c)\ \frac{\mathcal{O}(\vec{\psi}^{-1}(\vec{y}))}{|y|}\end{aligned} \tag{6.108}$$

Integrating this value over, say, a single tetrahedron Λ_e, we get

$$\begin{aligned}\mathcal{O}(\text{integral}) &= \mathcal{O}(\int_{\lambda_e} c\ \frac{\vec{\psi}^{-1}}{|y|}\ dy^3) \\ &= \mathcal{O}(c)\ \mathcal{O}(\vec{\psi}^{-1})\ |y|^2\end{aligned} \tag{6.109}$$

assuming c and $\vec{\psi}^{-1}$ are polynomial in $|y|$ within the context of the approximation.

For the FEM, we solve the linear equation

$$S_{ij}c_j = F_i$$

where $\boldsymbol{S}$ is the stiffness matrix, $\vec{c}$ is the interpolation coefficients, and $\vec{F}$ is the stiffness matrix. In the context of the approximation, we have

$$\mathcal{O}(\boldsymbol{S}) = \mathcal{O}(\vec{\psi}^{-1})|y|^2 \tag{6.110}$$

and

$$\mathcal{O}(\vec{F}) = 1 \tag{6.111}$$

At the very least, we need

$$\mathcal{O}(c)\ \mathcal{O}(\vec{\psi}^{-1})\ |y|^2 = 1 \tag{6.112}$$

for consistency.

To have the stiffness matrix independent of the coordinates, we could set $\mathcal{O}(\vec{\psi}^{-1}) = |y|^{-2}$. This would give us $\mathcal{O}(c) = 1$.

This appears to be the approach used in (Imhoff, Meunier, Brunotte, et al. 1990)

and (Brunotte, Meunier, and Imhoff 1992) to choose an appropriate transformation function.

Far Field Approximation Approach

Yet another approach was used in (Abert et al. 2013), by noting the far field approximation of ϕ for a magnetic scalar potential is

$$\phi(x) \sim \frac{1}{x^2}$$

Choosing a $\vec{\psi}^{-1}$ such that

$$\phi(\psi^{-1}(\vec{y})) \sim y$$

so the transformed functions are linear in the transformed region, it is found that

$$\phi(\psi^{-1}(\vec{y})) \sim \frac{1}{\psi^{-1}(\vec{y})^2} \sim y$$

works if $\mathcal{O}(\psi^{-1}) = |y|^{-\frac{1}{2}}$.

Transformation Functions and Jacobians

We will continue here with the integral based consideration, and use $\mathcal{O}(\psi^{-1}) = |y|^{-2}$.

In general, a suitable pair $\vec{\varphi}$ and $\vec{\varphi}^{-1}$ with $\mathcal{O}(\vec{\varphi}^{-1}(\vec{y})) = |y|^{-n}$ are

$$\vec{\varphi}(\vec{x}) = \hat{x} \left((R^{\texttt{inner}} - R^{\texttt{outer}}) \left(\frac{R^{\texttt{inner}}}{|x|} \right)^{\frac{1}{n}} + R^{\texttt{outer}} \right) \tag{6.113a}$$

$$\vec{\varphi}^{-1}(\vec{y}) = \hat{y}\, R^{\texttt{inner}} \left(\frac{R^{\texttt{inner}} - R^{\texttt{outer}}}{|y| - R^{\texttt{outer}}} \right)^{n} \tag{6.113b}$$

we want these for $n = 2$, so we will use

$$\vec{\psi}(\vec{x}) = \hat{x}\left((R^{\texttt{inner}} - R^{\texttt{outer}})\left(\frac{R^{\texttt{inner}}}{|x|}\right)^{\frac{1}{2}} + R^{\texttt{outer}}\right) \tag{6.114a}$$

$$\vec{\psi}^{-1}(\vec{y}) = \hat{y}\, R^{\texttt{inner}}\left(\frac{R^{\texttt{inner}} - R^{\texttt{outer}}}{|y| - R^{\texttt{outer}}}\right)^{2} \tag{6.114b}$$

It can be shown that the Jacobians that appear in the integral can be given

$$\left[\boldsymbol{J}(\vec{\psi}^{-1})\right]^{-1}_{ij}(\vec{y}) = \frac{\delta_{ij}|y|}{|\psi^{-1}(\vec{y})|} + \frac{y_i y_j (R^{\texttt{outer}} - (n+1)|y|)}{n|\psi^{-1}(\vec{y})||y|^2} \tag{6.115}$$

$$\left|\boldsymbol{J}(\psi^{-1})\right|(\vec{y}) = \frac{n|\psi^{-1}(\vec{y})|^3}{R^{\texttt{outer}}|y|^2 - |y|^3} \tag{6.116}$$

where we want $n = 2$.

Substituting these Jacobians back into the transformed regions is enough to specify a complete problem for the transformed region. Noting that these terms are singular at $|y| = R^{\texttt{outer}}$, it is clear that we shouldn't evaluate our integral there. In the FEM formulation, this is taken care of by using Dirichlet boundary conditions. When using Dirichlet conditions, the test function is uniformly zero at the boundary, so the integral isn't evaluated there. If we choose $\vec{\mu} = 0$, this will represent fixed boundary conditions, $\vec{u} = 0$, at infinity.

Given the complexity of these terms, an analytic formulation of the FEM matrices is not straightforward. In this case, a numerical integration scheme, like a weighted Gaussian integral, may be preferable. This is handled automatically by FEniCS. While this formulation wasn't implemented for this thesis, the extension of the existing FEniCS implementation should be straightforward.

Chapter 7

Example Modelling Results for Magnetostrictive Minerals with Free Boundaries

Here we present some results from micromagnetic models using MERRILL, including the full magnetic and elastic description of magnetoelastic materials, including the deformation independent surface tension term. The FEM matrices and vectors for mechanical equations and for the FEM energy gradient were built using the automated FEM assembly environment FEniCS (Wells, Mardal, and Logg 2012).

All the results presented in this chapter are original, and significant results.

7.1 Deformations for SD, FS, HSV, ESV States

7.1.1 Introduction

The formulation of magnetostriction we've presented involves directly computing the equilibrium displacement $\vec{u}$ of a material due to a given magnetization. The displacement can be used to visualize the deformation of a material using, for example, the "Warp By Vector" filter in ParaView.

We'd like to see how a number of typical magnetization states in nano-scale minerals deform the material.

7.1.2 Method

To most clearly visualize the deformations, a cubic geometry was chosen. The cube was given the magnetic, elastic and magnetoelastic parameters for Titanomagnetite (TM60), a highly magnetoelastic material.

To nucleate a desired state, e.g. a hard-aligned single vortex, the size of the cube was set to where the given state is at least meta-stable. Then, the magnetization was set to an approximation of the target state to encourage nucleation of that state, and the energy minimization was run. If the desired state was nucleated, the result was accepted. If not, the size of the cube was changed, and the approximation/minimization rerun.

This was done for a flower state (FS), a hard-aligned single vortex (HSV), and an easy-aligned single vortex (ESV). A uniform single domain (SD) state was also generated, but needed no minimization. When the desired state was found, the magnetization and displacement were output to disk. Visualizations of the magnetization and the deformation of the cube were generated using ParaView.

7.1.3 Results

Single Domain

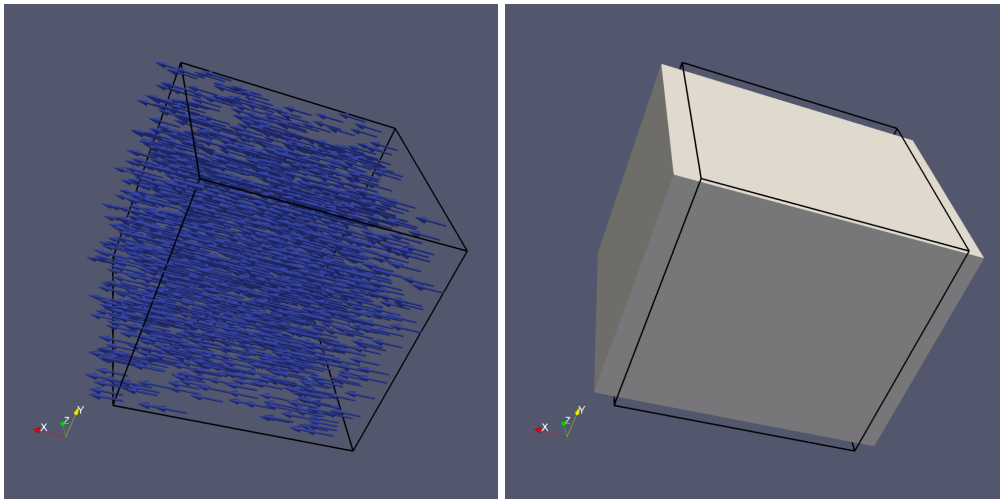

Figure 7.1: Magnetostrictive response of a Single Domain TM60 cube. Left is the magnetization colored by helicity $(\vec{\nabla} \times \vec{m}) \cdot \vec{m}$, right is the exaggerated deformation with amplification factor 1000. The undeformed cube is outlined in black.

Flower State

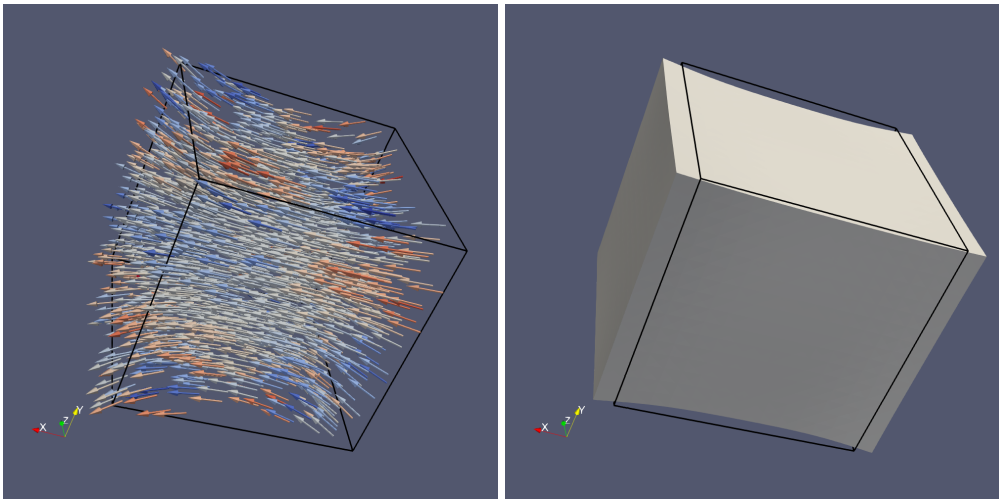

Figure 7.2: Magnetostrictive response of a Flower State TM60 cube. Left is the magnetization colored by helicity $(\vec{\nabla} \times \vec{m}) \cdot \vec{m}$, right is the exaggerated deformation with amplification factor 1000. The undeformed cube is outlined in black.

Hard-Aligned Single Vortex ([111])

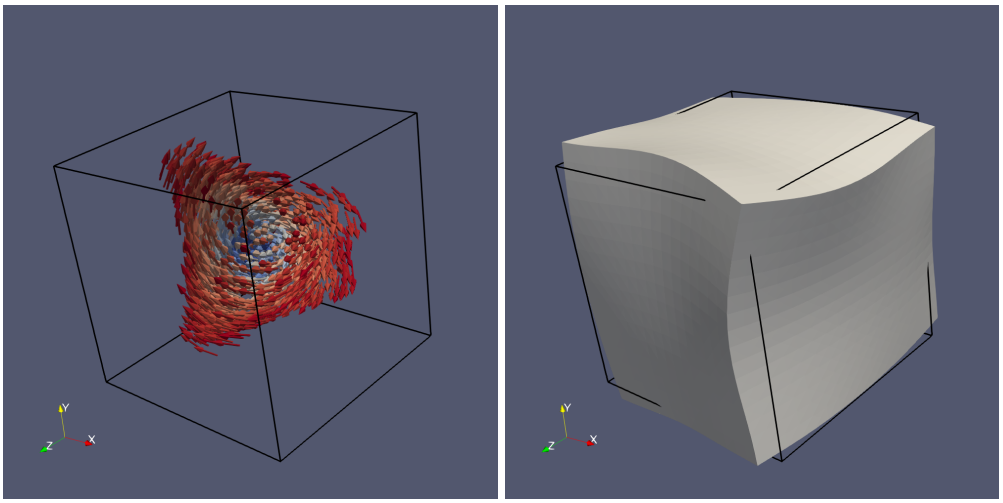

Figure 7.3: Magnetostrictive response of a Hard-aligned Single Vortex TM60 cube with a clockwise vortex pointed towards a cube corner, here pictured pointing out of the image. Left is the magnetization colored by helicity $(\vec{\nabla} \times \vec{m}) \cdot \vec{m}$, right is the exaggerated deformation with amplification factor 1000. The undeformed cube is outlined in black.

Easy-Aligned Single Vortex ([100])

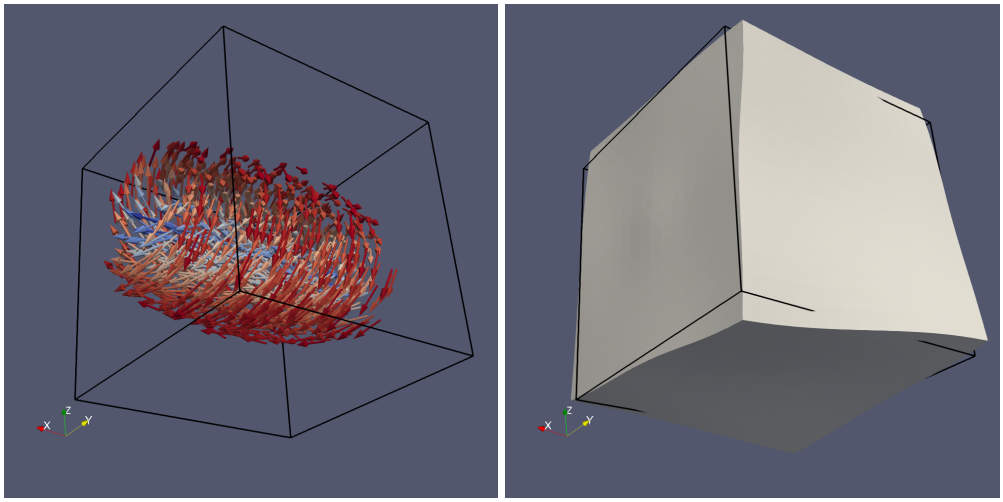

Figure 7.4: Magnetostrictive response of a Easy-aligned Single Vortex TM60 cube with a clockwise vortex pointed towards a cube face. Left is the magnetization colored by helicity $(\vec{\nabla} \times \vec{m}) \cdot \vec{m}$, right is the exaggerated deformation with amplification factor 1000. The undeformed cube is outlined in black.

7.1.4 Discussion

The ability to visualize the deformation in our formulation is quite useful for reasoning about how the material might behave, particularly the visualization of deformation due to non-uniform magnetizations.

While the stretching of the SD and FS states is expected, the twisting of the SV state was an interesting result. In particular, it may point to how previous simulations by Fabian and Heider (Fabian and Heider 1996) of a magnetoelastic material embedded in a larger non-magnetic material may have pushed the PSD range to a larger grain size. If this twisting of the material is inhibited, the nucleation of a SV state may be inhibited. While the stretching of the SD and FS states may also be inhibited, the energy needed to stretch the surrounding material, rather than twist it, may be much lower.

The twisting effect echoes the Wiedemann effect, where a helical magnetic field will generate a twist in a ferromagnet. This is likely an effect of the magnetizations aligning with the helical field looking like our vortex states. Here, the deformation due to the vortex states could be described as a sort of remanent Wiedemann effect.

7.2 Critical Grain Sizes for Magnetostrictive Materials

7.2.1 Introduction

Here we present how the critical grain sizes for a cube and a sphere differ between the Kittel Constant Stress (KCS) and Kittel Mechanical Equilibrium (KME) formulations.

We also plot the energy and the remanent magnetization versus grain size for the FS, HSV and ESV states, where they're meta-stable to see how the expected remanent magnetization strength differs between the theories.

We will be using the relative energies of the states versus size as a proxy for the stability of a grain. As shown in (Nagy et al. 2017), grains tend to be stable in the SD and PSD regions, but unstable around the transition between SD and PSD. This is likely due to the hard aligned vortex state being close in energy to the easy aligned states, presenting an easy path for the magnetization to pass through to transition from one remanent state to another.

7.2.2 Method

In each case, a FS, HSV, and ESV state was nucleated at a grain size stable for that particular state, and those states were stored as reference states. The grain was then scaled to 0.1 μESVD and the states minimized at that size, and the measurements made. This was repeated for 0.1, 0.11, 0.12, ... 0.26 μESVD. This was done to reliably minimize to the FS, HSV, and ESV meta-stable states, even where they were only minimally stable, so we could see how the energies of these specific states change versus grain size.

7.2.3 Results

7.2.4 Cube

Critical Edge Length

Kittel Constant Stress (KCS)

	ESVD (μm)	Energy (K_dV)
FS/HSV	0.143	18.821
HSV/ESV	0.156	17.421

Kittel Mechanical Equilibrium

	ESVD (μm)	Energy (K_dV)
FS/HSV	0.177	10.744
HSV/ESV	0.198	10.089

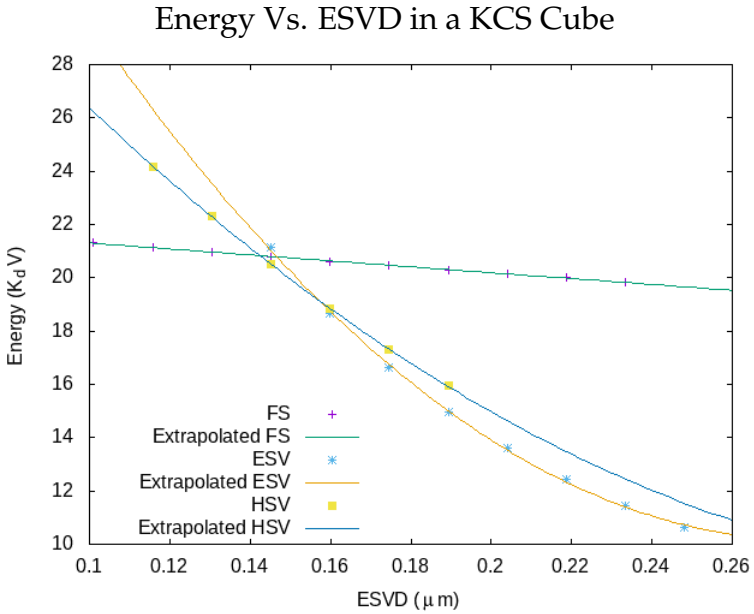

Figure 7.5: Energy vs. Equivalent Sphere Volume Diameter for a TM60 cube with magnetostriction calculated using the Kittel Constant Stress formulation. FS is a [100] Flower State, ESV is a [100] Easy-aligned Single Vortex, and HSV is a [111] Hard-aligned Single Vortex.

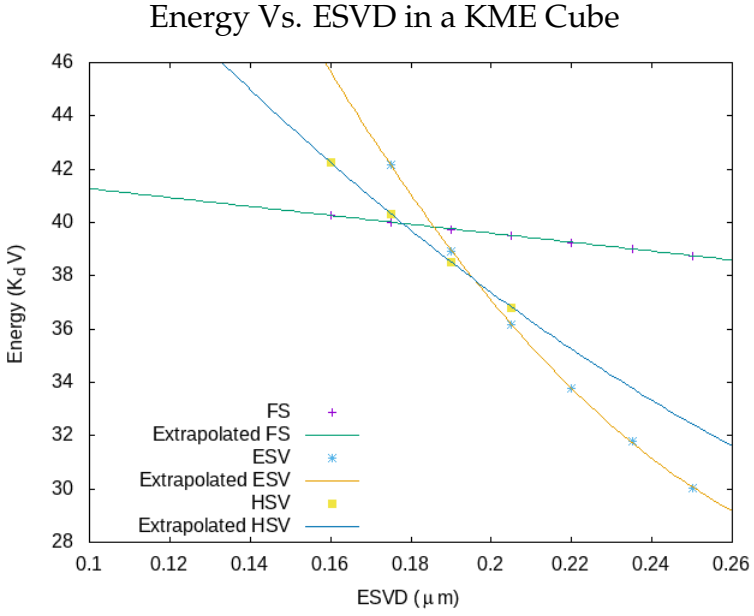

Figure 7.6: Energy vs. Equivalent Sphere Volume Diameter for a TM60 cube with magnetostriction calculated using the Kittel Mechanical Equilibrium formulation. FS is a [100] Flower State, ESV is a [100] Easy-aligned Single Vortex, and HSV is a [111] Hard-aligned Single Vortex.

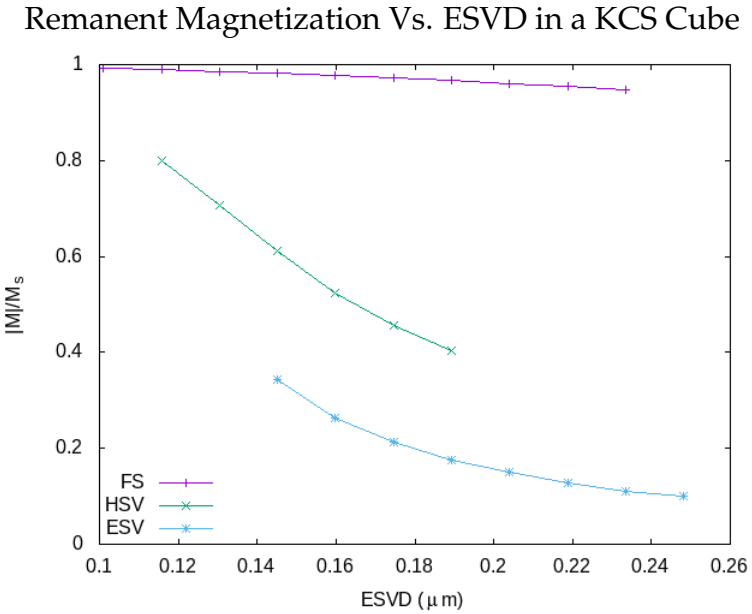

Figure 7.7: Remanent Magnetization vs. Equivalent Sphere Volume Diameter for a TM60 cube with magnetostriction calculated using the Kittel Constant Stress formulation. FS is a [100] Flower State, ESV is a [100] Easy-aligned Single Vortex, and HSV is a [111] Hard-aligned Single Vortex.

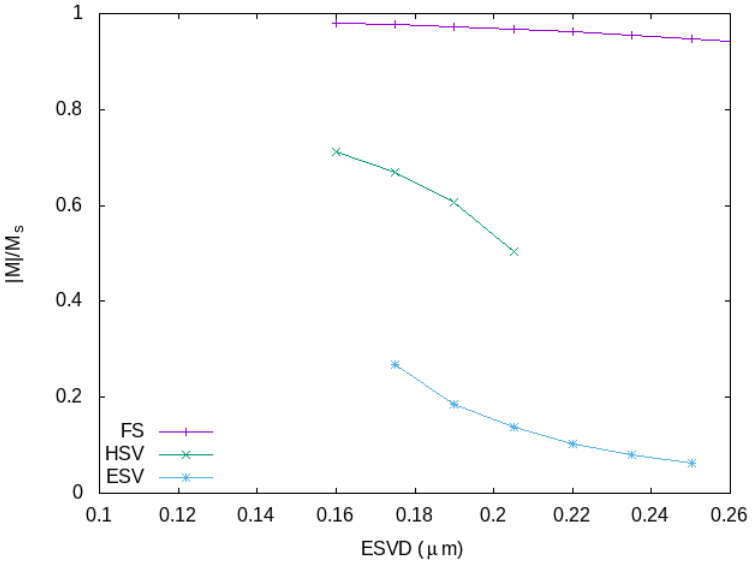

Figure 7.8: Remanent Magnetization vs. Equivalent Sphere Volume Diameter for a TM60 cube with magnetostriction calculated using the Kittel Mechanical Equilibrium formulation. FS is a [100] Flower State, ESV is a [100] Easy-aligned Single Vortex, and HSV is a [111] Hard-aligned Single Vortex.

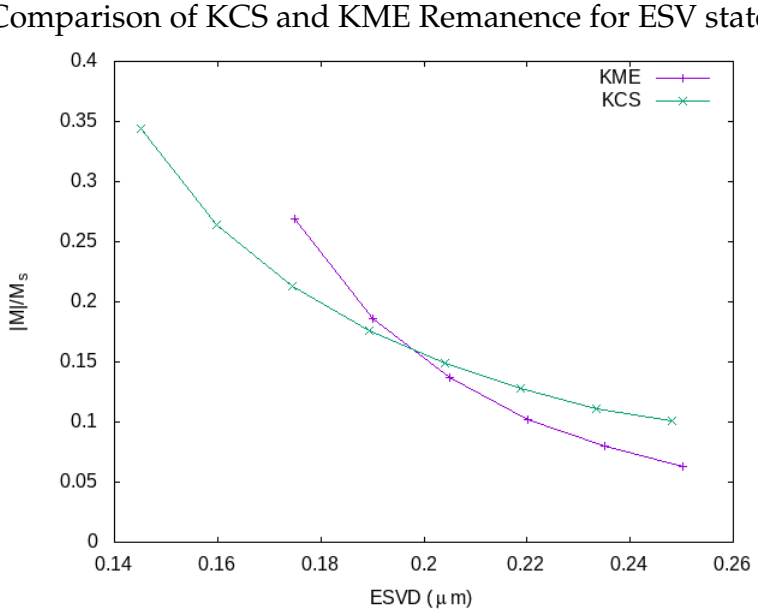

Figure 7.9: Remanent Magnetization vs. Equivalent Sphere Volume Diameter for an easy aligned vortex state in a TM60 cube for both Kittel Constant Stress and Kittel Mechanical Equilibrium formulations of magnetostriction.

7.2.5 Sphere

Critical Edge Length

Kittel Constant Stress

	ESVD (μm)	Energy (K_dV)
FS/HSV	0.129	20.151
HSV/ESV	0.151	17.191

Kittel Mechanical Equilibrium

	ESVD (μm)	Energy (K_dV)
FS/HSV	0.153	9.949
HSV/ESV	0.190	8.648

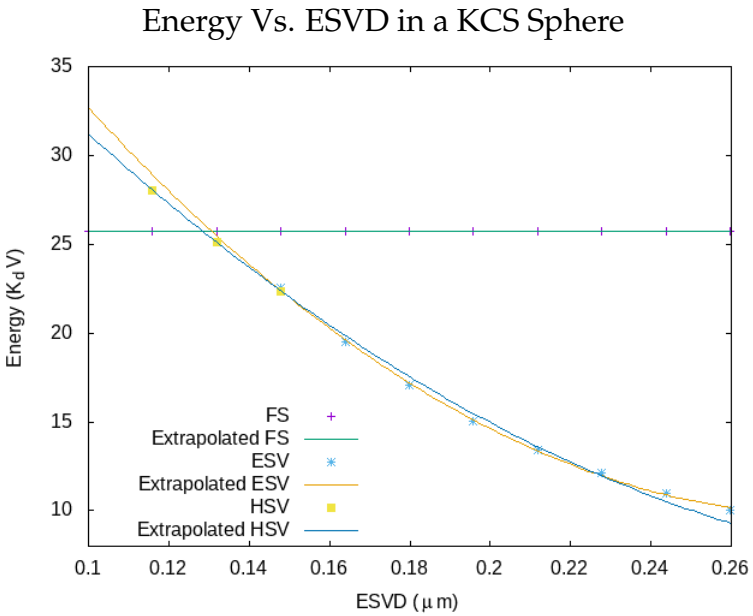

Figure 7.10: Energy vs. Equivalent Sphere Volume Diameter for a TM60 sphere with magnetostriction calculated using the Kittel Constant Stress formulation. FS is a [100] Flower State, ESV is a [100] Easy-aligned Single Vortex, and HSV is a [111] Hard-aligned Single Vortex.

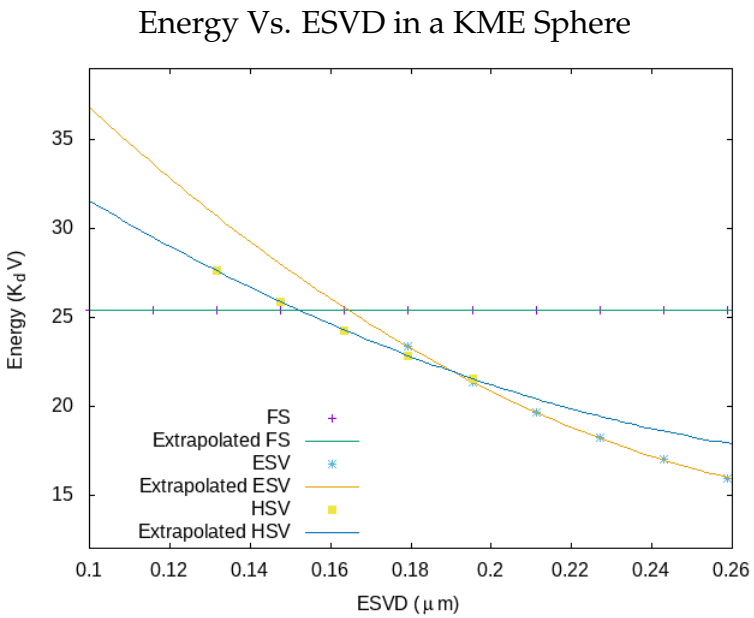

Figure 7.11: Energy vs. Equivalent Sphere Volume Diameter for a TM60 sphere with magnetostriction calculated using the Kittel Mechanical Equilibrium formulation. FS is a [100] Flower State, ESV is a [100] Easy-aligned Single Vortex, and HSV is a [111] Hard-aligned Single Vortex.

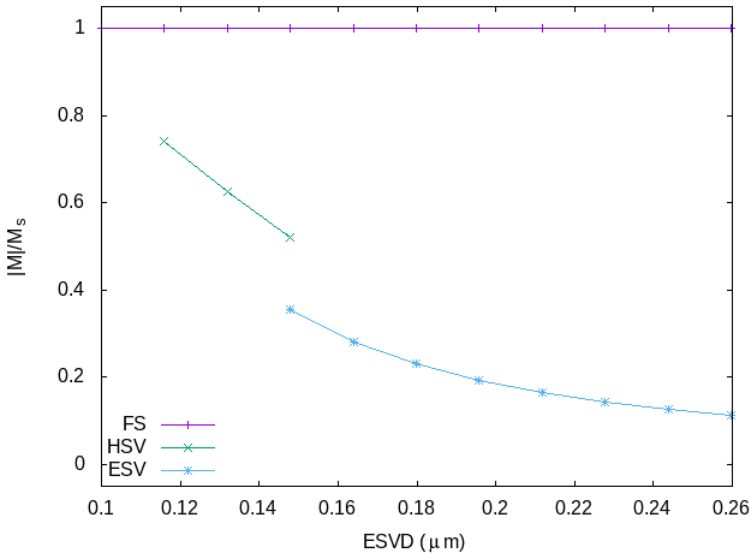

Figure 7.12: Remanent Magnetization vs. Equivalent Sphere Volume Diameter for a TM60 sphere with magnetostriction calculated using the Kittel Constant Stress formulation. FS is a [100] Flower State, ESV is a [100] Easy-aligned Single Vortex, and HSV is a [111] Hard-aligned Single Vortex.

Remanent Magnetization Vs. ESVD in a KME Sphere

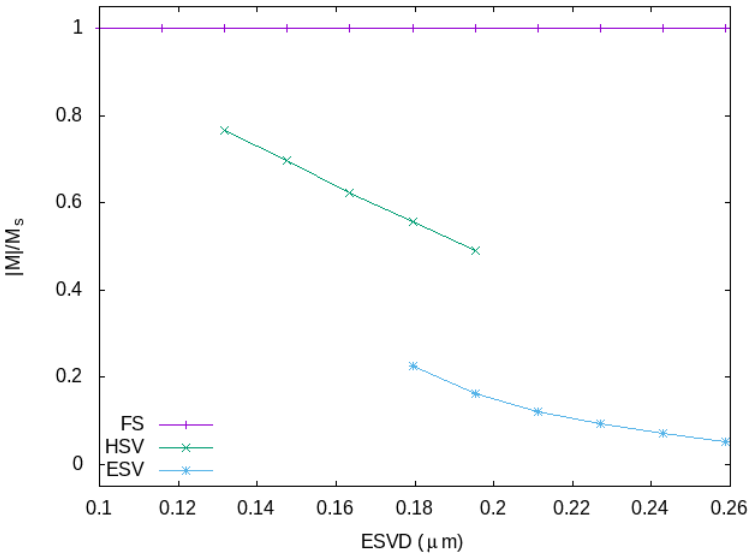

Figure 7.13: Remanent Magnetization vs. Equivalent Sphere Volume Diameter for a TM60 sphere with magnetostriction calculated using the Kittel Mechanical Equilibrium formulation. FS is a [100] Flower State, ESV is a [100] Easy-aligned Single Vortex, and HSV is a [111] Hard-aligned Single Vortex.

Comparison of KCS and KME Remanence for ESV states in a Sphere

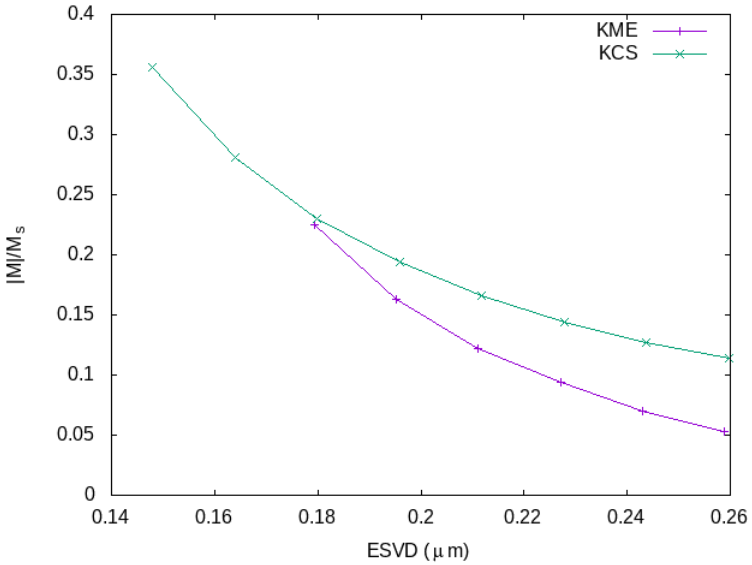

Figure 7.14: Remanent Magnetization vs. Equivalent Sphere Volume Diameter for an easy aligned vortex state in a TM60 sphere for both the Kittel Constant Stress and the Kittel Mechanical Equilibrium formulations of magnetostriction.

7.2.6 Discussion

Comparing figures 7.5 with 7.6, and 7.10 with 7.12, we see the full treatment of magnetostriction (using the KME formulation) pushes the FS-dominant grain size further ahead by about 0.04 ESVD. It also pushed the grain size for a stable HSV state ahead 0.05 ESVD. Stable here means a minimization retained the state, and didn't spontaneously nucleate a different state. It also causes the HSV and ESV energies to diverge faster, causing a larger energy gap between the two with increasing grain size, implying a more stable magnetization. However, the region where the FS, HSV, and ESV energies overlap is larger in the full magnetostriction case, implying a larger region of instability for the grain. In general, the KME formulation implies a larger SD range, but a larger region of instability.

Looking at 7.9 and 7.14, we see that the KME formulation predicts lower remanence in ESV states with increasing grain size. This might be explained by the magnetostrictive effect tending to resist incompatibilities due to varying magnetization.

7.3 Surface Tension Results

7.3.1 Introduction

In our magnetostrictive formulation, we have a tension term, $\vec{T}$, which we have so far set to zero. Here, we will explore the effect a non-zero $\boldsymbol{T}$ on the mechanical and magnetic behaviour of a magnetic cube. We also want to explore the behaviour of the system under varying approaches to treating mechanical equilibriation.

So far, we have been assuming instant mechanical equilibriation, which would put the elastic response of the system at a much smaller time-scale than the magnetic response. This was done to speed up and simplify numerical solutions, as the order in which both aspects come to equilibrium is irrelevant when simply looking for overall equilibrium solutions. In reality, the magnetic equilibriation happens on a much smaller time-scale than the elastic response. We will, therefore, also look at the magnetic response of the system for fixed elastic deformations, to get an idea of how magnetostriction might effect dynamical simulations.

7.3.2 Method

A Fortran program was written, using the MERRILL library, to run the magnetostriction solver in a number of different modes. A 100 nm cube was used with the parameters of titanomagnetite (TM60).

Three values for the surface tension were used: $\vec{T} = p\,\vec{n}$, $\vec{T} = p\,(\vec{n}\cdot[100])\vec{n}$, and $\vec{T} = p\,(\vec{n}\cdot[111])\vec{n}$, with $\vec{n}$ the surface normal. These represent a hydrostatic, $[100]$ uniaxial, and $[111]$ uniaxial surface tension respectively.

Four approaches to solving the mechanical equations were used, labelled dynamic, static-0, static-[100], and static-[111]. The dynamic approach is the instant mechanical equilibriation approach we've been using thus far, where the displacement is always set to the minimizing displacement for the given magnetization. The static approaches solve the mechanical equations for the given

surface tension and magnetization, but freeze the displacement at that value for subsequent magnetizations. For static-0, the magnetoelastic coupling is set to zero before solving the elastic equations. For static-[100] and static-[111], the magnetization is set to [100] and [111] respectively before solving the elastic equations.

For each of these surface tensions and solver schemes, the magnetostrictive energy due to the magnetization was found. The minimum energy of all these values was found and subtracted from the others, so the energies began at zero, without effecting the relative differences. This was output in the form of an energy surface The energy surface is a spherical plot, where the polar and azimuthal angles are the angles of the unit magnetization, and the radius is the energy. Or put another way, from the center, the unit direction is the direction of the magnetization, and the distance from the origin is the energy. For a point $\|r\|\,\hat{r}$ on the energy surface, we have

$$\begin{aligned} \hat{m} &= \hat{r} \\ E(\hat{m}) - E_0 &= \|r\| \end{aligned} \tag{7.1}$$

with E_0 the minimum energy. For each tension and scheme, the displacement was also output for $\hat{m} = [100]$.

7.3.3 Results

The given setup generates at least 12 cases to check, and for a range of pressures. To avoid wasting space, we present most results around 10^7 Pa, and present more results where the pressure makes a significant change to the energy surface.

The deformations presented are exaggerated by 1000x, except for $|T| = 10^8$, there the exaggeration is 800x.

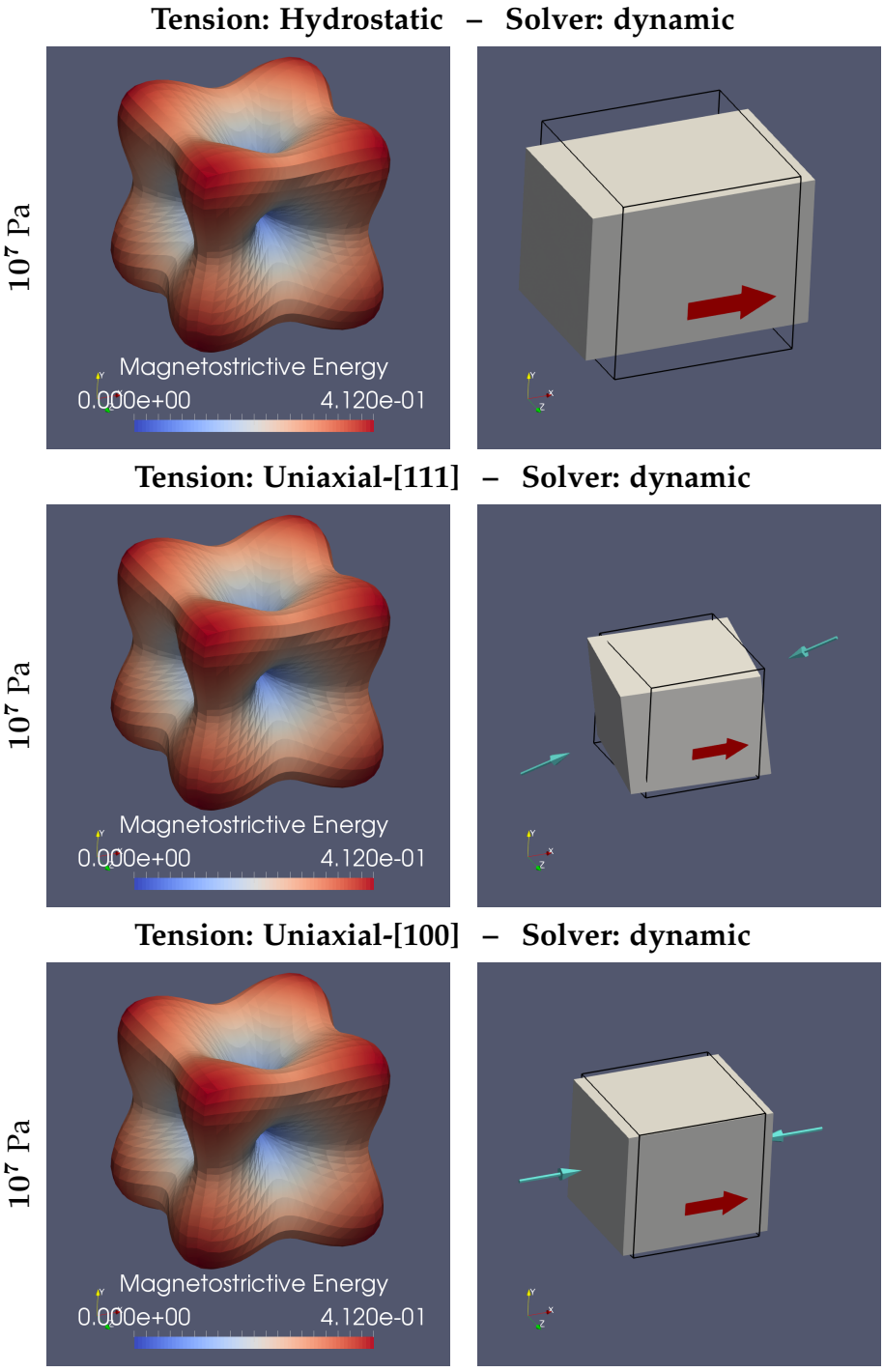

Figure 7.15: The effective anisotropy (left) for a fully dynamic magnetostrictive solver, and the corresponding deformation for a [100] magnetization (right). The top images are the results for a grain under a hydrostatic pressure, the center images are for a grain under a [111] uniaxial tension, and the bottom images are for a grain under [100] uniaxial tension. Only the results for a pressure of 10^7 Pa are shown here, but the value of $E_{\max}$ is the same for all pressures.

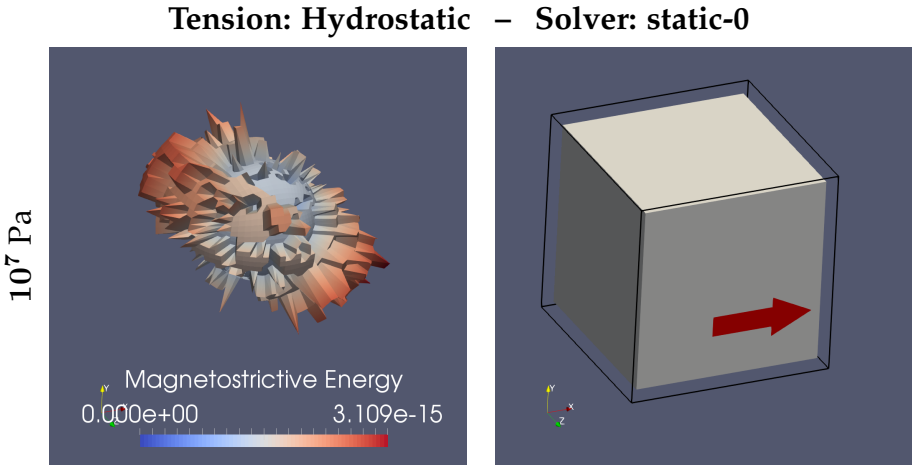

Figure 7.16: The effective anisotropy (left) and corresponding deformation under a [100] magnetization (right) for a solver where the equilibrium deformation is found for a non-magnetic material, frozen at that value, and then substituted into the magnetoelastic energy. This image represents an equilibrium found under a hydrostatic pressure. Only 10^7 Pa is shown here, but every pressure tested produced similar results.

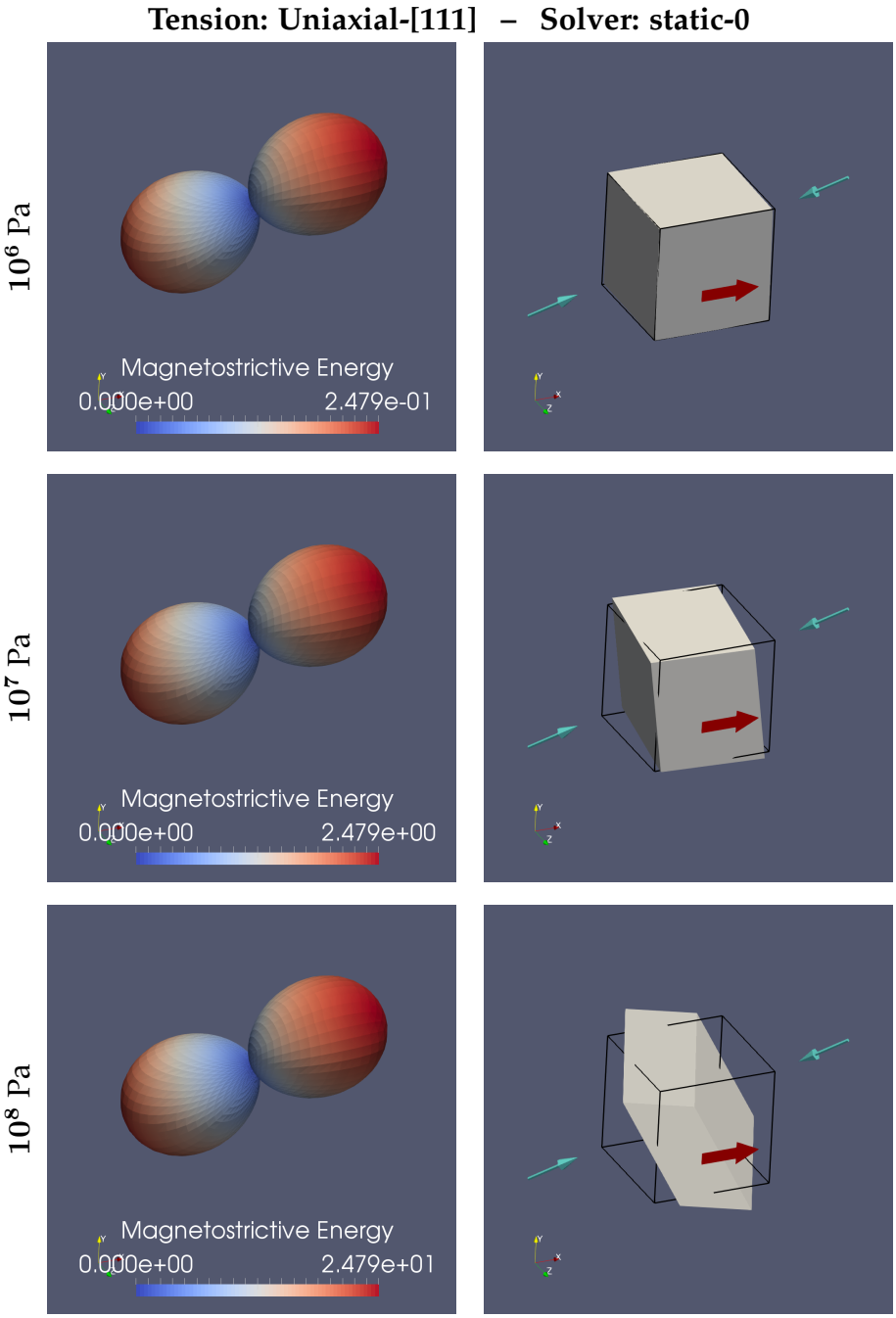

Figure 7.17: The effective anisotropy (left) and corresponding deformation under a [100] magnetization (right) for a solver where the equilibrium deformation is found for a non-magnetic material, frozen at that value, and then substituted into the magnetoelastic energy. The images here represent an equilibrium found under a [111] uniaxial tension from 10^6 Pa to 10^8 Pa.

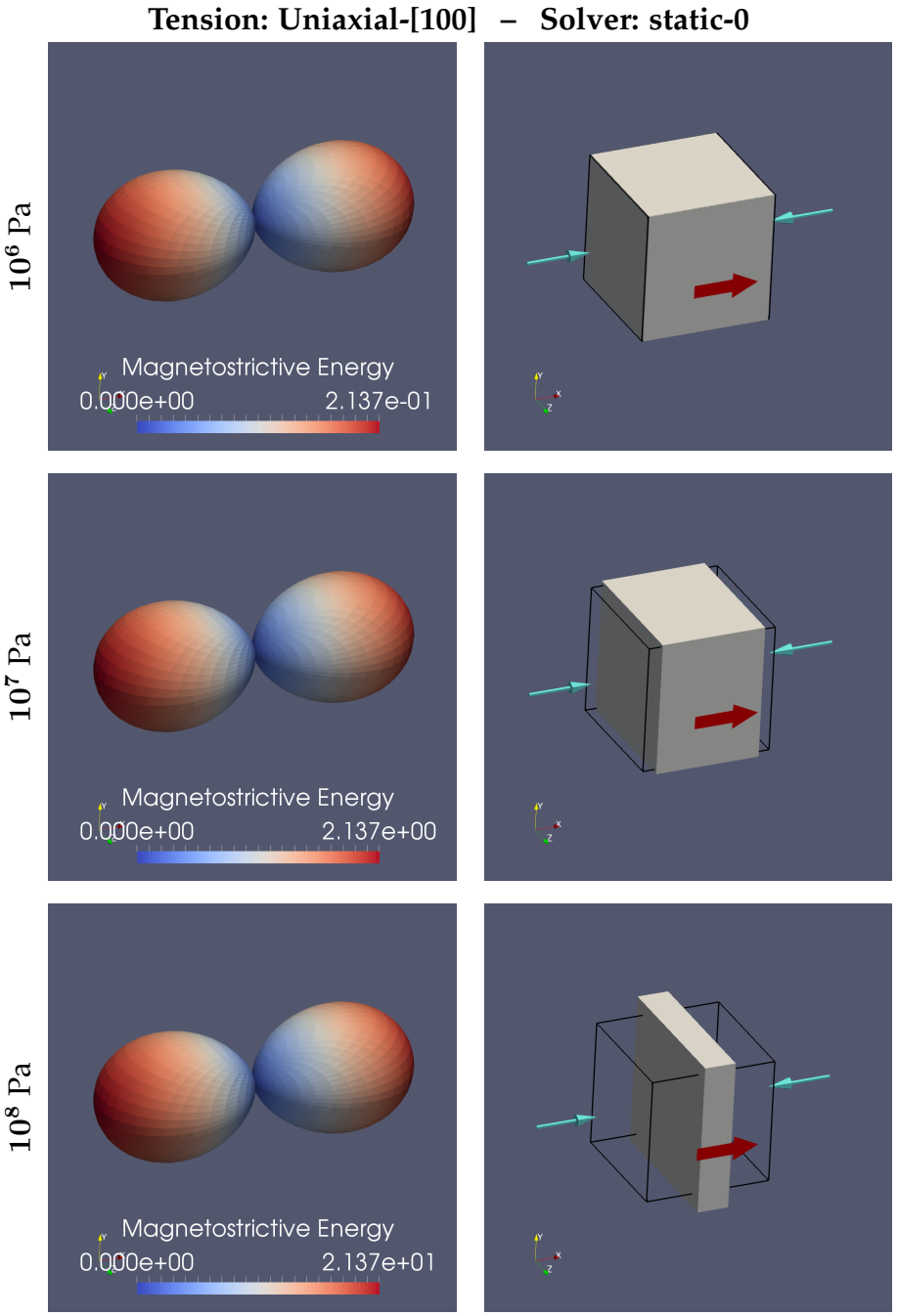

Figure 7.18: The effective anisotropy (left) and corresponding deformation under a [100] magnetization (right) for a solver where the equilibrium deformation is found for a non-magnetic material, frozen at that value, and then substituted into the magnetoelastic energy. The images here represent an equilibrium found under a [100] uniaxial tension from 10^6 Pa to 10^8 Pa.

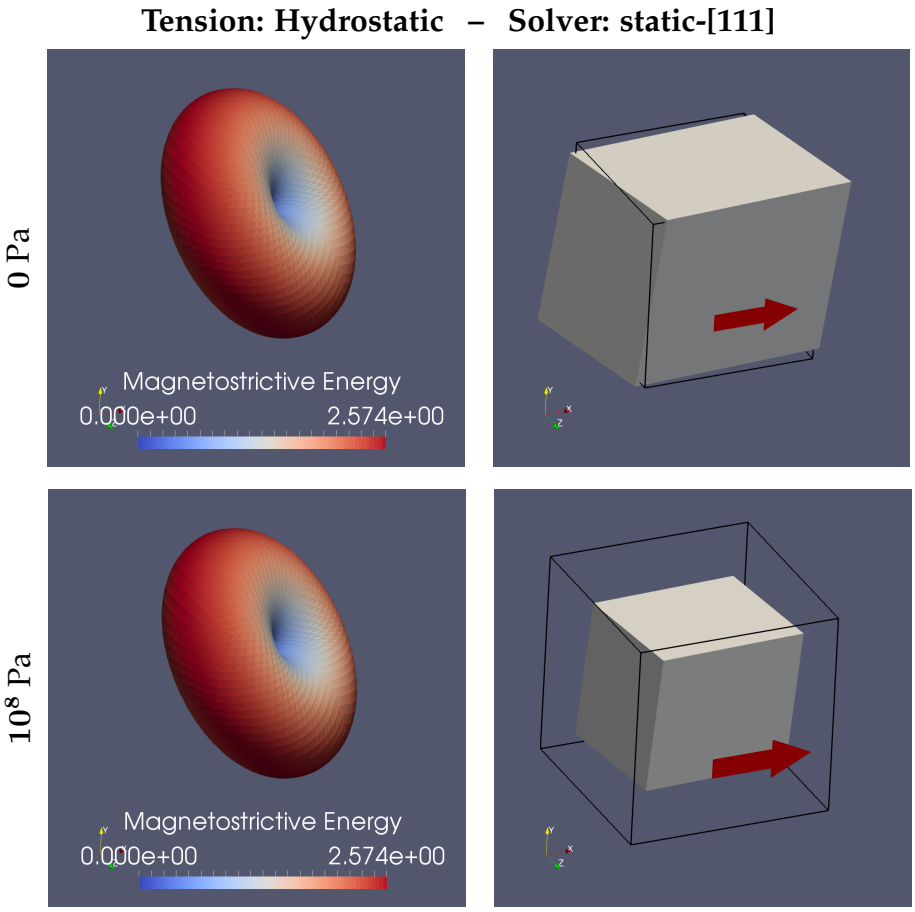

Figure 7.19: The effective anisotropy (left) and corresponding deformation under a [100] magnetization (right) for a solver where the equilibrium deformation is found for a [111] magnetization, frozen at that value, and then substituted into the magnetoelastic energy. These images represent a solutions under a hydrostatic pressure. Results for 0 Pa and 10^8 Pa are presented here. All values in between produce the same result.

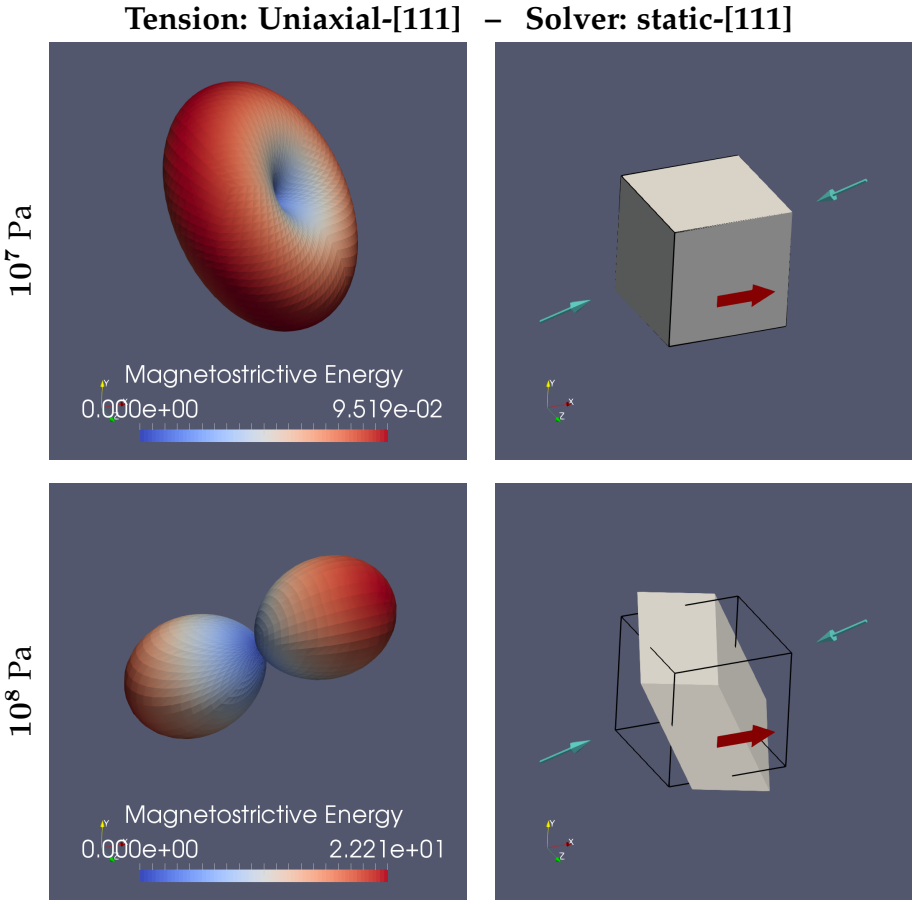

Figure 7.20: The effective anisotropy (left) and corresponding deformation under a [100] magnetization (right) for a solver where the equilibrium deformation is found for a [111] magnetization, frozen at that value, and then substituted into the magnetoelastic energy. The images here represent solutions under a [111] uniaxial tension. The solutions for 10^7 Pa and 10^8 Pa are presented here as they produce a significant change in shape. Solutions below 10^7 Pa produce the same shape results as the 10^7 Pa solution, and solutions above 10^8 produce the same shape results as the 10^8 Pa solution.

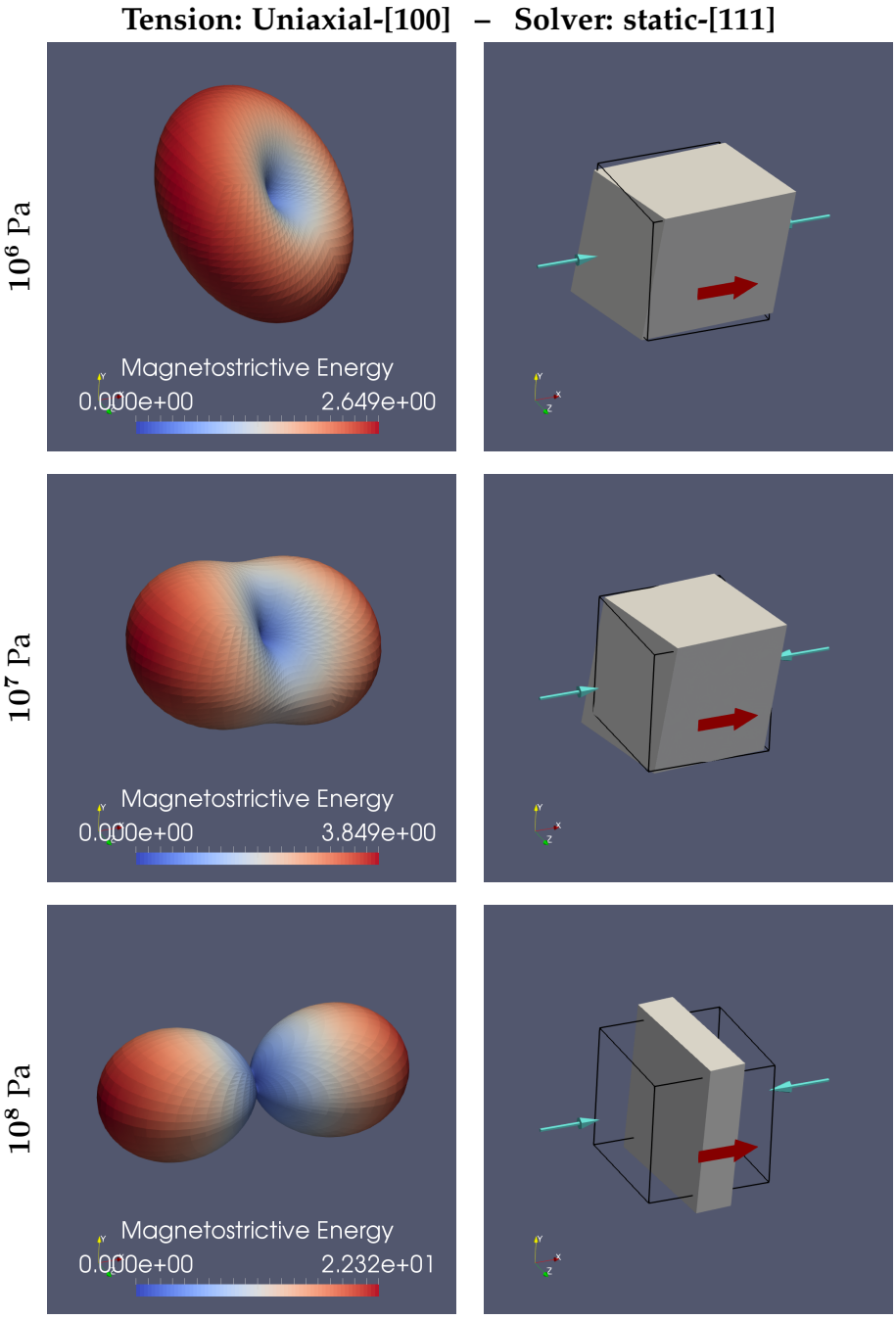

Figure 7.21: The effective anisotropy (left) and corresponding deformation under a [100] magnetization (right) for a solver where the equilibrium deformation is found for a [111] magnetization, frozen at that value, and then substituted into the magnetoelastic energy. The images shown here are for solutions under a [100] uniaxial tension for 10^6 Pa, 10^7 Pa, and 10^8 Pa. Below 10^6 Pa, solutions retain the [111] aligned donut shape, and above 10^8 Pa solutions retain the [100] aligned dumbbell shape.

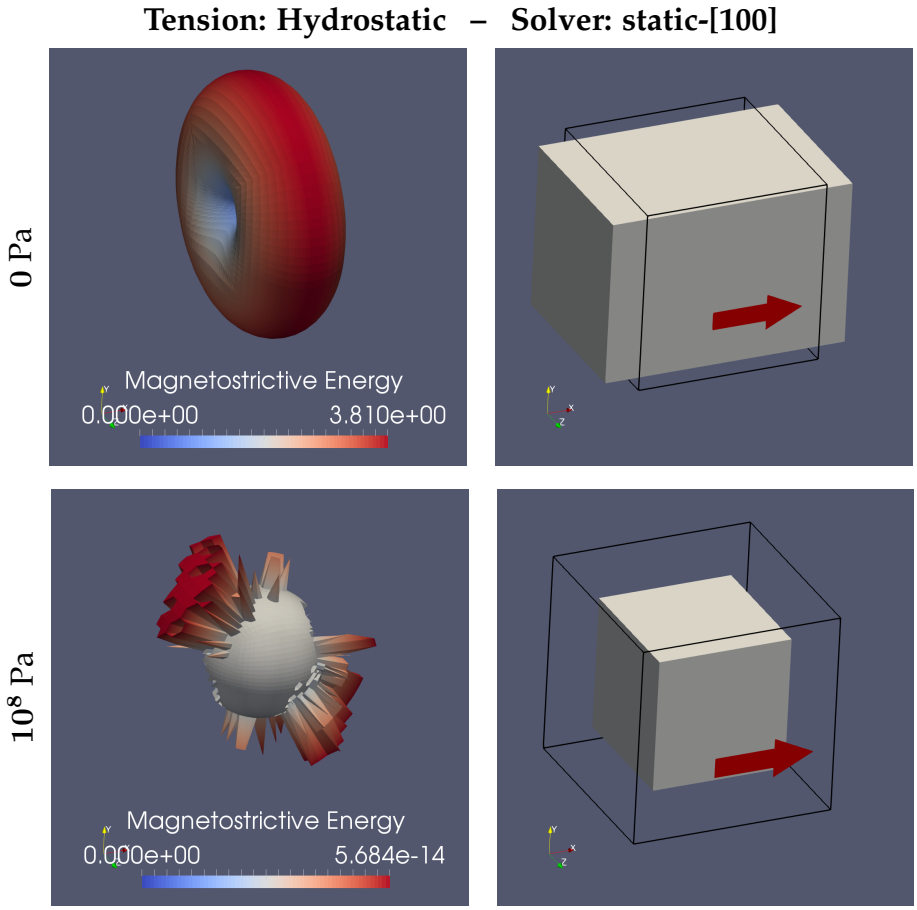

Figure 7.22: The effective anisotropy (left) and corresponding deformation under a [100] magnetization (right) for a solver where the equilibrium deformation is found for a [100] magnetization, frozen at that value, and then substituted into the magnetoelastic energy. These images are solutions for a hydrostatic pressure. All solutions above 10^8 Pa are also effectively zero.

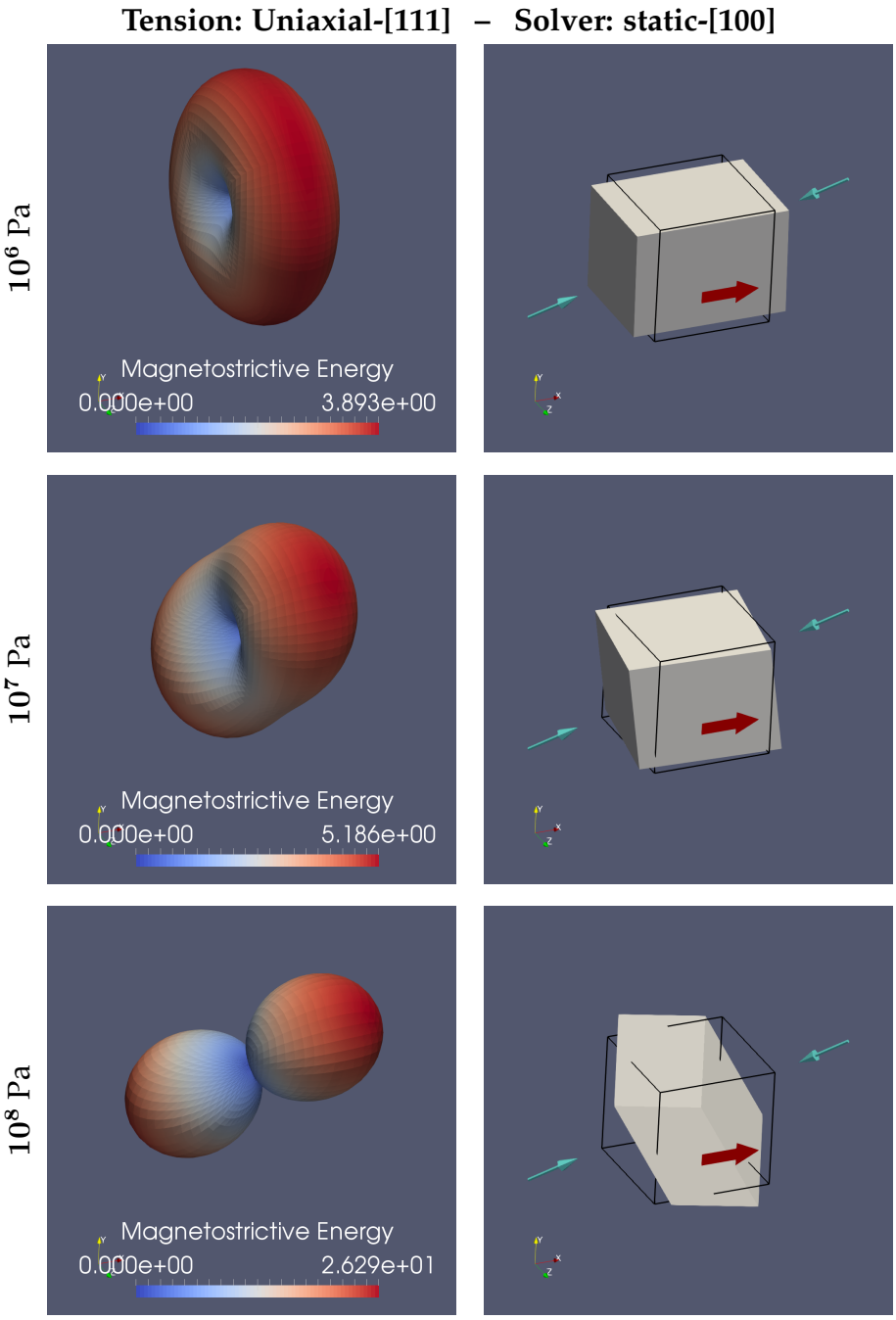

Figure 7.23: The effective anisotropy (left) and corresponding deformation under a [100] magnetization (right) for a solver where the equilibrium deformation is found for a [100] magnetization, frozen at that value, and then substituted into the magnetoelastic energy. The images here are for a [111] uniaxial tension. Pressures below 10^6 Pa retain the [100] aligned donut shape, and pressures above 10^8 Pa retain the [111] aligned dumbbell shape.

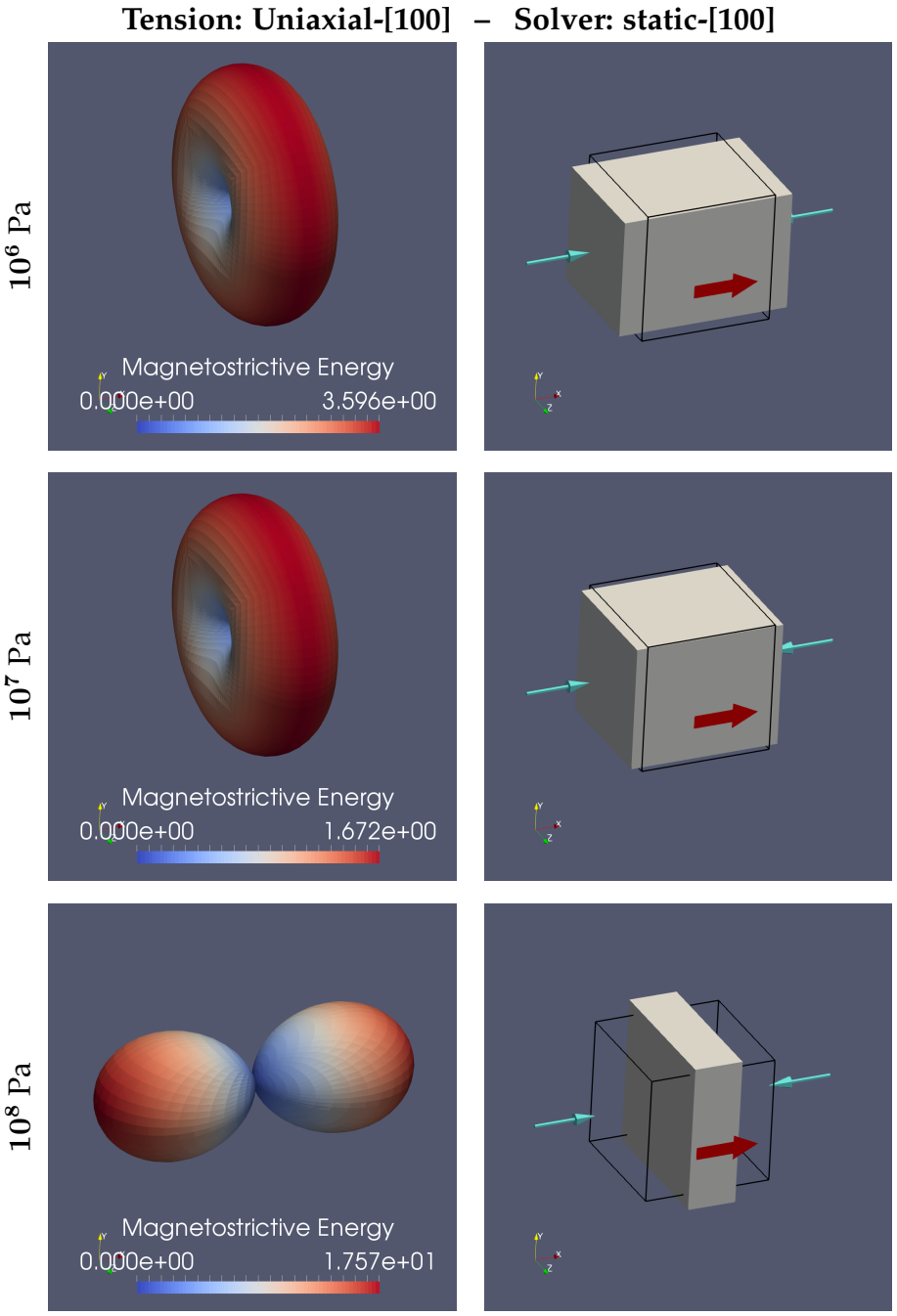

Figure 7.24: The effective anisotropy (left) and corresponding deformation under a [100] magnetization (right) for a solver where the equilibrium deformation is found for a [100] magnetization, frozen at that value, and then substituted into the magnetoelastic energy. The images here are for a [100] uniaxial tension. Pressures below 10^6 Pa retain the [100] aligned donut shape, and pressures above 10^8 Pa retain the [111] aligned dumbbell shape. The transition between the donut and dumbbell is very rapid about the point where the uniaxial tension exactly cancels out the magnetostrictive elongation.

7.3.4 Discussion

The energy surfaces can be interpreted as the highest/lowest energy points being the hard/easy axis directions. The slope of the energy surface can be interpreted as the magnetic field direction for the given magnetization.

Dynamic
The dynamic results confirms our assertion that under instant-equilibriation, the magnetic behaviour of the material is independent of the surface tension. This means the remanent magnetization should be independent of the surface tension. The energy surface of the dynamic solver is the same energy surface for a cubic anisotropy with negative anisotropy constant. This also confirms our formulation returns the typical anisotropy-shaped result.

Static-0 and Kittel's Uniaxial Formulation
The static-0 formulation — where the elastic deformation is solved for a non-magnetic material, and that deformation is then used for the magnetostrictive energy — is equivalent to Kittel's formulation for a uniaxial stress. The first failure of this approach can be seen in the hydrostatic results, which predict extremely low magnetic fields. In a physical sample, one would expect nominal fields for even low hydrostatic pressures. The static-0 uniaxial results also recover Kittel's $\frac{3}{2}\lambda T \sin^2(\theta)$ uniaxial result, which confirms that we are indeed modelling Kittel's solution. Another failure of this approach is the deformations are clearly lacking the characteristic magnetostrictive deformation, even at very low tensions. In particular, for 0 tension, the characteristic magnetostrictive deformation should appear, but it doesn't.

Static-[111] and Static-[100]
The static-[111] and static-[100] correspond to the magnetic energy, as experienced on a time-scale where the mechanical motion of the material is negligible. The static-[111] energies, for instance, represent the magnetoelastic energies experienced by a system which was in thermal equilibrium with a [111] magnetization, and is now out of equilibrium. The system will continue to experience this energy response until the magnetization comes to equilibrium, and the elastic response has had enough time to deform the material by a noticeable amount. And similar for the static-[100] energies.

From the general trends, we can see that the magnetic energy is lowest when the magnetization is pointing in a direction where the current deformation is close to the equilibrium deformation for that direction. This is most clearly shown in the static-[100], uniaxial-[100] series. Noting that $|T| = 10^6$ and $|T| = 10^7$ have deformations similar to the equilibrium deformation for $\hat{m} = [100]$, and the energy minimum is for $\hat{m} = [100]$. However, this trend is reversed at $|T| = 10^8$. We can see that the material is most extended in the yz-plane, and that the energy is lowest for $\hat{m}$ in the yz-plane. This is because the deformation in this plane is closest to the characteristic magnetostrictive deformation, compared to other directions.

Effective Easy and Hard Axes

This result gives us some tools for reasoning about how the magnetoelastic energy should behave under further constraints. For example, should a magnetoelastic grain be embedded in a rocky matrix of anisotropic elasticity, we should expect the magnetoelastic energy to be lower in whichever direction the material is best able to deform to the characteristic magnetoelastic deformation. This will result in an effective easy axis. Similarly, the direction of inhibition of deformation should result in an effective hard axis. This could be as simple as a material in a clamp, where the less deformable clamp results in a hard axis. This suggests the magnetoelastic behaviour of a material will be effected more by its surroundings than by its own stress or strain.

While Kittel's uniaxial result doesn't appear to hold in the current derivation, but does in experimental conditions, it is possible that this description of effective easy and hard axes is what is actually being measured in experiments. Rerunning this experiment in an infinite, anisotropic material of varying stress and elasticity could confirm this. Similarly, rerunning this with the $\frac{\partial T_i}{\partial u_j} u_j$ surface term, derived in the mechanical equations of motion, added to the magnetoelastic equations of motion could return a similar result.

Another potential source of this term is from dislocations, which act to minimize the energy due to deformation, but can couple to the magnetostrictive term. We will explore this coupling in the next chapter.

Chapter 8

Dislocations in a Magnetostrictive Theory

In this chapter, we will outline how a continuum theory of dislocations can be included in a model magnetostriction, and how the magnetostrictive effect can be used to mediate the effect of dislocations on the magnetic behaviour of a crystal. This will appear as a magnetoplastic coupling term.

I found the book by Weertman and Weertman (1992) presents a very clear introduction to plastic deformations, dislocations, and many of the concepts we'll be using here. However, it's not necessary reading, since we won't actually be deriving any of the deformations due to dislocations. We will be using results derived in other sources, particularly in van der Merwe (1950).

I haven't found the approach I take here to including dislocations and plastic deformations in the magnetostrictive energy in use in the literature, so I assume everything in this chapter is novel. However, it has been used implicitly in Fabian and Heider (1996) in treating the magnetostrictive deformation as a plastic deformation. Here, we will find that, while considering the magnetostrictive and plastic deformations separately, they will ultimately end up looking quite similar.

The use of plastic deformation to recover the uniaxial anisotropy due to uniaxial tension measures in physical experiments is a significant result. In par-

ticular, the derivation of the magnetoplastic coupling is original work. The result of finding a surface anisotropy for a magnetite-ilmenite lamellar structure, while already predicted by Shive and Butler (1969), presented here in terms of a magnetoplastic coupling is an original and significant result. Due to the success of the magnetoplastic coupling in deriving uniaxial anisotropy results — that we've seen in previous chapters can not be the result of a purely elastic coupling — I suspect the magnetoplastic coupling may be a significant part of magnetostrictive theory in the future.

8.1 Including Continuum Dislocations

One approach for including dislocations in the material is to use a continuum dislocations theory. This is the theory underpinning of Fabian and Heider's formulation of the magnetostriction. In such a theory, an intrinsic stress field $\boldsymbol{\sigma}'$ is calculated for the material at equilibrium due to dislocations within the material. Such a theory, like those presented by Kröner (Kröner 1958; Kröner 1981), and by Weertman and Weertman (Weertman and Weertman 1992), present techniques for calculating this stress field for the continuum approximation due to an arbitrary dislocation line / Burgers vector combination.

We might include this in our theory by first calculating the intrinsic stress due to dislocations for the non-magnetic material, and use include the resulting deformation into our magnetoelastic equations.

For a dislocation characterized by the Burgers vector $\vec{b}$, in a non-magnetic elastic material, we have the equations of motion

$$\int u'_i = -b_i \tag{8.1a}$$

$$\frac{1}{2}C_{ijkl}(u'_{k,l} + u'_{l,k})_{,j} = 0 \tag{8.1b}$$

$$C_{ijkl}\varepsilon'_{kl,j} = 0_i \tag{8.1c}$$

with $\varepsilon'_{kl} = \frac{1}{2}(u'_{k,l} + u'_{l,k})$ the dislocation strain. For a dislocation-free magnetic

material, we have the equations of motion

$$C_{ijkl}\varepsilon_{kl,j} + B^0_{ij,j} = 0_i \tag{8.2}$$

with $\varepsilon_{kl} = \frac{1}{2}(u_{k,l} + u_{l,k})$, the magnetic strain.

We will say the elastic deformation will tend towards the dislocation deformation in a non-magnetic material. Subtracting (8.1c) from (8.2), then, we have

$$C_{ijkl}(\varepsilon_{kl,j} - \varepsilon'_{kl,j}) + B^0_{ij,j} = 0 \tag{8.3}$$

which has a solution $\vec{u}^t$

$$\vec{u}^t = \vec{u} - \vec{u}' \tag{8.4}$$

For the dislocation stress $\boldsymbol{\sigma}'$, we will say

$$\sigma'_{ij} = C_{ijkl}\varepsilon'_{kl} \tag{8.5}$$

and for the pure elastic stress, we will say

$$\sigma_{ij} = C_{ijkl}\varepsilon_{kl} \tag{8.6}$$

Our equations of motion now read

$$\sigma_{ij,j} + B^0_{ij,j} - \sigma'_{ij,j} = 0 \tag{8.7}$$

where $\sigma_{ij,j}+B^0_{ij,j}$ represent the usual elastic and magnetoelastic term, and $-\sigma'_{ij,j}$ represents the tendency of the material to want to have the deformation that would result in the stress $\boldsymbol{\sigma}'$, as that actually represents a lower energy configuration here than the unstressed case. This also suggests a way of thinking about the magnetostrictive term, $\boldsymbol{B}^0$, as a term which shifts the equilibrium deformation away from 0. Rather than a material deforming to accommodate the magnetization, the magnetization actually changes the equilibrium spacing of the lattice, and the material is just returning to the new equilibrium spacing.

We look for solutions with varying $\boldsymbol{\varepsilon}$ and fixed $\boldsymbol{\varepsilon}'$, since the pure dislocation equations of motion, (8.1c), are dependent only on the geometry of the mate-

rial, and independent of the magnetization. We are particularly interested in energies that produce the equations of motion (8.7), and the magnetic equations of motion implied by those energies under instant elastic equilibriation.

An energy that produces the desired equations of motion is

$$f = \frac{1}{2}(\varepsilon_{ij} - \varepsilon'_{ij})C_{ijkl}(\varepsilon_{kl} - \varepsilon'_{kl}) + B^0_{ij}(\varepsilon_{ij} - \varepsilon'_{ij}) \tag{8.8}$$

in which $\boldsymbol{\varepsilon} = \boldsymbol{\varepsilon}'$ represents a minimum with respect to the elastic energy, as expected, but not with the inclusion of the magnetoelastic coupling. This approach also echoes Kröner's approach of finding equilibrium deformations after plastic deformation by reversing the incompatible plastic deformation, say ε', with an equal, but opposite elastic deformation, $-\varepsilon'$, and minimizing the compatible term, ε.

The equilibrium strain $\boldsymbol{\varepsilon}^0$ for this, away from the line of dislocation, where $\boldsymbol{\varepsilon}'$ is compatible, and for a uniform magnetization (so $\boldsymbol{S} : \boldsymbol{B}^0$ is compatible), is

$$\frac{\partial f}{\partial \varepsilon_{ij}}(\boldsymbol{\varepsilon}^0) = C_{ijkl}(\varepsilon^0_{kl} - \varepsilon'_{kl}) + B^0_{ij} = 0 \tag{8.9}$$

and multiplying across by the compliance tensor $\boldsymbol{S}$, remembering $S_{ijkl}C_{klmn} = \frac{1}{2}(\delta_{im}\delta_{jn} + \delta_{in}\delta_{jm})$

$$\varepsilon^0_{ij} = \varepsilon'_{ij} - S_{ijkl}B^0_{kl} \tag{8.10}$$

which represents an equilibrium deformation which accounts for both dislocation effects and magnetostrictive effects.

If we do the old trick of placing the equilibrium deformation into the energy, we get

$$\begin{aligned} f(\boldsymbol{\varepsilon}^0) &= \frac{1}{2}(\varepsilon^0_{ij} - \varepsilon'_{ij})C_{ijkl}(\varepsilon^0_{kl} - \varepsilon'_{kl}) + B^0_{ij}(\varepsilon^0_{ij} - \varepsilon'_{ij}) \\ &= \frac{1}{2}(-S_{ijkl}B^0_{kl})C_{ijkl}(-S_{ijkl}B^0_{kl}) + B^0_{ij}(-S_{ijkl}B^0_{kl}) \\ &= \frac{1}{2}B^0_{kl}S_{ijkl}B^0_{kl} - B^0_{ij}(S_{ijkl}B^0_{kl}) \\ &= -\frac{1}{2}B^0_{kl}S_{ijkl}B^0_{kl} \end{aligned} \tag{8.11}$$

which is independent of the deformation due to dislocations, is dependent

only on the magnetization, and is exactly the stress-free magnetostrictive result we had before. While it produces the mechanical equations of motion we want, it doesn't produce the magnetic equations of motion we might expect. We expect to find the inclusion of dislocations should produce some effect on the magnetization, as evidenced by phenomena like domain wall pinning and Barkhausen noise.

If instead, we treat the elastic and magnetoelastic components differently, despite our complaints in previous sections about other treatments doing exactly this, we can get something that works. We try

$$f = \frac{1}{2}(\varepsilon_{ij} - \varepsilon'_{ij})C_{ijkl}(\varepsilon_{kl} - \varepsilon'_{kl}) + B^0_{ij}\varepsilon_{ij} \tag{8.12}$$

noting the absence of the dependence on the equilibrium strain due to intrinsic stress on the magnetostrictive term. This energy results in the same mechanical equations of motion as our previous attempt, but crucially, different magnetic equations of motion.

This energy be physically reasoned as the magnetostrictive response depending on the deformation away from a perfect crystal lattice, and not on the actual elastic stress, strain, equilibrium strain, or any other mechanical property of the material itself. This echoes our previous suggestion that the magnetoelastic energy is a result of the magnetization changing the equilibrium lattice spacing, rather than actually introducing any sort of elastic deformation to the system itself. The dislocation deformation term then encodes the preference for the system to be away from the equilibrium lattice position, which depends on the elastic and magnetoelastic energies, to a mechanical equilibrium position due to intrinsic stress.

We find the equilibrium strain, away from the dislocation, for a uniform magnetization,

$$\begin{aligned} \frac{\partial f}{\partial \varepsilon_{ij}}(\boldsymbol{\varepsilon}^0) &= C_{ijkl}(\varepsilon^0_{kl} - \varepsilon'_{kl}) + B^0_{ij} = 0 \\ \Rightarrow \varepsilon^0_{ij} &= \varepsilon'_{ij} - S_{ijkl}B^0_{kl} \end{aligned} \tag{8.13}$$

exactly as before, and substituting back into the energy

$$\begin{aligned} f(\boldsymbol{\varepsilon}^0) &= \frac{1}{2}(\varepsilon^0_{ij} - \varepsilon'_{ij})C_{ijkl}(\varepsilon^0_{kl} - \varepsilon'_{kl}) + B^0_{ij}\varepsilon^0_{ij} \\ &= \frac{1}{2}(-S_{ijkl}B^0_{kl})C_{ijkl}(-S_{ijkl}B^0_{kl}) + B^0_{ij}(\varepsilon'_{ij} - S_{ijkl}B^0_{kl}) \\ &= -\frac{1}{2}B^0_{ij}S_{ijkl}B^0_{kl} + B^0_{ij}\varepsilon'_{ij} \end{aligned} \tag{8.14}$$

$$f = -\frac{1}{2}B^0_{ij}S_{ijkl}B^0_{kl} + B^0_{ij}\varepsilon'_{ij} \tag{8.15}$$

which now contains a $B^0_{ij}\varepsilon'_{ij}$ term, linking the magnetostriction and the deformation due to dislocations, which we will call the magneto-dislocation, or magnetoplastic coupling term. This also has the effect that the magnetic behaviour returns to the dislocation-free behaviour as $\boldsymbol{\varepsilon}' \to 0$.

In general, solutions to ε' can be quite complicated, and worse, the dislocation deformation can be quite large, nearing unity, particularly near the point of dislocation, and so, are potentially unsuitable for modelling using a linearized theory, such as the ones considered here. We can, however, get a qualitative idea of how a simple stress might effect the material.

8.2 A Model of Dislocation Mobility in Magnetoelastic Materials: Recovering Kittel's Uniaxial Stress Result

One approach to describing the plastic deformation of a material is to say it's proportional to the stress of the material. Here, however, we are interested not simply in stress-free deformations, but in deviations of the crystal lattice from a perfect lattice. We therefore describe this plastic deformation in terms of dislocation mobility.

Plastic deformation can occur when dislocations form and move in a material in a manner which minimizes the stress of the material. Their formation is

proportional to the stress of the material, and the intrinsic stress they create acts to minimize the stress of the material at the time of formation. Similarly, already formed dislocations tend to travel through the material to minimize overall stress. Since our dislocation terms have been defined to shift the equilibrium elastic stress position, we can set our dislocation terms proportional to the formational terms to achieve the desired effect.

We will therefore look at a dislocation stress, $\boldsymbol{\sigma}'$ which is proportional to the maximum stress, $\boldsymbol{\sigma}^{\max}$, such that

$$\boldsymbol{\sigma}' = \kappa\, \boldsymbol{\sigma}^{\max} \tag{8.16}$$

For a uniaxial tension, we have

$$\sigma_{ij}^{\max} = -T\gamma_i\gamma_j \tag{8.17}$$

and so

$$\sigma'_{ij} = -\kappa\, T\gamma_i\gamma_j \tag{8.18}$$

with a dislocation strain, $\boldsymbol{\varepsilon}'$ of

$$\varepsilon'_{ij} = -\kappa\, T S_{ijkl}\gamma_k\gamma_l \tag{8.19}$$

giving a magnetoplastic coupling term of

$$f = -\kappa T\; B_{ij}^0 S_{ijkl}\gamma_k\gamma_l \tag{8.20}$$

We borrow from Kittel's derivation of the uniaxial stress, considering $\boldsymbol{S}$ for an isotropic material. We will convert equation (8.20) into Voigt notation

$$f = -\kappa T\; B_i^{0,\mathrm{voigt}} S_{ij}\Gamma_j \tag{8.21}$$

with

$$\vec{B}^{0,\text{voigt}} = \begin{pmatrix} B_1\alpha_x^2 \\ B_1\alpha_y^2 \\ B_1\alpha_z^2 \\ B_2\alpha_x\alpha_y \\ B_2\alpha_y\alpha_z \\ B_2\alpha_z\alpha_x \end{pmatrix} \qquad \vec{\Gamma}^{\text{voigt}} = \begin{pmatrix} \gamma_x^2 \\ \gamma_y^2 \\ \gamma_z^2 \\ \gamma_x\gamma_y \\ \gamma_y\gamma_z \\ \gamma_z\gamma_x \end{pmatrix}$$

$$S = \begin{pmatrix} S_{11} & S_{12} & S_{12} & 0 & 0 & 0 \\ S_{12} & S_{11} & S_{12} & 0 & 0 & 0 \\ S_{12} & S_{12} & S_{11} & 0 & 0 & 0 \\ 0 & 0 & 0 & S_{44} & 0 & 0 \\ 0 & 0 & 0 & 0 & S_{44} & 0 \\ 0 & 0 & 0 & 0 & 0 & S_{44} \end{pmatrix} \tag{8.22}$$

Looking at a $B_1\alpha_x^2$ term, we have

$$\begin{aligned} &\kappa T B_1 \alpha_x^2 (S_{11}\gamma_x^2 + S_{12}(\gamma_y^2 + \gamma_z^2)) \\ &= \kappa T B_1 \alpha_x^2 (S_{11}\gamma_x^2 + S_{12}(\gamma_y^2 + \gamma_z^2 + \gamma_x^2) - S_{12}\gamma_x^2) \\ &= \kappa T B_1 \alpha_x^2 ((S_{11} - S_{12})\gamma_x^2 + S_{12}) \\ &= \kappa T B_1 (S_{11} - S_{12})\alpha_x^2\gamma_x^2 + \kappa T \alpha_x^2 S_{12} \end{aligned} \tag{8.23}$$

since $\gamma_x^2 + \gamma_y^2 + \gamma_z^2 = 1$, because $\vec{\gamma}$ is a directional cosine.

Combining the α_x^2, α_y^2, and α_z^2 terms, we get

$$\begin{aligned} &\kappa T B_1 (S_{11} - S_{12})\alpha_x^2\gamma_x^2 + \kappa T \alpha_x^2 S_{12} \\ &+\kappa T B_1 (S_{11} - S_{12})\alpha_y^2\gamma_y^2 + \kappa T \alpha_y^2 S_{12} \\ &+\kappa T B_1 (S_{11} - S_{12})\alpha_z^2\gamma_z^2 + \kappa T \alpha_z^2 S_{12} \\ &= 3\kappa T B_1 S_{12} + \kappa T B_1 (S_{11} - S_{12})(\alpha_x^2\gamma_x^2 + \alpha_y^2\gamma_y^2 + \alpha_z^2\gamma_z^2) \end{aligned} \tag{8.24}$$

since $\alpha_x^2 + \alpha_y^2 + \alpha_z^2 = 1$. Since $3\kappa T B_1 S_{12}$ is a constant, independent of the magnetization, or the direction of applied stress, we can drop it.

Finally, adding in the $\alpha_i\alpha_j\gamma_i\gamma_j$ terms, we get the expanded energy

$$\begin{aligned} f = &- \kappa T B_1 (S_{11} - S_{12})(\alpha_x^2\gamma_x^2 + \alpha_y^2\gamma_y^2 + \alpha_z^2\gamma_z^2) \\ &- \kappa T B_2 S_{44}(\alpha_x\alpha_y\gamma_x\gamma_y + \alpha_y\alpha_z\gamma_y\gamma_z + \alpha_z\alpha_x\gamma_z\gamma_x) \end{aligned} \tag{8.25}$$

This energy is what Kittel found, and used to derive his uniaxial term. Using that, we can write the magnetoplastic coupling energy

$$f = \frac{3}{2}\kappa\lambda T \sin^2\theta \tag{8.26}$$

where λ is the isotropic magnetostriction constant, and θ is the angle between the magnetization and the tension.

This recovers Kittel's uniaxial energy result, as seen in experimental data. Indeed, it describes the residual effective uniaxial anisotropy seen in samples after crushing. Our approach, however, derives it as a result of internal stresses due to dislocations. A similar result should hold for an embedding in a larger elastic material where the equilibrium elastic state has the magnetic material under a uniaxial tension, as seen in e.g. magnetic fabrics. It is important to note, however, that Kittel's formulation is not, by itself, enough to generate this result, as proven in section 5.1.2. An addition, such as the addition of crystal defects made here, is necessary to recover this result.

8.3 A Model of Magnetostriction at a Magnetite-Ilmenite Boundary

We take, for example, the interface between two materials of differing lattice sizes, such as in magnetite and ilmenite lamellae. A treatment of this boundary has been done by Shive and Butler (1969) using a treatment by van der Merwe (1950) for finding the optimum insertion of edge dislocations to minimize lattice misfit. Here, however, we will return to Merwe's treatment for the

mathematics, and use Shive and Butler's treatment for where the edge dislocations should be placed, and derive the strains ourselves. We will then find the average strain near the surface of the material, and determine the behaviour of the magnetization near the surface.

In van der Merwe (1950), dislocations in the xy-plane of an isotropic material are considered. The dislocation line is in the positive y direction and the Burgers vector in the positive x direction. He puts the material of larger lattice constant into the positive z direction. We will use this [001] formulation, along with the isotropic elastic constants presented by Shive and Butler (1969), and later rotate it into the proper [111] orientation to match the magnetite-ilmenite interface plane.

To present the displacements to edge dislocations due to lattice misfit by van der Merwe, we first need to present a number of prerequisite values. We have a and b, the lattice constants, with $a < b$. In our case, a is for ilmenite and $a = 1.34 \times 10^{-10}$ m, and b is for magnetite and $b = 1.48 \times 10^{-10}$ m. The value P is an integer value such that $Pb = (P + 1)a$. In our case, we will say $Pb \sim (P+1)a$, and so, $P = 10$. Next, we have the average lattice constant c such that $(P + \frac{1}{2})c = Pb$. This also acts as the Burgers vector of the edge dislocation where the Burgers vector in an edge dislocations. We have the wall spacing $p = Pb$ representing the spacing between edge dislocations. The value d represents the equilibrium separation between atoms in the magnetite plane and the ilmenite plane. Finally ζ is equivalent to the z coordinate, but measured from the first atom in the magnetite, a distance $d/2$ into the magnetite. In (van der Merwe 1950), he also introduces a number of variables which keep the equations relatively clean. We will present the relevant variables, along with the ones we've just described beside the displacement, (u_x^0, u_y^0, u_z^0), as presented in

his paper for the magnetite phase which extends from $\zeta = 0$ to $\zeta = +\infty$

$$a = 1.34 \times 10^{-10} \tag{8.27a}$$

$$b = 1.48 \times 10^{-10} \tag{8.27b}$$

$$P = 10 \tag{8.27c}$$

$$p = Pb = 1.48 \times 10^{-9} \tag{8.27d}$$

$$c = \frac{P}{P + \frac{1}{2}} b = 1.4067 \times 10^{-10} \tag{8.27e}$$

$$\mu = \mu_0 = 0.95 \times 10^{11} \tag{8.27f}$$

$$\nu = 0.28 \tag{8.27g}$$

$$\beta = \frac{\pi \mu c}{p \mu_0 (1 - \nu)} \tag{8.27h}$$

$$A = \sqrt{1 + \beta^2} - \beta \tag{8.27i}$$

$$X = \frac{2\pi x}{p} \tag{8.27j}$$

$$Z = \frac{2\pi \zeta}{p} \tag{8.27k}$$

$$R = \sqrt{1 + A^2 e^{-2Z} - 2Ae^{-Z} \cos(X)} \tag{8.27l}$$

$$u_x^0 = \frac{c}{2\pi} \tan^{-1}\left(\frac{Ae^{-Z} \sin(X)}{1 - Ae^{-Z} \cos(X)}\right) - \frac{cZe^{-Z} \sin(X)}{4\pi(1 - \nu)R^2} \tag{8.27m}$$

$$u_y^0 = 0 \tag{8.27n}$$

$$u_z^0 = \frac{(1 - 2\nu)c}{4\pi(1 - \nu)} \ln\left(\frac{R}{1 - A}\right) - \frac{cZAe^{-Z}(\cos(X) - Ae^{-Z})}{4\pi(1 - \nu)R^2} \tag{8.27o}$$

where care must be taken in a magnetic context that μ_0 is not the permittivity of free space, but rather an elastic constant dependent on the specifics of the interfacing materials. For simplicity, we set it to the value of magnetite when inside the magnetite region.

From Shive and Butler (1969), on the magnetite-ilmenite boundary, there is a rotational symmetry of $\pi/3$, so the edge dislocations are likely to occur along three lines from the position, say, $(x, y, z) = (0, 0, 0)$. We therefore need to rotate the displacements and coordinates to model these extra walls. The standard

rotation matrix in the xy-plane will work here

$$\Theta^{xy}(\theta) = \begin{pmatrix} \cos(\theta) & \sin(\theta) & 0 \\ -\sin(\theta) & \cos(\theta) & 0 \\ 0 & 0 & 1 \end{pmatrix} \tag{8.28}$$

To rotate the displacements, we will use the relation

$$\begin{aligned} u_i^\theta(\vec{x},\theta) &= \Theta^{xy}(\theta)_{ij} u_j((\Theta^{xy}(\theta))^T_{kl} x'_l) \\ &= \Theta^{xy}(\theta)_{ij} u_j(\Theta^{xy}(-\theta)_{kl} x'_l) \end{aligned} \tag{8.29}$$

noting the transpose of the rotation matrix is $(\Theta^{xy}(\theta))^T = \Theta^{xy}(-\theta)$. For magnetite with a $\pi/3$ rotational symmetry, we have

$$\vec{u}(\vec{x}) = \vec{u}^\theta(\vec{x},0) + \vec{u}^\theta(\vec{x},\frac{\pi}{3}) + \vec{u}^\theta(\vec{x},-\frac{\pi}{3}) \tag{8.30}$$

Already, this contains too many terms to deal with directly. Indeed, derivatives and plotting of the equations presented here was done symbolically and numerically in Mathematica.

As usual, the strain can be defined

$$\varepsilon'_{ij}(\vec{x}) = (u_{i,j} + u_{j,i})/2 \tag{8.31}$$

Figure 8.1 shows the magnitude of the strains in the plane $\zeta = 0$ described by the equations presented.

As can be seen from figure 8.1, there are regions of very large strain. Indeed, this can be seen from the dislocations, but it is much clearer from the presented image. In these regions, the assumptions of linear elasticity and of linear magnetostriction of small displacements break down. In particular, in these regions, the values tend towards infinity. We want to take an average of the strain over some small region near the interface surface to incorporate the elastic strains into a continuum theory on the same order of approximation as the magnetic continuum theory. However, the large values near the disloca-

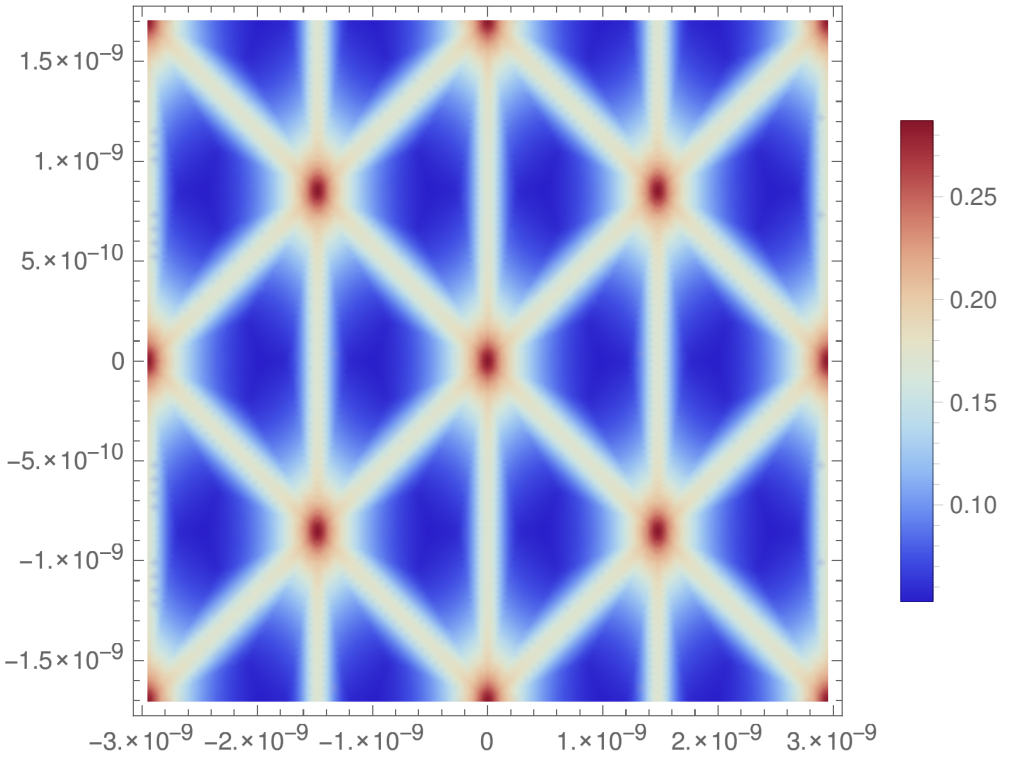

Figure 8.1: The magnitude of the strain, $|\varepsilon'|$, due to dislocation walls due to lattice misfit in the plane $\zeta = 0$ in the magnetite phase.

tion wall contribute significantly to the resulting average, while effecting only a region of around 10% of all the atoms. To that end, we will simply exclude a region extending a distance b from either side of the wall in the xy-plane, and a distance b extending into the material, and assume our values are at least 10% off. This should exclude the atoms in the edge dislocation and their immediate neighbours. The region outside the domain wall and neighbouring atoms can be described by the Boolean function

$$\begin{aligned}\Xi_B(x,y,z) = \big(& \\ & (\cos(\frac{2\pi}{b}x) < \cos\frac{2\pi b}{p}) \\ \&\& \quad & (\cos(\frac{2\pi}{b}(x\cos(\pi/3) + y\sin(\pi/3)) < \cos\frac{2\pi b}{p}) \\ \&\& \quad & (\cos(\frac{2\pi}{b}(x\cos(-\pi/3) + y\sin(-\pi/3)) < \cos\frac{2\pi b}{p}) \\ \big) \;||\quad & z > a\end{aligned} \tag{8.32}$$

and the windowing function is given

$$\Xi(x,y,z) = \begin{cases} 1 & \text{if } \Xi_B(x,y,z) == \texttt{True} \\ 0 & \text{if } \Xi_B(x,y,z) == \texttt{False} \end{cases} \tag{8.33}$$

The average of the strain is then found using

$$\langle \varepsilon' \rangle = \frac{\int_\Omega \varepsilon' \, \Xi \, dV}{\int_\Omega \, dV} \tag{8.34}$$

We must now determine an appropriate region of integration. From inspection of figure 8.1, the period in the x direction is not p, the distance between the walls, but 2 p, the distance between intersecting walls, punctuated by red "dots". The x range can, therefore, be $x \in [-p, p]$. It can be shown that the distance between red dots in the y direction is $\frac{2p}{\sqrt{3}}$. The y range can be set to $y \in [-\frac{p}{\sqrt{3}}, \frac{p}{\sqrt{3}}]$.

We will look at the purely surface effect, setting $\zeta = 0$ and $\Omega = [-p, p] \times [-p/\sqrt{3}, p/\sqrt{3}]$. The integration is done using Mathematica's `NIntegrate`

function. For the given values, we get

$$\langle \varepsilon' \rangle = \begin{pmatrix} -0.0192251 & 2.199979 \times 10^{-7} & -1.03469 \times 10^{-9} \\ 2.19979 \times 10^{-7} & -0.0192144 & 3.0011 \times 10^{-10} \\ -1.03469 \times 10^{-9} & 3.0011 \times 10^{-10} & 0.0149415 \end{pmatrix} \tag{8.35}$$

This shows a compression in the xy-plane, and a stretching in the z-direction, which is what we would expect. We note the values of $\langle \varepsilon'_{xx} \rangle$ and $\langle \varepsilon'_{yy} \rangle$ are equal to within 0.1%, and the off diagonal terms are approximately zero.

We now need to rotate this strain tensor to the correct orientation, from $[001]$ to $[111]$. For a rotation matrix Φ, the rotated strain tensor ε'' can be found by

$$\varepsilon''_{ij} = \Phi_{ik} \varepsilon'_{kl} \Phi^T_{lj} \tag{8.36}$$

For our transformation, after rotation, the z direction, $[001]$, needs to point in the $[111]$ direction. Then

$$\begin{aligned} \mathbf{\Phi} \cdot (0,0,1) &= (\frac{1}{\sqrt{3}}, \frac{1}{\sqrt{3}}, \frac{1}{\sqrt{3}}) \\ \Rightarrow (\Phi_{13}, \Phi_{23}, \Phi_{33}) &= (\frac{1}{\sqrt{3}}, \frac{1}{\sqrt{3}}, \frac{1}{\sqrt{3}}) \end{aligned}$$

Next, we align the x direction with the projection of the x direction in the $[111]$ plane. The projection of a vector $\vec{x}$ into a plane with normal $\vec{n}$ can be given $\vec{v}_\perp = \vec{v} - (\vec{v} \cdot \hat{n})\,\hat{n}$. In our case, we have $\vec{v} = (1,0,0)$, $\hat{n} = \texttt{norm}(1,1,1) = \frac{1}{\sqrt{3}}(1,1,1)$ and need $|v_\perp| = 1$, so

$$\begin{aligned} \mathbf{\Phi} \cdot (1,0,0) &= \texttt{norm}((1,0,0) - \frac{1}{\sqrt{3}}((1,0,0) \cdot (1,1,1))\frac{1}{\sqrt{3}}(1,1,1)) \\ \Rightarrow (\Phi_{11}, \Phi_{21}, \Phi_{31}) &= (\frac{2}{\sqrt{6}}, -\frac{1}{\sqrt{6}}, -\frac{1}{\sqrt{6}}) \end{aligned}$$

And finally, we find the vector perpendicular to $(1,1,1)$ and $(\frac{2}{\sqrt{6}}, -\frac{1}{\sqrt{6}}, -\frac{1}{\sqrt{6}})$ A cross product will give us this. The correct choice between $\vec{y}' = \vec{x}' \times \vec{z}'$ and $\vec{y}' = \vec{z}' \times \vec{x}'$ can be found from $\det(\Phi) = +1$ for a rigid body rotation. This

gives us $\vec{y}' = \vec{z}' \times \vec{x}'$. The wrong choice would give $\det(\Phi) = -1$, which would imply one of the axes has also been mirrored.

We have

$$\begin{aligned} \mathbf{\Phi} \cdot (0,1,0) &= (\frac{1}{\sqrt{3}}, \frac{1}{\sqrt{3}}, \frac{1}{\sqrt{3}}) \times (\frac{2}{\sqrt{6}}, -\frac{1}{\sqrt{6}}, -\frac{1}{\sqrt{6}}) \\ \Rightarrow (\Phi_{12}, \Phi_{22}, \Phi_{32}) &= (0, \frac{1}{\sqrt{2}}, -\frac{1}{\sqrt{2}}) \end{aligned}$$

All together, this gives

$$\Phi = \begin{pmatrix} \frac{2}{\sqrt{6}} & 0 & \frac{1}{\sqrt{3}} \\ -\frac{1}{\sqrt{6}} & \frac{1}{\sqrt{2}} & \frac{1}{\sqrt{3}} \\ -\frac{1}{\sqrt{6}} & -\frac{1}{\sqrt{2}} & \frac{1}{\sqrt{3}} \end{pmatrix} \tag{8.37}$$

and so, the correctly oriented average strain $\langle \varepsilon'' \rangle$ is

$$\langle \varepsilon'' \rangle = \begin{pmatrix} -0.00783619 & 0.011389 & 0.0113887 \\ 0.011389 & -0.007831 & 0.0113836 \\ 0.0113887 & 0.0113836 & -0.00783075 \end{pmatrix} \tag{8.38}$$

We plot the energy surface of the magnetoplastic coupling energy

$$f = B^0_{ij} \langle \varepsilon''_{ij} \rangle \tag{8.39}$$

at the magnetite-ilmenite boundary in figure 8.2. The maximum and minimum values found for this energy are

$$\begin{aligned} \max f &= \quad 2.26 \times 10^5 \\ \min f &= -5.69 \times 10^5 \end{aligned} \tag{8.40}$$

giving the range $\Delta f = 7.95201 * 10^5$.

The image in 8.2 looks like a uniaxial anisotropy $K \sin(\theta)$ with positive anisotropy constant and axis in the $[111]$ direction. We have for our $\langle \varepsilon'' \rangle$ that

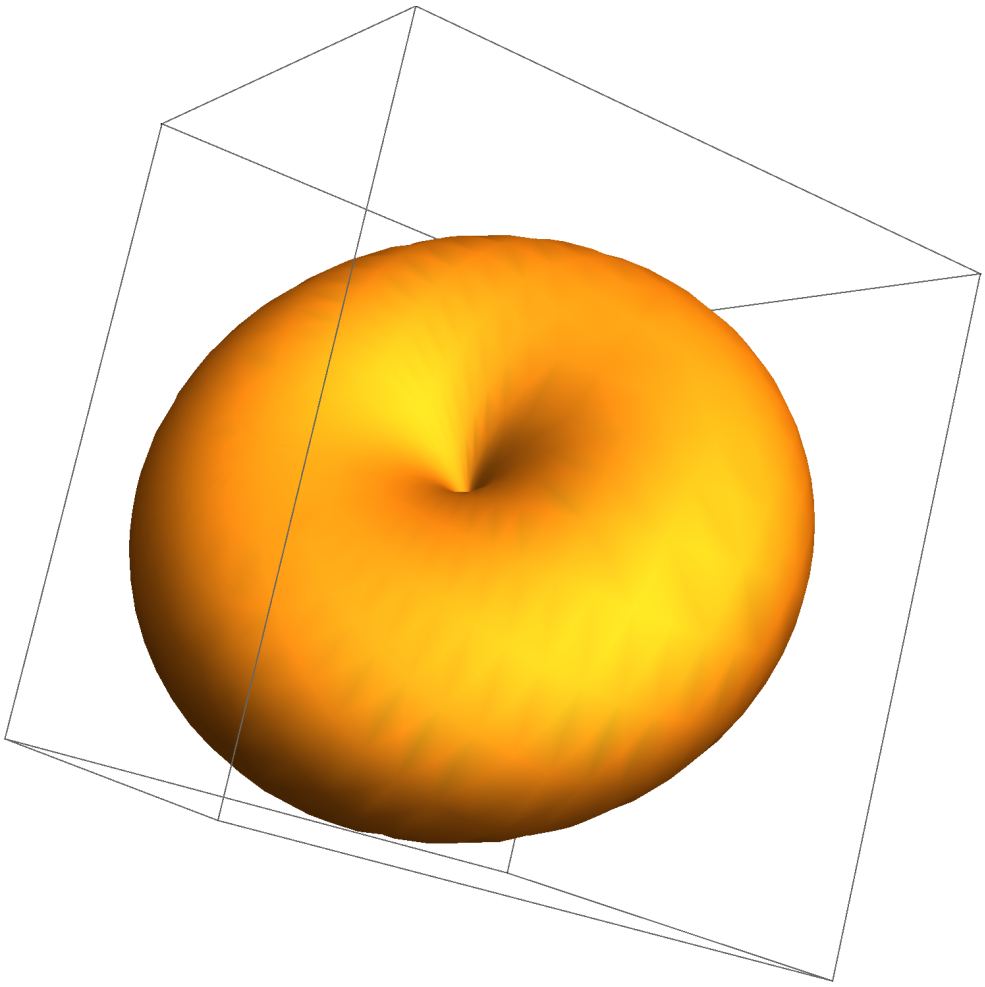

Figure 8.2: Energy surface of the magnetoplastic coupling energy at the magnetite-ilmenite boundary.

the diagonal terms $\langle \varepsilon''_{ii} \rangle$ all have nearly the same value ε_1, and the diagonal terms $\langle \varepsilon''_{ij} \rangle$ have nearly the same value ε_2. From this (remembering $|m| = 1 \Rightarrow \sum_i m_i^2 = 1$)

$$\begin{aligned} f &= B_1(\sum_i m_i m_i)\varepsilon_1 + B_2(\sum_{i \neq j} m_i m_j)\varepsilon_2 \\ &= B_1\varepsilon_1 + B_2(\sum_{i \neq j} m_i m_j)\varepsilon_2 \end{aligned} \tag{8.41}$$

we drop the term independent of $\vec{m}$, $B_1\varepsilon_1$, and add a constant term independent of $\vec{m}$, $B_2\varepsilon_2$

$$\begin{aligned} f &= B_2\varepsilon_2 + B_2(\sum_{i,j} m_i m_j)\varepsilon_2 \\ &= B_2(\sum_i m_i m_i)\varepsilon_2 + B_2(\sum_{i \neq j} m_i m_j)\varepsilon_2 \\ &= B_2(\sum_i m_i)(\sum_j m_i)\varepsilon_2 \\ &= B_2\left(\sqrt{3}\,\vec{m} \cdot (\frac{1}{\sqrt{3}}, \frac{1}{\sqrt{3}}, \frac{1}{\sqrt{3}})\right)^2 \varepsilon_2 \\ &= 3B_2\varepsilon_2 \cos^2(\alpha) \end{aligned} \tag{8.42}$$

where α is the angle of the magnetization wrt the uniaxial axis, $[111]$ in this case. Indeed, the value $3B_2\varepsilon''_{xy} = -7.95408 \times 10^5$ has the same magnitude as Δf to within 0.1%, and the correct sign for the magnetization aligned with the $[111]$ direction to represent an energy minimum. It is likely an exact integration of the region would result in the off-diagonal entries being more similar, and the values for $3B_2\varepsilon''_{xy}$ and Δf would match more closely.

Finally, we can say, for the magnetite-ilmenite boundary, where the strain $\varepsilon_{ij} = \varepsilon_2$ for $i \neq j$, that

$$f = 3B_2\varepsilon_2 \cos^2(\alpha) \tag{8.43}$$

8.3.1 Discussion

To recap, we derived the strain for the magnetite-ilmenite boundary for a $[100]$ orientation, averaged the strain over one period of the strain in the x and y directions at the interface and then rotated it to the correct $[111]$ orientation,

matching the expected lamellar interface orientation. From here, we noted that the magnetoplastic coupling energy depends only on the off-diagonal magnetostrictive coupling term and the off-diagonal strain term, and the squared cosine of the angle between the magnetization and the interface normal. This looks exactly like a uniaxial anisotropy with the coupling constant $K_{u\lambda} = 3B_2\varepsilon_2$. For the magnetite-ilmenite boundary, this value is $K_{u\lambda} = -7.954 \times 10^5$.

Comparing this value to the effective cubic anisotropy coupling constant for magnetite, including the uniform magnetostrictive response, which has the value $K_1 + K_\lambda = -1.326580 \times 10^4$, we see the effective uniaxial coupling due to the magnetoplastic coupling energy is approximately 10 times larger than the cubic anisotropy. This suggests the uniaxial anisotropy energy should dominate at the ilmenite-magnetite boundary, with the easy axis pointing normal to the interface boundary. The magnetoplastic anisotropy coupling drops exponentially with distance from the interface boundary. However, the uniaxial preference at the boundary of the material should be enough to break the cubic symmetry of the magnetite throughout the material via coupling with the exchange energy. The magnetization at the surface will prefer to point along the interface normal, and neighbouring magnetizations will prefer to point in the direction of their neighbours, and so on.

A magnetite-ilmenite lamellar structure should, therefore, experience a preference to magnetize parallel to the axis of the system. This is, indeed, seen in measurements made by N. Church during his PhD in which a magnetite-ilmenite structure tended to magnetize along the system axis. This chapter stands as a potential explanation for that phenomenon.

Chapter 9

Conclusions - Magnetostriction

One significant point demonstrated by this section of this thesis is that, even for a uniformly magnetized material, Kittel's equations for the effective magnetostrictive anisotropy due to a uniaxial tension cannot be correct. When under a fixed stress, the elastic terms and the magnetic terms in Kittel's formulation completely decouple. This was further cemented in the simulations performed for grains with free boundaries and fixed surface tension, where any applied surface tension resulted in exactly the same behaviours as the tension-free simulations. The simulations make no particular changes to Kittel's formulation of the energy, they simply find the deformation that minimizes the energy for the given magnetization. The two-factor proof, both from the mathematics and simulation results, mean Kittel's theory for the effective uniaxial anisotropy under uniaxial tension should no longer be used.

The chapter on including plastic deformations goes a long way towards recovering the uniaxial results. Specifically, the magnetoplastic coupling successfully predicts effective uniaxial anisotropies in situations of uniaxial internal stress. This is particularly important, as the uniaxial result is a well studied and commonly measured phenomenon in physical samples. Considering the power of the plastic deformation model to recover the results we had just proven were not a result of a pure magnetoelastic theory, this is a significant contribution to our understanding of magnetostrictive effects. Indeed, I think any recovery of the uniaxial results will be, at the very least, expressible in

terms of a magnetoplastic coupling.

The inclusion of a FEM magnetostriction solver into MERRILL represents a significant step towards accurate measurements for highly magnetostrictive materials like titanomagnetites. In particular, the compatibility between the magnetostriction solver and the nudged elastic band code in MERRILL means the stability of titanomagnetites can be accurately predicted. Again, this would go a long way towards reliable measurements of some of the oldest recordings of the Earth's magnetic field. The preliminary modelling results presented here for various geometries of titanomagnetite show that the KCS and KME approaches produce different critical grain sizes and slightly different saturation magnetizations — i.e. they behave differently, so KCS results may not be reliable. Further work must be done in this area to determine the particular effect this has on the stability of the grains, and the effect on less magnetostrictive materials. The only reason it wasn't done here was due to time constraints.

It should be noted that simulations of highly magnetostrictive materials simply aren't possible without a KME solver. A number of KME solver exist (e.g. Azoum, Besbes, and Bouillault (2004) and Azoum, Besbes, Bouillault, and Ueno (2006)), but no FEM solvers for arbitrary magnetizations which produce effective fields, and nothing fully integrated with a micromagnetics package like MERRILL. In particular, I am not aware of any other formulations of a magnetostrictive solver that explicitly includes time, which makes clear the assumptions made about relaxation times when finding solutions. Further, I've seen no attempts made to derive effective fields that represent what a magnetization might experience on the scale of the magnetic relaxation time, like we saw our uniform magnetization experiments in chapter 7.

The particular formulation presented in chapter 6 also makes it possible to see the deformation due to magnetostriction for non-uniform magnetizations. As an interesting example found here, the twisted deformation found for single vortex states echoes the Wiedemann effect. This is a good sign that the implementation presented here is correct. In particular, the Wiedemann effect is where a grain assumes a twisted deformation when exposed to a helical magnetic field. Indeed, a helical field in a paramagnetic grain would induce a magnetization similar in shape to a single vortex. This could be a promis-

ing route for direct comparison of the theoretical predictions made here for deformations due to non-uniform magnetizations.

The inclusion of magnetoelasticity in MERRILL, and the theory of magneto-plastic deformation represents a significant step towards accurate modelling of multi-phase materials. As previously mentioned, the most common measurements of magnetic materials made for GeoSciences applications, are of multi-phase materials. The multi-phase aspect and deformations of these materials is very often over-simplified or simply ignored. We can now fully model materials taking the mechanical deformation and interactions of their crystal lattices into account.

For core-shell grains of magnetite-maghemite, for example, the interaction of two incompatible lattices means an accurate FEM simulation would involve multi-phase micromagnetic FEM (solved in chapter 2), magnetostriction FEM (solved in chapter 6), edge dislocations on the interface (effective anisotropy derived in chapter 8), and determining the magnetic parameters in the interface region (left as an exercise for the reader).

At the closing of this part of the thesis, we are now in a good position, moving forward, to add all the necessary physics to micromagnetic models for fully describing the sorts of irregularly shaped, imperfect, multi-phase materials encountered in typical geophysical settings.

Part III

Electron Holography

Chapter 10

Electron Holography

Electron holography is an imaging technique that can extract magnetic information from a material at a nanometer scale. This is a particularly promising avenue for direct comparisons of experimental measurements and modelling results. This has already been done and published (Almeida et al. 2016) using the same simulation software, HoloMag, I wrote during my studentship, and was used to generate the results presented in this part of the thesis.

In this chapter, we will outline some mathematical results, primarily as presented by Keimpema (Keimpema, De Raedt, and De Hosson 2006), and present methods for using them to produce simulated holography images for micromagnetic models. We will also present some example holography images. By having a full picture of the magnetization, along with the accompanying electron hologram, we can paint a picture of how various magnetic structures contribute to electron holograms, some of the potential pitfalls when interpreting holography images, and how they might be mitigated.

While the idea to use a tessellation of boxes to approximate the magnetization to calculate the electron hologram is not an original idea, the specific derivations presented here using Keimpema's solutions for a uniformly magnetized brick are original. In particular, the approximation of the solutions near the box edges, suitable for numerical simulation. The derivation of the projection formulation, however, is entirely original work.

10.1 Background

Here we will present how the phase of an electron changes as it passes through a magnetic field, and how that translates to an electron hologram. Much of this is presented much better elsewhere, particularly in (Keimpema, De Raedt, and De Hosson 2006), (Keimpema 2008), and (Lehmann and Lichte 2002).

In electron holography, a point source, as in a Transmission Electron Microscope (TEM) generates an electron potential in the form of a plane wave from the source to the image plane. This wave is then considered in two halves. One half, say the left half from the point of view of an observer, will pass through a magnetized sample. We will refer to this as the probe wave. The other half, the right half, will not. This will be called the reference wave. For ease of thought, we can imagine these two waves are separated and moved far away from each other. After the probe wave has passed through the sample, the probe wave and the reference wave are moved such that they're overlapping, typically by passing them through a "Lorentz lens". When the overlapped wave is imaged, say by counting incident electrons on a CCD, it produces an interference pattern.

The interference pattern arises due to the way electric and magnetic fields effect the phase of an electron, and an electron wave.

The phase change of an electron as it travels along a path can be derived using the Klein Gordon equation. We won't go into it here, as delving into quantum mechanics is, perhaps surprisingly for this thesis, an unnecessary extra complication. A brief treatment, and presentation of many of the initial results used here can be found in Keimpema, De Raedt, and De Hosson (2006). The result using the Klein Gordon equation appears to differ from the Hamiltonian formulation used in the original Aharonov and Bohm (1959) paper by a factor of c, the speed of light. This could be an artefact of using "natural units" in Aharonov and Bohm (1959), where c is set to 1, and the other units are scaled to allow for this. This allows Aharonov and Bohm (1959) to quickly apply a relativistic generalization to derive the magnetic part. However, it is then difficult to see where c would be reintroduced. On the other hand, the Klein-Gordon formulation is defined relativistically from the ground up using

SI units. I decided not to investigate much further, and accept the SI formulation in Keimpema, De Raedt, and De Hosson (2006).

It can be shown that the phase, ϕ, of an electron travelling along a path L, parameterized by

$$\vec{l}(s) = (l_1(s), l_2(s), l_3(s)) \ , \quad s \in [0, 1] \tag{10.1}$$

can be written in terms of the magnetic vector potential, $\vec{A}$, that it passes through, and ignoring the contribution from any electric potential

$$\phi = -\frac{q}{\hbar} \int_L A_i \cdot \hat{l}_i \cdot dl \tag{10.2}$$

where q is the electron charge, and $\hbar$ is the reduced Planck constant. It can also be shown that the wave function for an electron travelling along the path L, using the integral above, can be written

$$\psi(\vec{l}(1)) = \psi(\vec{l}(0))\, e^{-i\phi} \tag{10.3}$$

which is equivalent to the wave at the point $\vec{l}(0)$, but with only a change in its phase. In this manner, it is clear that, since the magnetic vector potential experienced by the probe and reference waves as they travel from their source to the image plane is different, the phase of each electron wave at the point they are overlapped is different. We therefore expect this phase difference to produce an interference pattern.

From quantum mechanics, it can be shown that the probability of measuring an electron at a point $\vec{x}$, represented by a complex valued wave function ψ, assuming ψ has been normalized, is

$$P(\psi(\vec{x})) = |\psi(\vec{x})|^2 \tag{10.4}$$

with $|\cdot|$ the complex absolute value with

$$\begin{aligned} z &= a + ib \\ \Rightarrow |z| &= z\bar{z} = (a + ib)(a - ib) = \sqrt{a^2 + b^2} \end{aligned}$$

For a wave representing a single electron, as in our problem, and writing $\psi(\vec{l}(0)) = \psi_0$ we have

$$P(\psi(\vec{l}(1))) = |\psi(\vec{l}(0))\, e^{-i\phi}|^2 = |\psi_0|^2 \tag{10.5}$$

since $|e^{i\alpha}| = 1$. This simply represents the amplitude of the wave function, and ignores any change in the electron phase over space or time.

When the wave function consists of two overlapping electron waves, ψ_1 and ψ_2, as in our example, which travel along paths L_1 and L_2, parameterized by $\vec{l}_1(s)$ and $\vec{l}_2(s)$ respectively, which have the same start and end point, and have phase changes of ϕ_1 and ϕ_2, we have $\psi = \psi_1/2 + \psi_2/2$ and, again assuming ψ_0 is properly normalized,

$$\begin{aligned}
P(\psi(\vec{l}(1))) &= \frac{1}{4}|\psi_1(\vec{l}_1(1)) + \psi_2(\vec{l}_2(1))|^2 \\
&= \frac{1}{4}|\psi_0\, e^{-i\phi_1} + \psi_0\, e^{-i\phi_2}|^2 \\
&= \frac{1}{4}|\psi_0|^2\, |\cos(-\phi_1) + i\sin(-\phi_1) + \cos(-\phi_2) + i\sin(-\phi_2)|^2 \\
&= \frac{1}{4}|\psi_0|^2 \big(\cos(-\phi_1)^2 + \cos(-\phi_2)^2 + 2\cos(-\phi_1)\cos(-\phi_2)^2 \\
&\qquad + \sin(-\phi_1)^2 + \sin(-\phi_2)^2 + 2\sin(-\phi_1)\sin(-\phi_2)\big) \\
&= \frac{1}{4}|\psi_0|^2\big(2 + 2\cos(-\phi_1)\cos(-\phi_2) + 2\sin(-\phi_1)\sin(-\phi_2)\big) \\
&= \frac{1}{2}|\psi_0|^2\big(1 + \cos(-\phi_1 - \phi_2)\big) \\
&= \frac{1}{2}|\psi_0|^2\big(1 + \cos(\phi_1 + \phi_2)\big)
\end{aligned} \tag{10.6}$$

In our case, we can use L_1 to refer to the probe beam path and ψ_1 to refer to the probe beam, and L_2 to refer to the reference beam path and ψ_2 to refer to the reference beam. From here, we can see the probability of measuring an electron at the image plane is related to the cosine of the phase shifts of the probe and the reference waves.

Now, if we describe the magnetic vector potential, $\vec{A}$, using the Coulomb gauge condition, we have that $\vec{A} = 0$ at infinity. If we assume, then, the reference wave stays far from the magnetic region at all times, infinitely far, in fact, we

can say that $\vec{A} = 0$ in L_2, and so A_i in the integrand of (10.2) is uniformly zero, so the phase change ϕ_2 is zero. This also assumes that the electron source and the image plane are also infinitely far away from the magnetic material, since the start and end points of the two paths are the same. This actually suits the assumptions we will be making about the setup. We then get the probability of measurement is entirely due to the probe wave

$$P(\psi(\vec{x})) = \frac{1}{2}|\psi_0|^2(1 + \cos(\phi_1)) \tag{10.7}$$

When an image is taken of this overlapping wave function, the "brightness" of each pixel is proportional to the probability of measuring an electron at that point. As can be seen from the probability function described here, that probability is a product of both the electron phase, but also the amplitude. In our treatment, we neglect absorption of the electron beam by the sample, but this is an important consideration in experiments. There are a number of techniques used to separate the cosine contribution from the amplitude in experimental data. A commonly used one is Off-Axis Holography, which involves using Fourier Transforms to separate the phase varying factor from the constant amplitude factor. The details of this won't be discussed here, but these methods produce a 2D image of the $\cos(\phi_1)$ term for each L_1 travelling from the TEM source to the given pixel. This is the value we will be most interested in simulating, as this is what is typically presented in publications.

10.2 Tessellation Formulation

Outline:
We will now seek a formulation of the phase shift ϕ which makes reference only to the magnetization, M, of a material. We will take an integral-form solution of the phase shift from integral-form solutions to the Maxwell equations, and discretize them into a sum over contributions from uniformly magnetized boxes with closed, analytic solutions.

We will then resolve potential issues with the solutions near the sides and the corners of the boxes, and present a function which should work well in a computer implementation.

We will then show how to find the magnetization of these boxes.

This will be done with the aim of generating electron holograms of results from micromagnetic models. Given the simulated phase shift, we can then take the cosine to generate our simulated electron hologram.

We assume the TEM setup is as follows: The electron source is at a point $l(0) = (x, y, -\infty)$ and the image plane is at a point $l(1) = (x, y, +\infty)$. This implies that the source is at a different point for different parts of the electron wave. Indeed, the assumption we make here is that the electron wave begins as a plane wave. This can be reconciled with a point source by assuming the electron wave spreads out into a plane wave at a distance very far from the magnetic source where $\vec{A}$ is still effectively zero. We will then look at the phase change in the electron wave at a single point as it travels in a straight line from $(x, y, -\infty)$ to $(x, y, +\infty)$.

The integral over the line L_1 now represents an integral along the z-axis with $z \in [-\infty, \infty]$, and $\hat{l}$ is $\hat{z}$. The phase integral becomes

$$\phi_1(x, y) = -\frac{q}{\hbar} \int_{-\infty}^{\infty} A_z(x, y, z)\, dz \tag{10.8}$$

As previously mentioned, we will use the Coulomb gauge, where we can write

solutions to the Maxwell equations in a static, charge-free region

$$\begin{aligned} \vec{A}(\vec{x}) &= \vec{\nabla} \times \int_{\Omega} \frac{\vec{M}(\vec{x}\,')}{4\pi|\vec{x}' - \vec{x}|}\, dV' \qquad \text{in } \Omega \\ \partial_i A_i &= 0 \qquad \text{in } \Omega \\ A_i &= 0_i \qquad \text{in } \partial\Omega \end{aligned} \tag{10.9}$$

where $\vec{M}$ is the magnetization, and the domain Ω is over the whole magnetic material.

We will approximate the domain Ω by a tessellation of non-overlapping, axis-aligned cuboidal regions, denoting them with a box $\square_i$, with

$$\begin{aligned} \Omega &= \bigcup_i \square_i \\ i \neq j \rightarrow \square_i \cap \square_j &= \emptyset \end{aligned} \tag{10.10}$$

such that we can rewrite the above integral

$$\vec{A}(\vec{x}) \sim \sum_i \vec{\nabla} \times \int_{\square_i} \frac{\vec{M}(\vec{x}\,')}{4\pi|\vec{x}' - \vec{x}|}\, dV' \tag{10.11}$$

Now, if we choose the cuboidal region small enough that $\vec{M}$ is approximately constant, say $\vec{M}_i$ in the region $\square_i$, we get

$$\vec{A}(\vec{x}) \sim \sum_i \vec{\nabla} \times \int_{\square_i} \frac{\vec{M}_i}{4\pi|\vec{x}' - \vec{x}|}\, dV' \tag{10.12}$$

We can now find the phase

$$\phi(x, y) \sim -\frac{q}{\hbar} \sum_i \int_{-\infty}^{\infty} \vec{\nabla} \times \int_{\square_i} \frac{\vec{M}_i}{4\pi|\vec{x}' - \vec{x}|}\, dV'\, dz \tag{10.13}$$

The integral here, for uniform $\vec{M}$ over a cuboidal region with our boundary and gauge conditions has been solved in (Keimpema, De Raedt, and De Hosson 2006), so we can replace the integrals here with analytic solutions. The contribution ϕ_i to the phase due to box $\square_i$ with thicknesses (L_{xi}, L_{yi}, L_{zi}), and

center (x_i^0, y_i^0, z_i^0)

$$
\begin{aligned}
F_0(x,y) &= x\ln\left(x^2+y^2\right) - 2x + 2y\tan^{-1}\left(\frac{x}{y}\right) \\
\phi_i(x,y) &= \frac{\mu_0 M_i L_{zi}}{4\Phi_0}\Big(\\
&\quad -\Big(\quad F_0\left((x-x_i^0) - L_{xi}/2,\ (y-y_i^0) - L_{yi}/2\right) \\
&\qquad - \quad F_0\left((x-x_i^0) + L_{xi}/2,\ (y-y_i^0) - L_{yi}/2\right) \\
&\qquad - \quad F_0\left((x-x_i^0) - L_{xi}/2,\ (y-y_i^0) + L_{yi}/2\right) \\
&\qquad + \quad F_0\left((x-x_i^0) + L_{xi}/2,\ (y-y_i^0) + L_{yi}/2\right)\ \Big)\ m_x \\
&\quad +\Big(\quad F_0\left((y-y_i^0) - L_{yi}/2,\ (x-x_i^0) - L_{xi}/2\right) \\
&\qquad - \quad F_0\left((y-y_i^0) + L_{yi}/2,\ (x-x_i^0) - L_{xi}/2\right) \\
&\qquad - \quad F_0\left((y-y_i^0) - L_{yi}/2,\ (x-x_i^0) + L_{xi}/2\right) \\
&\qquad + \quad F_0\left((y-y_i^0) + L_{yi}/2,\ (x-x_i^0) + L_{xi}/2\right)\ \Big)\ m_y \\
&\quad \Big)
\end{aligned}
\tag{10.14}
$$

The full phase is then simply a sum of these contributions

$$\phi(x,y) = \sum_i \phi_i(x,y) \tag{10.15}$$

Noting the absence of dependence on the z coordinate, one simple optimization that can be made is to sum the magnetizations and lengths from boxes in the same z-aligned column. This is equivalent to choosing boxes that are long in the z-direction and averaging the magnetization in the column. This averaging and multiplying by the z-length also looks like integrating the value down in the z-direction onto a flat square. This is, I believe, the viewpoint taken by other authors in building this formulation.

10.2.1 Resolving Box Sides and Corners

We note there are potential infinities at $F_0(x,0)$ and $F_0(0,0)$, the box sides and corners, so we'll take limits and see what these values are. This is an important

step for a stable computer implementation.

We'll first look at $\lim_{y\to 0}$ for $x \neq 0$:

$$\lim_{y\to 0} F_0(x,y) = \lim_{y\to 0} x\ln(x^2+y^2) - 2x + \lim_{y\to 0} 2y\tan^{-1}(x/y) \tag{10.16}$$

The first term is simple enough

$$\lim_{y\to 0} x\ln(x^2+y^2) = x\ln(x^2) \tag{10.17}$$

For the second term, if we remember the domain of $\tan$ is the angle θ which, while not strictly bounded, is periodic. So the range of $\tan^{-1}$ will be that value θ, and fixing it on a single rotation about the unit circle, will be somewhere in $[-2\pi, 2\pi]$, depending on conventions. Importantly, $-2\pi < \lim_{v\to\infty}\tan^{-1}(v) < 2\pi$, so $\tan^{-1}$ is bounded. Then

$$\lim_{y\to 0} 2y\tan^{-1}(x/y) = 0 \tag{10.18}$$

Finally

$$\lim_{y\to 0} F_0(x,y) = x\ln(x^2) - 2x \tag{10.19}$$

If we now take the limit as $x \to 0$ of this value

$$\lim_{x\to 0}\lim_{y\to 0} F_0(x,y) = \lim_{x\to 0} x\ln(x^2) - 2x \tag{10.20}$$

To resolve the evaluation of $x\cdot\ln(x^2) = 0\cdot\infty$ in this limit, we use l'Hôpitale's rule. Writing

$$\lim_{x\to 0} x\ln x^2 = \lim_{x\to 0}\frac{2\ln(x)}{1/x} \tag{10.21}$$

we have $\frac{\infty}{\infty}$. Taking the first derivative should suffice

$$\lim_{x\to 0}\frac{2\ln(x)}{1/x} = \lim_{x\to 0}\frac{(2\ln(x))'}{(1/x)'} = \lim_{x\to 0}\frac{1/x}{-1/x^2} = \lim_{x\to 0} -2x = 0 \tag{10.22}$$

and so

$$\lim_{x\to 0}\lim_{y\to 0} F_0(x,y) = 0 \tag{10.23}$$

Taking limits in the opposite order

$$\begin{aligned}\lim_{x\to 0} F_0(x,y) &= \lim_{x\to 0} x\ln(x^2+y^2) - \lim_{x\to 0} 2x + \lim_{x\to 0} 2y\tan^{-1}(x/y)\\ &= 0\ln(y^2) + 0 + 2y0\\ &= 0\end{aligned} \tag{10.24}$$

and including the y limit

$$\lim_{y\to 0}\lim_{x\to 0} F_0(x,y) = 0 \tag{10.25}$$

so our limits converge.

In a computer implementation, however, we still come across the issue of, say in the $x\ln(x^2)$ term, a very small number multiplied by a very large number as $x \to 0$. A simple workaround is to create piece-wise functions, with the limits applied at a threshold distance ϵ

$$\begin{aligned}F'_{0x}(x,y) &= \begin{cases} x\ln(x^2+y^2) - 2x & \text{if } x > \epsilon \\ 0 & \text{otherwise}\end{cases}\\ F'_{0y}(x,y) &= \begin{cases} 2y\tan^{-1}(x/y) & \text{if } y > \epsilon \\ 0 & \text{otherwise}\end{cases}\\ F'_0(x,y) &= F'_{0x}(x,y) + F'_{0y}(x,y)\end{aligned} \tag{10.26}$$

10.2.2 Evaluating the Box Magnetization

We also need a way of computing $\vec{M}_i$. We've noted that the box should be small enough that $\vec{M}$ is essentially constant, but we've also noted that, due to the absence of z-coordinate, we can elongate the box in the z-direction and take the average. We will, therefore, take boxes, $\square_i$, short in the x and y direction, and long in the z direction, and compute $\vec{M}_i$ by taking the total average

$$\vec{M}_i = \frac{\int_{\square_i} \vec{M}\, dV}{\int_{\square_i} dV} \tag{10.27}$$

10.2.3 Example Implementation

This tessellated box technique was implemented as a ParaView plugin. We will show here the result of each step of the implementation.

We start with a 100 nm cube with a vortex state. The image to the right is the cube as it will be seen in the electron hologram, with the z-axis pointing into the page.

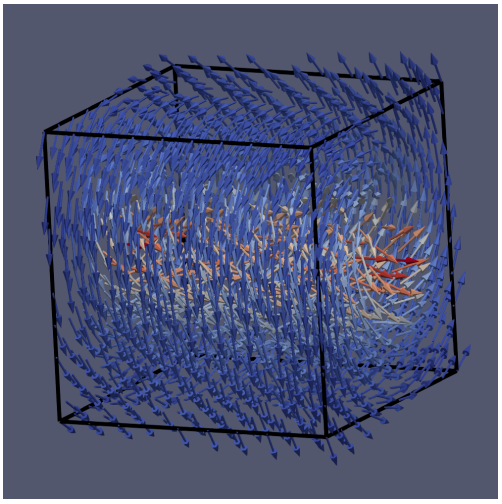

Next, we divide this into a grid of boxes, fine in the x and y directions, and extending at least the length of the cube in the z direction. The boxes should at least cover the magnetic region. The grid pictured here is a lower resolution than will actually be used.

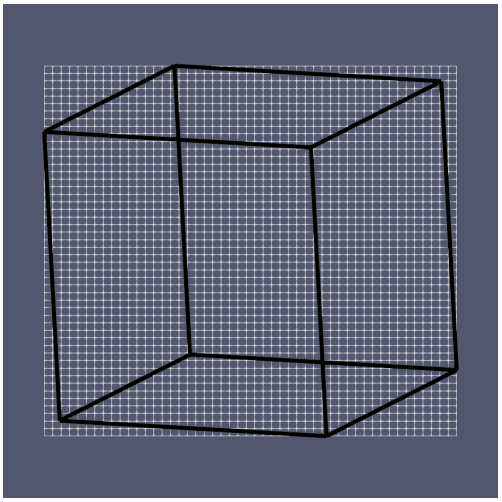

The average magnetization, $\vec{M}_i$ is then found for each box $\square_i$. It is found by uniformly sampling the magnetization within each box. The magnitudes of the average magnetizations are pictured here, along with vectors pointing in the magnetization direction. The projected outline of the cube is pictured here in white.

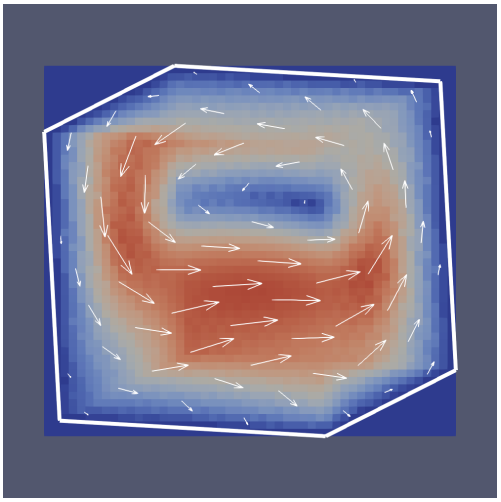

For each point (x, y) of the image, the electron phase

$$\phi(x, y) = \sum_i \phi_i(x, y)$$

is evaluated. Each ϕ_i depends on the $\vec{M}_i$ of each box $\square_i$.

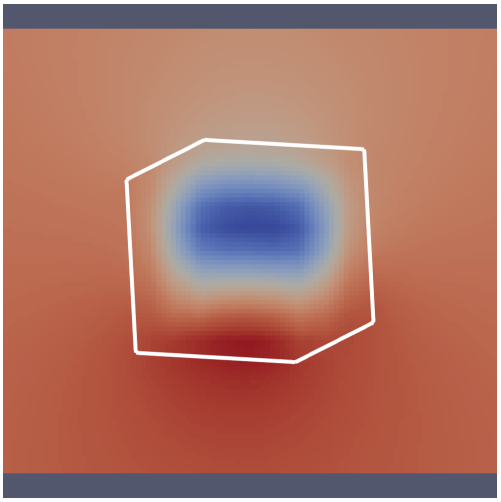

From the electron phase, the in-plane B-field, $\vec{B}^{\perp}$ is calculated by

$$\vec{B}^{\perp} = (-\partial_y \phi, \partial_x \phi)$$

The contour map and directions $\vec{C}$ are then calculated using

$$\vec{C} = \cos(\alpha\phi)\hat{B}^{\perp}$$

with α the "amplification factor", and colored based on the size and direction of this vector, as annotated on the image.

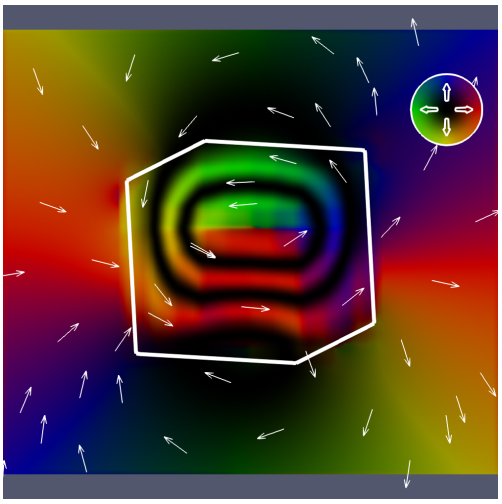

10.3 Projection Formulation

Outline:
We want to find a differential equation describing the electron phase in terms of the magnetization, similar to the PDE that describes the magnetic scalar potential in terms of the magnetization. With this, we may write a Finite Element solver for the electron hologram.

To do this, we will take the typical micromagnetic PDE for the magnetic vector potential and use the equations including $\vec{A}$, M_x and M_y. We will integrate both sides from $z = -\infty$ to $z = \infty$.

We will then show all terms in A_x and A_y vanish, and the terms in A_z can be written as terms in ϕ, the electron phase. This will give us the PDE we're looking for.

We will then look for suitable boundary conditions for the PDE, and then present a well defined problem of a PDE and Dirichlet boundary conditions. This will then be suitable for solving with the Finite Element Method.

In micromagnetism, we have

$$\vec{B} = \mu_0(\vec{H} + \vec{M}) \tag{10.28}$$

with

$$\begin{aligned} \vec{\nabla} \cdot \vec{B} &= 0 \\ \vec{\nabla} \times \vec{H} &= 0 \end{aligned} \tag{10.29}$$

from this, we can say B has no divergence, so it can be written in terms of a potential $\vec{A}$

$$\vec{B} = \vec{\nabla} \times \vec{A} \tag{10.30}$$

and so

$$\vec{\nabla} \times \vec{A} = \mu_0(\vec{H} + \vec{M}) \tag{10.31}$$

and taking the curl of both sides, and remembering $\vec{\nabla} \times \vec{H} = 0$

$$\vec{\nabla} \times \vec{\nabla} \times \vec{A} = \mu_0 \vec{\nabla} \times \vec{M} \tag{10.32}$$

which gives us our initial PDE relation.

We now want to isolate the A_z, M_x, and M_y components, since that is what contributes to our electron phase shift. Taking the 3rd component of (10.32), being a vector equality, and expanding out the curls, we get

$$\partial_x \partial_z A_x - \partial_x \partial_x A_z - \partial_y \partial_z A_y - \partial_y \partial_y A_z = -\partial_y M_x + \partial_x M_y \tag{10.33}$$

Now, we perform a line integral of both sides from $\vec{l} = (x, y, -\infty)$ to $\vec{l} = (x, y, +\infty)$, in line with the line integral we use to define our electron phase, $\phi = \int_{-\infty}^{\infty} A_z \, dz$. We hope that this integral will hit the A_z terms, and make the A_x and A_y terms vanish.

We get

$$\int_{-\infty}^{\infty} \big((\partial_x\partial_z A_x)(x,y,z') - (\partial_x\partial_x A_z)(x,y,z') \\ - (\partial_y\partial_z A_y)(x,y,z') - (\partial_y\partial_y A_z)(x,y,z')\big)\, dz' \\ = \int_{-\infty}^{\infty} (-(\partial_y M_x)(x,y,z') + (\partial_x M_y)(x,y,z'))\, dz' \quad (10.34)$$

We introduce the function application (x,y,z) to clarify the coordinate being integrated over, and make liberal use of braces to clarify that the derivatives act on the vector valued function $\vec{A}$, not on the resulting value of $\vec{A}(x,y,z)$. However, this becomes a little confused as integrals and derivatives are commuted. Suffice it to say, derivatives will always be acting on the function $\vec{A}$, even if it appears to have the coordinates applied. Indeed, it would be cleaner to consider the integral as a functional like the derivative, i.e. $(\mathcal{S}_z\xi)(x,y) = \int_{-\infty}^{\infty} \xi(x,y,z')\, dz$ and define derivatives $(\partial_\gamma \mathcal{S}_z\xi)(x,y) = \int_{-\infty}^{\infty}(\partial_\gamma\xi)(x,y,z')\, dz$ and show that $\partial_\gamma\mathcal{S}_z\xi = \mathcal{S}_z\partial_\gamma\xi$ representing the commutation of the derivatives and the integral. For this short section, however, I think that would probably be even *more* confusing. Suffice it to say the chain rule will never be needed in this section.

Since the line of integration has no variation in x and y, the derivatives ∂_x and ∂_y commute with the integral. We can say

$$\int_{-\infty}^{\infty} \partial_x\partial_x A_z(x,y,z')\, dz' = \partial_x\partial_x \int_{-\infty}^{\infty} A_z(x,y,z')\, dz' \quad (10.35)$$

recalling

$$\phi(x,y) = -\frac{q}{\hbar}\int_{-\infty}^{\infty} A_z(x,y,z')\, dz' \quad (10.36)$$

then

$$\partial_x\partial_x \int_{-\infty}^{\infty} A_z(x,y,z')\, dz' = -\frac{\hbar}{q}(\partial_x\partial_x\phi)(x,y) \quad (10.37)$$

and similar for $\partial_y\partial_y A_z$. We can also say

$$\int_{-\infty}^{\infty} (\partial_y M_x)(x,y,z')\, dz' = \partial_y \int_{-\infty}^{\infty} M_x(x,y,z')\, dz' \quad (10.38)$$

and similar for $\partial_x M_y$. For convenience, we will write

$$\vec{M}^{\perp}(x,y) = \left(\int_{-\infty}^{\infty} M_x(x,y,z')\, dz' \,, \int_{-\infty}^{\infty} M_y(x,y,z')\, dz' \right) \tag{10.39}$$

and call $\vec{M}^{\perp}$ the projection of $\vec{M}$ onto the image plane, or simply the in-plane magnetization.

We now write

$$\begin{aligned} \int_{-\infty}^{\infty} (\partial_x \partial_z A_x(x,y,z') - \partial_y \partial_z A_y(x,y,z'))\ dz' + \frac{\hbar}{q}\partial_x \partial_x \phi(x,y) + \frac{\hbar}{q}\partial_y \partial_y \phi(x,y) \\ = -\partial_y M_x^{\perp}(x,y) + \partial_x M_y^{\perp}(x,y) \end{aligned} \tag{10.40}$$

Since $\int_a^b \partial_z A_i(x,y,z')\, dz' = A_i(x,y,z')|_{z'=a}^{z'=b}$, we have

$$\begin{aligned} \int_{-\infty}^{\infty} (\partial_x \partial_z A_x)(x,y,z')\, dz' &= \partial_x \int_{-\infty}^{\infty} (\partial_z A_x)(x,y,z')\, dz' \\ &= \partial_x (A_x(x,y,\infty) - A_x(x,y,-\infty)) \end{aligned} \tag{10.41}$$

and similar for the other term.

We want these A_x and A_y terms to vanish so we're left with just ϕ. We can prove that derivatives of $\vec{A}$ go to zero at $z = \pm\infty$. Assuming a Coulomb gauge, we can write integral solutions for $\vec{A}$

$$\begin{aligned} A_x(x,y,z) &= -\partial_z \int \frac{M_y(x',y',z')}{4\pi|\vec{x}-\vec{x}'|}\, dV' + \partial_y \int \frac{M_z(x',y',z')}{4\pi|\vec{x}-\vec{x}'|}\, dV' \\ &= \int \frac{(z-z')\cdot M_y(x',y',z')}{4\pi|\vec{x}-\vec{x}'|^3}\, dV' - \int \frac{(y-y')\cdot M_z(x',y',z')}{4\pi|\vec{x}-\vec{x}'|^3}\, dV' \end{aligned} \tag{10.42}$$

and taking derivative with respect to x

$$\begin{aligned}\partial_x A_x(x,y,z) &= \partial_x \int \frac{(z-z')\cdot M_y(x',y',z')}{4\pi|\vec{x}-\vec{x}'|^3}\,dV' \\ &\quad - \partial_x \int \frac{(y-y')\cdot M_z(x',y',z')}{4\pi|\vec{x}-\vec{x}'|^3}\,dV' \\ &= -\int \frac{3(x-x')\cdot(z-z')\cdot M_y(x',y',z')}{4\pi|\vec{x}-\vec{x}'|^5}\,dV' \\ &\quad + \int \frac{3(x-x')\cdot(y-y')\cdot M_z(x',y',z')}{4\pi|\vec{x}-\vec{x}'|^5}\,dV'\end{aligned} \tag{10.43}$$

and taking the limit as $z \to \pm\infty$, we can commute the limit and the integral since the region of integration is independent of the limit

$$\begin{aligned}\lim_{z\to\infty} \partial_x A_x(x,y,z) &= -\lim_{z\to\infty} \int \frac{3(x-x')\cdot(z-z')\cdot M_y(x',y',z')}{4\pi|\vec{x}-\vec{x}'|^5}\,dV' \\ &\quad + \lim_{z\to\infty} \int \frac{3(x-x')\cdot(y-y')\cdot M_z(x',y',z')}{4\pi|\vec{x}-\vec{x}'|^5}\,dV' \\ &= -\int \lim_{z\to\infty} \frac{3(x-x')\cdot(z-z')\cdot M_y(x',y',z')}{4\pi|\vec{x}-\vec{x}'|^5}\,dV' \\ &\quad + \int \lim_{z\to\infty} \frac{3(x-x')\cdot(y-y')\cdot M_z(x',y',z')}{4\pi|\vec{x}-\vec{x}'|^5}\,dV' \\ &= \int 0\,dV' - \int 0\,dV' \\ &= 0\end{aligned} \tag{10.44}$$

as expected, assuming the magnetic region is finite. Similarly, we can say $\lim_{z\to\pm\infty}(\partial_y A_y)(x,y,z) = 0$. And so we're left with

$$\partial_x\partial_x\phi(x,y) + \partial_y\partial_y\phi(x,y) = -\frac{q}{\hbar}\partial_y M_x^{\perp}(x,y) + \frac{q}{\hbar}\partial_x M_y^{\perp}(x,y) \tag{10.45}$$

and dropping the (x,y), we get

$$\partial_x\partial_x\phi + \partial_y\partial_y\phi = -\frac{q}{\hbar}\partial_y M_x^{\perp} + \frac{q}{\hbar}\partial_x M_y^{\perp} \tag{10.46}$$

Noting that the LHS looks like a 2d Laplacian operator, and the RHS looks like

a 2d curl, we will write

$$\nabla^2\phi = \frac{q}{\hbar}\nabla \times \vec{M}^{\perp} \tag{10.47}$$

where ∇ is defined over 2d functions as $\vec{\nabla} = (\partial_x, \partial_y)$. Unfortunately, I couldn't think of a clear and consistent way of differentiating between the two, but the 2d and 3d cases shouldn't overlap from here on.

To find some boundary conditions, we will look at ϕ on the infinite boundary.

$$\begin{aligned}
-\frac{\hbar}{q}\phi(x,y) &= \int_{-\infty}^{\infty} A_z(x,y,z'')\, dz'' \\
&= \int_{-\infty}^{\infty} \Bigg(-\partial_y \int \frac{M_x(x',y',z')}{4\pi|(x,y,z'') - \vec{x}'|}\, dV' \\
&\qquad + \partial_x \int \frac{M_y(x',y',z')}{4\pi|(x,y,z'') - \vec{x}'|}\, dV' \Bigg)\, dz'' \\
&= \int_{-\infty}^{\infty} \Bigg(\int \frac{(y-y')\cdot M_x(x',y',z')}{4\pi|(x,y,z'') - \vec{x}'|^3}\, dV' \\
&\qquad - \int \frac{(x-x')\cdot M_y(x',y',z')}{4\pi|(x,y,z'') - \vec{x}'|^3}\, dV' \Bigg)\, dz'' \\
&= \int\int_{-\infty}^{\infty} \frac{(y-y')\cdot M_x(x',y',z')}{4\pi|(x,y,z'') - \vec{x}'|^3}\, dz''\, dV' \\
&\quad - \int\int_{-\infty}^{\infty} \frac{(x-x')\cdot M_y(x',y',z')}{4\pi|(x,y,z'') - \vec{x}'|^3}\, dz''\, dV'
\end{aligned} \tag{10.48}$$

The integral over z'' converges in both integrals if $|(x,y)| > |(x',y')|$. Since we are looking for ϕ at infinity and we've assumed the magnetic region is finite, this is true. Now

$$\begin{aligned}
-\frac{\hbar}{q}\lim_{|x,y|\to\infty}\phi(x,y) &= \lim_{|x,y|\to\infty}\Bigg(\int \frac{(y-y')\cdot M_x(x',y',z')}{2\pi|(x,y) - (x',y')|^2}\, dV' \\
&\qquad - \int \frac{(x-x')\cdot M_x(x',y',z')}{2\pi|(x,y) - (x',y')|^2}\, dV' \Bigg) \\
&= 0
\end{aligned} \tag{10.49}$$

and so, we can say ϕ vanishes at infinity.

We now have all the pieces necessary to write out a well defined PDE, suitable for a FEM formulation. We will denote the "shadow" of the magnetic region Ω_M as $\Omega_{M^\perp}$, in line with our notation for the projection of the magnetization.

We will denote the region outside this shadow as Ω_0. And noting the magnetization is uniformly zero in Ω_0

$$\nabla^2\phi = \frac{q}{\hbar}\,\nabla \times \vec{M}^{\perp} \quad \text{in } \Omega_{M^{\perp}} \tag{10.50a}$$

$$\nabla^2\phi = 0 \quad \text{in } \Omega_0 \tag{10.50b}$$

$$\phi = 0 \quad \text{in } \partial\Omega \tag{10.50c}$$

10.3.1 Weak Forms

We will now outline a weak form that will solve (10.50). This will involve first outlining the initial weak forms, and then ensuring each function has at most one derivative applied to it. Next, we will move the derivative terms off the $\vec{M}^{\perp}$ terms so uniform magnetizations work as expected. Finally, we will include a domain transformation to perform the infinite integration over a finite domain.

From here on, we will drop the $\frac{q}{\hbar}$ term. The simplest way to account for it is to solve the equations without it, knowing the solution for ϕ will then be off by a factor of $\frac{q}{\hbar}$. In a similar manner, $\hat{m}^{\perp}$ is typically used in a practical implementation instead of $\vec{M}$, and M_s accounted for afterwards. This turns out to be necessary for the implementation of a stable numerical solver. With this in mind, knowing these factors must be accounted for in the final implementation, we drop them for the sake of clarity.

By multiplying both sides of the equation by a test function, v, and integrating both sides over their respective domains, we get the weak form (remembering we're in 2D)

$$\int_{\Omega} (\nabla^2\phi)v \; dS = \int_{\Omega_{M^{\perp}}} (\nabla \times \vec{M}^{\perp})v \; dS \tag{10.51}$$

Using the usual partial integration / divergence theorem transformation, we have

$$\int_{\Omega} \phi_{,ii} v \; dS = \int_{\partial\Omega} n_i \phi_{,i} v \; dl - \int_{\Omega} \phi_{,i} v_{,i} \; dS \tag{10.52}$$

where $\vec{n_i}$ is a directed tangent of the boundary $\partial\Omega$. Since we are using Dirichlet conditions for ϕ on $\partial\Omega$, our test function v is set to zero on the boundary, so we

can drop the surface term

$$\int_{\Omega} \phi_{,ii} v \, dS = -\int_{\Omega} \phi_{,i} v_{,i} \, dS \tag{10.53}$$

and our weak form is now

$$-\int_{\Omega} \phi_{,i} v_{,i} \, dS = \int_{\Omega_{M^\perp}} (\nabla \times \vec{M}^\perp) v \, dS \tag{10.54}$$

Next, we want to move the derivatives off the $\vec{M}^\perp$ terms. We can use the Kelvin-Stokes theorem to do this which states

$$\int_{\Omega_{M^\perp}} \left(v(\nabla \times \vec{M}^\perp) + (\nabla v) \times \vec{M}^\perp \right) \, dS = \int_{\partial\Omega_{M^\perp}} v M_i^\perp n_i \, dl \tag{10.55}$$

so we have

$$\int_{\Omega_{M^\perp}} (\nabla \times \vec{M}^\perp) v \, dS = -\int_{\Omega_{M^\perp}} (\nabla v) \times \vec{M}^\perp \, dS + \int_{\partial\Omega_{M^\perp}} v M_i^\perp n_i \, dl \tag{10.56}$$

putting this into our weak form, and taking care of signs, we now have

$$\int_{\Omega} \phi_{,i} v_{,i} \, dS = \int_{\Omega_{M^\perp}} (\nabla v) \times \vec{M}^\perp \, dS - \int_{\partial\Omega_{M^\perp}} v M_i^\perp n_i \, dl \tag{10.57}$$

which is now very close to what we want.

10.3.2 Infinite Domain Transform

Outline:
In this section, we will transform the integral over the infinite domain Ω to an integral over the finite domains Ω^R and Λ. This will be done with an appropriate change of variable using a transformation function.

Next, we will find the appropriate transformation function to use based on keeping the order of the whole integral independent of the coordinate, and keeping the test and trial functions linear in the coordinates.

Change of Variable

Noting the domain Ω on the LHS of (10.57) is the infinite domain, this weak form is unsuitable for solving on a computer. We must introduce some technique for solving over this infinite domain. One approach would be to use the Boundary Element Method, which is perfectly possible, given $\nabla^2\phi = 0$ in the non-magnetic region and out to infinity, just as in the MERRILL equations. However, here we will use the surface transformation techniques laid out in section 6.3.

We denote the domain Ω^R as the region from the origin out to a circle of radius $R^{\texttt{inner}}$, and the region Ω^{R+} as the region from $R^{\texttt{inner}}$ out to infinity. We split our weak form based on these regions

$$\int_{\Omega^R} \phi_{,i} v_{,i}\, dS + \int_{\Omega^{R+}} \phi_{,i} v_{,i}\, dS = \int_{\Omega_{M^\perp}} (\nabla v) \times \vec{M}^\perp\, dS - \int_{\partial\Omega_{M^\perp}} v M_i^\perp n_i\, dl \quad (10.58)$$

We are looking to transform the integral over Ω^{R+}.

We will denote the diffeomorphism $\vec{\psi}$ which maps the region Ω^{R+} to a finite region Λ between two circles or radius $R^{\texttt{inner}}$ and $R^{\texttt{outer}}$ about the origin. We will use the variables $\vec{x} \in \Omega$ and $\vec{y} \in \Lambda$ and the relation

$$y = \vec{\psi}(\vec{x}) \quad (10.59)$$

from which we get the transformations

$$\begin{aligned} \Lambda &= \vec{\psi}(\Omega^{R+}) \\ \vec{x} &= \vec{\psi}^{-1}(\vec{y}) \\ dx_i &= \psi^{-1}_{i,j}(\vec{y}) dy_j \end{aligned} \quad (10.60)$$

We transform the variable of integration over Ω^{R+} to Λ

$$\int_{\Omega^{R+}} \phi_{,i}(\vec{x})\, v_{,i}(\vec{x})\, dx^2 = \int_{\Lambda} \phi_{,i}(\vec{\psi^{-1}}(\vec{y}))\, v_{,i}(\vec{\psi^{-1}}(\vec{y}))\, \left|\boldsymbol{J}(\vec{\psi^{-1}})(\vec{y})\right|\, dy^2 \quad (10.61)$$

with $\boldsymbol{J}(\vec{\psi^{-1}})$ the Jacobian of $\vec{\psi^{-1}}$, where $J(\vec{\psi^{-1}})_{ij}(\vec{y}) = \frac{\partial \psi_i^{-1}}{\partial y_j}(\vec{y})$.

We will use the functions φ and η on Λ as the analogs of ϕ and v on Ω^{R+}, defining them

$$\begin{aligned} \varphi &= \phi \circ \vec{\psi^{-1}} \\ \Rightarrow \phi &= \varphi \circ \vec{\psi} \end{aligned} \tag{10.62}$$

and

$$\begin{aligned} \eta &= v \circ \vec{\psi^{-1}} \\ \Rightarrow v &= \eta \circ \vec{\psi} \end{aligned} \tag{10.63}$$

We can now apply the chain rule to find derivatives of ϕ and v wrt $\vec{x}$ in terms of derivatives of φ and η wrt $\vec{y}$

$$\begin{aligned} \frac{\partial \phi}{\partial x_i}(\vec{x}) &= \frac{\partial \varphi}{\partial y_j}(\vec{\psi}(\vec{x}))\frac{\partial \psi_j}{\partial x_i}(\vec{x}) \\ \phi_{,i} &= (\varphi_{,j} \circ \vec{\psi})\ \psi_{j,i} \\ &= (\varphi_{,j} \circ \vec{\psi})\ J(\vec{\psi})_{ji} \end{aligned} \tag{10.64}$$

with $\boldsymbol{J}(\vec{\psi})$ the Jacobian of $\vec{\psi}$, and so, the $\phi_{,i}(\vec{\psi^{-1}}(\vec{y})) = (\phi \circ \vec{\psi^{-1}})(\vec{y})$ terms in the integral are

$$\phi_{,i} \circ \vec{\psi}^{-1} = \varphi_{,j}\ (J(\vec{\psi})_{ji} \circ \vec{\psi}^{-1}) \tag{10.65}$$

and from the Inverse Function Theorem, $\boldsymbol{J}(f) \circ f^{-1} = \boldsymbol{J}^{-1}(f^{-1})$, so

$$\phi_{,i} \circ \vec{\psi}^{-1} = \varphi_{,j}\ \left[J(\vec{\psi}^{-1})\right]^{-1}_{ji} \tag{10.66}$$

and similarly

$$v_{,i} \circ \vec{\psi}^{-1} = \eta_{,j}\ \left[J(\vec{\psi}^{-1})\right]^{-1}_{ji} \tag{10.67}$$

The integral over Ω^{R+}, as it now stands is

$$\begin{aligned} &\int_{\Omega^{R+}} \phi_{,i}(\vec{x})\ v_{,i}(\vec{x})\ dx^2 \\ &\quad = \int_{\Lambda} \varphi_{,j}(\vec{y})\ \left[J(\vec{\psi}^{-1})\right]^{-1}_{ji}(\vec{y})\ \eta_{,k}(\vec{y})\ \left[J(\vec{\psi}^{-1})\right]^{-1}_{ki}(\vec{y})\ \left|\boldsymbol{J}(\vec{\psi^{-1}})(\vec{y})\right|\ dy^2 \end{aligned} \tag{10.68}$$

Choosing a Transformation Function

From discussion in section 6.3, we want the integral to be independent of $\vec{y}$, and the functions φ and η to be linearly dependent on $\vec{y}$. We have

$$\begin{aligned}\mathcal{O}(\texttt{integrand}) = \\ &\mathcal{O}\left(\varphi_{,j}(\vec{y})\right)\ \mathcal{O}\left(\left[J(\vec{\psi^{-1}})\right]^{-1}_{ji}(\vec{y})\right) \\ &\mathcal{O}\left(\eta_{,k}(\vec{y})\right)\ \mathcal{O}\left(\left[J(\vec{\psi^{-1}})\right]^{-1}_{ki}(\vec{y})\right) \\ &\mathcal{O}\left(\left|\boldsymbol{J}(\vec{\psi^{-1}})(\vec{y})\right|\right)\end{aligned} \tag{10.69}$$

with (for $\dim(\Lambda) = 2$)

$$\begin{aligned}\mathcal{O}(\varphi_{,i}) = \mathcal{O}(\eta_{,k}) &= 1 \\ \mathcal{O}(J(\psi^{-1})) &= \frac{\mathcal{O}(\psi^{-1})}{|y|} \\ \mathcal{O}\left(\left[J(\psi^{-1})\right]^{-1}\right) &= \frac{|y|}{\mathcal{O}(\psi^{-1})} \\ \mathcal{O}\left(\left|\boldsymbol{J}(\psi^{-1})\right|\right) &= \frac{\mathcal{O}(\psi^{-1})^2}{|y|}\end{aligned} \tag{10.70}$$

giving us

$$\frac{|y|}{\mathcal{O}(\psi^{-1})}\frac{|y|}{\mathcal{O}(\psi^{-1})}\left(\frac{\mathcal{O}(\psi^{-1})}{|y|}\right)^2 = 1 \tag{10.71}$$

so, in fact, the specific function used for ψ^{-1} isn't strictly important for a stable formulation in 2D. In our implementation, we used $\mathcal{O}(\psi^{-1}) = |y|^{-1}$.

We have

$$\begin{aligned}\vec{\psi}^{-1}(\vec{y}) &= \hat{y}R^{\texttt{inner}}\left(\frac{R^{\texttt{inner}} - R^{\texttt{outer}}}{|y| - R^{\texttt{outer}}}\right) \\ |\psi^{-1}|(\vec{y}) &= R^{\texttt{inner}}\left(\frac{R^{\texttt{inner}} - R^{\texttt{outer}}}{|y| - R^{\texttt{outer}}}\right) \\ \left[\boldsymbol{J}(\vec{\psi}^{-1})\right]^{-1}_{ij}(\vec{y}) &= \delta_{ij}\frac{|y|}{|\psi^{-1}|(\vec{y})} + \frac{y_i y_j(R^{\texttt{outer}} - 2|y|)}{|\psi^{-1}|(\vec{y})\ |y|^2} \\ \left|\boldsymbol{J}(\vec{\psi}^{-1})\right| &= \frac{(|\psi^{-1}|(\vec{y}))^2}{R^{\texttt{outer}}|y| - |y|^2}\end{aligned} \tag{10.72}$$

which can be substituted back into (10.68), providing the transformation we need from an infinite to a finite domain.

All together

We can now put the entire weak form together. We remember that the region Ω^R refers to the region from the origin to the radius $R^{\texttt{inner}}$, and the region Λ refers to the region from $R^{\texttt{inner}}$ to $R^{\texttt{outer}}$. We also drop the explicit application of the variable of integration. At this point, it is unnecessary, and in the actual implementation, it is irrelevant. We replace the transformed φ and η with the original test and trial functions, ϕ and v, since they will be in the same function space in the FEM implementation. However, when interpreting results, we must remember values of ϕ in the region Λ are for the transformed function φ.

Putting the original equation and the transformed equations together, we get

$$\begin{aligned}\int_{\Omega^R} \phi_{,i}\, v_{,i}\, dS + \int_{\Lambda} \phi_{,i}\, v_{,j} \left[\boldsymbol{J}(\vec{\psi}^{-1})\right]^{-1}_{ik} \left[\boldsymbol{J}(\vec{\psi}^{-1})\right]^{-1}_{kj} \left|\boldsymbol{J}(\vec{\psi}^{-1})\right| \, dS \\ = \int_{\Omega_{M^\perp}} (\nabla v) \times \vec{M}^\perp \, dS - \int_{\partial\Omega_{M^\perp}} v M_i^\perp n_i \, dl \qquad (10.73) \\ \phi = 0\,,\ v = 0 \quad \text{on } \partial\Lambda\end{aligned}$$

which should produce the electron phase ϕ over the region Ω^R.

10.3.3 Example Implementation

This projection technique was implemented as a ParaView plugin. We will show here the result of each step of the implementation, similar to the tessellated box technique.

For a practical implementation, we still need a method to find the outline of the material to determine the region $\Omega_{M^\perp}$, we need to implement a 2d mesh of the region $\Omega_{M^\perp} \cup \Omega^R \cup \Lambda$ and we need to project the values of the 3d volume onto the region $\Omega_{M^\perp}$. Each of these is a reasonably complex task, and each

worth a full section of discussion. However, these implementation details will be omitted from this section, and the results simply presented.

We start with a 100 nm cube with a vortex state. The image to the right is the cube as it will be seen in the electron hologram, with the z-axis pointing into the page.

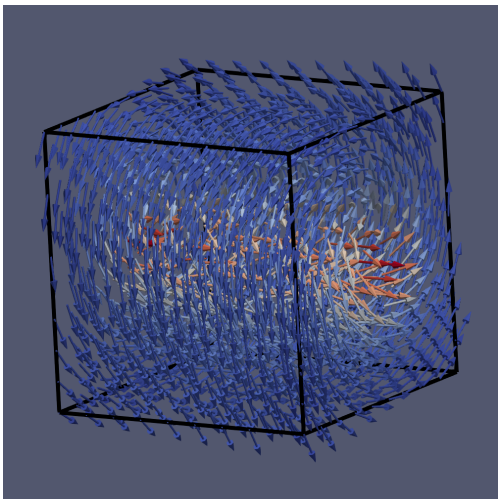

Next, we divide this into a grid of boxes, fine in the x and y directions, and extending at least the length of the cube in the z direction. The boxes should at least cover the magnetic region. The grid pictured here is a lower resolution than will actually be used.

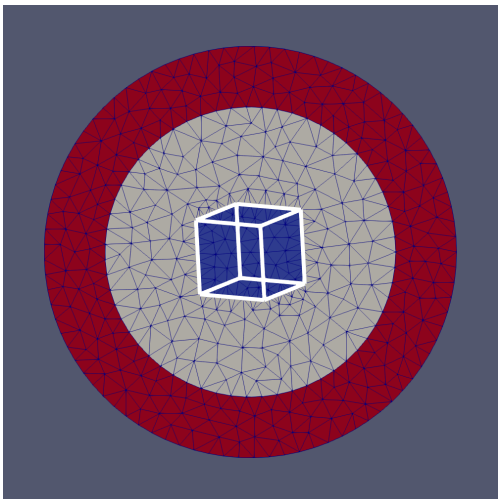

The average magnetization, $\vec{M}_i$ is then found for each box $\square_i$. It is found by uniformly sampling the magnetization within each box. The magnitudes of the average magnetizations are pictured here, along with vectors pointing in the magnetization direction. The projected outline of the cube is pictured here in white.

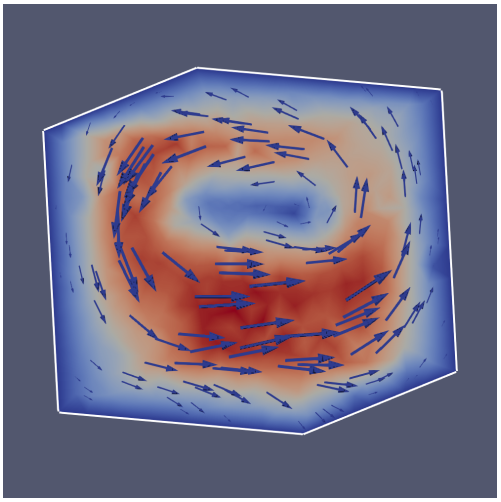

For each point (x, y) of the image, the electron phase

$$\phi(x, y) = \sum_i \phi_i(x, y)$$

is evaluated. Each ϕ_i depends on the $\vec{M}_i$ of each box $\square_i$.

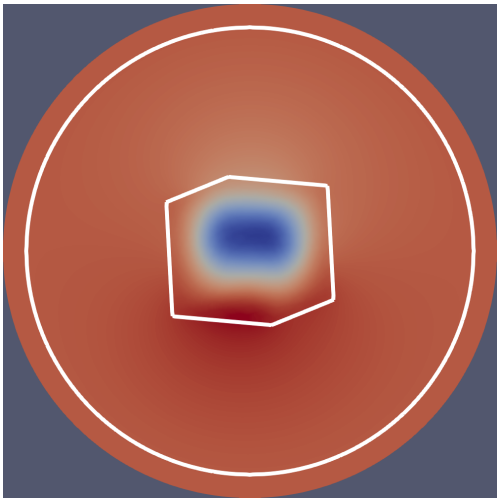

From the electron phase, the in-plane B-field, $\vec{B}^{\perp}$ is calculated by

$$\vec{B}^{\perp} = (-\partial_y \phi, \partial_x \phi)$$

The contour map and directions $\vec{C}$ are then calculated using

$$\vec{C} = \cos(\alpha\phi)\hat{B}^{\perp}$$

with α the "amplification factor", and colored based on the size and direction of this vector, as annotated on the image.

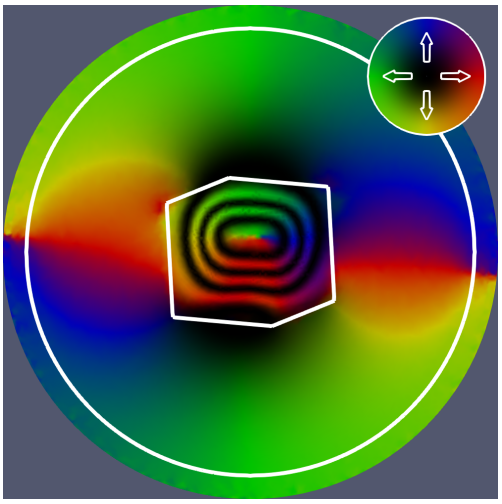

Chapter 11

Example Electron Holography Modelling Results

11.1 Electron Holograms for Reference Magnetic States

11.1.1 Introduction

Electron holography is a useful experimental tool for gathering information about the magnetization of a material at the nano-scale. However, the image generated is a projection of the 3D magnetization onto a 2D surface. As a result, some information is lost. By looking at how the electron holograms generated by 3D magnetic states, typical of the nano-scale magnetic minerals, change with angle and grain geometry, we can begin to develop an intuition for how some features of the 2D image translate to features of the 3D magnetization. We can also see which 3D features cannot be easily recovered.

The HoloMag software package was developed for just this purpose. It contains a plugin for the ParaView visualization suite. With HoloMag and ParaView, a solution from a micromagnetic model can be loaded in, and using a visual interface, the electron hologram generated. Most usefully, however, the magnetic grain can be rotated about, and the electron hologram updated in

near-real time. This is particularly useful for developing an intuition for how a 3D magnetization translates into a 2D hologram based on its angle with the image plane, and so an intuition for which features of a 2D hologram might translate back to a 3D magnetization.

Some key intuitions are presented here. Although, they are not a substitute for developing the intuition oneself, by playing with states in the software.

All the results and analyses presented here are original work.

11.1.2 Method

The MERRILL library was used to nucleate a number of states in a 80 nm cube with the magnetic parameters of magnetite. To nucleate [111] uniform, flower, and vortex states, the magnetization was first set to an approximation of the state, and then minimized. However, for the uniform state, no minimization was done. While this may nucleate weakly stable, or unstable states, we're more interested here in realistic states, indicative of real world states, to study how they translate to a hologram, rather than actual real world states.

To nucleate the [100] states, the anisotropy constant, K_1, of magnetite was first set to $K_1 = |K_1|$, to make [100] the easy axis, and then the above procedure was carried out.

Once the appropriate state was nucleated, it was loaded into ParaView and HoloMag, was used to generate the hologram. Visualizations of the magnetization, the projected magnetization, and the electron hologram were generated and output to disk.

11.1.3 Results

We present a number of comparative images. They are labelled e.g.

$$\langle \hat{m} \rangle\text{: [111] } - \text{ Rotation: } (45^\circ, 0^\circ).$$

The "$\langle \hat{m} \rangle$: [111]" refers to the direction of the average magnetization, in this case along the [111] diagonal. The "Rotation: $(45^\circ, 0^\circ)$" refers to the axes about which the grain was rotated, and the angle at which it was rotated, in this case 45° about the vertical axis, and 0° about the horizontal axis. The values for the rotation are meant as a rough guide, as it can be difficult to conceptualize how an Euler rotation — progressive rotations applied one after the other — actually effects the orientation of a 3D object. In all cases, we've described where the direction of the magnetization is pointing with respect to the page, and the reader should be able to determine from the images the orientation of the cube and the crystal axes.

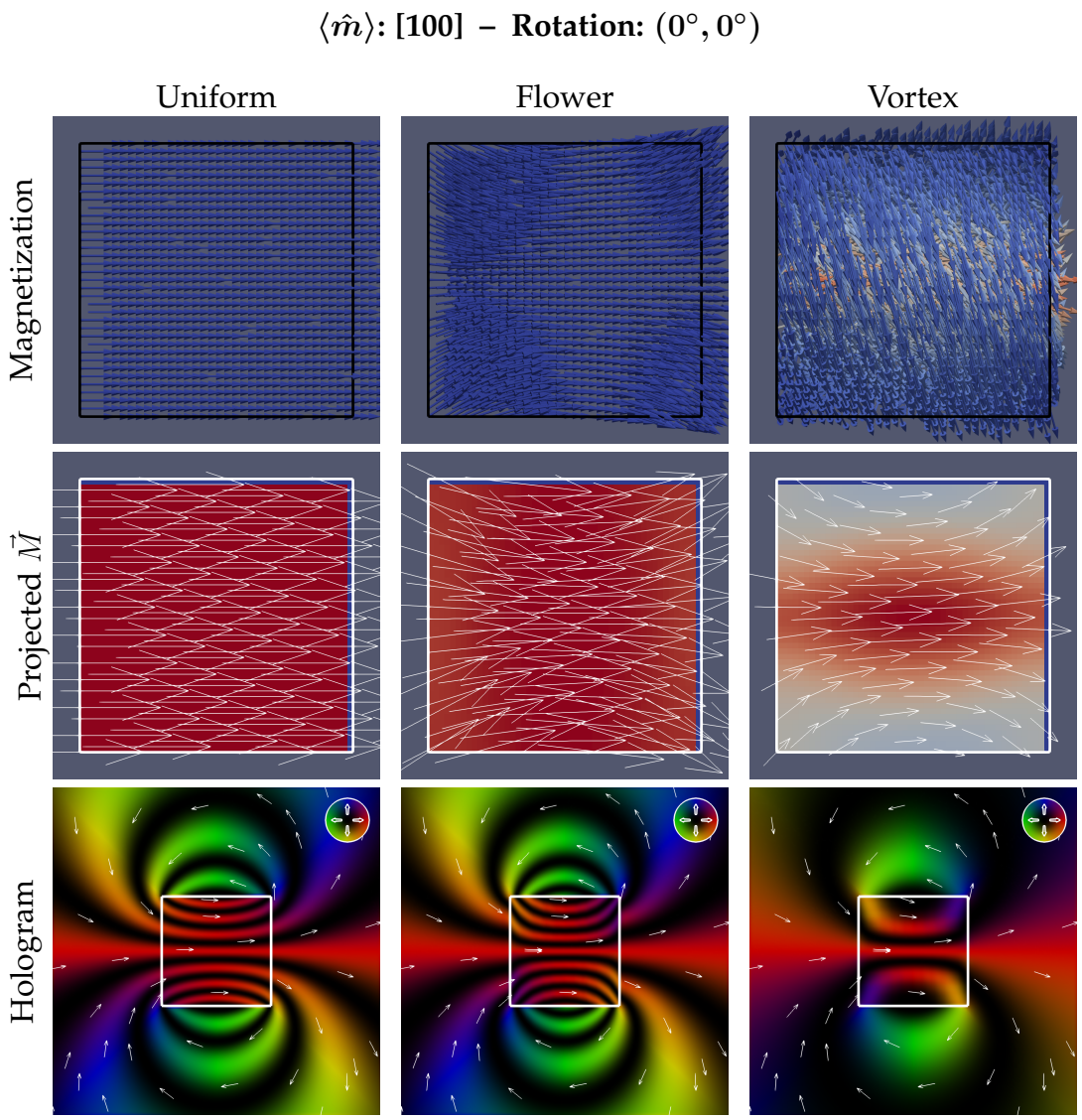

Figure 11.1: The magnetization, projected magnetization, and electron hologram for a cube of magnetite with average magnetization pointing in the [100] direction. Here, the [100] direction is the face of the cube pointing to the right and perfectly in the plane of the page. Results for a uniform magnetization, a flower state, and a single vortex are shown. The vortex is a right hand vortex with core pointing in the [100] direction.

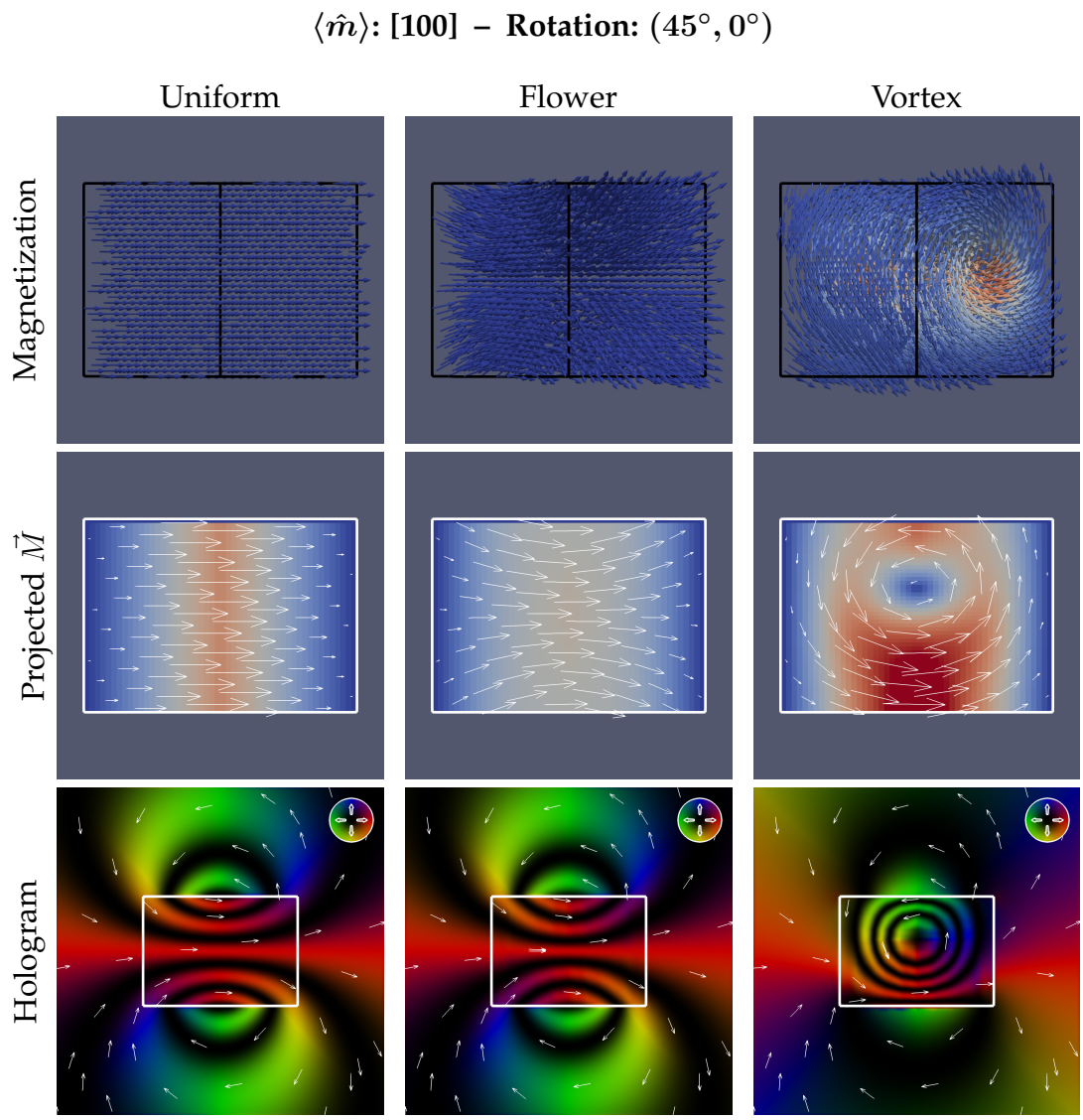

Figure 11.2: The magnetization, projected magnetization, and electron hologram for a cube of magnetite with average magnetization pointing in the [100] direction. Here, the [100] direction is the face of the cube pointing to the right and $45°$ out of the page. Results for a uniform magnetization, a flower state, and a single vortex are shown. The vortex is a right hand vortex with core pointing in the [100] direction.

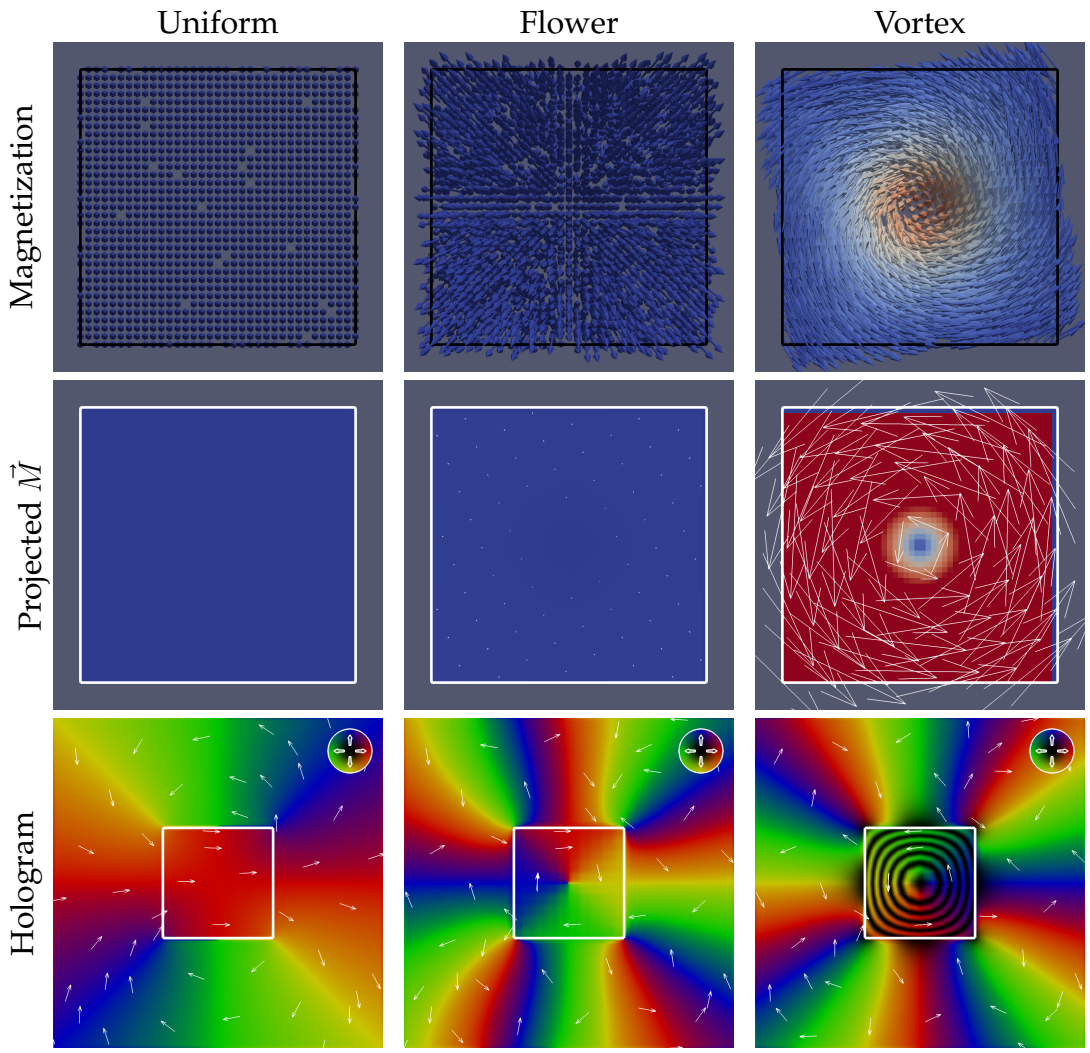

Figure 11.3: The magnetization, projected magnetization, and electron hologram for a cube of magnetite with average magnetization pointing in the [100] direction. Here, the [100] direction is the face of the cube pointing out of the page. Results for a uniform magnetization, a flower state, and a single vortex are shown. The vortex is a right hand vortex with core pointing in the [100] direction.

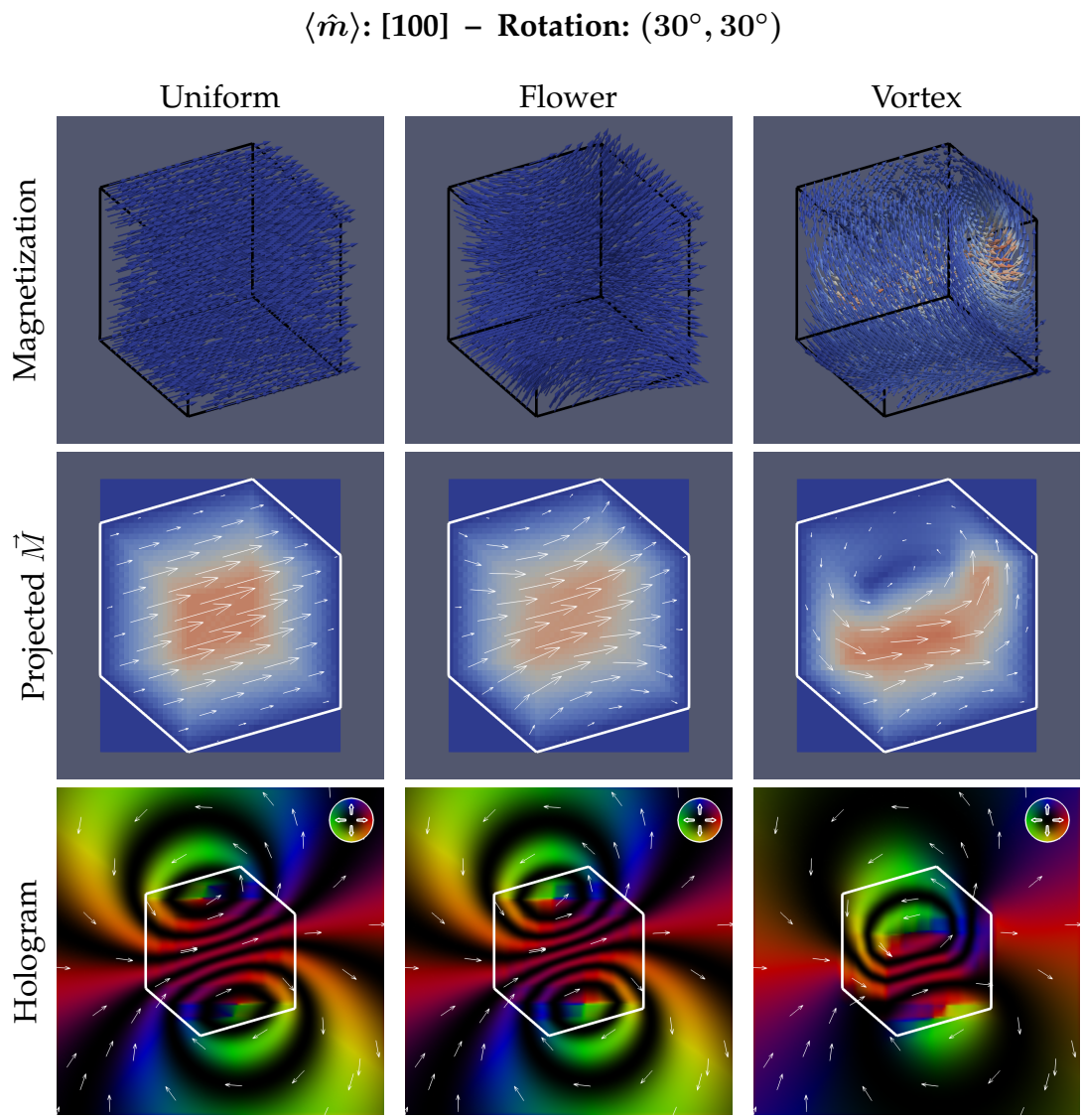

Figure 11.4: The magnetization, projected magnetization, and electron hologram for a cube of magnetite with average magnetization pointing in the [100] direction. Here, the [100] direction is the face of the cube pointing towards the top right, and about $30°$ out of the page. Results for a uniform magnetization, a flower state, and a single vortex are shown. The vortex is a right hand vortex with core pointing in the [100] direction.

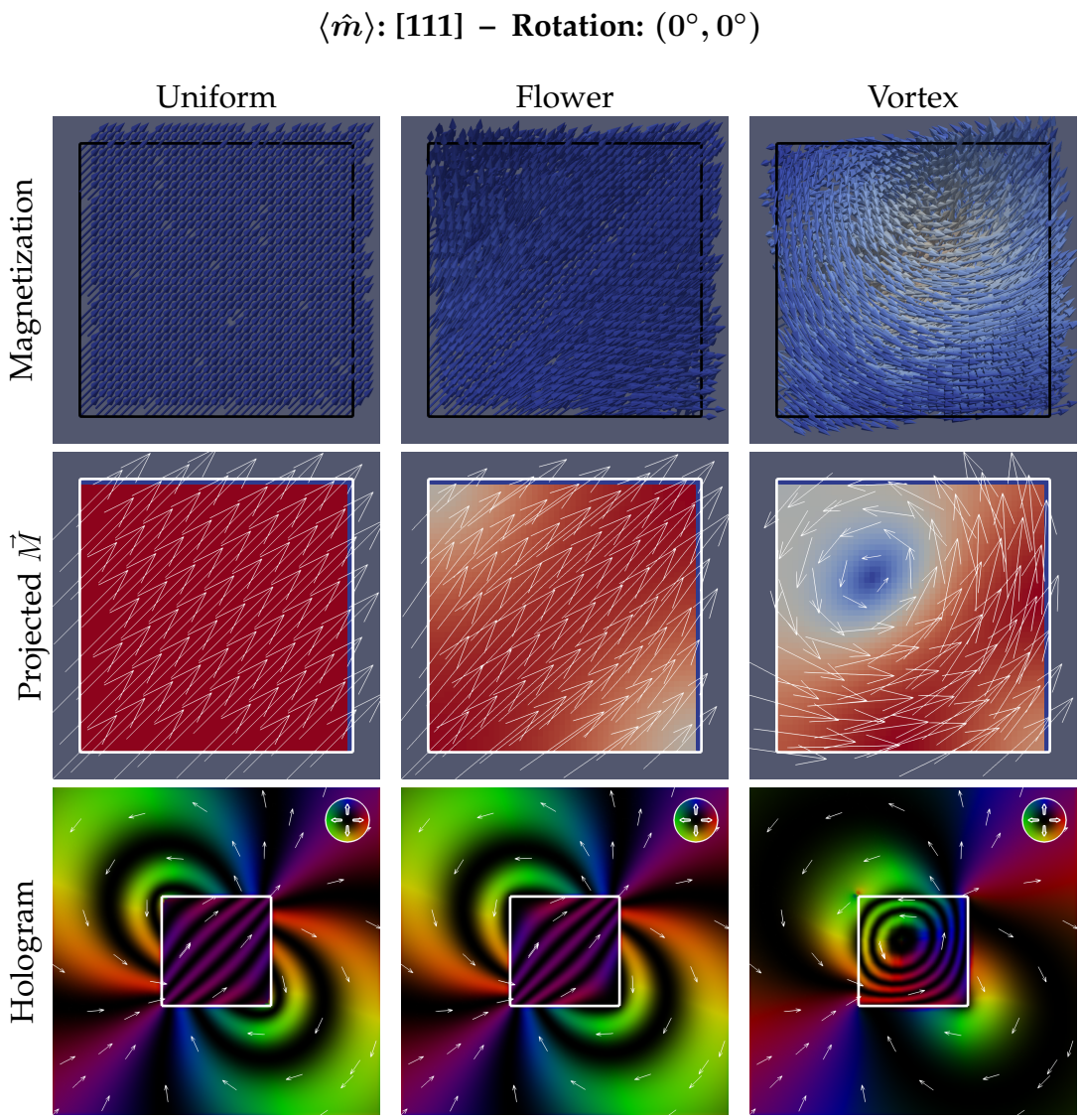

Figure 11.5: The magnetization, projected magnetization, and electron hologram for a cube of magnetite with average magnetization pointing in the [111] direction. Here, the [111] direction is the corner of the cube pointing towards the top right, and about $30°$ out of the page. Results for a uniform magnetization, a flower state, and a single vortex are shown. The vortex is a right hand vortex with core pointing in the [111] direction.

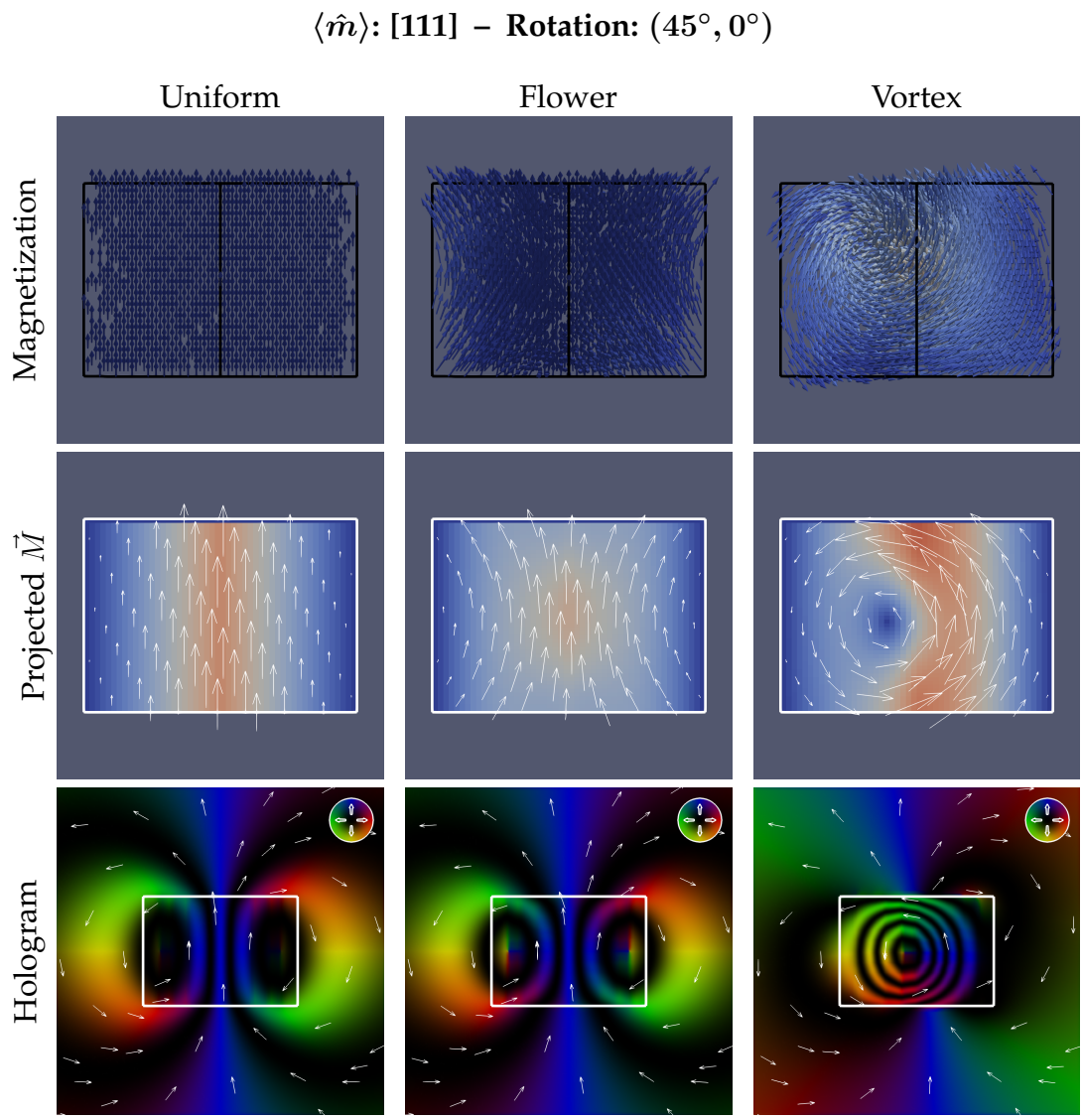

Figure 11.6: The magnetization, projected magnetization, and electron hologram for a cube of magnetite with average magnetization pointing in the [111] direction. Here, the [111] direction is the corner of the cube pointing towards the top, and about $30°$ out of the page. Results for a uniform magnetization, a flower state, and a single vortex are shown. The vortex is a right hand vortex with core pointing in the [111] direction.

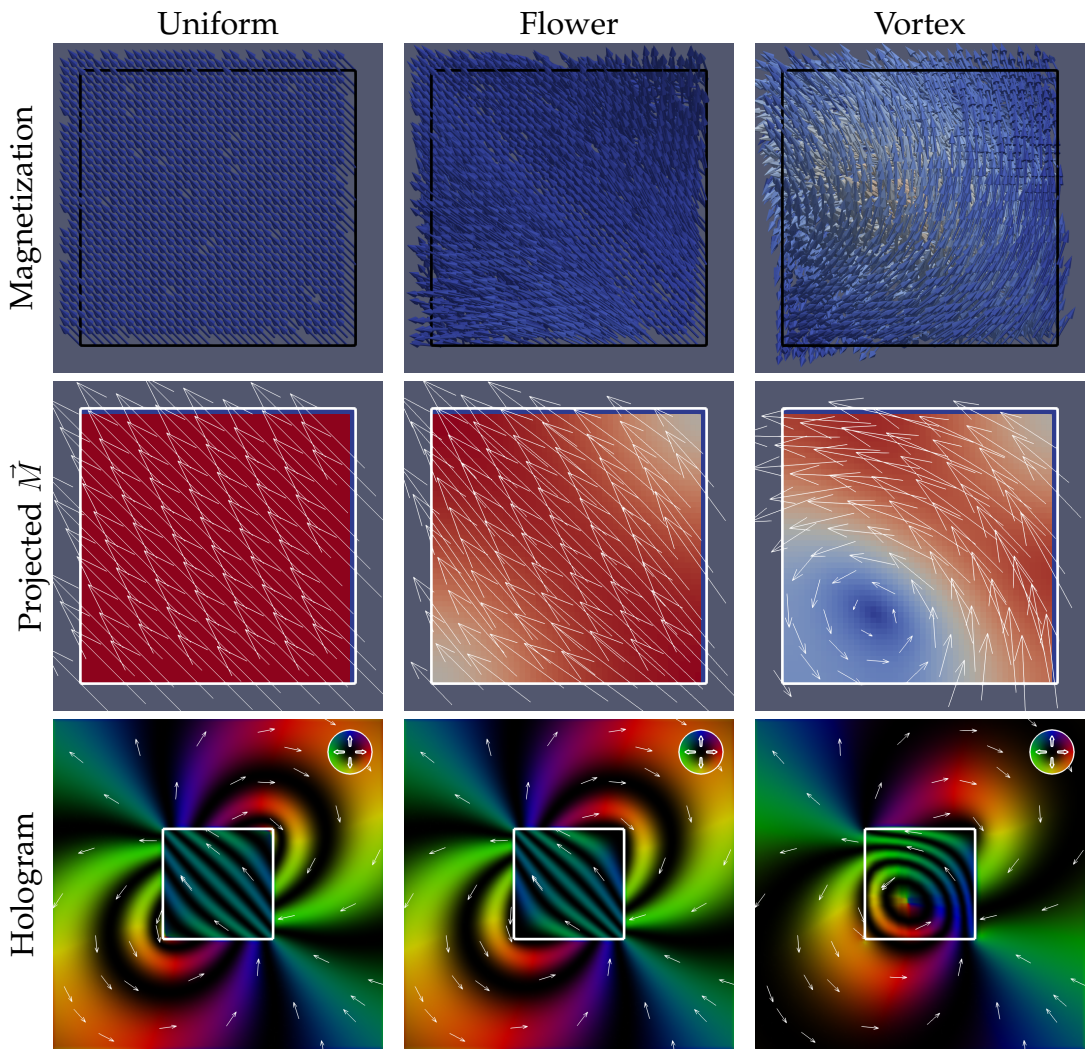

Figure 11.7: The magnetization, projected magnetization, and electron hologram for a cube of magnetite with average magnetization pointing in the [111] direction. Here, the [111] direction is the corner of the cube pointing towards the top left, and about $30°$ out of the page. Results for a uniform magnetization, a flower state, and a single vortex are shown. The vortex is a right hand vortex with core pointing in the [111] direction.

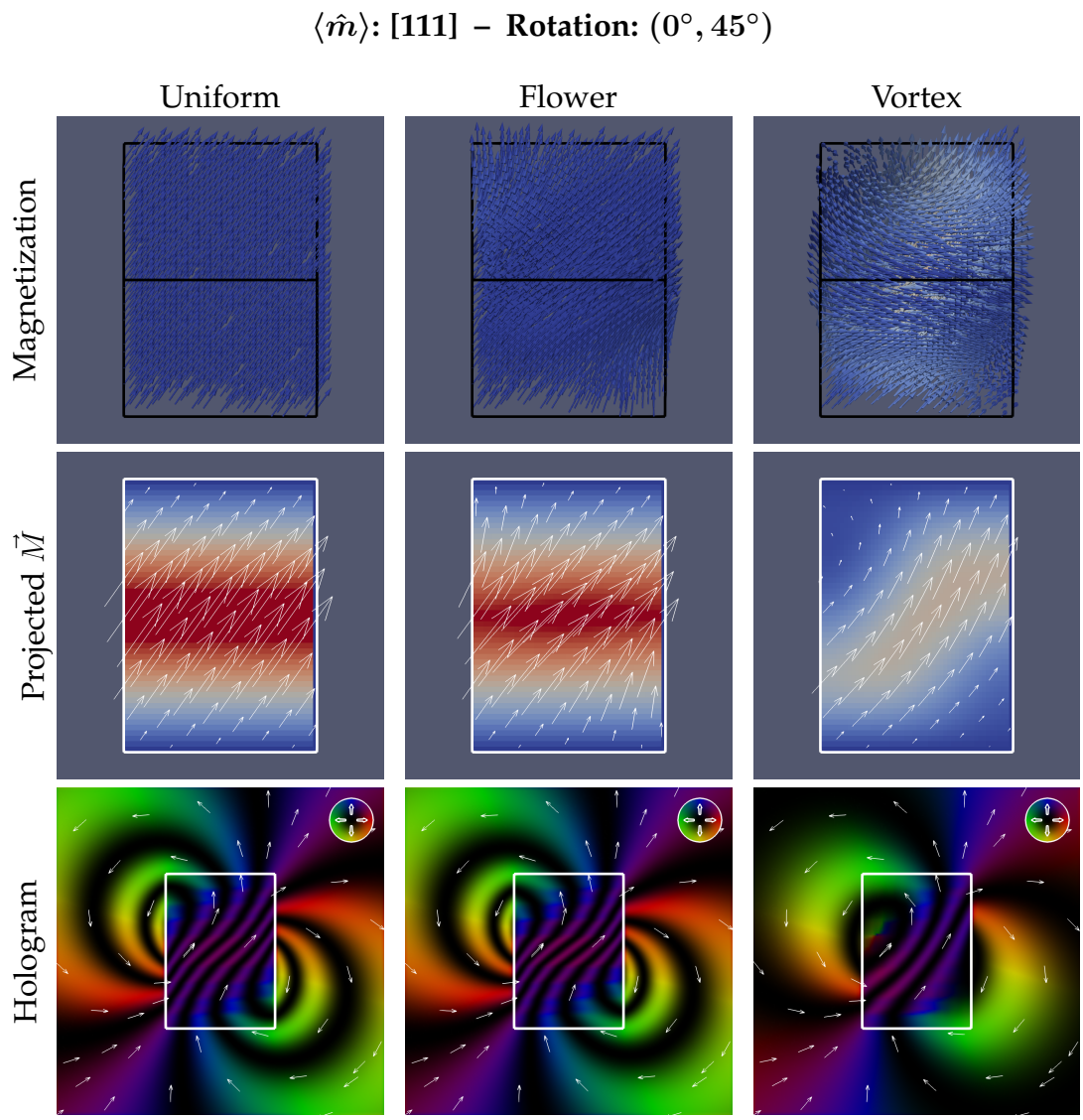

Figure 11.8: The magnetization, projected magnetization, and electron hologram for a cube of magnetite with average magnetization pointing in the [111] direction. Here, the [111] direction is the corner of the cube pointing towards the top left, and perfectly in the plane of the page. Results for a uniform magnetization, a flower state, and a single vortex are shown. The vortex is a right hand vortex with core pointing in the [111] direction.

11.1.4 Discussion

In the following discussion, we will contract the label e.g.

$$\langle \hat{m} \rangle \text{: [111] – Rotation: } (45^\circ, 0^\circ)$$

to [111] $(45^\circ, 0^\circ)$. This is done to refer more concisely to a group of images.

Uniform vs Flower State

While there is a visible difference between the SD and FS magnetizations and projected magnetizations, there appears to be little difference between their electron holograms. There is a slight difference between the uniform and the flower state in the [100] $(45^\circ, 0^\circ)$ holograms (figure 11.2). There is a slight flattening of the contours towards the center of the grain. This difference, however, would likely be unnoticeable in an experimental image, and could be indistinguishable from noise. Therefore, an electron hologram is not suitable for distinguishing a uniform state from a flower state.

Thickness Effects

In off-axis electron holography, significant effort is taken to separate changes in beam amplitude due to absorption in the material, and changes due to magnetic fields. In the uniform [111] $(0^\circ, 45^\circ)$ images (figure 11.8), we can see some very clear effects on material thickness on the electron hologram, specifically, a significant "kink" in the contour at the center of the grain. Comparing the [111] $(0^\circ, 45^\circ)$ image to the [111] $(45^\circ, 0^\circ)$ image (figures 11.8 and 11.6), it is clear the orientation of the grain and the projected thickness can still play a significant role in the resulting electron hologram. Interestingly, looking at the vortex image for [111] $(0^\circ, 45^\circ)$, the thickness effect is significantly less pronounced, while one might have expected a vortex to be less well behaved. It appears curving lines in a hologram, which could look like a curving magnetization or curving vortex core, are no guarantee of an interesting magnetization. They could simply be a manifestation of an interesting geometry.

These effects occur because the hologram relies on the projection of the magnetization, and that projection can be described as $\langle\vec{M}\rangle L_z$, where L_z is the thickness of the material at the point (x, y) of the image. For a uniform magnetization, one can expect the value of $|\langle\vec{M}\rangle|$ to be independent of (x, y), leaving only L_z as the deciding factor. So while absorption due to material thickness has been eliminated, other subtle effects due to material thickness have not.

Comparing the kinked uniform holograms versus the vortex holograms, the deciding factor appears to be the number of kings. The vortex cores have a single curvature, which we will later relate to its handedness and in-plane / out-of-plane orientation, while the uniform magnetizations have two kinks. The two kinks in, say, the [111] $(0°, 45°)$ images (figure 11.8), are due to the region of high projection magnetization towards the center of the image. Here, we are not seeing a kink, so much as an increase in the number of contours in this region. This explains, then, why the vortex core doesn't experience as much of a kinking, as the projection magnetization doesn't have a band of such high value, and the region it does have follows the direction of the average magnetization.

In-Plane vs. Out-Of-Plane Vortex Cores

Some clear in-plane SV images can be seen for [100] $(0°, 0°)$, and [111] $(0°, 45°)$ (figures 11.1 and 11.8). These are distinguished from the out-of-plane images by looking like uniform images with two roughly equal ring structures, while the out-of-plane images have either one ring, or two asymmetric rings.

The in-plane vortex images can be distinguished from the uniform images by the contour density. The uniform images have a much larger projected magnetization, and so a much denser internal and external contouring.

One significant difference between partial out-of-plane, e.g. [100] $(45°, 0°)$, and the fully out-of-plane, e.g. [100] $(90°, 0°)$, is the external field (figures 11.2 and 11.3). In the fully out-of-plane image, the external field is very weak, with little to no contouring. In the partial out-of-plane image, there is a significant external field. Indeed, given an experimental image, it may be possible to use this external field in a single vortex grain to estimate the angle of the vortex with

the image plane. By playing with the HoloMag ParaView plugin, a researcher may be able to get a feel for how the external field changes for a vortex with angle, and apply that understanding to interpretation of experimental images.

Another significant detail is the asymmetry between the two contour centers. The amount of asymmetry can be used as an indicator for how out-of-plane the vortex core is. Once the asymmetry is so large that one contour center has disappeared, we can say the vortex is very out-of-plane, if not fully out-of-plane. One must be careful in interpreting these contour centers, as the contour center coincides with the vortex center *only* when the vortex is fully out-of-plane. Similarly, there are many more ways to interpret a contour ring than an out-of-plane vortex, as an accompanying ring, even a small one, implies some in-plane component. It is also important to note that even a small asymmetry in contour ring pairs implies some out-of-plane component.

Vortex Cores and Image Asymmetries

From the images of the partial out-of-plane vortices, it can be seen that the orientation of the core plus the direction of the core produce an asymmetric bias in the in-plane magnetization, and an asymmetry in the contour centers. Figure 11.9 presents a schematic of how the asymmetry in the in-plane magnetization happens. It depicts a right hand (RH) vortex coming out of the page, and the direction of the magnetization around its outside. By right hand, we mean if you make a "thumbs up" gesture with your right hand, and align your thumb in the direction of the average magnetization of the vortex core, your fingers will point in the direction of the magnetization around the outside of the vortex. Similarly, we define a left hand (LH) vortex in a similar manner, but with a left hand "thumbs up."

The asymmetry in the magnitude of the projected magnetization can be explained as follows for a RH vortex coming out of the page: The upper magnetization tends to come out of the page and to the left. The lower magnetization tends to go into the page and to the right. By adding an extra bias towards the right, the leftward component of the upper magnetization is reduced, and that overall magnetization is moved further out of the page, further out-of-plane.

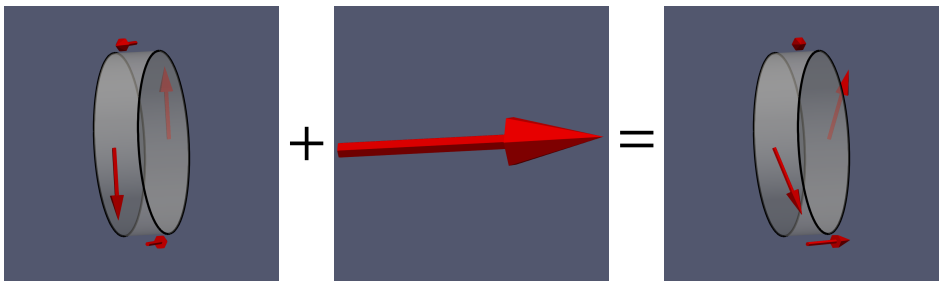

Figure 11.9: A schematic of how a perfect vortex plus a small axial bias can create an asymmetric in-plane magnetization.

Conversely, the rightward component of the lower magnetization is increased, and that overall magnetization is moved further in-plane. In this manner, we should expect an asymmetry in the projection magnetization of a vortex core. This can be seen in the result (rightmost image) in figure 11.9, and considering the in-plane magnetization it would produce.

For a RH vortex, pointed to the right, and coming out of the page (OTP), as in [100] $(45°, 0°)$ (figure 11.2), we can now explain the higher projection magnetization, and tighter contours towards the bottom of the image. We can expect to see the same thing happen for a LH vortex, pointing to the left, and OTP. This means for a LH OTP vortex pointing rightwards, the higher projection magnetization will be at the top of the image. We can expect the exact opposite to happen, for these two states if they instead point into the page (ITP). That is, rightwards facing RH ITP will have higher projection magnetization towards the top of the image, and rightwards facing LH ITP will have higher projection magnetization towards the bottom of the image.

This can be summarized for a rightward pointing core

Dense Contours	Vortex
Bottom	RH OTP or LH ITP
Top	RH ITP or LH OTP

and can be rotated around to fit the direction of the external field of the hologram being studied.

Figure 11.9 also explains where the contour rings come from, as each slice of the vortex, itself, creates a ring of magnetization. Unfortunately, looking at the direction of the internal contour ring doesn't help. Again, taking the external field pointing to the right, we expect RH ITP to cause clockwise contours; RH OTP to cause anti-clockwise contours; LH ITP to cause anti-clockwise contours; and LH OTP to cause clockwise contours. As can be seen, RH ITP has the same contour direction as LH OTP, and similar for RH OTP and LH ITP.

Due to symmetry, then, we cannot distinguish RH OTP vs. LH & ITP, or RH & ITP vs. LH & OTP. With a low enough symmetry in the grain, however, it may be possible to determine through micromagnetic modelling if the vortex is pointing ITP or OTP, by determining which of ITP of OTP is possible. If only one is possible, then with the other option eliminated, we can determine if the vortex is RH or LH. Similarly, if ITP and OTP are both possible, but only RH or LH can be nucleated, then we can tell the vortex direction. Although, symmetry suggests the vortex core direction should be less constrained by geometry.

The most important thing to note here, though, is a perfectly centered vortex pointing perfectly in rightwards, can look crooked. One could assume the [100] $(45°, 0°)$ vortex (figure 11.2) was pointing upwards, rather than rightwards. One might, at least, assume there is some upwards component. This is, however, just an effect of asymmetry of RH vs. LH and OTP vs. ITP. Even more interesting is the [111] $(0°, 0°)$ vortex (figure 11.5), where the contours would suggest the vortex core is pointing towards the top left of the image, rather than the top right. In all these cases, the external field is a clear indicator of where the vortex core is actually pointing. In these cases, it's clear. However, if the external field is not clearly visible, e.g. the vortex begins and ends somewhere inside the material, this is an important consideration. Indeed, in most cases where the vortex is not highly out of plane, the center of the contours is not indicative of the center of the vortex. The position of the center of the vortex in these cases is a result of RH/LH OTP/ITP. To determine the actual direction of a vortex core, in the absence of an external field, it is then important to be able to distinguish these orientations.

In the vortex states presented, there is another distinguishing feature. The vortex states present two lobes. One with dense contouring, which we've been

discussing, and one with low or extremely low contouring. In [100] $(45°, 0°)$, for example, the low contour is at the bottom, and in [111] $(45°, 0°)$, it's at the right (figures 11.2 and 11.6). Between these centers are contour lines that manage to escape the magnetic region, and connect directly with the external region. In all cases, the direction of these lines has roughly aligned with the direction of the vortex core, with an added curve. In this manner, rather than looking at the position of the contour centers, one should be looking at the direction of this "central" contour line to determine the direction of a vortex core, and taking the extra curving from the high contour region into account. The asymmetric contours can therefore be used to indicate an out-of-plane vortex, and the central line its in-plane direction. The position of the contour center, for partially out-of-plane vortices, should not be considered.

Chapter 12

Conclusions - Electron Holography

We've seen here two methods for simulating electron holographic images from micromagnetic models. The first is an existing approach (although as-yet unpublished) developed independently by a colleague, and the second is an original approach. Both methods are adequate for holography simulation, and both are packaged into a ParaView plugin which update the simulated hologram at near-real-time with changes in magnetization and rotation of the grain. The plugin is a highly effective tool for gaining intuition of how magnetizations translate into electron holograms. The intuition gained informed the preliminary study presented here, showing holograms for uniformly magnetized, flower state, and single vortex cubes.

We demonstrated that single vortex holograms produce counter-intuitive results. For a vortex core aligned out-of-plane, the center of the contour rings coincides with the center of the vortex. Following that observation, one might expect the center of the contours for a partially-out-of-plane vortex core to also coincide with the center of the vortex. However, we saw that it actually moves perpendicular to the motion of the core, i.e. if the core moves towards the top of the image, the contour center moves to the left or the right. Indeed, the best indicator of the direction of the core is the stray field line that passes closest to the closed rings. We also saw some information about the core orientation

is fundamentally lost. There is an ambiguity between core handedness and whether the core is pointing into or out of a hologram.

The discussion of these results highlights one important fact: one cannot make any certain conclusions about the magnetization from the electron hologram alone. This reinforces the assertion made in previous conclusion chapters: the primary method available to researchers for visualizing the 3D magnetization of 3D grains is micromagnetic modelling.

From the data presented here, any existing papers making assertions about the shape and direction of the magnetizations based on the holograms alone may need reinterpretation. In particular, any study that claims to have resolved a flower state from a single domain state should be reinterpreted, any study that declared the center of a vortex to be at the center of the contour rings (for anything other than perfectly out-of-plane) should be reinterpreted, and any study that interpreted a kink in the hologram as anything other than a uniform magnetization should be reinterpreted. Given that the thickness of the sample down the axis of the hologram isn't always easy to measure, or available, previous studies with kinked holograms may need to be completely redone with the thickness measured. In all cases, a coupled micromagnetic model would be a very quick route towards producing the correct interpretation, with the electron hologram acting as a verification of the model.

For future studies in electron holography, another option exists: tomography. It can be shown that performing an electron holographic tomograph about, say, the x-axis can recover the x-component of the $\vec{B}$ field. It might be possible to use this component to break the irresolvability features previously mentioned (e.g. distinguishing between RH OTP or LH ITP vortices). Even taking the electron hologram from two different angles might suffice to make the resolution. Further study into interpretations of electron holograms (of the sort done here) should be done to see if either of these approaches would produce enough data to make an interpretation without an accompanying model.

Of course, this is not always possible. Where an experiment requires a constant field across the grain, it might not be possible to rotate the sample to measure a second electron hologram. Similarly, given the delicacy and complexity of specimen holders for different experiments, it may be infeasible to consider ro-

tating the sample. In these cases, as always, an accompanying micromagnetic model is needed. The FEM and BEM formulations presented in this paper, the mechanical effects studied, and the volume and surface integrals evaluated should be a significant step towards including the physics necessary to model these situations, leaving little excuse to forgo a modelling step.

Part IV

Reflections

Chapter 13

Discussion

In this chapter, we will discuss some of the results, and implications of the results of this thesis. This will be a much more speculative chapter, outlining pieces of the story left out, potential issues, and future work.

This thesis focused mainly on the *scientific* work I've done during my PhD, rather than the engineering. In particular, it focuses on the theoretical physics and modelling results. A general theme has been to present some theoretical derivation of a phenomenon and then present some computer experiment using results from a model implementing that derivation. The missing link between these two chapters, in every instance presented here, has been the implementation details.

Most of the time that went into the work presented in this thesis has actually been to implement the numerical models. Rather than going into detail about the programs written, I decided instead to focus on presenting the theory behind them, and the results they produce, as that presented a more coherent story. A chapter was planned for a number of programs I wrote during my PhD, particularly some of the meshing software I wrote. Unfortunately, due to time and space constraints, it wasn't included.

There are two significant pieces of software I wrote: HoloMag for electron holography simulations of micromagnetic models, available at `bitbucket.org/poconbhui/holomag`, and MEshRRILL for generating tetrahedral meshed

geometries for use with MERRILL, available at `bitbucket.org/poconbhui/meshrrill`. I also made significant contributions to MERRILL, available at `bitbucket.org/wynwilliams/merrill` and `rockmag.org`, which I will talk about in more depth here.

13.1 Micromagnetism

MERRILL represents a significant step forward in user friendly micromagnetic simulation. It's already in widespread use in the Earth Sciences community. The addition of multi-phase solvers is, I think, a significant improvement.

Something left out of this thesis is the amount of software engineering work that went into MERRILL. As with other implementation details, it didn't add significantly to the stories I was presenting. In particular, I spent a long time cleaning it up, making it ready for contributions from outside sources. I also got it running orders of magnitude faster than before, to the point where there was some doubt about whether I had broken it with my changes, until we found the results were correct.

There is still more work to be done on MERRILL. There are already others, not just myself, making some changes to the source code, so I would consider my cleanup of the code to be a success. Ideally, MERRILL should still be maintainable if I fall out of touch with the Edinburgh group.

Some parts of MERRILL are still very messy, and I foresee mistakes being introduced, simply because someone forgot to update the various disparate parts in various disparate files that control saving and loading of variables. The matrix storage, as an example, needs to be made more generic, so *one* function can be written to save and load them and *one* type can be used to reference them. There are a lot of instances of matrices where one variable holds the matrix data, one variable holds the column indices and one variable holds the column offsets. These should be combined into a derived type. Further, there are instances of arrays which hold arrays of these matrix variables to "save" them for later loading, interpolation etc. These "save" type arrays should be holding derived types representing the arrays, and *one* clear operation should

automatically find / save / load the appropriate parts of each matrix. And *even* further, these "save" type arrays should be linked lists, so they can be dynamically resized with little memory overhead. And even further *again*, the active matrices could be pointers into this linked list, further reducing memory overhead. With these in place, running several models in parallel while sharing matrix data would be reasonably straightforward.

What I hope to convey with this convoluted phrase is that there are some fundamental architectural issues with MERRILL. To fix them would require some significant effort, and a change in the paradigm MERRILL was programmed in. Specifically, it was initially programmed in a purely procedural style, while I am advocating an object oriented style here. However, they payoff would be a faster program with a lower memory footprint, and easy parallelization. Unfortunately, however faster the program may be, however smaller the memory usage, however more maintainable by a software engineer, one must remember the audience it is aimed at: Earth Scientists. As it stands, the community has been able to use and edit MERRILL as needed, and any increase in complexity runs the risk of making it unusable and unmodifiable to the target audience.

13.1.1 Future Work

Multi-Phase Modelling

I would recommend taking full advantage of the multi-phase capabilities in MERRILL. There are numerous problems to be investigated on various combinations of different materials. So far, most multi-phase simulations have been on regularly shaped geometries. We could easily do these now for arbitrary geometries.

First, however, a number of things need to be implemented and researched. First, we need to implement surface energies. In particular, surface anisotropies to account for the magneto plastic effect along the interface planes, and surface exchange energies to account for the exchange energy of the mixed crystal. We need an FEM formulation for the surface anisotropy energy and surface an-

isotropy effective field. Given the discussion here and in Davies (2011), that should be reasonably straightforward. We also need the effective magneto-plastic anisotropy energy. I was only able to find that here thanks to the work by van der Merwe (1950) and Shive and Butler (1969). I suspect for systems that don't resemble the magnetite-ilmenite interface, this might be a more difficult problem.

Parallelization

MERRILL is suitable for parallelization on a shared-memory architecture without any major change in the implementation approach or the physics. That is, when running on a computer with, say, 64 cores, it could be parallelized reasonably well to the 64 cores. To be clear, a machine like Archer in Edinburgh with over 100,000 cores is a distributed-memory architecture, made up of a number of shared-memory nodes. Each shared-memory node on Archer contains 24 cores, which means 24 cores is the maximum efficient parallelism MERRILL could reach on this machine. The primary reason it can't be effectively parallelized on a distributed-memory system is the dense matrix used for the BEM.

I tried to parallelize MERRILL a few times with OpenMP, but couldn't quite find the bottlenecks at the time. I believe I know where the issue is now. The preconditioner for the Poisson FEM matrices does an approximate LDU factorization. Solving the L and U matrices, a step in the preconditioned conjugate gradient solver, doesn't parallelize well. A simple solution is to swap to a parallel-friendly preconditioner scheme instead. After that, parallelization with OpenMP would be trivial.

There exists another possibility for parallelism for MERRILL, which is GPU based parallelism. This would allow matrix operations to be parallelized quite well. However, memory management would be a significant issue here. In particular, a top-of-the-line (as of the time of writing) Tesla P100 GPU has around 16 GB of memory. That means the models that would run well on this platform would need to be under 16 GB. Beyond that, managing moving data on and off the card could contribute enough overhead that any performance

gain would be lost.

Abstraction

The energy calculators in MERRILL should be extracted into derived types. Similar to what was mentioned for the matrices, there is a lot of redundant spaghetti code attached to the energy calculators. This has already been done to a certain extent, and is used for loading the magnetostriction solver as a plugin. However, the core energies — demag, anisotropy, exchange, Zeeman, NEB fields (which I don't understand...) — should be similarly packaged up.

One upside to this would be the ability to add "dirty" bits to the energies. A dirty bit is a flag set to say something has been changed. For example, we might set a dirty bit for the mesh, the material parameters, or for the magnetization. That way, we might ask the energy to do any necessary precomputations (e.g. building the FEM matrices for the demag calculator) every time it's called, but only have it run if the pieces it depends upon (i.e. the mesh, the subdomains, and the material parameters) change.

The application I have in mind is that Brown's full magnetostrictive energy, including the demag-elastic effect involves the demag field. While solving for Brown's magnetostriction, it would make sense to calculate the demag field only once, however, there is no strict guarantee in MERRILL that the demag field has already been calculated when the magnetostriction solver runs.

Of course, knowing MERRILL intimately, I know the demag solver runs first, but there is no guarantee someone won't change that behaviour in the future. Making the order explicit by calling the demag solver in the magnetostriction solver, but only have it run once for a given magnetization, would be ideal.

13.2 Magnetostriction

The derivation of the magnetostrictive effect here for micromagnetic models isn't new math. However, the FEM derivation suitable for inclusion in a

FEM/BEM based model, along with the implementation is. However, the approach taken here, generalizing Kittel's model to a non-uniform magnetization is limited. In particular, it fails to account for the deformation of a material due to its demagnetization field. This is the phenomenon that causes large magnets to tear themselves apart. It also doesn't account for, say, the change in the exchange interaction due to the deformation of the material. Brown's formulation does.

The approach taken here, however, is *inspired* by Brown's. Indeed, including the extra behaviours predicted by Brown's full theory should be straightforward given the ground work laid out here. However, I would expect the demag-magnetostrictive effect to be small in the grains we're interested in, and there aren't many measurements of the effects of deformation on exchange, anisotropy etc. for the materials we're interested in. There are hardly even measurements of the elastic or magnetic constants for the materials we're interested in! In short, I'm not sure including the extra effects from Brown's theory are feasible at the moment, or that they will make a significant difference. It would still be interesting to do for a material with all the required material parameters well measured. As mentioned, some changes to MERRILL should be made before some of these can be implemented reliably.

The simulations performed here are the first of their kind, as far as I can find. In particular, an appropriate simulation of magnetostriction for non-uniformly magnetized ferromagnets, along with the deformation. They make direct, quantitative predictions about the deformations due to flower and single vortex states. A good follow up for the simulations presented here would be high resolution measurements in an electron microscope to see if my predictions are accurate. There is also a prediction made here of a remanent Wiedemann effect, where I predict the grain will assume a helical torsion due to a vortex magnetization. This might actually be a way of getting vortex orientations from electron holograms: information which might otherwise be lost.

The magnetoplastic effect presented here is also quite interesting. Of course, it is just the simplest thing I think will work, and that makes sense to me. The result, however, is that I still don't understand all the consequences and implications of the equations I've derived. A lot more work and investigation

needs to be done in this direction, as it's the only promising route I've seen for recovering Kittel's uniaxial result.

13.2.1 Future Work

FEM Implementation

The implementation used for the magnetostriction used FEniCS to build the FEM matrices. This has a significant issue that the system must be "assembled" on each run. In particular, if the material parameters remain the same from one solve to the next, the elasticity matrix can be kept as-is. However, the magnetoelastic matrix is build with contributions from the displacement vector. So any change to the magnetization implies a change to the displacement vector, meaning the FEM matrix for the magnetoelastic fields must be rebuilt.

By using a rank-3 tensor to store the magnetoelastic FEM contributions, it may be possible to keep the displacement independent of this tensor, meaning it need not be reconstructed for every new magnetization. Most of the math and a rough implementation of the necessary Fortran code has been presented in this thesis. Baking the material parameters into the magnetostrictive tensor would lower the indices needed by the tensor, potentially reducing the storage needs and calculation time. However, the implementation of dirty bits, as previously mentioned, would be needed to do this effectively.

Magnetoplasticity

The magnetoplastic coupling is a rich source of future work. I've only written down the general form. Some more work needs to be done in interpreting exactly what is described by the equations, and what can be described by them. There is also still much to do in finding solutions for the particular systems common in GeoSciences.

The magnetoplastic coupling needs to be included in an FEM model. I've shown what the surface anisotropy for a magnetite-ilmenite lamellar system looks like, on a scale suitable for micromagnetic modelling. However, I've

made no effort to formulate it in a manner suitable for surface integration for a FEM implementation. Given all the work presented here on multi-phase surface integrals etc. this should be reasonably straightforward though.

13.3 Electron Holography

The electron holography simulation software presented here has already proven to be very useful, and very popular, with results already in use in publications. Unfortunately, it's also completely untested, and prone to crashing. The results *look* good, and match some experimental data, but some more work needs to be done to add unit testing, and debug the typical cases where the code crashes or hangs.

One significant body of work left out of this thesis, actually, is the meshing work I've done. My implementation for generating the outline for the grain, for example, may well be an original contribution to computational geometry. This, along with the 2D meshing needed to generate the projection mesh has been completely glossed over, but represented a significant difficulty to be overcome, and a significant amount of time in terms of implementation.

13.3.1 Future Work

Some better testing needs to be added to HoloMag. In particular, some experimental electron holograms of a well measured geometry with a well known magnetization is needed to ensure the results generated by HoloMag are correct. While I've said repeatedly throughout this thesis that a micromagnetic model is currently the best measurement of the internal magnetization, that's not good enough in this case, because the electron hologram might be used as a verification of the model. A single domain cube of magnetite would be ideal, along with a single vortex cube.

The projection code in needs work, as it frequently crashes. Due to the complexity of generating the outline and the mesh, and the size of the libraries it relies upon, debugging is not straightforward. The environment in which

it's run — as a plugin for ParaView — also makes it quite difficult to test and debug.

13.4 Closing Remarks

It was touched upon in the various conclusions chapters in the thesis, but the work done here will have an impact on any GeoSciences application that deals with ferromagnetism like paleomagnetism, rock magnetism, and magnetic fabrics. The implications are even wider than that: it should have an impact on any field that uses ferromagnets, like biomagnetism, nano-wires, and magnetic ram to name a few. We've demonstrated throughout this thesis that we have provided many of the necessary pieces to consider all the physics occurring in a given system within the continuum approximation, along with the mechanical deformation of the crystal lattices, for ferromagnets of arbitrary shape and composition.

I hope the work done here and detailed derivations are useful in future research and to future students. I've made every effort to expand all the steps I've taken as fully as possible, which is something I would have liked to have starting out.

I also hope the various pieces of software written for this thesis finds use in research environments. I've found them quite useful in my research, and I expect others will as well.

Bibliography

μMAG (2017). *μMAG - Micromagnetic Modeling Activity Group*. URL: http://www.ctcms.nist.gov/~rdm/mumag.org.html (visited on 08/29/2017).

Abert, Claas et al. (Nov. 2013). "magnum.fe: A micromagnetic finite-element simulation code based on FEniCS". In: *Journal of Magnetism and Magnetic Materials* 345, pp. 29–35. ISSN: 0304-8853. DOI: 10.1016/j.jmmm.2013.05.051.

Aharonov, Yakir and David Bohm (Aug. 1959). "Significance of Electromagnetic Potentials in the Quantum Theory". In: *Phys Rev* 115 (3), pp. 485–491. DOI: 10.1103/PhysRev.115.485.

Almeida, Trevor P. et al. (Aug. 2016). "Direct observation of the thermal demagnetization of magnetic vortex structures in nonideal magnetite recorders". In: *Geophysical Research Letters* 43.16, pp. 8426–8434. DOI: 10.1002/2016gl070074.

Amar, Henri (July 1958). "Magnetization Mechanism and Domain Structure of Multidomain Particles". In: *Phys. Rev.* 111.1, pp. 149–153. ISSN: 1536-6065. DOI: 10.1103/physrev.111.149.

Appel, E. and Heinrich C. Soffel (Mar. 1984). "Model for the domain state of Ti-rich titanomagnetites". In: *Geophys. Res. Lett.* 11.3, pp. 189–192. ISSN: 0094-8276. DOI: 10.1029/gl011i003p00189.

Arnold, Douglas N. (Dec. 1, 2002). "Differential complexes and numerical stability". In: *Proceedings of the ICM, Beijing 2002, vol. 1, 137–157*. arXiv: math/0212391v1 [math.NA].

Azoum, K., M. Besbes, F. Bouillault, and T. Ueno (Oct. 2006). "Modeling of magnetostrictive phenomena. Application in magnetic force control". In: *Eur. Phys. J. Appl. Phys.* 36.1, pp. 43–47. ISSN: 1286-0050. DOI: 10.1051/epjap:2006102.

Azoum, Karim, Mondher Besbes, and Frédéric Bouillault (2004). "3D FEM of magnetostriction phenomena using coupled constitutive laws". In: *International Journal of Applied Electromagnetics and Mechanics* 19.1, pp. 367–371.

Brown, William F. Jr. (1966). *Magnetoelastic Interactions*. Springer. 168 pp. ISBN: 3642873987.

Brunotte, X., G. Meunier, and J.F. Imhoff (Mar. 1992). "Finite element modeling of unbounded problems using transformations: a rigorous, powerful and easy solution". In: *IEEE Trans. Magn.* 28.2, pp. 1663–1666. ISSN: 0018-9464. DOI: 10.1109/20.124021.

Butler, Robert F. and Subir K. Banerjee (Oct. 1975). "Theoretical single-domain grain size range in magnetite and titanomagnetite". In: *Journal of Geophysical Research* 80.29, pp. 4049–4058. ISSN: 0148-0227. DOI: 10.1029/jb080i029p04049.

Davies, A. J. (2011). *The Finite Element Method: An Introduction with Partial Differential Equations*. Oxford University Press, USA. ISBN: 0199609136.

Day, R., M. Fuller, and V.A. Schmidt (Jan. 1977). "Hysteresis properties of titanomagnetites: Grain-size and compositional dependence". In: *Physics of the Earth and Planetary Interiors* 13.4, pp. 260–267. ISSN: 0031-9201. DOI: 10.1016/0031-9201(77)90108-x.

Einsle, Joshua F. et al. (Sept. 2016). "Multi-scale three-dimensional characterization of iron particles in dusty olivine: Implications for paleomagnetism of chondritic meteorites". In: *American Mineralogist* 101.9, pp. 2070–2084. DOI: 10.2138/am-2016-5738ccby.

Fabian, Karl and Franz Heider (Oct. 1996). "How to include magnetostriction in micromagnetic models of titanomagnetite grains". In: *Geophys. Res. Lett.* 23.20, pp. 2839–2842. ISSN: 0094-8276. DOI: 10.1029/96gl01429.

Fredkin, D. and T. Koehler (Sept. 1987). "Numerical micromagnetics by the finite element method". In: *IEEE Trans. Magn.* 23.5, pp. 3385–3387. ISSN: 0018-9464. DOI: 10.1109/tmag.1987.1065578.

Fredkin, D.R. and T.R. Koehler (Mar. 1990). "Hybrid method for computing demagnetizing fields". In: *IEEE Transactions on Magnetics* 26.2, pp. 415–417. DOI: 10.1109/20.106342.

Halgedahl, Susan L. (1991). "Magnetic domain patterns observed on synthetic Ti-rich titanomagnetite as a function of temperature and in states of ther-

moremanent magnetization". In: *Journal of Geophysical Research* 96.B3, p. 3943. ISSN: 0148-0227. DOI: 10.1029/90jb00014.

Imhoff, J.F., G. Meunier, X. Brunotte, et al. (1990). "An original solution for unbounded electromagnetic 2D- and 3D-problems throughout the finite element method". In: *IEEE Trans. Magn.* 26.5, pp. 1659–1661. ISSN: 0018-9464. DOI: 10.1109/20.104482.

Imhoff, J.F., G. Meunier, and J.C. Sabonnadiere (Mar. 1990). "Finite element modeling of open boundary problems". In: *IEEE Trans. Magn.* 26.2, pp. 588–591. ISSN: 0018-9464. DOI: 10.1109/20.106385.

Keimpema, Aard (2008). "Electron Holography of Nanoparticles". PhD thesis. Zernike Institute for Advanced Materials, University of Groningen.

Keimpema, K., H. De Raedt, and J. Th. M. De Hosson (2006). "Electron Holography Image Simulation of Nanoparticles". In: *Journal of Computational and Theoretical Nanoscience* 3.3, pp. 362–374. DOI: doi:10.1166/jctn.2006.003.

Kittel, Charles (Oct. 1949). "Physical Theory of Ferromagnetic Domains". In: *Rev. Mod. Phys.* 21.4, pp. 541–583. ISSN: 0034-6861. DOI: 10.1103/revmodphys.21.541.

Kröner, Ekkehart (Jan. 1, 1958). *Kontinuumstheorie der Versetzungen und Eigenspannungen*. Springer. 188 pp. ISBN: 3540022619.

– (1981). "Physique des défauts = Physics of Defects (Les Houches : école d'été de physique theoretique : Session XXXV) (English and French Edition)". In: ed. by Roger Balian, Maurice Kléman, and Jean-Paul Poirier. North-Holland Publishing Company. Chap. Continuum Theory of Defects, pp. 215–315. ISBN: 0444862250.

Lehmann, Michael and Hannes Lichte (Dec. 2002). "Tutorial on Off-Axis Electron Holography". In: *Microscopy and Microanalysis* 8.06, pp. 447–466. ISSN: 1435-8115. DOI: 10.1017/s1431927602020147.

Lindholm, D. (Sept. 1984). "Three-dimensional magnetostatic fields from point-matched integral equations with linearly varying scalar sources". In: *IEEE Transactions on Magnetics* 20.5, pp. 2025–2032. ISSN: 0018-9464. DOI: 10.1109/tmag.1984.1063254.

Morrish, A. H. and S. P. Yu (Aug. 1955). "Dependence of the Coercive Force on the Density of Some Iron Oxide Powders". In: *Journal of Applied Physics* 26.8, pp. 1049–1055. DOI: 10.1063/1.1722134.

Moskowitz, Bruce M. (Apr. 1980). "Theoretical grain size limits for single-domain, pseudo-single-domain and multi-domain behavior in titanomagnetite (x = 0.6) as a function of low-temperature oxidation". In: *Earth and Planetary Science Letters* 47.2, pp. 285–293. ISSN: 0012-821X. DOI: 10.1016/0012-821x(80)90045-x.

Nagy, Lesleis et al. (2017). "Stability of equidimensional pseudo-single-domain magnetite over billion-year timescales". In: *Proceedings of the National Academy of Sciences*.

Néel, Louis (1949). "Théorie du traînage magnétique des ferromagnétiques en grains fins avec application aux terres cuites". In: *Annales de Géophysique* 5, pp. 99–136.

Shive, Peter N. and Robert F. Butler (1969). "Stresses and Magnetostrictive Effects of Lamellae in the Titanomagnetite and Ilmenohematite Series". In: *Journal of geomagnetism and geoelectricity* 21.4, pp. 781–796. DOI: 10.5636/jgg.21.781.

Tauxe, Lisa (2010). *Essentials of Paleomagnetism*. University of California Press. ISBN: 0520260317.

Tonomura, Akira et al. (1980). "Direct observation of fine structure of magnetic domain walls by electron holography". In: *Physical Review Letters* 44, pp. 1430–1433. DOI: 10.1103/PhysRevLett.44.1430.

Valdez-Grijalva, Miguel A. et al. (Feb. 2018). "The magnetic structure and palaeomagnetic recording fidelity of sub-micron greigite (Fe 3 S 4)". In: *Earth and Planetary Science Letters* 483, pp. 76–89. DOI: 10.1016/j.epsl.2017.12.015.

van der Merwe, J H (1950). "On the Stresses and Energies associated with Inter-Crystalline Boundaries". In: *Proceedings of the Physical Society. Section A* 63.6, p. 616. DOI: 10.1088/0370-1298/63/6/310.

Weertman, Johannes and Julia R. Weertman (1992). *Elementary Dislocation Theory*. Oxford University Press. 228 pp. ISBN: 0195069005.

Wells, Garth, Kent-Andre Mardal, and Anders Logg (2012). *Automated Solution of Differential Equations by the Finite Element Method: The FEniCS Book (Lecture*

Notes in Computational Science and Engineering). Springer. ISBN: 3642230989. DOI: 10.1007/978-3-642-23099-8.

Williams, Wyn and David J. Dunlop (Feb. 1989). "Three-dimensional micromagnetic modelling of ferromagnetic domain structure". In: *Nature* 337.6208, pp. 634–637. ISSN: 0028-0836. DOI: 10.1038/337634a0.